Universidad de Oviedo

Física Fundamental y Aplicada

AEROSOL NANOPARTICLE SIZE SPECTROMETRY AND CLASSIFICATION METHODS BASED ON CORONA UNIPOLAR CHARGING

maidá domat rodríguez

MAIDÁ DOMAT RODRÍGUEZ

AEROSOL NANOPARTICLE SIZE SPECTROMETRY AND CLASSIFICATION METHODS BASED ON CORONA UNIPOLAR CHARGING

Universidad de Oviedo

Física Fundamental y Aplicada

SUPERVISORS:

Dr. D. Julio Manuel Fernández Díaz

Prof. Dr.-Ing. Frank Einar Kruis

Maidá Domat Rodríguez:*Aerosol nanoparticle size spectrometry and classification methods based on corona unipolar charging*
Tesis Doctoral

SUPERVISORS:
Dr. D. Julio Manuel Fernández Díaz
Prof. Dr.-Ing. Frank Einar Kruis

UNIVERSIDAD DE OVIEDO

JUNIO 2014

Dedicated to the loving memory
of M^{a} Ángeles Rodríguez Braña

Out of the cradle
onto dry land...
here it is standing...
atoms with consciousness
... matter with curiosity.

Stands at the sea...
wonders at wondering... I...
a universe of atoms...
an atom in the universe.

— Richard P. Feynman

ACKNOWLEDGMENTS

This thesis is the final part of a long (longer than it should) and hard (harder than it seemed) work, which could not be performed without the help and support of several people and institutions. Therefore I would like to thank many persons who have direct or indirectly helped me to accomplish a work that seemed never end. There have been so many people during my academic life from who I've learned something that I'm afraid of forgetting someone, but I'll try to name the most of them without taking another 200 pages.

I wish to start from my supervisor, Julio Manuel Fernández Díaz, who have invested plenty of time and effort to lead this project to a successful end.

Special thanks to Mª Ángeles Rodríguez Braña, who has perpetually encouraged me to complete this work and was always available whenever I needed some help. I have to thank her, besides from the academic life, the important lesson of strength, courage and passion for their work that has given us all, and for being a great company in conferences, a great teacher and a better friend.

I shall not forget to mention professors Rosario Díaz Crespo, Laura Elbaile and Blanca Hernando, who always were concerned about my progresses despite being from different groups.

Since most of the work presented here was performed in the University of Duisburg-Essen, I want to show my gratitude to Prof. Dr.-Ing. Frank Einar Kruis for accepting me in their laboratories and being always ready to contribute with his experience and clarifying ideas, even long after leaving the group. Without doubt, he has been fundamental for the completion of this work.

I have to thank the complete group of NST, leaded by Prof. Dr. Roland Schmechel, for his warm acceptance and help, specially Marcel Rouenhoff, Shubbra Kala, Aruna Ivalluri and Aleksandar Nedic for their inestimable back up at the lab, Christoph Kleinert and Felix Bensel for advice in technical issues and speed and precision at work. And of course, for the enjoyable lunch breaks with them, Claudia Busch and Heidi Giesen. Thanks as well to Nkwenti L. Azong-Wara, who collaborate with me in the inversion problem and whose input was key to develop the program.

I want to mention also Esther Hontañón for her recommendation and advice when I applied to go to Germany, as well as for their help at the laboratory in Mieres.

Thanks as well to the University of Oviedo, where the main part of my research was done, and the Spanish Education and Science Department, which has funded my fellowship under grant BES-2006-12469 and supported the research project CGL2005-05244 in which I have participated.

Likewise, thanks to all my friends, starting from my colleagues in the University of Oviedo (Bárbara, Carla, Víctor,...), colleagues during the PhD, Pablo (*por hacer*

de Pepito Grillo), Rosalía (*podemos!*), Tatiana, Irene and Borja, and many others with whom I've enjoyed our "physicists dinners".

My close friends Ana, Vane, Arabela, Carla, Sarus, Sarina (*cachorras*), Cuetos, Nico, María, Bego, África, a Corne (*puertuchiqueños*), Guti, Fran, Martin, Vera, Cris, Michael, Björn (*"helau!"*), Lucía (*kombat-mate*), Sonia, Andrea and the rest of my *École troupe* and many others (sorry if I've forgotten you!), for giving me such a great support and endless fun all this good years and the ones to come.

And last but not least, I would like to thank my parents, Amparo and Akram, and my grandparents, Hortensia and Efrén, for his support, patience and confidence. Thanks to them I can truly say that they are the giants on whose shoulders I rise.

* * *

ABSTRACT

The accurate determination of the particle size distribution function is a fundamental problem in aerosol science. It is usually determined by electrical mobility-based measurements, where the electrical charge to particles is usually applied by radioactive bipolar chargers, although new electrical charging techniques are arising.

An efficient and versatile unipolar corona charger was developed. It has separated ion generation and particle charging regions. Ions are generated by a needle electrode and then driven to the charging region by a sheath flow in order to reduce the electrostatic loss of nanoparticles. The distance of the electrode to the walls can be adjusted by a micrometer, being a much more efficient way to regulate the $N_i t$-product, and therefore the intrinsic and extrinsic charging efficiencies. Experimental results indicate that the generated ion current is practically the same independently of the variation in applied voltage or corona current. The charging efficiency can vary from high values, comparable to the higher efficiencies from the state of the art corona unipolar chargers, to lower levels such as reached with bipolar chargers.

An extended model for unipolar charging of nanoparticles based on the Fuchs birth-and-death theory is developed. As a novelty, it includes both diffusional and electrical losses for particles and ions. Electrical losses are modeled by inclusion of a radial electric field, which is caused by space charge associated to the ion and charged particle concentration in the charging region. The model predicts the initial ion concentration and mean radial electric field from data of charge distribution fractions, and thus the figure of merit of the particle chargers, the $N_i t$-product. It was successfully applied to experimental results from three different unipolar chargers, including the corona device presented in this work. It is a general purpose model, independent of the geometry of the charger, that can be used to assist the operation of unipolar chargers, e.g. by predicting charging efficiencies for particle sizes which are not experimentally attainable and reducing then the complexity of the experimental process.

Once the characteristics of the particle charging are defined, the inversion of the particle size distribution from electrical mobility measurements is analyzed. Three different methods are adapted for a dot-matrix approach to the problem, especially for non-square or singular matrices, and applied to the electrical mobility measurements from fixed or scanning voltages. Multiple charged particles, diffusion losses, arbitrary voltage steps and noise have been considered, which results in non-adjoining and overlapping transfer functions. The individual contributions of the transfer functions in each size interval was geometrically estimated, requiring only its characteristic mobilities. The choice of the number of data and size channels is shown to be especially important, since it alters the rank of the kernel matrix and the accuracy of the inverted results. The methodology is applied to unipolar and bipolar chargers, being extrapolable to any charging method with a defined charge distribution, and retrieval of the singly charged particle distribution and mean charge from a Tandem-DMA configuration was successfully demonstrated.

RESUMEN

La determinación precisa de la función de distribución por tamaños de partículas es un problema fundamental. Normalmente se determina mediante medidas basadas en la movilidad eléctrica de las partículas, donde la carga eléctrica se aplica a las partículas por lo general mediante cargadores bipolares radiactivos, aunque están surgiendo nuevas y eficaces técnicas de cargado eléctrico.

Se ha desarrollado un cargador corona unipolar eficiente y versátil. Tiene estructura de cargado indirecto, con las zonas de ionización y carga separadas. Los iones se generan mediante un electrodo con forma de aguja y son conducidos a la región de carga por un flujo de aire auxiliar con el fin de reducir la pérdida electrostática de las nanopartículas. La distancia del electrodo a las paredes se puede ajustar por un micrómetro, variando así el voltaje inicial y el producto $N_i t$, y por tanto también las eficiencias de carga intrínseca y extrínseca. Los resultados experimentales indican que la corriente iónica generada es prácticamente independiente de la variación en el voltaje o corriente aplicados al electrodo de descarga. La eficiencia de carga puede variar desde valores altos, comparables a los cargadores más eficientes presentados en la literatura, a niveles similares a los alcanzados con cargadores bipolares.

Se ha desarrollado asimismo una extensión del modelo para la carga unipolar de las nanopartículas basado en la teoría de balance *creación-destrucción* de Fuchs. Incluye tanto pérdidas por difusión como eléctricas para partículas e iones. Las pérdidas eléctricas se representan mediante la inclusión de un campo eléctrico radial que es causado por la carga espacial asociada a la concentración de iones y partículas cargadas en la zona de cargado. El modelo es capaz de predecir la concentración iónica inicial y el campo eléctrico radial medio a partir de los datos de la distribución de carga, y por tanto obtener el parámetro clave de los cargadores de partículas, el producto $N_i t$. Su aplicación a los resultados experimentales de tres cargadores unipolares diferentes, incluyendo el dispositivo de descarga corona presentado en este trabajo, ha resultado satisfactoria. Se trata de un modelo de propósito general, independiente de la geometría del cargador, que puede utilizarse en la simulación del funcionamiento de cargadores unipolares, por ejemplo, mediante la predicción de la eficacia de carga en tamaños de partículas que no son experimentalmente accesibles, reduciendo por tanto la complejidad del proceso experimental.

Una vez que las características del cargado de partículas están definidas, se analiza la inversión de la distribución de tamaños de las partícula a partir de medidas de movilidad eléctrica. Se han adaptado tres métodos diferentes a un enfoque matricial del problema, especialmente para matrices singulares, y se aplican a las medidas de movilidad eléctrica mediante voltajes fijos o variables en modo de escaneo. Se han tenido en cuenta la carga múltiple de partículas, las pérdidas por difusión, la variación arbitraria de voltajes y el ruido o error experimental en las medidas, que se traduce en funciones de transferencia no contiguas y superpuestas. Las contribuciones individuales de las funciones de transferencia en cada intervalo de tamaño se estimaron geométricamente, requiriendo sólo sus movilidades características para ello. La elección del número de medidas y de datos de salida es especialmente importante, ya que altera el rango de la matriz del núcleo y la exactitud de los resultados de la inversión. La metodología se aplica a cargadores unipolares y bipolares, siendo extrapolable a cualquier método de carga con una distribución de carga definida. También se consiguió la estimación de la distribución de partículas con una sola carga y la obtención de la carga media a través de una configuración experimental de Tándem-DMA.

CONTENTS

LIST OF FIGURES

LIST OF TABLES

LISTINGS

ACRONYMS

CPC	Condensation Particle Counter
CN	Condition Number
DBD	Dielectric Barrier Discharge
DDE	Difference-Differential Equation
DE	Differential Evolution
DMA	Differential Mobility Analizer
DMPS	Differential Mobility Particle Sizer
EAA	Electrical Aerosol Analyzer

ESP	Electrostatic Precipitator
FMPS	Fast Mobility Particle Sizer
FWHM	Full Width at Half Maximum
GSD	Geometric Standard Deviation
GCV	Generalized Cross-Validation
LC	L-Curve
LS	Least Squares
MSE	Mean Squared Error
NNLS	Non-Negative Least Squares
NTP	Normal Temperature and Pressure
PSD	Particle Size Distribution
RMSE	Root Mean Square Error
SIM	Semi-Implicit Method
SMAC	Surface-discharge Microplasma Aerosol Charger
SMPS	Scanning Mobility Particle Sizer
SVD	Singular Value Decomposition
TDMA	Tandem Differential Mobility Analysis
TF	Transfer Function
a	particle radius
C_c	Cunningham slip correction factor
c_i	mean thermal velocity of ions
C_{in}	inlet concentration of uncharged aerosol before charger
C_{out}^{off}	outlet concentration with the charger turned off
C_{out}^{on}	outlet concentration with the charger turned on
C_{out}^{q}	outlet concentration of charged particles with charger on
C_{out}^{0}	outlet concentration of uncharged particles with charger on
D_{gap}	vertical distance from needle tip to output of ionizing region in corona
D_p	particle diameter
D_{pg}	geometric mean diameter

E	electric field strength
e	elementary unit of charge (1.602×10^{-19}) C
F_d	Stokes drag force
ff	flow factor
I_c	corona current
I_{in}	ion current in the discharge region
I_{out}	current at the output of the mixing region
J	current density
k_B	Boltzmann's constant (1.380×10^{-23}) J/K
K_n	Knudsen number
L_{diff}	losses by diffusional factors
L_{el}	losses by electrical factors
L_T	total losses
m	number of measurement intervals
M_m	instrument response for mobility measurements
M_g	molecular weight of the gas
M_i	molecular weight of the ions
$M_p(i)$	measured aerosol number concentration
n	number of output intervals
N_A	Avogadro's constant (6.022×10^{23} mol^{-1})
$N(n)$	real aerosol number concentration
N_p	total number of particles in a PSD
N_i	total number of ions
P	pressure
P_n	penetration
Pe	Peclet number
q	number of elementary charges on a particle
Q_i	ion dilution flow
Q_a	aerosol flow

Q_{ex}	excess flow
Q_m	aerosol monodisperse flow
Q_{sh}	sheath flow
S_h	Sutherland constant (111 K for N_2, 120 K for air)
T	temperature
u	velocity
t_{res}	residence time
V_0	corona onset voltage
V_c	corona voltage
V_{cv}	visual critical voltage
V_{sp}	spark voltage
Z_c	centroid mobility of transfer function
Z_i	electrical ion mobility
Z_p	electrical particle mobility
$\mathcal{D}$	diffusion coefficient
δ	limiting sphere radius
ϵ_0	dielectric constant in vacuum (8.854×10^{-12}) F/m
ϵ	dielectric constant of particles
ϵ_{int}	intrinsic charging efficiency
ϵ_{ext}	extrinsic charging efficiency
ϕ	interaction potential
$\mathcal{K}$	kernel matrix
λ	mean free path (68.0×10^{-9}) nm
λ_r	regularization parameter
μ	dynamic viscosity (1.8×10^{-5}) Pa s
ρ	space charge density
Ω	Transfer Function

1

INTRODUCTION

Aerosols are generally defined as a suspension of fine solid particles or liquid droplets in a fluid, whose mass and size are large compared to the molecules around them. From here on, it will be assumed that the environment in which the aerosols are embedded is a gas.

Aerosols can be generated either in natural or artificial processes, basically by conversion of gases to particles or by disintegration of solids and liquids. For example, natural process of generation of aerosols are volcanic emissions, fires, sea sprays, etc. The artificial generation of aerosols is due both to unwanted side effects (chemical and metallurgical industries, vehicle emissions) and to controlled generation in industrial and medical processes (drug inhalers, manufacture of materials, cleaning processes).

1.1 ULTRAFINE PARTICLES

The aerosol can be seen as a population of particles, each consisting of by a whole number of molecules or monomers. If they are of the same chemical species, it is said that the spray is monocomponent, and if it has different species, multicomponent. Similarly, an aerosol containing particles of various sizes is said to be *polydisperse*, otherwise is said to be *monodisperse*. It is the general case that occurs in nature, and their classification is often used histograms of sizes, representing number of particles binned by size.

Measurement capabilities are required to gain understanding of the particle dynamics. Important physical properties of airborne particles are: size, shape, number, mass, surface area and density. The sizes of the particles are of great interest because they determine the location and amount of airborne particles deposited [111].

The study of chemical and physical properties of aerosols is a very topical subject nowadays with applications in diverse fields, such as [60, 147]:

- environment (emission control from traffic, industry, and energy production, air quality control)
- meteorology and climate (cloud formation and precipitation, greenhouse effect)
- medicine (inhalation of particles, biotechnology, pharmaceutical products)
- industrial processes (nanotechnology, semiconductor manufacturing, instrumentation, clean room technology, materials synthesis)

Knowledge of the properties of aerosols is of practical importance. However, a discrete method of characterization is useless in practice due to the huge range of particles sizes and concentrations that even small sample of aerosols has.

Among them, ultrafine particles ($D_p \lesssim 20\,\text{nm}$) have several remarkable properties that distinguish them from larger particles. Firstly, their weigh is practically negligible, so they can stay airborne for a long time and easily move by small pressure differences, and diffusion has an important effect on them. Secondly, they have generally huge surface areas, which has influence in phenomena such as catalyst activity, light scattering, sintering properties, electrostatic properties, moisture retention and many other, as well as concerns about their effects on human health. A number of toxicological studies have confirmed that ultrafine particles are able to penetrate deep into the lung where they have deposition efficiencies as high as 50%. Thirdly, they have very large number per unit mass. For example, in $1\,\text{cm}^3$ of air at Normal Temperature and Pressure (NTP) conditions (293.15 K, 101.325 kPa), there are about 2.5×10^9 molecules of submicron sizes, of which about 10^3 are electrically charged, as well as large numbers of particles that can range from 10^3 in relatively clean air to 10^5 in polluted air. The range of diameters covered by these particles makes a differences of several orders of magnitude in mass or volume. For this reason, these sets of particles are usually represented by a continuous distribution function in a variable associated with the size of the particles, known as *spectrum* or Particle Size Distribution (PSD). Measurement capabilities are required to gain an accurate understanding of these particle aggregates.

1.2 PARTICLE SIZE DISTRIBUTION

Many physical properties of aerosol depend on the particle size, thus the size distribution is often needed in order to obtain information on different aerosol-related processes. Particle size distributions are analogous to non-normalized probability density functions.

The number of particles per unit volume $\mathrm{d}N$ having diameters in the range D_p to $D_p + \mathrm{d}D_p$ is $dN = n(D_p)\mathrm{d}D_p$, where $n(D_p)$ is the *number distribution function* of aerosol particles. The total number of particles per unit volume, i.e. the *total number concentration* is

$$N = \int_0^\infty n(D_p)\mathrm{d}D_p. \tag{1.2.1}$$

In some contexts is it useful to express the distributions as functions of other quantities than diameter. For example, it can be calculated the mass of particles per unit volume, $\mathrm{d}M$, in the size range $[D_p, D_p + \mathrm{d}D_p]$ considering the mass as the weight function in the above eq. (1.2.1). Similarly, the dispersion of aerosol is sometimes expressed in terms of the surface area and volume distributions $f_S(D_p)$ and $f_V(D_p)$, respectively.

To characterize the particles by size, regardless of shape, we introduce different equivalent diameters, such as aerodynamic diameter, Stokes diameter, electrical mobility equivalent diameter, diffusion equivalent diameter, etc. The *equivalent diameter* is defined then as the diameter of a sphere that would have the same value of a particular physical property as that of the irregular particle. Here, it will be considered all particles having spherical shape to use simpler geometric relationships.

The dispersion of certain property of an aerosol is sometimes expressed with *cumulative distribution functions*. A cumulative number distribution gives the number concentration of particles with diameter larger or smaller than a given D_p, defined as:

$$C_{N_1} = \int_{0}^{D_p} n(D_p)\mathrm{d}D_p \quad \text{or} \quad C_{N_2} = \int_{D_p}^{\infty} n(D_p)\mathrm{d}D_p,$$

being $C_{N_1}(D_p) + C_{N_2}(D_p) = N_{\mathrm{tot}}$, the total number concentration.

Most aerosol distributions show asymmetric tails in the graphs. This causes a bad adjustment of the normal distribution functions, since they are symmetrical. Another problem is that since the size range may cover several orders of magnitude, the normal size distribution function requires some values to be negative, which is physically impossible. Statistics based on lognormal distributions, as shown in eq. (1.2.2), are frequently the most suitable method for fitting real PSD. This mathematical form meets the physical implications of the distribution: is a function only defined for positive diameters, null at zero (since there are no particles of $D_p = 0$) and tends to zero as diameter tends to infinity. If the data range is narrow, the lognormal distribution approximates a normal distribution.

$$\frac{\mathrm{d}N}{\mathrm{dln}D_p} = \frac{N_{\mathrm{tot}}}{\sqrt{2\pi}\ln\sigma_g} \exp\left[-\frac{\left(\ln D_p - \ln D_{\mathrm{pg}}\right)^2}{2\ln^2\sigma_g}\right]. \tag{1.2.2}$$

Besides of the total number of particles N_{tot}, this distribution is characterized by two parameters: one locates the center or midpoint of the distribution and the other its width or magnitude. They are the geometric mean diameter (D_{pg}) and the Geometric Standard Deviation (GSD), σ_g, respectively expressed as:

$$\ln D_{\mathrm{pg}} = \frac{\sum_{i=1}^{n} N_i \ln D_{\mathrm{p,\,i}}}{N_{\mathrm{tot}}}, \tag{1.2.3}$$

and

$$\ln\sigma_g = \sqrt{\frac{\sum_{i=1}^{n} N_i \cdot (\ln\, D_{\mathrm{p,\,i}} - \ln\, D_{\mathrm{pg}})^2}{N_{\mathrm{tot}}}}. \tag{1.2.4}$$

.

In a lognormal distribution, 67% of the particles fall within a range $\left({}^{D_{pg}}/_{\sigma_g},\, D_{pg}\sigma_g\right)$, and 95% of the total fall between $\left({}^{D_{pg}}/_{\sigma_g^2}\,, D_{pg}\sigma_g^2\right)$. It has also the useful property that when the cumulative distribution function is plotted, the diameter corresponding to the cumulative fraction of 0.5 is the geometric mean diameter.

1.3 CHARGED AEROSOLS

The electrical behavior of aerosol particles is a fundamental factor to consider in motion of particles. Firstly, because in nature almost all aerosols have electrical charge. Secondly, because the electric field generated by these charges affect greatly to its motion, so that it can create a force on the particle that overwhelms other forces present, such as gravity.

The analysis of these electrical forces offers a wide range of study because it is not yet fully understood, and there is an interest for application in several fields, ranging from the medical to the industrial environment. For instance, in electrostatic precipitation, which is since 1900 one of the main methods for gas cleaning [47]. In fact, the first accurate measurement of the elementary charge of an electron, given by the physicist Robert A. Millikan in 1909, was measuring the charge distribution present in aerosol particles.

The trajectories of particles in an electrical field depend not only on the magnitude of the field, but also on the number of charges and sign that each particle carries. The electric force on a particle is defined as:

$$\vec{F} = n\vec{E}, \tag{1.3.1}$$

where $n = qe$, is the particle charge and q the units of elementary charge $e = 1.602 \times 10^{-19}C$. The drag force (in this case fluid friction) given by Stokes Law:

$$F_r = \frac{3\pi\mu D_p u_e}{C_c(D_p)}, \tag{1.3.2}$$

being μ the dynamic viscosity of the fluid and C_c the Cunningham correction factor (as we assume particles smaller than 1 μm, turbulence is almost negligible).

When balancing the electrical and drag forces on the particle, is obtained a steady migration velocity given by:

$$\vec{u}_e = \frac{qe\vec{E}}{F_r}, \tag{1.3.3}$$

being used to compare the movement of particles with different sizes and charges.

We define the electrical particle mobility (Z_p) as the ratio of the speed achieved within the electrical field and the magnitude of such a field:

$$Z_p = \frac{|\vec{u}_e|}{\left|\vec{E}\right|} = \frac{qe}{F_r} = \frac{qeC_c(D_p)}{3\pi\mu D_p}. \tag{1.3.4}$$

This equation relates the behavior of the particle in an electric field depending on the diameter. Through the mobility analysis, the particle size is represented by a sphere with the same mobility as the particle. The equivalent diameter is called here the *mobility diameter*. In the sub micrometer range, gravitation and inertia are negligible. Therefore the velocity of a particle is independent of its mass. However it is not a direct relation, since different combinations of sizes and number of charges can lead to the same value of mobility. Moreover, it gets more complicated when the field changes in time and space $\vec{E} = E(x, y, z, t)$, or q varies in time for the same particle or from particle to particle.

1.4 ELECTRIFICATION OF PARTICLES

Aerosol particles, whenever they are natural or artificially generated, are to some extend electrically charged, either as a result of the way the aerosol particles are produced or due to the environment the aerosols are in. Since particle size distribution is commonly classified by the electrical mobility, a known net charge distribution must be imposed on the aerosol. Therefore, charging mechanism shall be determinant on prediction of particle size.

There are different methods to provide electrical charge to a set of particles [47, 107]. These methods are resumed in four mechanisms: *flame charging, static electrification, diffusion charging* and *field charging*, and can act alone or in combination. In the last two, the aerosol particles are charged due to collisions with ions. Since ions will be the principal mechanisms of particle charging in this study, their working theory will be briefly introduced.

- **Diffusion charging** occurs at very low or in the absence of an electric field and is independent of particle properties. It is the dominant charging process for small aerosol particles (below $0.1\,\mu m$), even in the presence of an electrostatic field. The physical background is that gaseous ions diffuse (by Brownian motion) toward the surface of the particles and impact upon the surface by chance. The charge carried by these ions is transferred to the particles. When ions accumulate on an aerosol particle, the electrical field becomes stronger and the chance that new ions impact on the particle becomes smaller.

  For a spherical particle of diameter D_p and a constant ion density of mean thermal speed c_i, the number of charges acquired by the particle can be calculated by the expression [47, 140]:

  $$q_{\text{diff}}(t) = \frac{2\pi\epsilon_0 k_B T}{e^2} D_p \ln\left(1 + \frac{c_i e^2}{8\epsilon_0 k_B T} D_p N_i t\right). \tag{1.4.1}$$

  In theory there is no upper limit on this mechanism of charging since the above equation has no limit when $t \to \infty$. Diffusion charging of particles can be unipolar or bipolar depending on the polarity of the ions colliding to the particles.

  - *Bipolar diffusion charging* leads to a charge equilibrium, which has low charging efficiencies [60].

  - *Unipolar diffusion charging* has advantages over bipolar diffusion as it does not reach an equilibrium charge distribution, which may enable the attainment of a higher charging efficiency. The charging efficiency results a key factor for high sensitivity of size measurement through the electrical mobility classification.

- **Field charging** occurs in the presence of a strong electric field and is dependent on particle properties. Ions follow the electric field lines, colliding and releasing the charge on the aerosol particle. The charged particle will repel the closer ions, altering the configuration of the field and causing a decrease in charging rate until the saturation charge of the particle is reached.

  When diffusion charging can be neglected, the number of charges acquired by a particle of diameter D_p and dielectric constant ϵ within an electric field E is expressed [47, 140]:

  $$q_{\text{field}}(t) = q_{\text{sat}} \frac{\pi K_E e Z_i N_i t}{1 + \pi K_E e Z_i N_i t}, \tag{1.4.2}$$

  where $K_E = {}^1\!/_{4\pi\epsilon_0}$ to simplify notation and q_{sat} is the saturation charge, the maximum charge attained after sufficient time. This term is proportional to the surface area of the particle and to the electrostatic field strength, and depends on the material of the particle, as can be seen in eq. (1.4.3):

  $$q_{\text{sat}} = \frac{3\epsilon}{2+\epsilon} \frac{E D_p^2}{4 K_E e}. \tag{1.4.3}$$

- **Combined diffusion and field charging.** In an applied electric field, charging depends on both the orderly flow of ions and on their random motion within the electric field, so a complete theory should consider both simultaneously: $q_{\text{fd}} = q_{\text{field}} + q_{\text{diff}}$.

  However there are some difficulties due to their differences. The most remarkable is that diffusion charging has no upper limit on the number of charges that a particle can acquire, while in the field charging exists a limit and is well defined. For particles bigger than $1\,\mu\text{m}$, field charging is dominant, while for ultrafine particles ($D_p < 0.1\,\mu\text{m}$), diffusion charging becomes relevant due to thermal diffusion. In the size range in-between, both mechanisms show varying degree of effect.

There are several methods to generate ions for unipolar diffusion charging in a gas: *photoemission from UV-light radiation*, *electrical discharge* (such as *corona discharge* or *Dielectric Barrier Discharge* (DBD)), and *radiation from α-, β- or γ- ray (X- ray) sources*.

Different chargers have been used for charging aerosol particles, based solely on field or diffusion charging or on a combination of the two charging mechanisms. Commonly used chargers are radioactive chargers, being corona chargers among the most common alternative to the previous, since it is a cheap and easy technique that can produce high ion concentrations.

Corona discharge is produced by a nonuniform electrostatic field between two two asymmetric electrodes, such as that between a needle or wire (high curvature) and a plate or a concentric tube (low curvature compared to the other one). The high curvature ensures a high potential gradient around one electrode, so that the electric field creates a conductive region, a plasma around the electrode.

Air and other gases can undergo electrical breakdown when the electric field strength is high enough. This breakdown occurs is in a very thin layer at the electrode's surface. In this region, electrons have sufficient energy to knock an electron from gas molecules creating positive ions and free electrons. If the flow of aerosol particles is directed to this field, is then charged by attachment of ions produced by the corona discharge. Ions can be transported by the electric field, a gas flow and/or by thermal diffusion, and the amount of ion deposition on the particle surface depends on resident time, particle radius and shape, electric field, etc.

Coronas may be positive or negative, determined by the polarity of the voltage applied on the highly-curved electrode The physics of positive and negative coronas are strikingly different, as a result of the great difference in mass between electrons and positively charged ions. For instance, under corona processes in air, a negative corona generates much more ozone than the positive one.

1.5 MEASUREMENT TECHNIQUES

In general, instruments used for the determination of size distributions are called *aerosol spectrometers*. There are several types, based on different principles of the aerosol particles:

- **Diffusion systems.** The net transport of particles from higher particle concentration to lower concentrations is called *diffusion,* while collisions of gas molecules against small particles is called *Brownian motion*. Both are characterized by the particle diffusion coefficient,$\mathcal{D}$, that is related to the particle size as:

  $$\mathcal{D} = \frac{K_B T C_c}{3\pi\mu D_p}. \tag{1.5.1}$$

  The basic principle of diffusion batteries is to introduce the aerosol into a system where diffusional deposition from a laminar aerosol flow to the surfaces takes place and measure the input and output particle concentrations to obtain information on diffusion coefficient and particle size [144, 107]. It can be seen from eq (1.5.1) that the diffusional deposition rate depends on particle size. The diffusional loss of particles can be determined theoretically as [47, 107]:

  $$P_{\text{diff}}(\phi) = \frac{N_{\text{output}}}{N_{\text{input}}}, \tag{1.5.2}$$

  where the dimensionless parameter ϕ is defined for cylindrical tubes as:

  $$\phi = \frac{L\mathcal{D}}{Q}. \tag{1.5.3}$$

  Diffusional deposition does not depend on the tube diameter for a given flow rate, which means that only residence time determines the amount of particles lost by diffusion, given by the length or flow rates applied to the experiment.

- **Inertial systems,** such as *impactors,* separates particles by their aerodynamic diameter (the diameter of a unit-density sphere with the same gravitational settling velocity as the particle of interest). Their operation principle is rather simple, a jet of airborne particles is directed against a collection plate. The streamlines of the gas flow bend near the plate and some particles cannot follow them, impacting on the collection plate. The time resolution of the conventional impactors is poor and they are not suitable for real-time measurements due to relatively long collection times and time-consuming gravimetric analysis [144, 134].

- **Optical systems.** They base their operation principles in the fact that aerosol particles illuminated by a light beam absorb and scatter some fraction of the incident beam intensity. Light scattering and absorption properties of a single particle essentially depends on the wavelength and polarization of the incident beam, refractive index of the particle and particle shape and size, as can be seen in Maxwell's equations.

  Typical detection sensitivity of the light blocking method is 1 ¯m or larger, while the light scattering method is useful for particles greater than 0.05 ¯m in size. However, the most typical available optical detectors are the Condensation Particle Counters (CPCs) which allow a higher detection sensitivity in particle sizes down to nanometer range.

  The principle of the CPCs consists of three processes: the first one, the creation of supersaturated vapor, usually from $n-$butanol or water. It can be done by several methods, adiabatic expansion of an aerosol-vapour mixture [92], thermal diffusivity [112] or mixing cool and warm saturated air [71, 72, 137].

  Secondly, the growth of particles by condensation of the supersaturated vapor, the particles act as condensation nuclei and grow quickly to droplets of a detectable size.

  Finally, optical detection of the grown droplets by light scattering [43, 88, 117, 138]. The droplet flow is focused in a nozzle and introduced into a counting optic, passing a laser beam where each single particle creates a light pulse. Pulses with an amplitude above a certain threshold are counted. The particle number concentration can be calculated by knowing the aerosol flow rate. Modern CPCs operate with continuous aerosol flows and are able to count each single particle.

- **Electrical systems.** The most widespread devices are based on the classification of particles depending on their differential electrical mobility, since the electrical mobility depends on the particle diameter, D_P, as shown in eq. (1.3.4). The mobility analysis presents great advantages, like high resolution in the submicrometer diameter region or that the particles can remain airborne during the process.

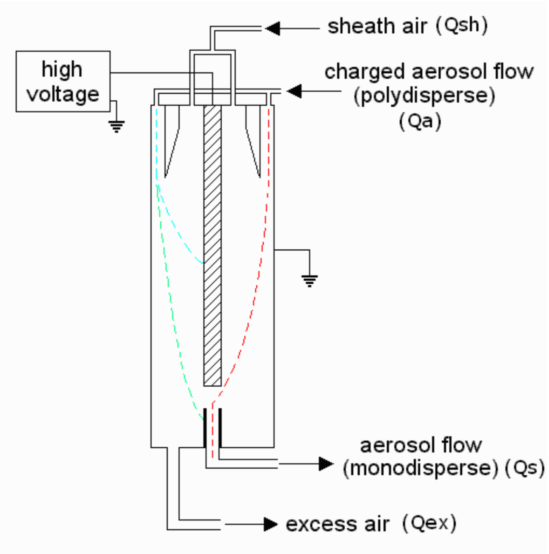

Figure 1.5.1: Schematic figure of a DMA.

Several electrical instruments are based on this principle, but the development of the Electrical Aerosol Analyzer (EAA) and Differential Mobility Analizer (DMA), [70]) are predominant in electrical size distribution measurements. Nowadays EAA systems have been almost entirely replaced by DMA systems.

This device consists on two electrodes, arranged parallel or concentric (as shown in fig. 1.5.1), and a laminar particle-free sheath air flow Q_{sh} to which the aerosol flow Q_a carrying aerosol particles with predictable charge distribution is introduced. When a potential is applied between the two electrodes, charged particles are deflected and only a narrow range of particles can pass through the outlet slit. Particles of different mobilities can be selected from the aerosol by varying the voltage. The particles that have the proper mobility to pass through the DMA are then counted by a CPC.

According to this, the system is called Scanning Mobility Particle Sizer (SMPS) when the voltage is varied in a continuous way or Differential Mobility Particle Sizer (DMPS) when it is varied step-wisely [31]. Despite of the high size resolutions this system offers (from a few nanometers to about a micrometer), they are relatively slow, since to sweep a range of particle sizes it will need to spend some minutes.

Another type of scanners work sorting and counting particles at the same time. The counting is done through the electric current from charged particles using very precise electrometers (currents are of order of pA). In this type of device, called Fast Mobility Particle Sizer (FMPS), the response time is approximately one second [18, 56, 136]. This factor is critical when studying phenomena of rapid evolution, such as nucleation from exhaust waste of cars. However, the number of electrometers used in the device determines the size resolution.

> By knowing the charge distribution [141], the DMA transfer function [50, 87], and the CPC counting efficiency function [44], the particle number size distribution can be calculated from the measured mobility distribution [49].

Whatever method of measurement is used, the next problem is to determine accurately the size distribution from the data device. This is known as *inversion* of data. Due to the imprecision of the measurements (such as rigid transfer functions or counting particles with same mobility but different diameter and number of charges) and some experimental errors, the calculated PSD is actually an estimate. In mathematical terms this is called an *ill-posed problem*, in the sense that simply from the measurements it cannot be inferred an exact solution.

Therefore, some background information has to be included in the calculation process. The goal is to find an agreement between the previous assumptions and the measured data so as to eliminate from the solution the effects without physical meaning.

1.6 MOTIVATION AND GENERAL OBJECTIVES OF THIS THESIS

The main aim of this thesis is to characterize a new system to electrically charge ultrafine particles and accurately calculate their size distribution function using and comparing several mathematical inversion techniques.

For this purpose it has been developed a corona charger device with a predictable and reproducible charge distribution and adaptable efficiencies in a wide range of charging levels. The feasibility of an accurate estimate of the $N_i t$-product and the charge per particle is also considered.

In the same way, inversion techniques for calculation of the particle distribution by sizes from mobility measurements were tested. It encompass the mathematical tools and considerations relative to the transfer functions which improve the present methods, and is available for the corona charger in use.

Some of the results have already been published (see Publications) and the objective is to summarize the conclusions, give further results and discuss some aspects in more detail.

1.6.1 *Organization and structure*

The main structure is divided into three parts. Firstly, in *Part I* is completely characterized the unipolar charging of particles by a corona device.

In *Chapter 2* the basic mechanism of unipolar charging is analyzed, reviewing the presented methods of diffusion charging and its strong points versus its drawbacks and needings. Based on these, a new indirect corona charger is presented, and a basic study of the gas flows inside the device and the neccessary setup to test it is presented.

In *Chapter 3*, the electrical characteristics of the corona discharge are studied, to better understand the subsequent charging process. The fluctuation of the current created by the discharge with a variable current or voltage applied to the electrode is studied, as well as the generated ionic and charged particle current separatedly. The working ranges of an electrostatic precipitator able to efficiently remove excess ions or remaining charged particles without causing losses are analyzed.

In *Chapter 4* the main experimental characterization of the corona charger is expound. First, it has been focused on the measurements of the particle deposition and charging efficiencies. Based on the results, the unipolar charge distribution is estimated, and from these results a complete theoretical study of the ion concentration and electric fields generated by the migration of charged particles and ions in the charger is presented in *Chapter 5* and compared with experiments.

In *Part II* is analyzed the particle size retrieval from electrical measurements. The main inversion theory and techniques are reviewed in *Chapter 6*, along with the results obtained from applying them to simulated and experimental data. Apart from the reconstruction of the complete size distribution function, the methodology to recover the mean charge or the singly charged particle distribution is explained and applied.

Finally, *Part III* outlines the most important conclusions which can be drawn from this work, and sketchs some future work derived from the results.

In the *Appendices* it can be found deeper information about basic aspects presented in the thesis, such as drafts and photos of the corona device from *Chapter* 2 in *Appendix A*, the complete characterization of the geometrical area of the trasfer function from *Chapter* 4 in *Appendix B* and in *Appendix C*, the scripts used to obtain the ion concentration and electrical losses of *Chapter* 5.

Part I

CORONA UNIPOLAR CHARGER

2

FUNDAMENTALS OF THE CORONA DISCHARGE

Providing electrical charge to particles is a fundamental requirement for particle characterization by mobility analysis. The calculation of the aerosol size distribution requires an accurate knowledge of the charge distribution of the incoming aerosol. Although bipolar radioactive chargers are the most widely used due to their well defined charge distribution, unipolar diffusion chargers are still focusing interest, specially the electrical chargers, due to their simplicity.

Due to the absence of ion recombination, unipolar ionization results in higher ion concentrations than bipolar ionization. As a consequence, unipolar charging is largely more efficient, in terms of total fraction of charged particles and particle charge level than bipolar charging [68].

When the voltage across conductors in a gas or a mixture of gases (such as air) exceeds the dielectric strength of the gas, it becomes ionized and begins to conduct electricity. This is known as *electrical breakdown*, it may occur either in AC or DC circuits.

Electrical discharges play a key role in technologies such as semiconductor fabrication, high-efficiency lighting, arc welding, high-voltage switchgear, plasma displays and chemical treatments of gases, liquids and surfaces. Due to the complexity of the plasma created by such discharges, their application is still largely based on empirical knowledge. There are four distinct types at atmospheric pressure, namely arc, spark, glow and corona discharges [131].

- An *electric arc* is a type of breakdown of short duration between two conductive electrodes in which the voltage is rather low and the current is relatively high, resulting in a very high temperature capable of melting most materials. Since the electric arc has a non-linear relationship between voltage and current, uncontrolled arcs can become tremendously destructive, because once is initiated, it will induce an increasing current from a fixed voltage supply until the apparatus is destroyed.

- The *spark breakdown* is nearly the opposite: high voltage and relatively low current. An electric arc is a continuous discharge, while a similar electric spark discharge is momentary, producing a brief emission of light and sound. Perhaps the best known example of a natural spark is a lightning strike, but static electricity is also a type of such a breakdown. Sparks can cause serious explosions because of the high temperatures reached.

- An *electric glow discharge* is created by passing a current through a gas (typically neon or other noble gases), ionizing their particles by random processes (thermal collisions between atoms or with alpha particles, for example) and creating therefore a plasma.

  Glow discharges differs from electric arcs in that the voltage is higher for a glow discharge. It is also sometimes confused with corona discharge, but they have one important distinction: glow discharges are relatively "cold" breakdowns, used in neon signs and fluorescent tubes, whereas coronas are considerably "hot" breakdowns that can destroy wire insulation, even made of porcelain.

- An electrical *corona discharge* occurs when one of two electrodes of differing voltages has a pointed shape, resulting in a highly concentrated electric field at its tip that ionizes the gas around it. The space charge distortion cannot reduce the field strength and there results a self sustained discharge. This means that once generated, corona discharge can be maintained in the absence of another electrode by photoelectric ionization of the gas.

  Corona can occur naturally at high points (such as church spires, treetops, or ship masts) during thunderstorms, which is traditionally known as St. Elmo's Fire. Corona discharge has been used in many industrial processes, such as electrostatic coating or as ozone generators, which have been used for more than 30 years in the water and air purification processes.

2.1 MECHANISM OF CORONA DISCHARGE

Ion production by corona discharge is explained in detail in White [140] or Reist [107], but a brief description of its mechanism will be given here.

When the electric field strength of a gas close to a curved electrode is high enough, the gas undergoes and electrical breakdown in a very thin layer at the electrode surface. In this corona region, electrons have sufficient energy to knock an electron from gas molecules creating positive ions and free electrons (see fig. 2.1.1).

The electric field then separates these charged particles preventing their recombination and imparting each of them with kinetic energy. Further ion-electron pairs are created by collision with neutral atoms from the gas. The same separating process continues occurring, creating an electron avalanche and therefore a uniform plasma glowing blue and white (although many of the emissions are in the ultraviolet).

Both positive and negative coronas rely on electron avalanches, but they differ in the ion species created in this series of avalanches. A positive corona is created when the electrode with the sharpest curvature is connected to the positive output of the power supply, generating positive ions, and a negative corona in the contrary. The corresponding ion is then attracted to the flat electrode, completing the circuit and sustaining the current flow.

During this process, aerosol particles can be charged by attachment of ions produced. Ions are transported by the electric field, by thermal diffusion and/or by a dilution flow. The amount of ion deposition on the particle surface, and therefore the charging efficiency, depends on resident time, particle radius and shape, electric field, and many other variables.

In 1889, Paschen [98] published what has become known as *Paschen's Law*. The law states that the breakdown characteristics of a gap are $V = f(P{\cdot}d)$, a function generally not linear of the product of the gas pressure P and the gap distance d.

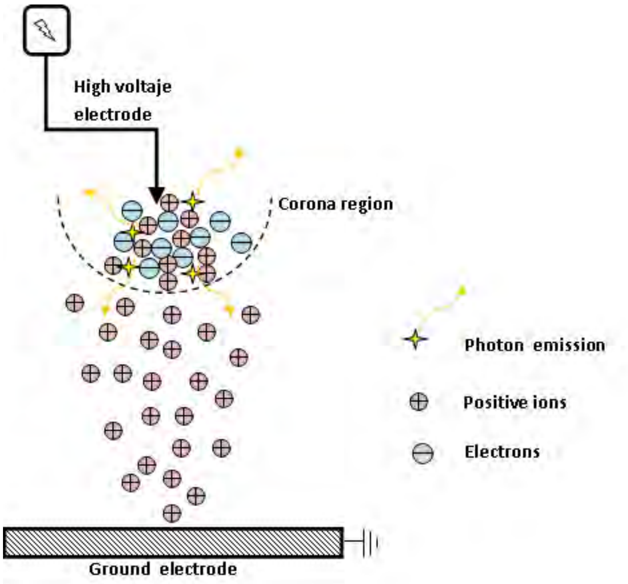

Figure 2.1.1: Schematic diagram of positive corona discharge mechanism in a point-to-plane configuration.

Paschen's Law reflects the Townsend breakdown mechanism in gases, that is, a cascading of secondary electrons emitted by collisions in the gap. In general, an equation for breakdown is derived, and suitable parameters chosen by fitting to empirical data.

Since the magnitude of the field is inversely proportional to the radius of curvature, sharper edges break down sooner. Dust or water particles on the surface of the object reduce the corona starting voltage, probably by providing local areas of tighter curvature, and hence higher field stress. Running the system at high pressure or with an insulating gas will increase the corona starting voltage [12, 146].

Coronas have two important voltage parameters [99]: the disruptive or corona onset voltage (V_0), the minimum voltage at which this ionization occurs, and the visual critical voltage (V_{cv}). Once V_{cv} is reached, the corona remains visible to the naked eye in the dark. In a cylindrical geometry, a needle near the tip has an approximate voltage:

$$V_0 = m_0 E_0 \delta \left(1 + \frac{0.0308}{\sqrt{r}}\right) r, \tag{2.1.1}$$

$$V_{\text{cv}} = m_v E_0 \delta \left(1 + \frac{0.0308}{\sqrt{\delta r}}\right) r \ln\left(\frac{R}{r}\right), \tag{2.1.2}$$

where r is the radius of curvature of the tip of the needle, R is the outer radius or distance from the tip to the electrode and $0.0308\,\text{m}^{1/2}$ is an empirical constant for cylindrical geometry. The air density factor, $\delta = {}^{3.92P}/_{T}$, is equal to 1 for NTP, and $m_v = m_o$ is the wire roughness factor, which takes values 1 for polished wires, 0.98 to 0.93 for roughened, dirty or weathered wires and 0.87 to 0.83 for cables.

The disruptive critical voltage gradient in air, $E_0 = 3.1 \times 10^6\,{}^{\text{V}}/_{\text{m}}$, is a value empirically calculated for the starting electric field at NTP conditions, and is around a 15% greater when the gas is nitrogen.

From the eq. (2.1.2), when V_{cv} is reached, the electric field at the surface of the wire is given by the Paschen Law for concentric cylinders as:

$$E_{\mathrm{cv}} = E_0\delta\left(1+\frac{0.0308}{\sqrt{\delta\cdot r}}\right). \tag{2.1.3}$$

Now, the air surrounding the conductor will ionize and begin to conduct. At this point, the effective radius of the tip has been increased since the gas surrounding is acting like a conductor. The effective radius of the high voltage electrode is:

$$R_{\mathrm{eff}} = r\cdot {}^{E_c}/_{E_0} = r\left(1+\frac{0.0308}{\sqrt{r}}\right). \tag{2.1.4}$$

In some cases, if the voltage is too high and the distance between the conductors too small, a spark-over will occur. The spark-over voltage is affected by several factors (eq. (2.1.5)): electrode shape, spacing, air temperature, humidity, etc, and it is not linear with gap distance. It rises as air pressure is increased [99].

$$V_{\mathrm{sp}} = \frac{BPd}{\ln(APd)-\ln\left(\ln\left(1+{}^{1}/_{g}\right)\right)}. \tag{2.1.5}$$

For a gas such as nitrogen, the constants $A = {}^{9}/_{\mathrm{m\cdot Pa}}$, $B = 256.5\,{}^{\mathrm{V}}/_{\mathrm{m\cdot Pa}}$ $g = 0.025$, while for air $A = {}^{11.25}/_{\mathrm{m\cdot Pa}}$, $B = 273.75\,{}^{\mathrm{V}}/_{\mathrm{m\cdot Pa}}$ [51]. The distance d denotes the space between the electrodes.

When spark is reached, particles are being generated in the electrodes, which is undesirable. Spark provokes too a strong erosion at the needle tip, which can affect the charge distribution of the device.

Before electrical classification by means of size–mobility relationship, aerosols must be electrically charged having a well defined charge distribution. Corona chargers have been studied for a long time [3, 13, 16, 46, 61, 73, 82, 89]. They can attain higher charging levels than radioactive chargers, and are exempt from expensive safety precautions and severe legal restrictions caused by the use the radioactive sources.

However, loss of charged particles, ozone generation, and nanoparticle generation by sputtering of the discharging electrode would be problematic [67, 77]. For application to size selection of nanoparticles, the unipolar charger must lead to acceptable fractions of singly charged particles with minor fractions of multiply charged particles. Therefore, there is a need to improve the corona discharge unipolar charger.

Generally, an ideal charger provides a balance between a high ion concentration and low particle losses, the capacity to work at various ambient conditions with no gas-to-particle conversion, low coagulation levels between charged particles and a predictable charge distribution for application to size selection of nanoparticles. The unipolar charger must lead to acceptable fractions of singly charged particles with minor fractions of multiply charged particles. Therefore, there is an interest to improve the unipolar diffusion charger.

2.2 REVIEW OF PREVIOUS STUDIES

Commonly used chargers are corona chargers. There are multiple modifications for specific applications or particle size ranges, and numerous extensive studies in the past have been done [46, 82, 140, 142]. A good summary of the different configurations developed up to date can be seen on Intra and Tippayawong [60, 62].

Among all the corona charger designs, they can be classified into two basic configurations, *wire* or *needle* chargers. These can be arranged depending on the type of electrical field used to generate the ions (AC or DC), the way the ions and particles are mixed or whether a flow or a low electric field is used to drive the ions out of the electrode.

The zone where ions are generated is known as *ionization* or *discharge region*, while the place where particles and ions are mixed and the charge is transferred, is known as *mixing* or *charging region*. In some charger configurations both regions coincide, these are called *direct corona* chargers. If these two parts are separated, the charger is called *post-charging* device or *indirect corona* charger. Is in these last ones where a method to drive the ions is necessary, either to apply a a stream flow or a small voltage to attract the ions from the ionization to the charging region.

One of the first to develop a wire-corona charger was Hewitt [46]. The charger consisted of a cylinder with a concentric corona wire placed along the axis, separated from the aerosol path by a metallic mesh where AC voltage was applied to reduce particle losses, although they were severe.

Several following devices have adopted this configuration, such as the charger used in the Electrical Aerosol Analyzer (EAA, TSI model 3030; [82]). This design had also sheath flow for particles, in order to displace the aerosol stream away the discharge region, but as well, significant particle loss was reported below 10 nm.

Another modification of this design was investigated by Büscher et al. [16]. They connected all the surfaces in contact with the aerosol to the ground, to avoid particle losses, but they found that penetration decreased and diffusion losses raised for small particles.

Kruis and Fissan [73] duplicated the ion production zones and made the aerosol to flow between them. Ions were generated by gold wires. Their design shows a square section, in which the charging zone is separated from the discharge regions by metallic meshes connected to square-wave voltage supplies of opposite phases, in order to prevent the penetration of particles into the ionization zones. It was found out that for each flow rate exists an optimal length of the charging channel which minimizes losses of charged particles.

Another relevant wire-corona design was proposed by Biskos et al. [13, 14]. It is also a Hewitt type with a tungsten wire inside two concentric cylinders. The inner one where the wire is placed is the ion generation zone, and is separated from the outer by a metallic mesh with an AC voltage applied on it, to force ions to enter the charging region and collide with the particles, transferring the charge. the authors reported significant space charge effect for high ions concentration (from 5×10^{13} $\#\mathrm{m}^{-3}$).

A new model for high volume electrostatic charging was designed by Cheng et al. [21], in which gold wires were incrusted in a Teflon rod and the sheath air with particles flowed in the annular region parallel to the wires.

A recent design is proposed in Tsai et al. [127, 128], with four gold wires of 25 μm in diameter and 26 nm in length fixed to an inner Teflon core because the length of wires was too long (which may result in high charged particle loss), a Teflon tube was used to cover unnecessary length of wires. Hence, the effective length of the wires was cut down to 15 nm to reduce the possible particle loss and deposition. With the multiple wires layout, the extrinsic charging efficiency of nanoparticles was enhanced by using sheath air near the wall of the charger.

Many other designs for wire-chargers have been investigated, but there were the needle-chargers that have attracted most interest. The first needle-charger was developed by Whitby [139], consisting of a sharp needle held at a small sonic orifice to generate the ions. The device was a direct corona charger, where the aerosol inlet passed through the orifice plate obtaining 100% efficiency.

The design of Medved et al. [89] is a post-charging device which consists of a central mixing chamber with two adjacent chambers, the ion-generation region and the aerosol inlet, one in front of the other and connected to the mixing chamber via an orifice. The opposite inlets for ions and particles created turbulent conditions in the mixing chamber, reporting more efficient charging than in wire-chargers. It is the current device employed by the TSI 3070A Electrical Aerosol Detector (EAD) [52].

As it happened with the twin-design of Hewitt of Kruis and Fissan [73], an improvement of the previous design of Medved et al. [89] was developed by [85] duplicating the number of needles for ion generation. As well, it is a post-charging device where the two needles connected to a DC supply pass the generated ions to the charging region by means of a combination of sheath air and AC voltage, with the aerosol flowing perpendicular to the ion flow in the mixing chamber. The authors reported high charging efficiencies for particles up to 100 nm.

A simpler design was proposed by Hernandez-Sierra et al. [45], in which a stainless steel needle was connected to a DC high voltage source inside a cylindrical piece with conical section at the outlet. The aerosol entered directly by the rear part of the ionization chamber through a series of orifices made in a circular piece of Teflon. A modification of this design was developed by Alonso et al. [6], in which the aerosol flow entered perpendicular to the needle, avoiding the losses caused by the Teflon piece. This design is used in the corona charger CC-8020 from Ioner, Ramem [106].

Again, a twin charger with indirect performance was proposed by Qi et al. [103]. Two discharge regions with tungsten needles and were attached with an angle of 45^o to a cylindrical charging region, injecting sonic-jet flows from each of the two ionizers. The aerosol stream is introduced aligned with the charger axis. Particle loss by diffusion and the space charge effect is minimized by the angular injection of the ionizer flow and the rapid exit of charged particles, but it was reported that operation with one corona ionizer gave higher extrinsic charging efficiency than operation with two ionizers.

Also from Qi et al. [104], a unipolar mini-charger for a personal nanoparticle sizer was proposed. The discharge and charging regions were separated but one within the other. A tungsten needle was confined into a porous cage with micro-perforated end in which an ion driving voltage was applied. At the outer of this cage, particles flow. In this work, the extrinsic charging efficiency was optimized for different aerosol flow rates: the intrinsic charging efficiency is higher at low flow rate due to the longer residence time, the extrinsic charging efficiency is, however, higher for the higher flow rate as a result of charged particle loss in the prototype.

A more recent DC post-charging device is investigated by Li and Chen [80]. It consists of an outer metal case and a tungsten needle inside a tube with a metal screen at one end, in which an ion driving voltage was applied. Particles and ions flow parallel along the axis and once the particles are electrically charged, they quickly exit the device, thus reducing the loss of charged particles.

Many other prototypes are described in literature [3, 61, 95, 94, 96, 97, 132, 133]. All cases have distinct performances due to their different configurations (see table 4.2.1), and therefore their pros and cons are analyzed and taken into account when it comes to building a new device.

2.2.1 *Other charging devices*

Alternatively, another particle charging devices were developed to replace the radioactive sources.

Kwon et al. [75, 76, 77] developed a unipolar charger for nanoparticles called Surface-discharge Microplasma Aerosol Charger (SMAC). Unipolar ions are generated by the surface discharge of a single micro-structured electrode located on a dielectric barrier sheet by applying DC pulse. This discharge is usually called Dielectric Barrier Discharge (DBD), and occurs between two electrodes separated by an insulating dielectric barrier. The plasma created is a source of ions.

Penetration and charging were carried out for nanoparticles in the size range of 3 to 15 nm. The authors reported that more than 90% of inlet nanoparticles penetrated the charger (less than 10% of particles were lost) without the use of sheath air. It was also shown that the measured charging efficiencies agreed well with the diffusion charging theory.

It seems that the barrier discharge can achieve higher electrical power densities, but the corona discharge may be easier scalable to large gas flows. The dielectric barrier prevents arc formation but involves an alternative polarization of the system, and is more complicated since it is a combination of a gas discharge and a surface discharge along the dielectric. Moreover, it is known for being an ozone production discharge [131].

Another charger concept using photoemission was developed for the same purpose. Photoelectric charging is derived from photoelectric effect, which occurs when high energy electromagnetic radiation, such as ultraviolet light, is incident on the surface of a metal. There are two ways in which the photoelectric effect may be used to charge aerosols: (i) by aerosol photoemission whereby the aerosol is exposed directly to light, and (ii) by using photoelectric effect indirectly, whereby the aerosol is bathed in the electrons produced by irradiating a nearby metal.

Schmidt-Ott and Federer [110] used the photoemission from ultrafine aerosols to measure the particle size distribution. Shimada et al. [113] used soft X-ray to generate bipolar ions for aerosol charging. Their soft X-ray bipolar charger produced 3.5 times higher concentrated bipolar ions than an ^{241}Am charger, however, an inability to clearly describe the charging probability for particles larger than 30 nm made it impossible to determine the equilibrium charging state for this particle size range.

Lee et al. [79] applied a soft X-ray charger to the size distribution measurement of polydispersed NaCl particles having a size range of 1 to 100 nm, and later, Hontañon and Kruis [48] demonstrated the suitability of a UV photocharger to deliver monodisperse nanoparticles at high aerosol flow rates (up to 100 lpm) in comparison to a radioactive bipolar charger. The UV photocharger behaved as a quasi-unipolar charger for polydisperse aerosols with particle size less than 30 nm and number concentrations about $10^7\,\mathrm{cm}^{-3}$. Recently, TSI has developed a soft X-ray neutralizing chamber to work as a drop-in replacement for the older radioactive neutralizers in TSI instruments, the Advanced Aerosol Neutralizer 3087.

Unipolar photoelectric charging of aerosol particles by UV light exhibits in general a better charging efficiency for fine and ultrafine particles. However, this technique is limited to particle materials such as metals which have a work function (threshold energy for an electron to leave a crystal) below the UV irradiation energy [142], since its charging efficiency strongly depends on particle compositions. The photons will ionize particles as well as the impurities of carrier gases. Furthermore, the method is difficult to apply due to the recombination of electrons and positively charged particles which reduces the charging efficiency of particles significantly.

This unwanted mechanisms makes the charging efficiency rather unstable and thus, it is undesirable for most practical applications. Compared with the photo-ionization method, the ion-attachment method is less dependent on particle compositions. The ion-attachment method gives stable charging efficiency as long as the ion concentration is stable [19].

In ion-attachment chargers, particles are either exposed to bipolar or unipolar ion environments. As have been described earlier, the bipolar chargers give very low charging efficiency for nanoparticles. A constant ion production leads to a constant $N_i t$ value, and as a result, to a stable charging process. The simplest way to create unipolar ions is with a corona discharge. It is valid for all particle materials and a versatile setup, since construction, modification or replacement of pieces is easy and cheap.

This new corona charger is designed to be applied where radioactive neutralizers have been traditionally used. Ideally, it will have the possibility of identical sizing to radioactive neutralizers in order to easily replace them, and since it can be turned on and off there are no transportation restrictions making it a good choice for field studies. There is no particle generation inside the device, and it is designed for minimal waste of the needle and for a quick and easy replacement without major changes in the charging efficiency.

2.2.2 *Drawbacks of previous devices*

Some difficulties have to be evaluated and overcome before designing a new prototype. Reported problems are related with the following items:

- Ozone production:

During an electrostatic discharge in a gas such air (78% N_2, 21% O_2 approx.), the diatomic oxygen molecules from air are split and recombined to form ozone (O_3), which is unstable, a toxic gas, and reacts with metals (is a strong oxidant).

The production of ozone can be up to one order of magnitude less in the positive than in the negative corona. This difference is due to the greater number of electrons in the negative corona [20]. Ozone generation rate is linear with respect to current and increases with increasing wire radius. As the air temperature is raised, ozone production rate decreases.

The discharge electrode of the corona device can be altered as a result of the oxidation caused by the ozone, and therefore the charging conditions of the corona device. For this reason, the use of a gas distinct than air shall be used.

In the present work, the selected gas was pure nitrogen (purified with Oxisorb, 99, 9999% purity) because it is closest to air in its material properties (its breakdown voltage is only about 15% greater than air) and avoids the ozone generation. It has to be mentioned that N_2 is a non-electron attaching gas, efficient in slowing down electrons and thus is not able to form negative ions [115]. If negative ions appear, they are due to impurities present in the N_2 gas (the main impurities could be H_2O and O_2 and in consequence ozone might be generated in low proportions).

- Nanoparticle generation:

  One of the reasons to prefer the radioactive charger to the corona setup is the stability that the first ones offer. They can last more than 10 years with small changes in their efficiencies. However, in the corona devices the usage time of the electrode can be responsible for the change on charging efficiency levels, since the electrode gets worn out and can change its geometry.

  Corona discharge can promote the formation of new particles, either from erosion and sputtering from the corona electrode itself or from gaseous contaminants present in the system; the presence of water being a decisive factor in the particle generation process [6, 68].

  In this work, a tungsten needle was used because it has the highest melting point and lowest vapor pressure of all metals, thereby allowing it to be heated for electron emission. To prevent precipitation or break-up of aerosol particles due to the strong electric field when passing through the charger, the so-called indirect corona charger layout was developed. Thus, it attenuates the erosion of the needle, and may continue for longer stable.

- AC vs DC electric field:

  Although the previously presented corona devices used either direct or alternate current, it has been reported recently that the AC field offers no benefit compared to the DC field [85].

  Comparing the devices with AC [14, 16, 73, 133] and DC [19, 45, 80, 104], an AC electric field in the mixing zone of ions and particles do not reduce losses of nanoparticles, even under laminar flow conditions. The AC field seems to only affect the amount of ions reaching the charging region.

This is probably explained by the fact that nanoparticles are more susceptible to hydrodynamic forces from the ion wind or flow disturbances, which makes transport to the walls unavoidable, irrespective of an additional electric field. So the loss reducing effect of an AC field is somewhat inversely proportional to the charging intensity.

- LOSSES OF PARTICLES:

  There are two ways the concentration of particles can decrease during the charging process:

  - *Diffusional losses* (L_{diff}) refer to the particle losses inside the charger without an electric field applied in the charging region (no ions). These losses are negligible for particles larger than 20 nm.
  - The *electrical losses* (L_{el}) are additional losses of charged particles due to space charge effects.

  For small particles, losses are very strong because two effects influence the total losses: since the charging efficiency of ultrafine particles is lower than the rest of particles, the non-charged particles will suffer diffusional losses, while the electrical losses will decrease, also because of their higher mobility.

  A reduction of the electric field strength in the charging region leads to a reduction of the particle losses inside the charger [142]. This can be done separating the ionization and mixing zones, as it is done in the indirect corona chargers. Also, the introduction of a surrounding sheath air flow at the boundary between the aerosol stream and the wall allows more space for the charged particles to flow through the charger without precipitating on the charger walls [62]. However, the application of a large sheath gas flow can result in aerosol dilution.

2.3 DESIGN OF THE UNIPOLAR CORONA CHARGER

Taking into account the items analyzed in sec. 2.2.2, it was designed a needle post-charging device with separated ion generation and charging chambers as can be seen in figs. 2.3.1 and 2.3.2 (a more detailed scheme of the corona device components can be found in app. A). This avoids contamination of the needle which results in a longer life time [75, 103]. A tungsten needle is mounted on a micrometer-supported base, so that the distance to the output of the ionizing chamber can be modified and therefore the distance to the ground electrode can be precisely controlled during the experiment, as well as the $N_i t$-product.

The ion chamber is concentric to and surrounded by the particle flow, which as shown in a theoretical study [7] is the best configuration for unipolar chargers. The advantage of cylindrical geometry is that distortion of electric field between electrodes is minimal due to the absence of corners and edges [58].

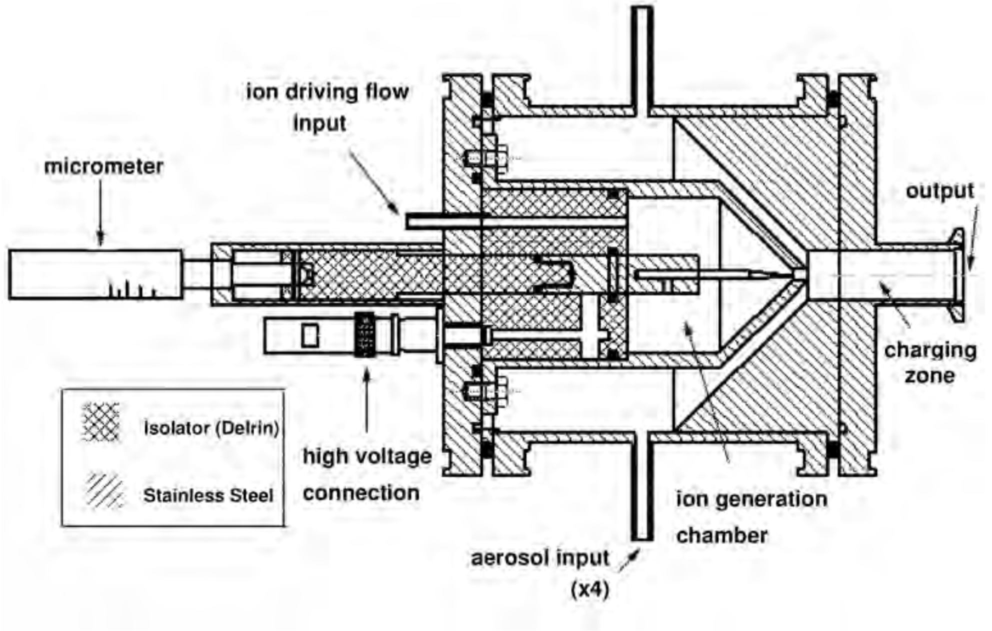

Figure 2.3.1: Cross-section of the corona device. The inner part consist of the needle, the high voltage connection and the ion driving flow. The outer part, where particles come in, is separated from the inner up to the charging region, where the particle flow surrounds the ion flow.

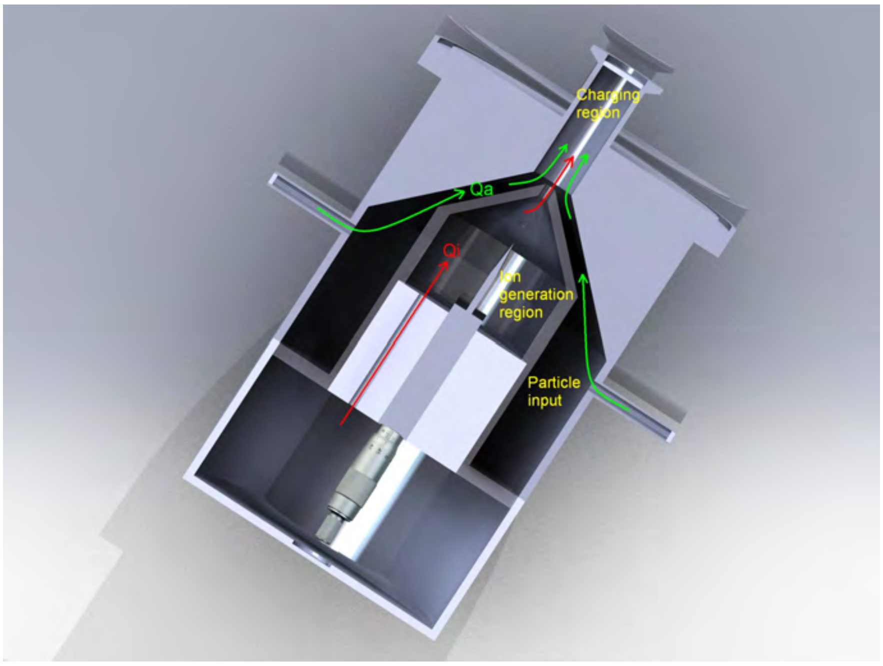

Figure 2.3.2: Simulation of the corona device in 3D.

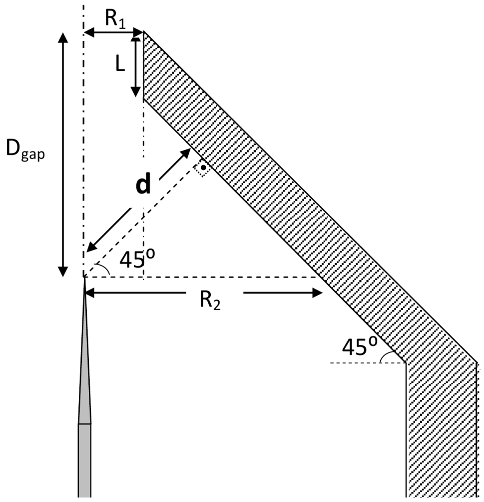

Figure 2.3.3: Distance between electrodes in the conical part of the discharge region.

Two different flows are applied for carrying ions, Q_i, and aerosol particles, Q_a. It is known that this dilution flow might impair the performance of the charger, but without sheath air, the particle loss impairs the performance of the unipolar charger [76]. The particle-free flow that transports the ions out of the generation region prevents the penetration of particles into the corona discharging zone, while the 45° of inclination of the particle flow with respect to the ion flow helps the mixing of ions and particles.

As it can be seen in fig. 2.3.3, the distance between electrodes is different depending on the position of the needle. The corona discharge will be produced at the tip of the needle, and the field lines will be straight and perpendicular to the earthed surface. This means that for a position of the micrometer (D_{gap}) between 0 and 5 mm of distance from the needle tip to the outlet of the discharge region, the shorter distance to the earthed electrode will be the radius of the tube, since it has cylindrical geometry. For gaps from 5 mm onward, the shape of the earthed electrode is conical, and the perpendicular distance d to the surface can be calculated by trigonometry: all angles are 45^o, then considering isosceles right triangles, the distance: $2d^2 = R_2^2$. To calculate R_2 from the conical frustum: $R_2 = R_1 + R'$, where $R' = D_{\text{gap}} - L$, obtaining the perpendicular distance between electrodes: $d = (R_1 + D_{\text{gap}} - L)/\sqrt{2}$.

In our geometry, $R_1 = 2\,\text{mm}$ and $L = 5\,\text{mm}$, so for the positions of the needles used, the real distances are

$$D_{\text{gap}} = 3\,\text{mm} \Rightarrow d = 2.0\,\text{mm},$$

$$D_{\text{gap}} = 7\,\text{mm} \Rightarrow d = 2.83\,\text{mm},$$

$$D_{\text{gap}} = 10\,\text{mm} \Rightarrow d = 4.95\,\text{mm}.$$

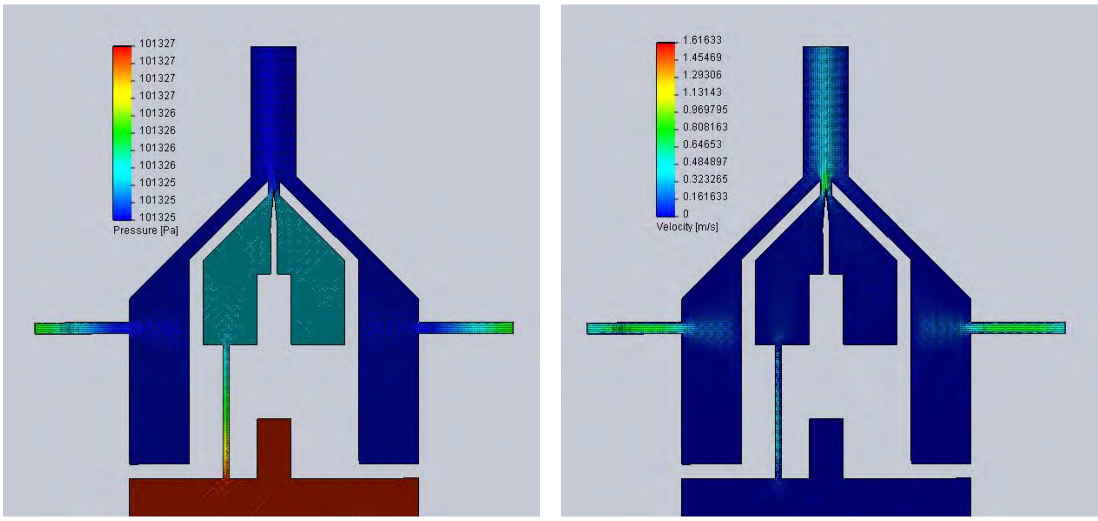

(a) (b)

Figure 2.3.4: Pressure (a) and velocity (b) profiles for flow rates of $Q_i = 0.5\,\text{lpm}$ and $Q_a = 1.5\,\text{lpm}$.

For simplicity we will refer these distances from now on as the D_{gap} value, bearing in mind that the actual values of the distance between electrodes are the related d.

This configuration allows modification of a wide number of parameters such as the ion and aerosol driving flows, the length of the charging region by replacing or adding another tube, or the distance between the needle electrode to the earthed wall. All these features influence on the operation of the device, therefore determining the $N_i t$-product.

2.3.1 *Study of flows inside the charger*

The change of pressure and velocity of the flows inside the device was simulated with SolidWorks and represented graphically in fig. 2.3.4 for different distances between electrodes. Operation at laminar flow conditions is required so that particle trajectories can be accurately determined.

The Reynolds number is calculated to characterize the flow regime:

$$\text{Re} = \frac{\rho v L}{\mu}, \tag{2.3.1}$$

where ρ is the density of the fluid, v the mean velocity of the object relative to the fluid, L is the traveled length of the fluid and μ its dynamic viscosity.

For the case in study, with nitrogen as applied gas ($\rho(N_2) = 1.165\,\text{kg/m}^3$ and $\mu(N_2) = 1.781 \times 10^{-5}\,\text{Pa}\cdot\text{s}$ at NTP), an applied total flow rate of 2 lpm and a travel length in the charging region of 5 cm, the Reynolds number is 43.38, clearly laminar (it would remain laminar up to 180 lpm).

A critical point is at the output of the ion generation chamber, where both flows converge. It is also a narrow channel, therefore pressure and velocity of the flow undergo some changes. Distances considered vary from the input of the ion flow to the output of the ionizing chamber in the case of the ion flow, and from the entrance of the aerosol flow to the output of the charging region in the case of the mix of aerosol and ion flows.

Although there is laminar flow in every moment, in fig. 2.3.5 is compared the effect of laminar or turbulent flow for fixed positions of the needle at $D_{\text{gap}} = 24\,\text{mm}$ (in practice, there is space to move the needle up to this distance, but the micrometer only reaches 10 mm). Inside the conduct for the ion flow (2.3.5 (a)) there is ambient pressure, experiencing a slightly increase when entering the ion generation chamber, and remaining constant there. This increase is smaller for a turbulent flow, but taking into account that this difference is less than a ten-thousandth, we can consider ambient pressure in any case.

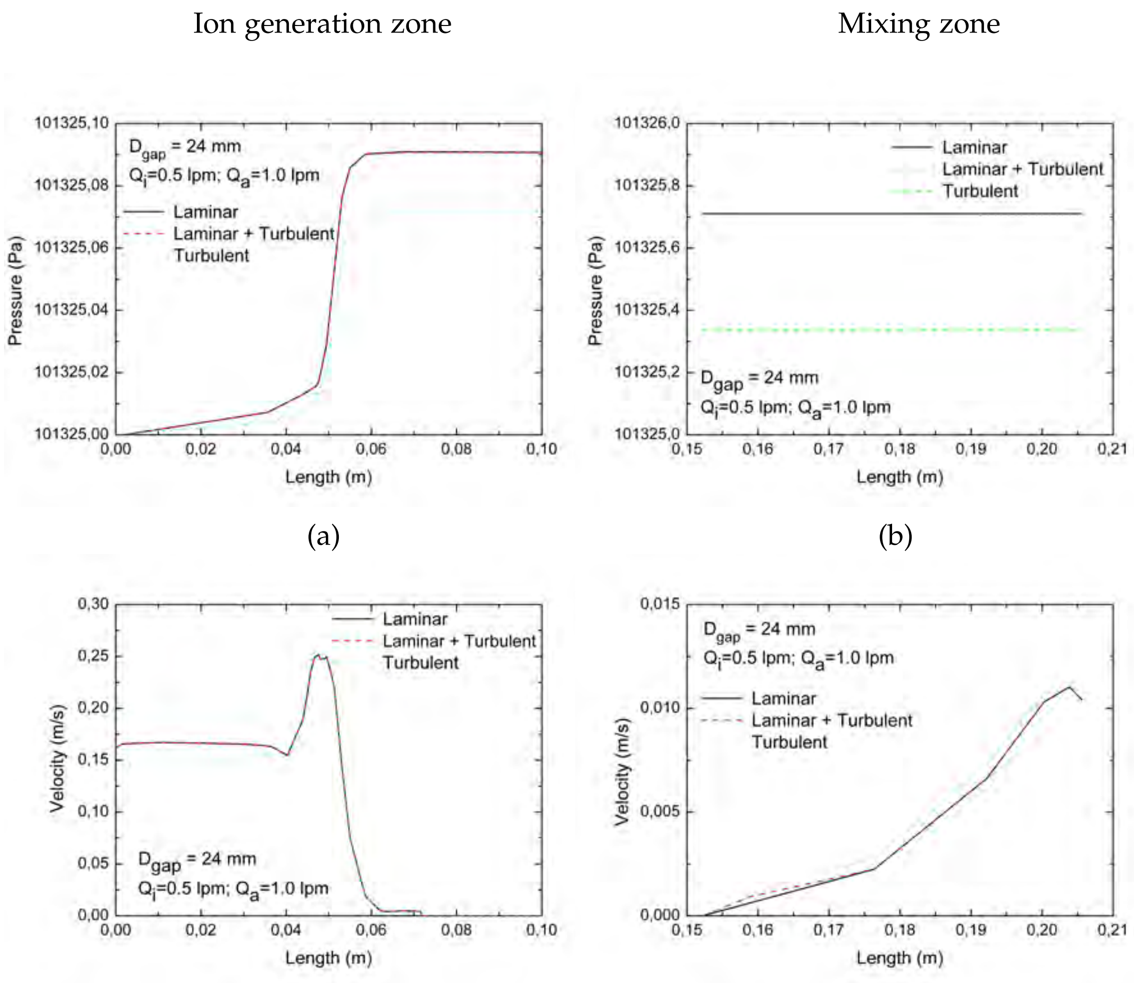

(a) (b)

(c) (d)

Figure 2.3.5: Pressure and velocity profile in the distinct sections of the charger for $D_{\text{gap}} = 24\,\text{mm}$ and different flow characteristics.

In the aerosol charging zone (2.3.5 (b)), the pressure remains constant through the whole tube at a higher value than in the discharge region, since now the total flow is larger. Anyway, this increase is again less than a thousandth part even for the turbulent type. This means that we can consider laminar flow at NTP conditions at any time.

The momentary increase in velocity shown in fig. 2.3.5 (c) corresponds to the narrow exit of the input flow tube to the corona discharge region. Once there, the volume of the chamber is greater, so velocity is stabilized and slows down. Again, in the charging region (2.3.5 (d)), there is a slight increase in velocity because of the addition of a major aerosol flow rate. Therefore, the effects of considering a laminar or turbulent flow are despicable at the selected flow rates.

We compare now the effects of different flow rates and distances between electrodes for the velocity and pressure profiles. The higher the applied ion flow in the ionizer zone, the greater is the pressure in the chamber (figs. 2.3.6 (a) and (c)). There is not a remarkable influence of the distance of the needle into the pressure or gas velocity, since it does not act as an obstacle.

A separate study along the charging zone of the flow velocities, from the position where the two streams coincide, shows the portion of the tube occupied by ions as they diffuse to the walls, mixing with the particles. Considering the flow velocity along the axial direction as the volume flow over the area of the cross section, the velocity of the ions at the output of the ionizing region (with radius R_i) is:

$$u_\mathrm{i} = \frac{Q_i}{\pi R_i^2}, \tag{2.3.2}$$

while at the output of the charging zone, the mix of ions and particles fill all the space of the cylinder:

$$u_\mathrm{out} = \frac{Q_\mathrm{tot}}{\pi R_\mathrm{ch}^2}, \tag{2.3.3}$$

being R_ch the radius of the charging zone.

It is evident that the ion stream will expand in a wider place such as the charging tube. To know how much of this area is the ion flow occupying, at the exit of the charging zone both velocities must be the same, therefore:

$$R_{i\,\mathrm{fin}} = R_\mathrm{ch} \sqrt{\frac{Q_i}{Q_\mathrm{tot}}}. \tag{2.3.4}$$

For the given flow rates of $Q_i = 0.5\,\mathrm{lpm}$ and $Q_a = 1.5\,\mathrm{lpm}$, the ion stream finally occupies a radius of 4 mm, half of the charging region. This implies that mixing with particles could be improved by increasing the ion flow, since the optimal situation would be where ions and particles are totally mixed in the whole area of the charging tube.

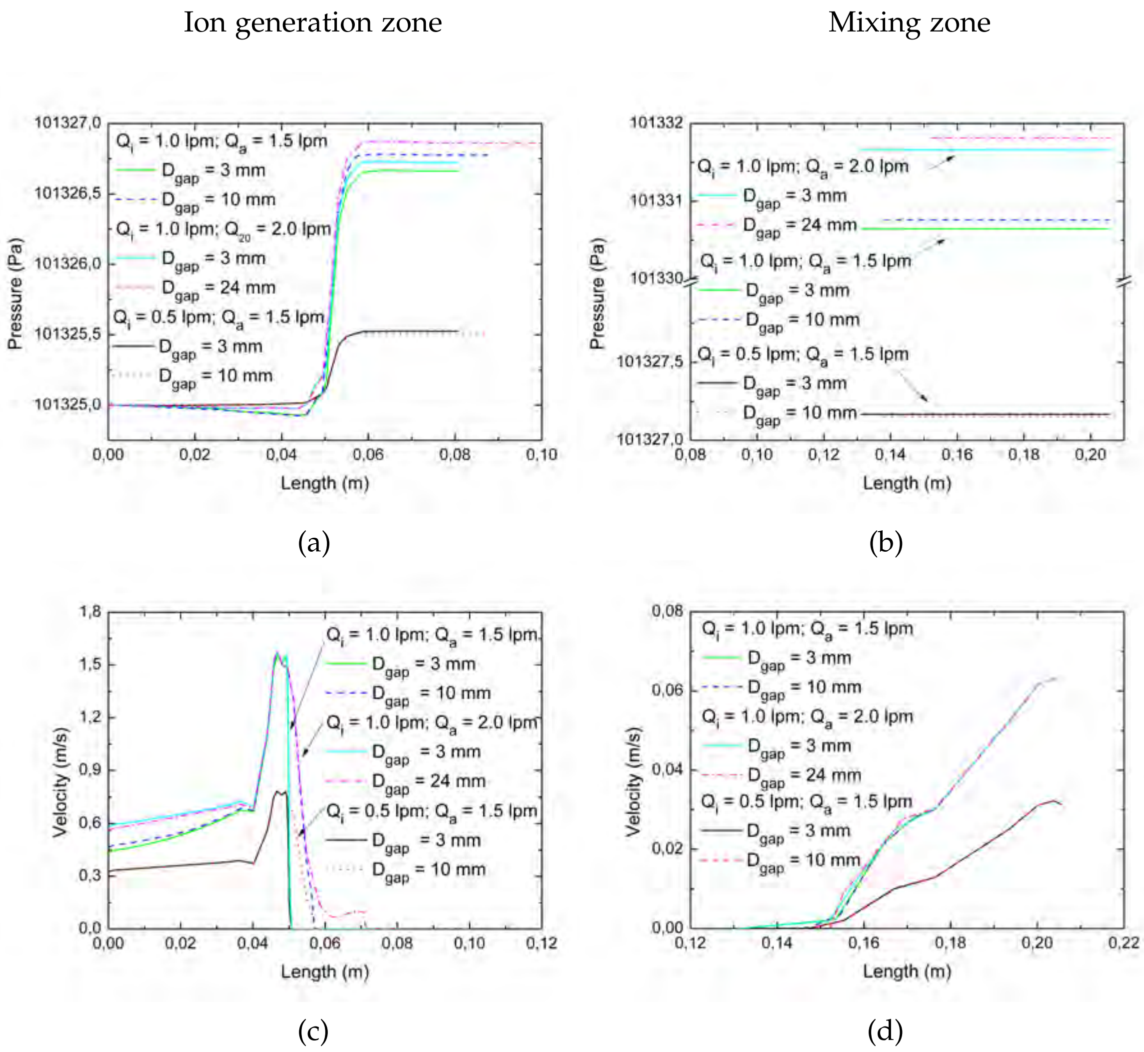

(a) (b)

(c) (d)

Figure 2.3.6: Pressure and velocity profiles in the different sections of the charger for laminar flow at different rates and distances to the output.

2.4 EXPERIMENTAL SETUP

To characterize the designed charger prototype, the experimental setup shown in fig. 2.4.1 was used.

A distribution of SnO nanoparticles with an electrical mobility diameter below 60 nm were generated by the well-known evaporation-condensation technique [109]. A ceramic boat containing the powder material to be aerosolized is placed inside the tube furnace, which is heated to achieve a high enough vapor pressure of the material.

The carrier gas passed through the furnace is nitrogen (purified with Oxisorb, 99, 9999% purity to avoid both oxidation of the needle and ozone generation) at 1.5 lpm, and the material vapor condenses into an aerosol.

The aerosol passes first through a ^{85}Kr electrostatic neutralizer with an activity of 370 MBq, where the particles acquire a charge distribution. A Nano-DMA (TSI-8085, Minneapolis, USA) with a fixed operating voltage classifies particles based on the electrical mobility. The monodisperse particle distribution passes then through a second identical ^{85}Kr neutralizer to neutralize the charged particles afterwards through an Electrostatic Precipitator (ESP) to remove the remaining charged particles. Only neutral particles with known size and concentration C_{in} are introduced in the test charger.

At the exit of the prototype charger, monodisperse particles pass through a SMPS (TSI-3080 with NanoDMA-8085 [53, 54]) and the ^{85}Kr neutralizer from the SMPS removed) in combination with a CPC (TSI-3775 [55]) to scan the size distribution, alternatively with the voltage on and off (C_{out}^{on} and C_{out}^{off} respectively) to measure the amount of charged particles and particle losses inside the device.

Since the proportion of charged particles cannot be directly measured, aerosol must be again uncharged by means of a second precipitator after the corona device. There, C_{out} is obtained, and the difference between $C_{\mathrm{out}}^{\mathrm{on}}$ and C_{out} will give the concentration of charged particles.

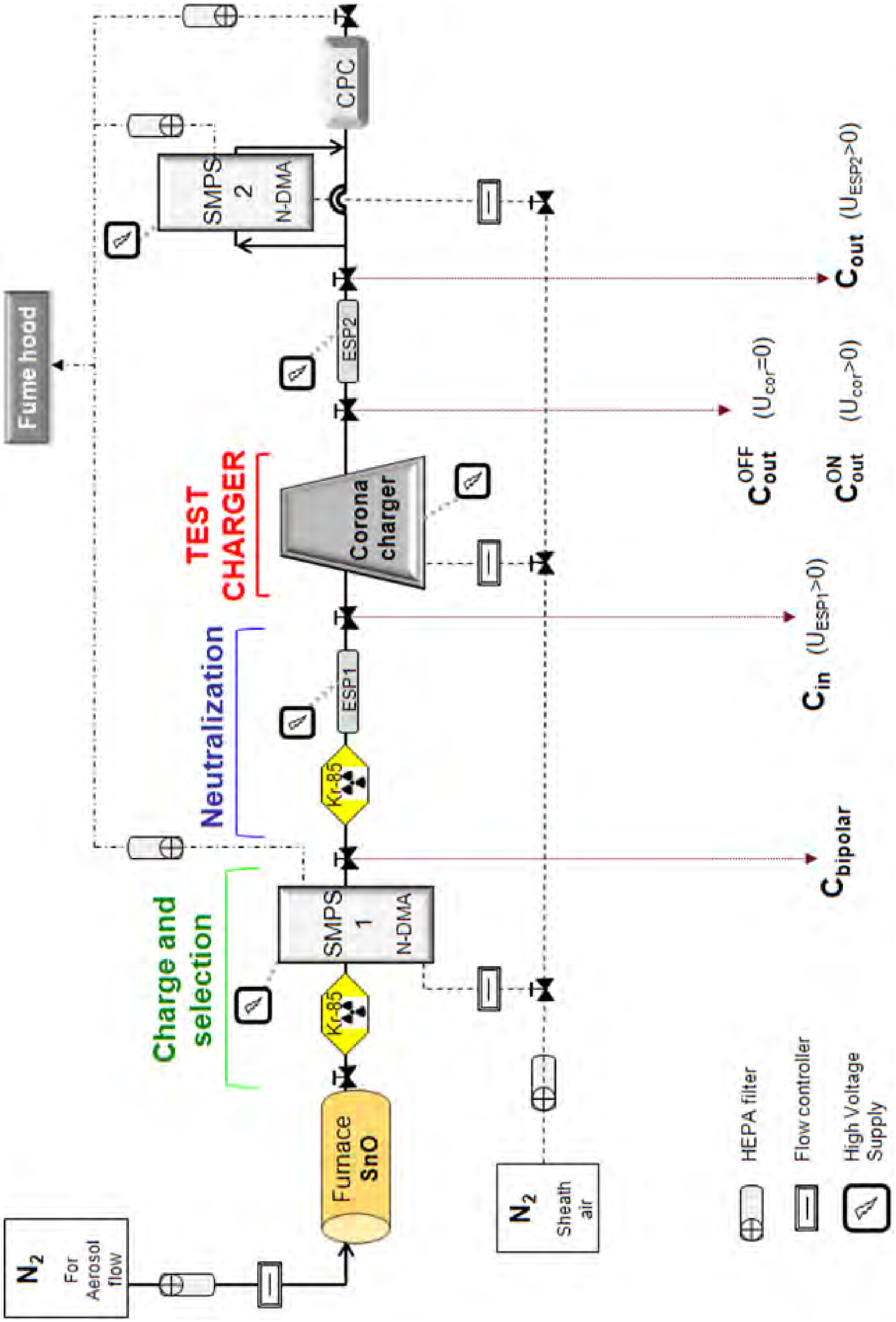

Figure 2.4.1: Experimental setup for characterization of the corona charger.

3

ELECTRICAL CHARACTERIZATION OF THE CORONA CHARGER

The preceding chapters were related to conceptual aspects of the unipolar charging, such as backgrounds, theories and designing. Following chapters will analyze the experimental results from the previous assumptions. First of all, a complete characterization of the electrical properties of the corona discharge is done. The output voltage and current of the ions or charged particles are analyzed in function of the flow rates, geometry of the electrodes and applied input voltage and current to the electrodes, thus selecting the optimal characteristics for a stable operation of the corona device.

3.1 ION CURRENT

The electrodes used to generate the corona discharge are needles made of pure tungsten (99, 97% minimum of W), having a diameter of 2.4 ± 0.1 mm, a 10°±1° cone curvature and a starting tip of 50 ± 20 μm of diameter, as shown in fig. 3.1.1 (all tolerances provided by the manufacturer company Wolfram Industrie GmbH). It has been exposed in [10] that the electric field at the tip of a corona point depends on its radius of curvature, but for point radii less than 50 μm no further current gain occurs as electrode sharpness is increased, because the corona discharge becomes so conducting that it shields the electrode tip.

Measurement of the ion current is done by means of an electrometer (IONER from Ramem, model EL-5010) which works in the femtoammeter range. It performs current measurements in a 4-decade range from 0.1 fA. A preamplifier is placed in a Faraday cage after corona output in order to decrease electrical noise, and then connected to a current detector (IONER from Ramem, model EL-5020) especially conceived for the measurement of ultra low currents (fA) at high voltage applications (kV).

A bias voltage of ±12 V is applied into the Faraday cage to better attract the ions to the collector. Only ion driving flow Q_i is considered and several sets are measured, each of them made of an average of around 2 minutes of continuous current measurement every single second at each selected corona voltage. Errors are calculated.

The gases used were mainly pure nitrogen and filtered clean air, in order to test negative corona, since pure N_2 is a non-attaching gas (electron 'insulating' gas) and only arcing is reached but not negative corona [121].

The mobility of positive ions is considered as $Z_i^+ = 1.4 \times 10^{-4} \mathrm{m^2/Vs}$ for positive and $Z_i^- = 1.90 \times 10^{-4} \mathrm{m^2/Vs}$ for negative ions [1].

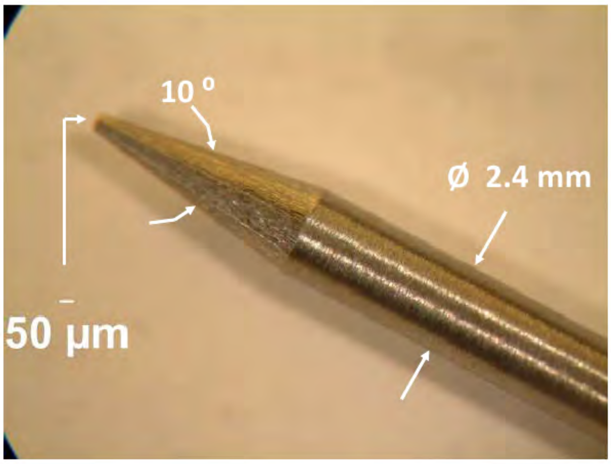

Figure 3.1.1: Characteristics of the needle used as discharge electrode.

Form Maxwell's theory, the electrical field where there exists a non-zero space charge density ρ can be expressed by means of the *Poisson's equation* as:

$$\nabla \vec{E} = \frac{\rho}{\epsilon_0}, \tag{3.1.1}$$

where $\epsilon_0 \approx 8.854 \times 10^{-12}\,{}^{\mathrm{F}}/_{\mathrm{m}}$ is the vacuum permittivity. The ion current density has the form [148]:

$$\vec{j} = \rho(Z_i\vec{E} + \vec{u_g}) - \mathcal{D}_i \cdot \nabla\rho, \tag{3.1.2}$$

being $\vec{u_g}$ the velocity due to the gas flow, $Z_i\vec{E}$ the ion drift velocity, $\mathcal{D}_i = {}^{k_B T Z_i}/_{e}$ the diffusion coefficient of ions and $\rho = eN_i$ the charge density. The last term of eq. (3.1.2) can be neglected, since the diffusion is very small compared with the other forces present, as it will be shown in the following.

If the current density is uniform and flows straight into an area A, the current through this area is:

$$I = \oint \vec{j} \cdot dA \rightarrow j = \frac{I}{A}. \tag{3.1.3}$$

Accordingly, the electric field in the charging region will be treated as an axial field, since is along the axial dimension where the flow drives the ions through the mixing tube. This can result in a loss of precision, since the actual corona discharge occurs in the radial direction inside the discharge region, as well as the electrostatic migration of particles to the walls, but it will be valid for a first approximation [40, 73]. Then, the eq. (3.1.1) results:

$$\nabla \vec{E} = \frac{\partial \vec{E}}{\partial x} = \frac{I}{\epsilon_0 A(u_g + Z_i E_x)}, \tag{3.1.4}$$

which can be expressed:

$$\frac{1}{2Z_i}\mathrm{d}(u_g + Z_i E_x)^2 = \frac{I}{\epsilon_0 A}\mathrm{d}x. \tag{3.1.5}$$

Table 3.1.1: Electrical field at the output of the ion generation region for the case with drag ion flow of $Q_i = 0.5\,\text{lpm}$ and the stationary case. Three distances of the needle are tested.

D_{gap} (mm)	A (m^2)	u_g (m/s)	E_x (V/m) (eq. (3.1.6))	E_x (V/m) (eq. (3.1.7))
3	3.8×10^{-5}	0.221	271.65	961.47
7	2.0×10^{-4}	0.042	398.49	628.73
10	3.8×10^{-4}	0.022	363.70	496.25

Integrating eq. (3.1.5) between the electrodes from $x = 0$ as the starting point of the mixing region, where the field strength is E_{x_0}, the electric field E_x:

$$E_x = \sqrt{\frac{2I}{\epsilon_0 A Z_i} x + \left(\frac{u_g}{Z_i} + E_{x_0}\right)^2} - \frac{u_g}{Z_i}. \tag{3.1.6}$$

The initial field in the charging region E_{x_0} shall not be confused with the Peek's initial discharge value E_0, since the field decays rapidly with the distance from the electrode, being in practice negligible outside the ionizing region.

The eq. (3.1.6) can be simplified for the stationary case, $u_g = 0$, where the velocity of ions is imposed by the electric field generated by the corona discharge. Some authors [40, 124] neglect as well the value of the electric field at the edge of the electrode against the other variables, resulting:

$$E_x = \sqrt{\frac{2I}{\epsilon_0 A Z_i} x}. \tag{3.1.7}$$

Results of both cases, with and without drag ion flow, are shown in table (3.1.1) for three different gaps between electrodes. It can be seen that when the ion flow is applied, contrary to the stationary case, the electric field is not inversely proportional to the distance between electrodes, but also there is a maximum. This is due to the compromise between the greater area in which the ions are generated, proportional to the distance of the needle to the output, and the slower drag flow velocity for the same flow rate that this causes.

From the ion current, it can be calculated the mean number concentration of ions, N_i, in the discharge zone of the ionizer in the absence of aerosol particles. Comparing eqs. 3.1.3 and. 3.1.2, the space charge density is obtained:

$$\rho = \frac{I}{A(u_g + Z_i E_x)}, \tag{3.1.8}$$

and therefore the mean number concentration of ions:

$$\mathrm{N_i} = \frac{I}{eA(u_g + Z_i E_x)}, \tag{3.1.9}$$

which for the electrode distances previously calculated, gives an ion concentration of 4.62×10^{12}, 2.24×10^{12}, $1.31 \times 10^{12}\,\mathrm{m}^{-3}$ for the gap distances of 3, 7 and 10 mm respectively.

Calculations of the ion concentration and axial electric field shown here are enough for a first approximation, to have an idea of the order of these magnitudes. However, it will be shown in section 5.3 that both variables are related and more parameters must be considered for an accurate estimation of the two.

3.1.1 *Measurement of the ion current*

Measurement of the ion current is done by means of an electrometer (model EL-5010, RAMEM, Madrid, Spain) which can measure in the femtoammeter range. The ion current at the outlet of the charging region was measured by means of a Faraday cup fabricated by RAMEM too (fig. 3.1.2). The collector was a stainless steel tip connected with the electrometer device and isolated from the outer walls of the cage. The tip was fed with an applied bias voltage of 12 V to attract the ions to the collector.

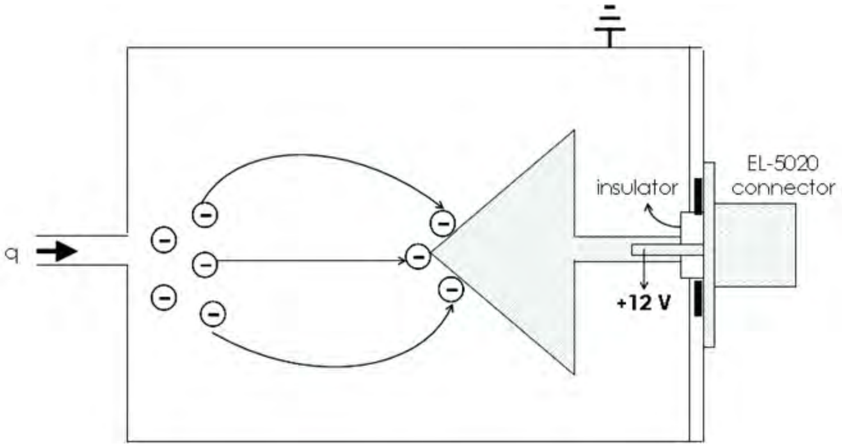

Figure 3.1.2: Faraday cup for ions *(Image from Ramem)*.

A commercial DC high voltage power supply was used to maintain the voltages and currents in the ranges between 2.0 – 4.5 kV and 1 – 12 μA. The ions produced inside the charger are then led into the Faraday cup.

The use of the bias voltage in both environments, synthetic air and pure nitrogen, incremented the collection of ions around 15% for positive corona, even higher (30%) when the transport flow was lower (figs. 3.1.3a, 3.1.4a), and as much as a 100% for negative corona (fig. 3.1.4b).

The difference in gain switching on and off the bias voltage is related with the mobility of ions. The mobility of negative ions is higher than that of positive, their

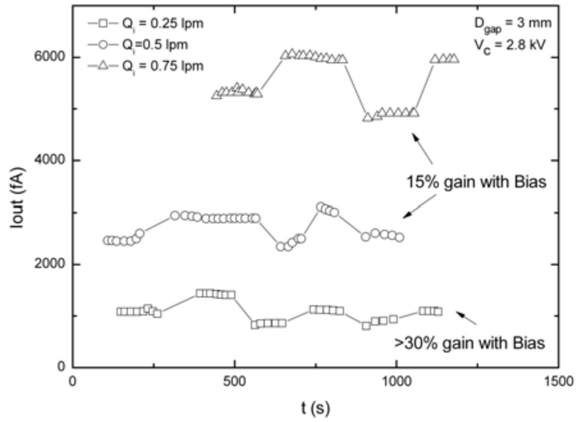

(a) $D_{\text{gap}} = 3\,\text{mm}$

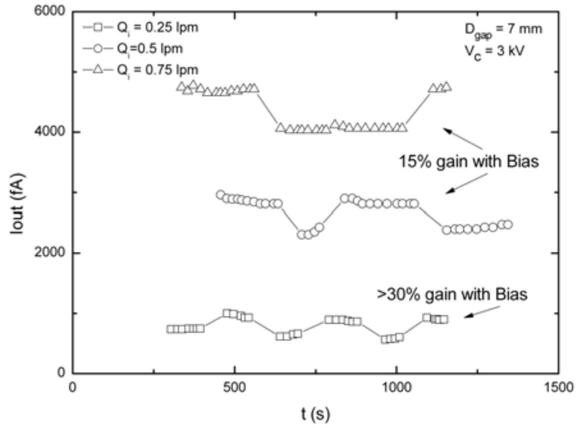

(b) $D_{\text{gap}} = 7\,\text{mm}$

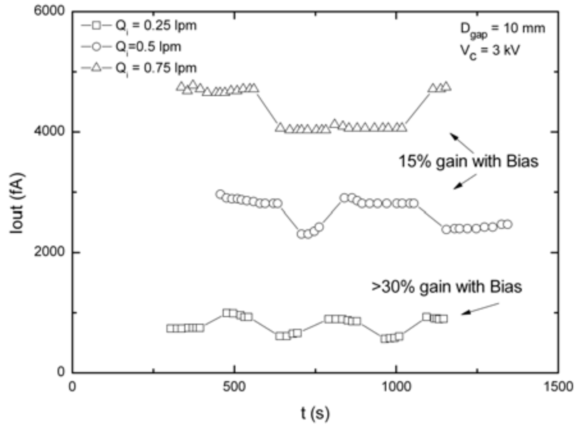

(c) $D_{\text{gap}} = 10\,\text{mm}$

Figure 3.1.3: Difference with or without bias voltage in ion collection within the Faraday cup at an applied voltage of 3 kV. Gas used is pure nitrogen. Only positive corona is tested.

velocity is higher as well but their penetration is lower; they are electrostatically lost within the ionizer to a higher extent, since they are more likely to impact and deposit on the outer electrode wall of the charger [59, 61].

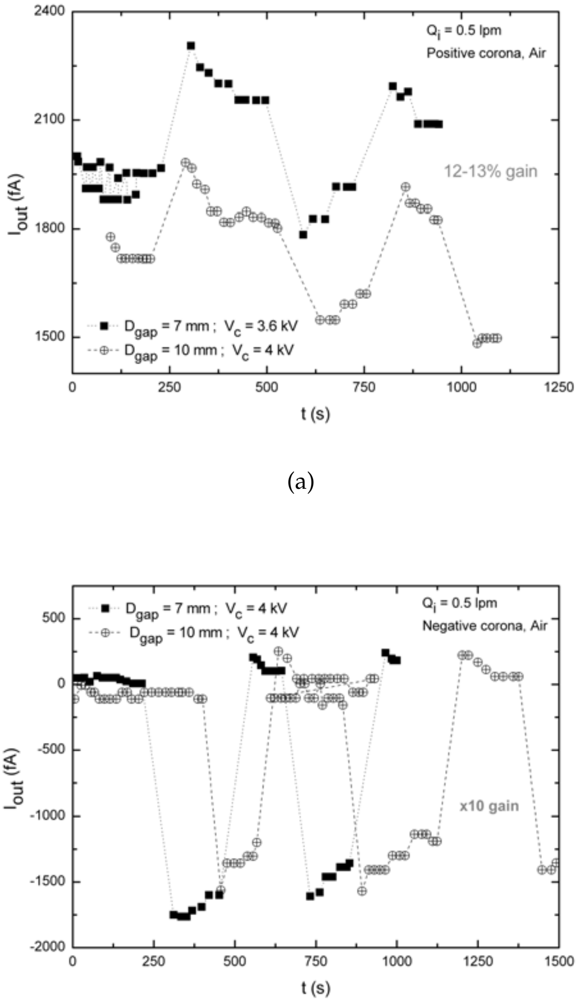

(a)

(b)

Figure 3.1.4: Differences in current when driven gas is clean air for *(a)* positive and *(b)* negative corona.

The relation between ion velocity and mobility $(Z_i = \vec{u}/\vec{E})$ is also reflected in the fact that the lower the ion flow, the higher the gain with bias, that is, the slower they go, the better are captured (fig. 3.1.3). But too slow ions can be lost by electrostatic forces or simply by diffusion (see section 4.1). We also take in account that it will be mixed with the particle flow coming out from the first DMA and then flow into a second SMPS. Considering that the maximum flow supported by this device is 20 lpm and the best ratio to work with aerosol is $10 : 1$, since the maximum concentration is obtained (otherwise is somehow diluted), the best rate will be $Q_i = 0.5\,\mathrm{lpm}$ and $Q_a = 1.5\,\mathrm{lpm}$.

A higher current is reached with nitrogen than with air, as seen in fig. 3.1.5, even for a greater applied voltage in air. This can be related with the nature of the ions created, since nitrogen is monocomponent and in air other gases are involved, creating ions with different mobilities and therefore different velocities for the same applied potential.

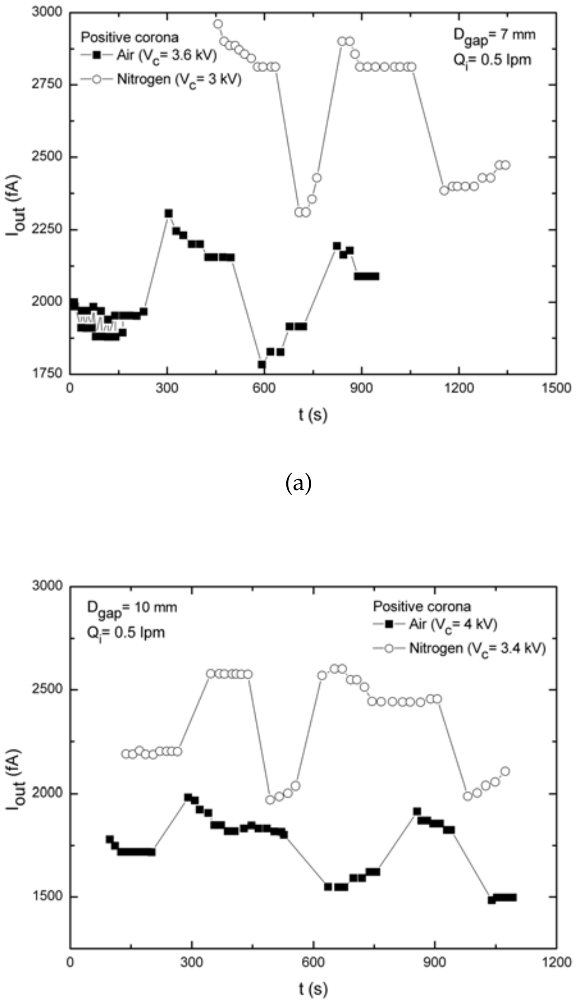

(a)

(b)

Figure 3.1.5: Differences in current when driven gas is clean air or pure nitrogen.

3.1.2 *The current-voltage relation in the corona discharge*

The relationship between output current and potential applied to the electrodes has been derived by Townsend [126] for a coaxial cylinder geometry, valid also for needle-to-plane geometry. The averaged I – V relation of a corona discharge is usually approximated by the dependence:

$$I = k(V_c - V_0)^n, \tag{3.1.10}$$

where k is a dimensional factor subject to the inter-electrode distance, the needle electrode radius, the ion mobility in the drift region and other geometrical factors, n a parameter taking values between $1.5 - 2$ [90]. It was empirically found that for small currents, the data is better described by a relation of the form: $I = kV_c(V_c - V_0)$ [40]. V_c is the applied voltage and V_0 is the onset corona voltage.

To determine the dependance of k in eq. (3.1.10), the voltage is calculated from eq. (3.1.6), since $\vec{E} = -\vec{\nabla} V$. We will consider again only an axial field as in the beginning of the present section for simplification:

$$\Delta V = -\int_0^L E_x \mathrm{d}x. \tag{3.1.11}$$

Substituting eq. (3.1.6) and operating:

$$\Delta V = \frac{\epsilon_0 A Z_i}{3I}\left[\left(\frac{2I}{\epsilon_0 A Z_i}L + \left(\frac{u_g}{Z_i} + E_0\right)^2\right)^{\frac{3}{2}} - \left(\frac{u_g}{Z_i} + E_0\right)^3\right] - \frac{u_g}{Z_i}L. -] \tag{3.1.12}$$

Considering first the simpler case of the stationary state ($u_g = 0$), eq. (3.1.12) is simply:

$$\Delta V = \frac{2L}{3}\left(\frac{2I}{\epsilon_0 A Z_i}L\right)^{\frac{1}{2}}. \tag{3.1.13}$$

Then, the current is related with the voltage as:

$$I = \frac{9}{8}\frac{\epsilon_0 A Z_i}{L^3}\left(V_c - V_0\right)^2. \tag{3.1.14}$$

On the other hand, under the influence of a moving airstream and considering $\frac{2I}{\epsilon_0 A Z_i}L \gg u_g$, the current is given in the one dimensional case by:

$$\Delta V = \frac{\epsilon_0 A Z_i}{3I}\left[\left(\frac{2I}{\epsilon_0 A Z_i}L\right)^{\frac{3}{2}} + \frac{3}{2}\left(\frac{2I}{\epsilon_0 A Z_i}L\right)^{\frac{1}{2}}\left(\frac{u_g}{Z_i}\right)^2 - \left(\frac{u_g}{Z_i}\right)^3\right] - \frac{u_g}{Z_i}L. \tag{3.1.15}$$

Introducing a velocity ratio parameter:

$$u_r = \frac{u_g}{Z_i}\left(\frac{\epsilon_0 A Z_i L}{2I}\right)^{1/2}, \tag{3.1.16}$$

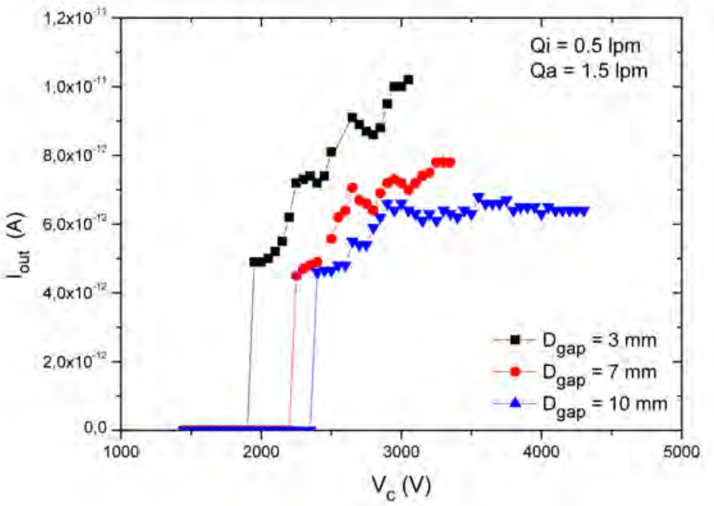

Figure 3.1.6: Corona applied voltage versus output current at an ion dilution flow of 0.5 lpm and a sheath aerosol flow of 1.5 lpm.

$$V_0 - V_c = \frac{2}{3} L \left(\frac{2I}{\epsilon_0 A Z_i} L \right)^{1/2} + \frac{u_g}{Z_i} \left[u_g - \frac{2}{3L} u_r^2 - L \right]. \tag{3.1.17}$$

When $u_r \ll 1$, the term within square brackets can be approximated to $-L$, and the eq. (3.1.17) results:

$$V_0 - V_c = \frac{2}{3} L \left(\frac{2I}{\epsilon_0 A Z_i} L \right)^{\frac{1}{2}} - \frac{u_g}{Z_i} L. \tag{3.1.18}$$

Then, solving for I in the non-stationary case:

$$I = \frac{9}{8} \frac{\epsilon_0 A Z_i}{L^3} \left((V_c - V_0) + \frac{u_g L}{Z_i} \right)^2. \tag{3.1.19}$$

This equation expresses the characteristics of the discharge in an airstream. To check its validity, a simpler form is used. Since is easier to fit a linear plot of the form: $y = ax + b$, square root of eq. (3.1.19) is taken, being the independent variable $V_c - V_0$, the dependent variable $I^{1/2}$, and the coefficients:

$$a = \left(\frac{9}{8} \frac{\epsilon_0 A Z_i}{L^3} \right)^{1/2} \quad \text{and} \quad b = \frac{3}{2} u_g \left(\frac{\epsilon_0 A}{2 Z_i L} \right)^{1/2}. \tag{3.1.20}$$

Firstly, the value of the corona onset voltage must be known. It is believed that V_0 is independent of the current and applied voltage, but has a strong dependence on the electrode tip radius and the inter-electrode distance [42]. Despite of the experimental and theoretical efforts made to predict an accurate value of V_0, its practical value varies under different conditions.

The corona onset voltage can be determined experimentally as the point at which the current intersects the voltage axis V_c in fig. 3.1.6. Measured and calculated corona onset voltages differ substantially, obtaining experimentally 1.95, 2.25 and 2.40 kV for electrode distances of 3, 7 and 10 mm, while calculated results are 2.03, 2.54 and 2.95 kV respectively. In the literature, the initial corona voltage is often identified with the ignition voltage or V_{cv}.

As expected, ion current increases as D_{gap} decreases: $I_{\text{out}}(3\,\text{mm}) > I_{\text{out}}(7\,\text{mm}) > I_{\text{out}}(10\,\text{mm})$. The current experiences a first increase when the corona starts and then again rapidly increases when spark-over is reached. The corona discharge starts at lower voltages for a gap of 3 mm, while for the gap of 10 mm the range of applicable corona voltages is greater, as can be seen in fig. 3.1.6. But while the current of the 3 mm gap increases with applied voltage, in the case of 10 mm it tends to grow slowly, remaining approximately constant.

The reason is that the ion current depends exclusively on corona voltage only within a narrow interval [61]. At larger voltages it practically becomes constant, independent of the corona voltage, since a higher degree of ion loss is inevitable with a large number of ions, e.g. due to space charge effects.

The fitting of the data is shown in fig. 3.1.7 with R-square over $0,9295$. The coefficients a and b from eq. (3.1.19) have different values depending on the inter-electrode distance, being shown in the plot. The dimensions considered are L as the length of the charging tube plus the extra distance that travels inside the charging region, but since it was proven in eq. (2.3.4), only between a quarter to half of the area of the charging region for the selected flowrates is considered. Also the precision of the y-intercept is subjected to an accurate approximation of the value of V_0, which as it was commented previously, is difficult to know with exactitude. This conditions the accuracy in the calculation of the fit parameters.

3.1.3 *Influence of the flow rate*

Following the Ohm's Law, $V = I \cdot R$, when the the flowrate or distance from the needle tip to the electrode are modified, the resistance of the air between the electrodes changes. There is higher resistance for lower flow rates or larger distances from the needle to the output, and vice versa. This means that for a given voltage and a high resistance, the current will be lower, as $I_{\text{out}}(3\,\text{mm}) > I_{\text{out}}(7\,\text{mm}) > I_{\text{out}}(10\,\text{mm})$. The results presented in fig. 3.1.8 show that at a fixed corona voltage, an increase in the gas flow rate results in an increase of the ion current.

Ion current is proportional to flowrate due to the gas velocity (eq. (3.1.9)), but a higher current also leads to higher losses for ions and lower ion concentrations. There must be a compromise between the ion current and the flow rate to give a high ion concentration with few losses of ions. A high flow rate when a high voltage is applied is followed by a decrease in current, as fig. 3.1.8 shows for $D_{\text{gap}} = 10\,\text{mm}$.

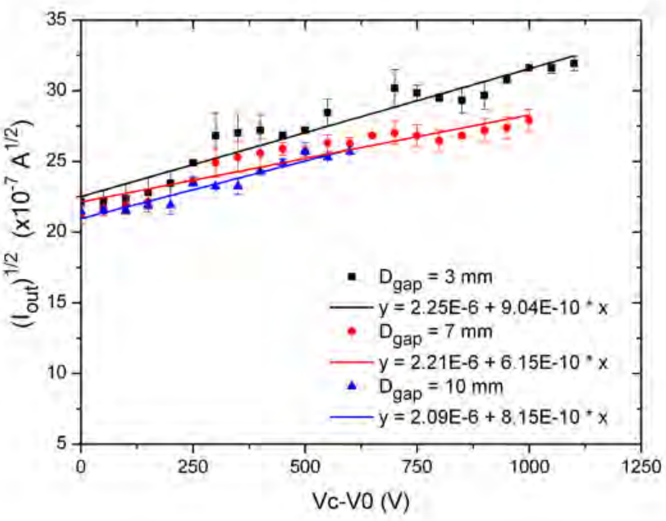

Figure 3.1.7: Fitting of the ion current and corona voltages.

An increase in the ion flowrate among the total dilution rate causes as well a slight increase in the onset corona voltage. An addition of a flowrate decreases the voltage at which corona starts.

It can be seen that the measured ion current at the output of the charger is higher for the closest position of the electrode to the wall ($D_{\text{gap}} = 3\,\text{mm}$), and increases with higher voltages. Meanwhile, for $D_{\text{gap}} = 10\,\text{mm}$ an increase of applied voltage leads to an almost constant current, as was commented in the previous section. This is even more evident in fig. 3.1.9, where instead of the applied voltage V_c is shown the applied current I_c to the needle electrode at a fixed $V_c = 3.5\,\text{kV}$.

In fig. 3.1.10 the variation in corona voltage is shown in the lower axis for a fixed applied current of 0.07 mA, and the variation of corona current for a fixed applied voltage of $V_c = 3.5\,\text{kV}$ in the upper axis. The measured output current is practically the same independently of the variation in applied voltage or current. Therefore in the following, unless the contrary is indicated, we will work by varying the voltage at fixed $I_c = 0.07\,\text{mA}$ for simplicity reasons, and only results for $D_{\text{gap}} = 3\,\text{mm}$ and 10 mm will be compared, since are the most representative distances of the effect of the gap between electrodes.

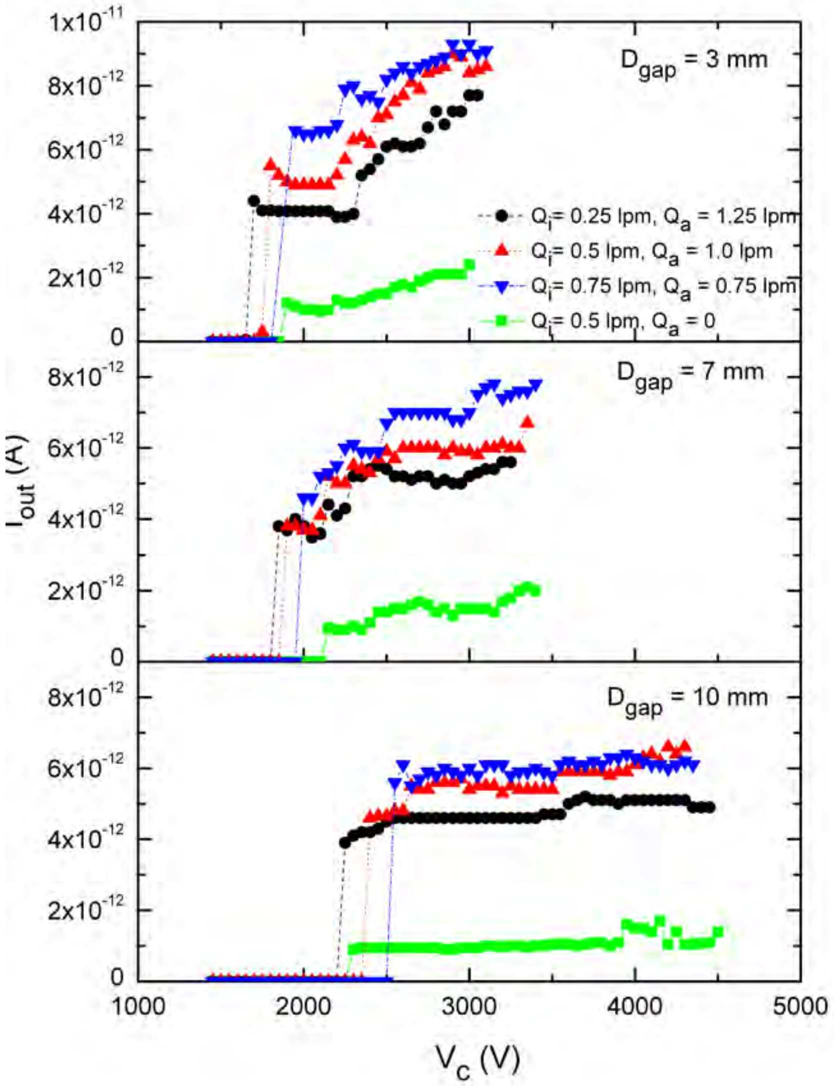

Figure 3.1.8: Measured current at the output of the charger depending on applied voltages and flows.

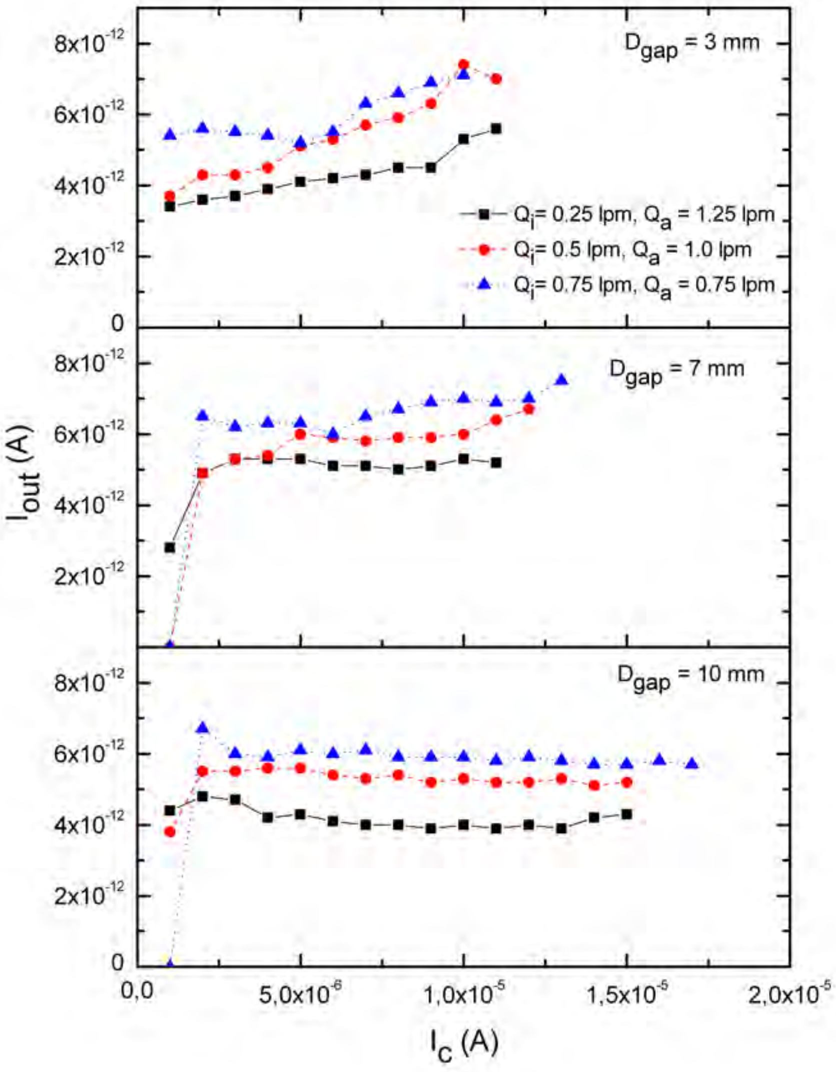

Figure 3.1.9: Measured current at the output of the charger dependent on applied current and flows.

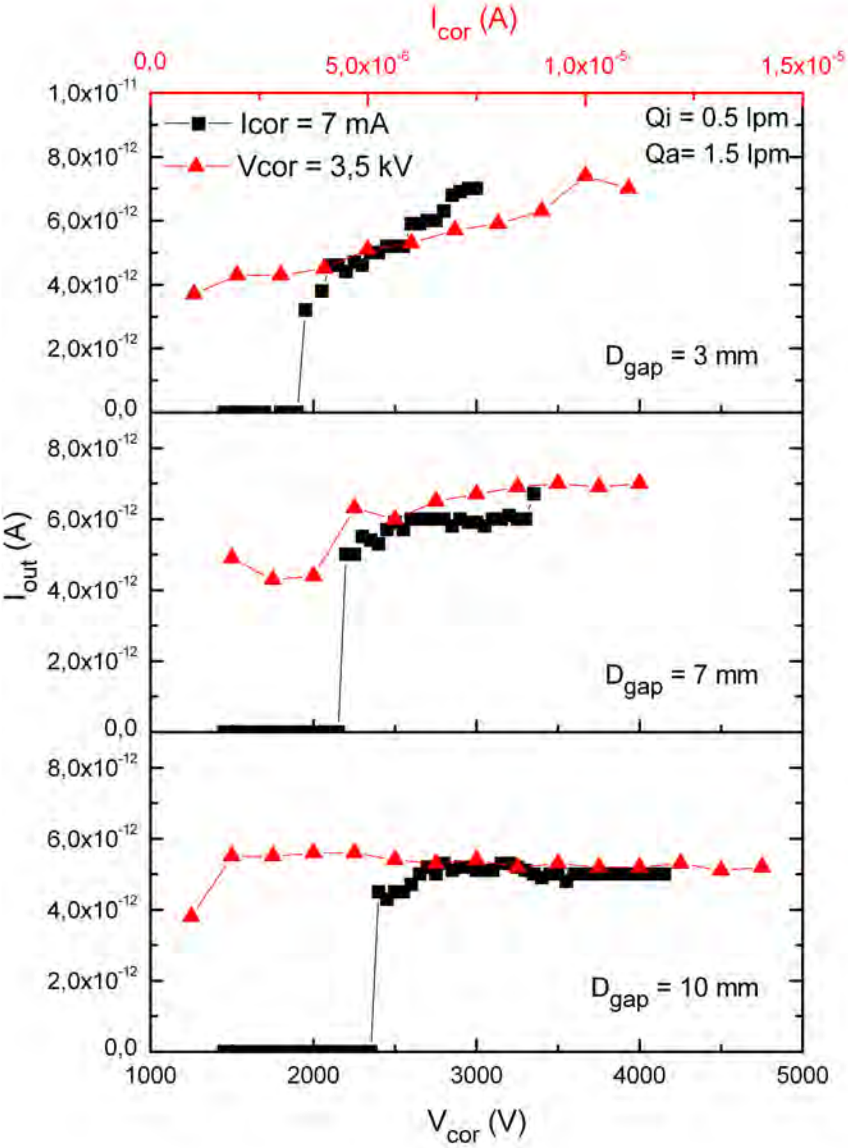

Figure 3.1.10: Measured output current for variation of the applied current (upper axis) at a fixed corona voltage of $V_c = 3.5\,\mathrm{kV}$ and the applied voltage (lower axis) at a constant corona current of $I_c = 7\,\mu\mathrm{A}$.

3.1.4 *Erosion of the electrode needles*

Three tungsten needles with the characteristics of fig. 3.1.1 were used for the tests, which due to the usage time their tip sharpness become eroded as listed in table 3.1.2.

Table 3.1.2: Aspect of the needle tips after use.

Final tip diameter (μm)	Usage time
46.4 μm 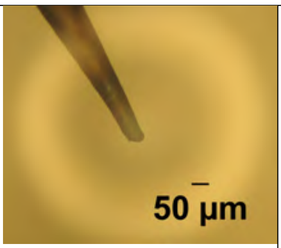	3 months
75 μm 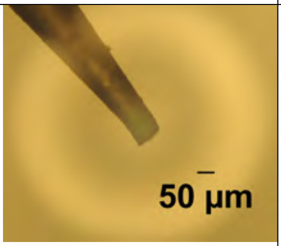	2 months
128.6 μm 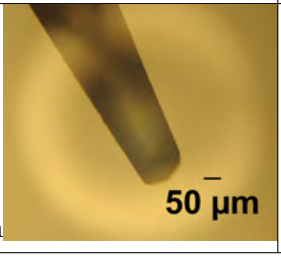	7 months

Because of the variable distance between electrodes in our corona charger, the Paschen equations (2.1.2, 2.1.3) are dependent of D_{gap}. In the conical part of the discharge region, the necessary voltage for starting the corona increases logarithmically with the distance to the walls (fig. 3.1.11). The curvature of the tip is also an influential factor for the corona onset, since a rounder tip increases the value of the starting voltage.

Although the effect of the rounder tip on the starting voltage is measurable, the final effect on the measured current is almost irrelevant, as fig. 3.1.12 demonstrates. the differences are within the error measurement.

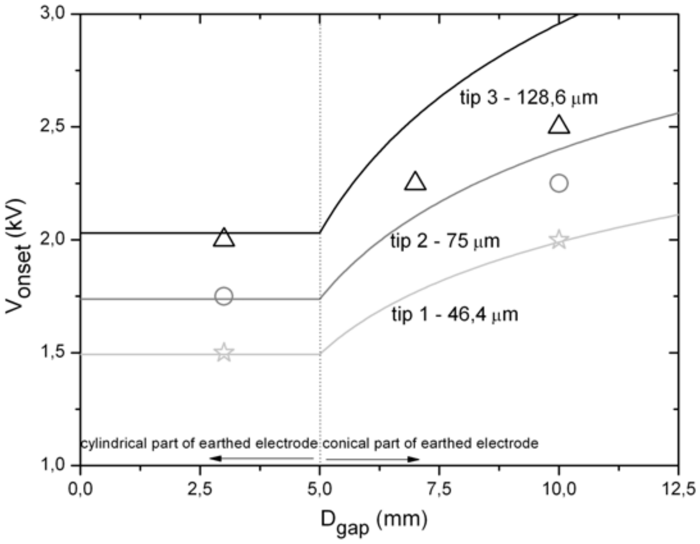

Figure 3.1.11: Corona onset voltage depending on the distance between electrodes.

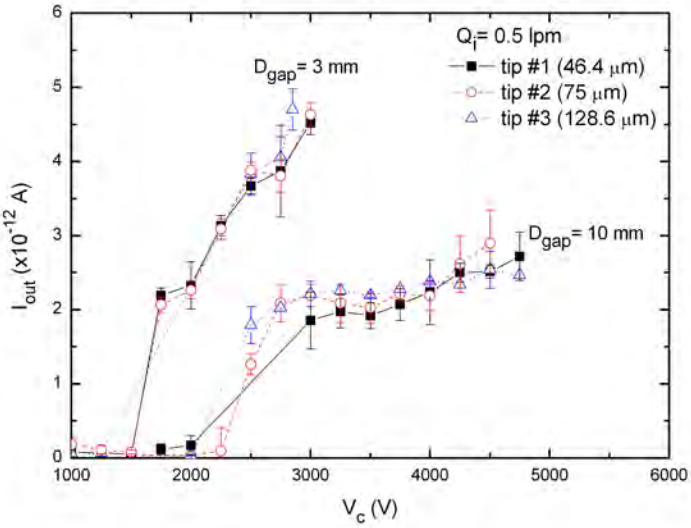

Figure 3.1.12: Final measurements from three needles with different rounder tips.

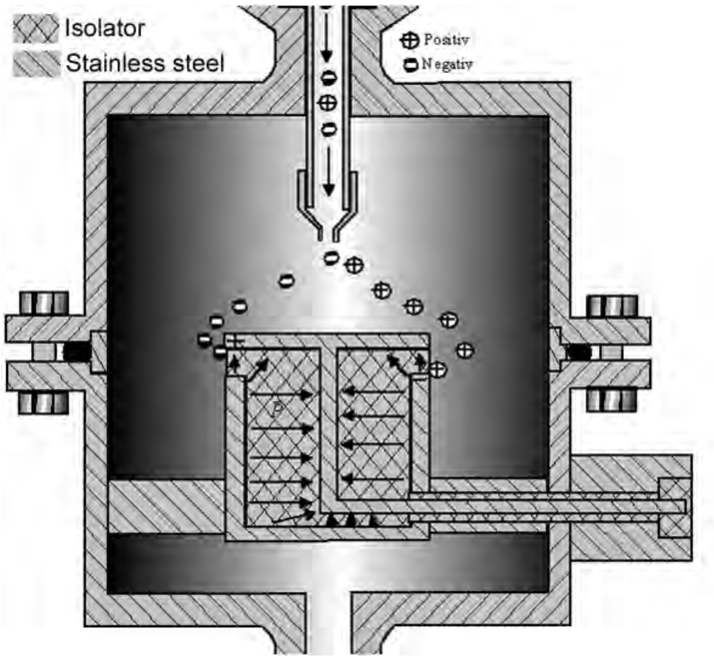

Figure 3.2.1: Faraday cup for the measurement of charged particle current.

3.2 PARTICLE CURRENT

The current generated by the charged particles is measured with an EL-5020 from Ramem and a Faraday cup after corona output. A bias voltage is not applied in this case, since is a different device as for ion current measurements and a bias applied would provoke overflow on the electrometer. The design of the Faraday cup can be seen in fig. 3.2.1. Charged particles pass through a filter where they imprint their electrical charge to a spring connected with the electrometer. Ion and particle flow are considered together. Several sets are taken, each of them made of an average of around 2 minutes of continuous current measurement at each corona voltage. Errors are calculated.

The particle current is as well an output current, since is measured at the same point as the ion current, after the charging zone. But an electrostatic precipitator is mounted to remove the excess of free ions and avoid false signals, so the distance covered by the particles is larger than in the case of ions (see 3.3).

In fig. 3.2.2 is shown that the current of the charged particles is higher as the distance of the needle is closer to the output, since more ions are generated. But is also much higher in all cases than the bipolar one. This makes sense, since the bipolar recombines positive and negative ions to attain equilibrium, reducing the charging efficiency. It is also seen that, even for a higher applied corona voltage, the larger the gap distance of the electrodes, the lower the particle current, which will have an effect on the number of charges acquired by the particles.

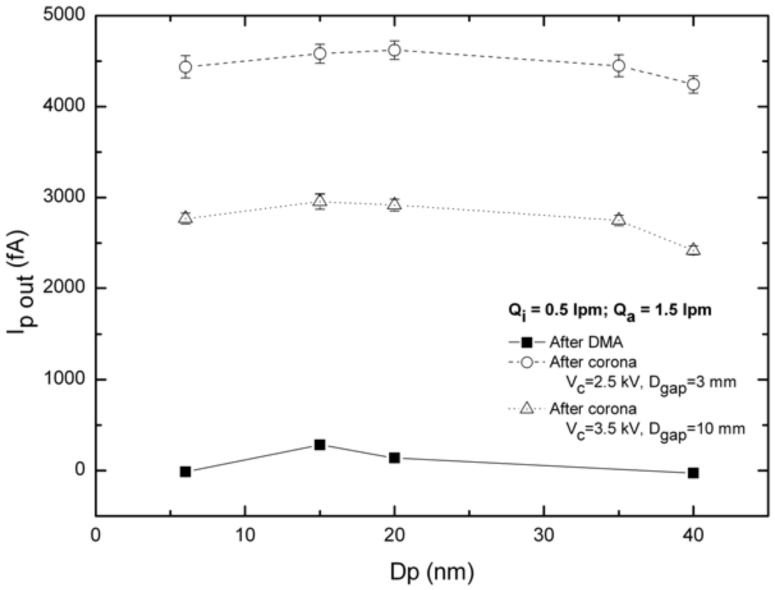

Figure 3.2.2: Measured current of particles for different particle diameters.

The raw graphs on fig. 3.2.3 show that there is not a strict correlation between particle diameter and measured current. It would be logic to think that a bigger particle would acquire more charges, and therefore induce a higher current. But it seems that this increment has a maximum for a given diameter, and then decreases for bigger particles, even for particles charged in the bipolar environment (fig. 3.2.3a), and is probably due to the electrostatic losses, as it will be analyzed in sec. 4.1.

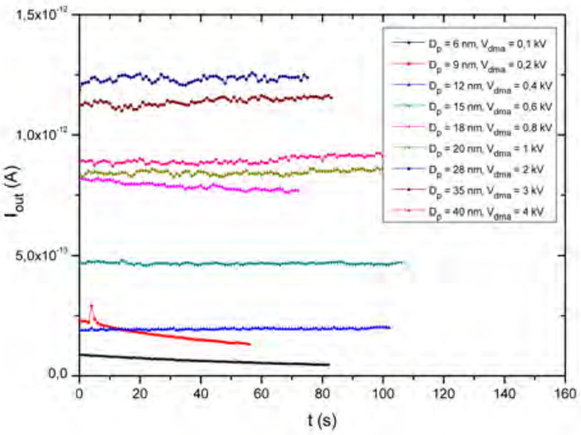

(a) Measured after the bipolar charger and selection from the first DMA.

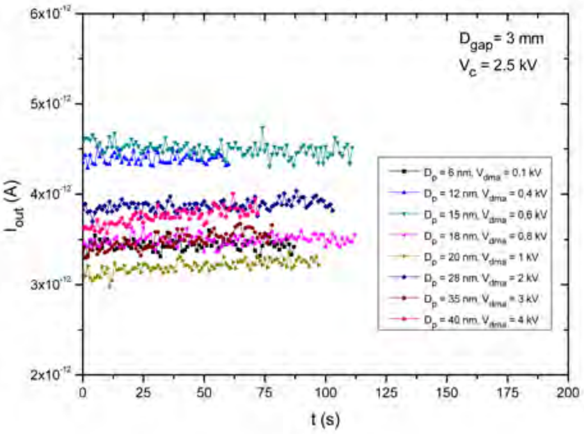

(b) Measured after the unipolar corona charger for $D_{\text{gap}} = 3\,\text{mm}$

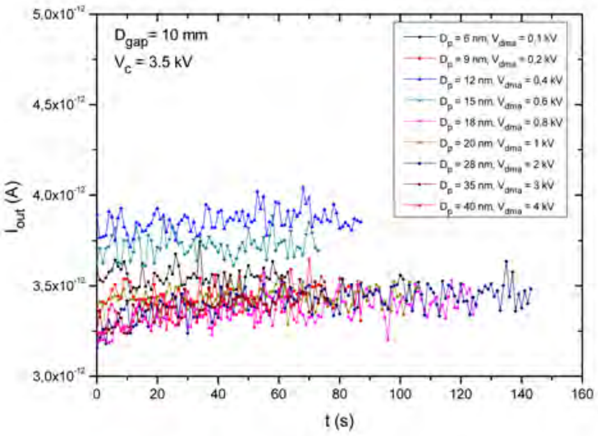

(c) Measured after the unipolar corona charger for $D_{\text{gap}} = 10\,\text{mm}$

Figure 3.2.3: Raw measurements of particles from different diameters.

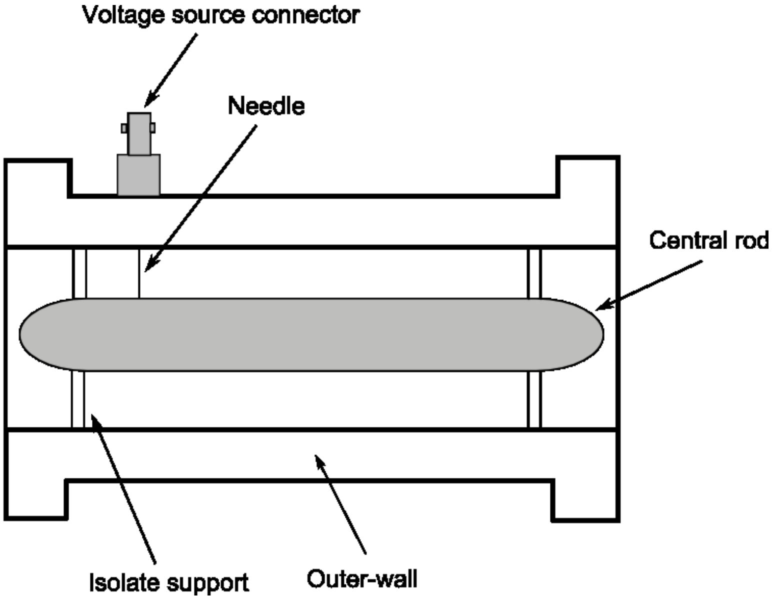

Figure 3.3.1: Schematic diagram of the electrostatic precipitator used.

3.3 ELECTROSTATIC PRECIPITATION

After a diffusion charging process there is always an excess of free ions. If they are not removed, these ions will be precipitated together with the charged particles in the particle counters, making undesirable contributions to the signal current to be measured. To prevent this, an ESP is necessary to separate the remaining ions from the charged particles. Although ESPs are initially designed to precipitate particles, they are suitable for depositing ions when a proper voltage is applied to the central rod. Ions and charged particles have quite different electrical mobilities, being the one of ions in general much higher than that of particles. Therefore, a weak electrostatic field may be strong enough to deposit only the ions while charged particles can pass through smoothly.

Figure 3.3.1 shows the basic configuration of a typical ESP as the one used in our experiments. It is homemade in the laboratories of the NST at the University of Duisburg-Essen. It has a simple geometry, consisting in a central rod of length L_{esp} about 140 mm connected to a low voltage source by a needle with its tip touching the surface of the rod, and a grounded outer-wall. The the radius of the central rod r_i and inner radius of the outer wall r_o are 10 mm and 16 mm respectively. An electrostatic field is established in the space between the central rod and the outer wall. The radial electric field strength E_r is given by:

$$E_r = \frac{U_{\text{esp}}}{r \ln \left({}^{r_o}/_{r_i} \right)}; \text{ for } r_i \leq r \leq r_o, \tag{3.3.1}$$

where r is the radial location and U_{esp} is the voltage applied. This voltage ensures that all undesirable ions can be deposited while most charged particles can pass through without losses. The determination of the voltage U_{esp} is stated as follows.

The particle velocity u_p and ion velocity u_i can be discomposed in axial and radial velocities with the form:

$$u_x = \frac{\mathrm{d}x}{\mathrm{d}t}, \tag{3.3.2}$$

$$u_r = \frac{\mathrm{d}r}{\mathrm{d}t} = Z_i E_r = \frac{Z_i U_{esp}}{r \ln\left({}^{r_o}/_{r_i}\right)}. \tag{3.3.3}$$

These velocities are assumed to be the same as the flow velocity, u_g, that is:

$$u_i = u_p = u_g. \tag{3.3.4}$$

The flow velocities on the surface of the central rod and the outer wall are zero, i.e., $u_g(r_i) = 0$ and $u_g(r_o) = 0$ respectively, and its profile is parabolic, then the flow velocity at the inlet of the electrical precipitator can be expressed by:

$$u_g = 2\frac{Q}{\pi\left(r_o^2 - r_i^2\right)}\left(1 - \left(\frac{2r - r_o - r_i}{r_o - r_i}\right)^2\right); \text{ for } r_i \leq r \leq r_o. \tag{3.3.5}$$

Combining the equations 3.3.2 and 3.3.3:

$$\mathrm{d}x = \frac{u_x \cdot \ln\left({}^{r_o}/_{r_i}\right)}{Z_i \cdot U_{esp}} \cdot r\,\mathrm{d}r. \tag{3.3.6}$$

Since all the velocities are equivalent, substituting in the previous expression the equation 3.3.5 and integrating, we can obtain an expression for the distance covered by the ions:

$$\begin{aligned} x(r) \quad = \quad & \frac{2 \cdot Q \cdot \ln\left({}^{r_o}/_{r_i}\right)}{\pi\left(r_o^2 - r_i^2\right) \cdot Z_i \cdot U_{\mathrm{esp}}} \left[\frac{r^2}{3\left(r_o - r_i\right)^2}\left(4r(r_o + r_i) - 6r_o r_i - \right.\right. \\ & \left.\left. -3r^2\right) + \frac{r_i^3(2r_o - r_i)}{3(r_o - r_i)^2}\right]. \end{aligned} \tag{3.3.7}$$

If it is considered that particles or ions near the electrodes get stuck there straight after entering the precipitator, that is, $x(r_i) = 0;\ x(r_o) = 0$, for ions to be completely deposited within the precipitator, it must be fulfilled that $x(r_o) \leq L_{esp}$. From this condition, the minimum required voltage to remove the ions:

$$U_{\mathrm{esp}_{min}} = \frac{2Q \ln\left({}^{r_o}/_{r_i}\right)}{3\pi Z_i \cdot L}. \tag{3.3.8}$$

This expression shows that the removal of ions depends strongly on the geometry of the precipitator (r_o, r_i, L_{esp}), as well as at the flow rate Q and nature of the ions generated (Z_i).

Based on eq. (3.3.8), the minimum voltages for ion precipitation under different flow rates are calculated. For a total flowrate of 2 lpm and a positive corona, $U_{\mathrm{esp}_{min}} = -0.17\,\mathrm{V}$. Since the required precipitating voltages are quite low, lower than the precision of the voltage supply controller, a minimum voltage of $-1\,\mathrm{V}$ was applied. It can be seen in fig. 3.3.2 that all the ions, starting from those further from the wall, near the inner rod, can be deposited at these voltage values.

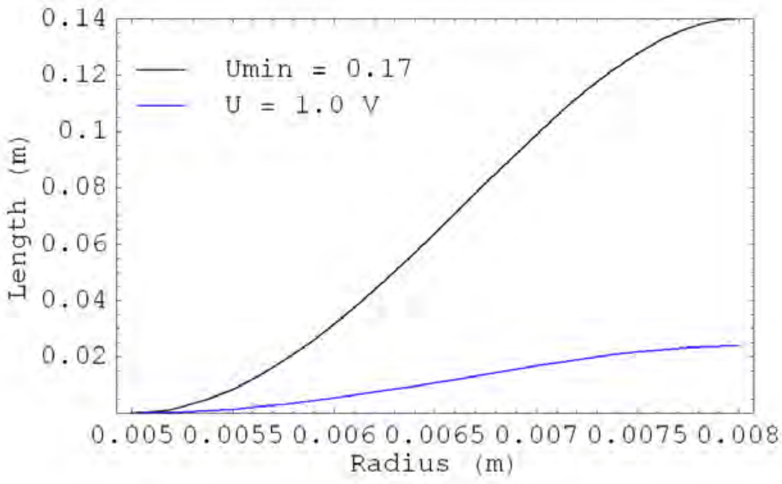

Figure 3.3.2: Ion trajectories starting at the central rod within the ion precipitator. Total flowrate of 2 lpm. Black line is the calculated minimum voltage $-0.17\,\mathrm{V}$, blue line is $-1\,\mathrm{V}$ applied to the ESP central rod.

It is still necessary to prove that this voltage has minimum influence on the charged particles. This can be easily done by calculating the trajectories of the particles within the ion precipitator at the voltage $U_{\mathrm{esp}_{min}}$. The governing equations of particles are identical to the ones for ions (eqs. 3.3.2 and 3.3.5), with the only exception that electrical mobility of the ions Z_i in equation 3.3.3 must be replaced by particle mobility Z_p (eq. (1.3.4)).

The largest electrical mobility corresponds to singly charged particles with the smallest diameter possible, which in our case is 6 nm. It can be seen from the plots in fig. 3.3.3 that with the minimum voltage, 96% of the 6 nm particles can safely pass through the precipitator, but for the real applied voltage of $-1\,\mathrm{V}$ this percentage is reduced to 89% of the particles passing. This is an acceptable value though, since some loss of particles close to the outer wall is unavoidable, and since the flow is parabolic, the concentration of particles near the surfaces is much lower. Therefore we can say that most of the particles can pass through the ESP smoothly, while the ions are safely removed.

The second use of the ESP is to neutralize the possible remaining particles after the selection of the monodisperse sample. Particles are initially charged at the SMPS with a ^{85}Kr source. Another ^{85}Kr source is used to neutralize the distribution, but some particles remain charged and ESP removal is required. Removal of charged particles is used as well after the diffusion charging. By removing the charged particles we can know the percentage of them from the total amount of particles.

Since particles have different diameters and charges, required ESP voltages are much greater than in previous ion removal calculation. In fig. 3.3.4 is shown the ESP applied voltage by diameter. As commented before, some electrical loss inside the

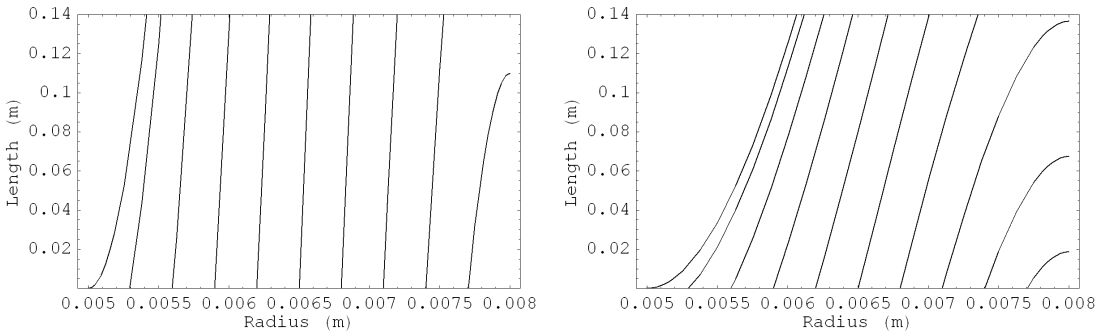

(a)

(b)

Figure 3.3.3: Particle trajectories starting at the central rod for particles of 6 nm at a total flowrate of 2 lpm, with the minimum calculated voltage of −0.17 V applied in *(a)* and in *(b)* with −1 V applied to the ESP central rod.

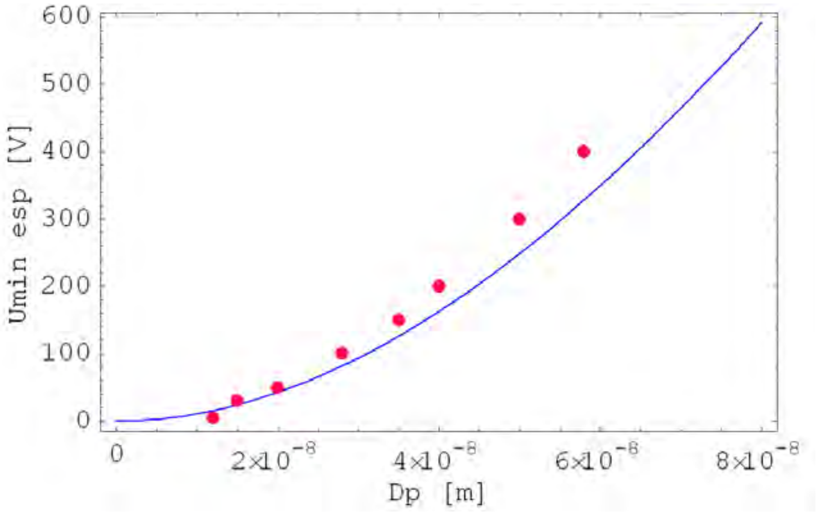

Figure 3.3.4: Minimum applied voltage required at the ESP. Dots are experimental values, line calculated.

ESP is inevitable, but also some diffusional loss. However, this last is near negligible since the penetration of particles through the device with no voltage applied is over 96% for all cases.

The electrical settings of the corona device have been characterized, obtaining that the ion current depends on the nature of the ions, transport flow, and distance and geometry of the electrodes, although measured output current is practically independent of the variation in applied voltage or current. On the other hand, the particle current is inversely proportional to the distance between electrodes although it the output current generated by the charged particles is affected by losses to the point that there is not a strict correlation between particle diameter and measured current. Also the operational features to remove the remaining charges by ESP are studied.

From the obtained conclusions, in the following the applied corona current will be fixed at $I_c = 0.07\,\mathrm{mA}$ and gap distances of $3\,\mathrm{mm}$ and $10\,\mathrm{mm}$ will be compared, representing the shorter and larger distances between electrodes, respectively.

4

EXPERIMENTAL RESULTS

An accurate characterization of the charger device can be obtained from combination of simpler measurements, such as the electrical current (giving the total electrical charge carried by the aerosol, see Sec. 3.2), volumetric flowrates and particle concentration at four different points of the setup. These points, shown in fig. 2.4.1, are the inlet concentration C_{in} of uncharged aerosol before entering the corona, the outlet concentration with the test charger turned off, $C_{\text{out}}^{\text{off}}$, the outlet concentration with the charger turned on, $C_{\text{out}}^{\text{on}}$, and the outlet concentration of uncharged particles with charger on, C_{out}^{0}, bearing in mind that the total concentration at the outlet is the sum of the charged C_{out}^{q} and uncharged particles: $C_{\text{out}}^{\text{on}} = C_{\text{out}}^{q} + C_{\text{out}}^{0}$. The concentration C_{out}^{0} is measured by removing the charged particles by means of an electrostatic precipitator (see Sec. 3.3).

4.1 LOSSES INSIDE THE CHARGER

The presence of particle losses can impose significant uncertainties in determining the true charging efficiency. They can be distinguished into two types of losses, the losses of neutral particles, mainly caused by diffusion,

$$L_{\text{diff}} = 1 - ff\frac{C_{\text{out}}^{\text{off}}}{C_{\text{in}}}, \tag{4.1.1}$$

and losses of charged particles, related to the effect of electrostatic forces,

$$L_{\text{el}} = ff\frac{C_{\text{out}}^{\text{off}} - C_{\text{out}}^{\text{on}}}{C_{\text{in}}}. \tag{4.1.2}$$

The additional flow for driving ions Q_i makes it necessary to consider an auxiliary flow factor for aerosol dilution,

$$ff = \frac{Q_i + Q_a}{Q_a} = \frac{Q_{\text{out}}}{Q_{\text{in}}}. \tag{4.1.3}$$

The different ratios between flow rates are shown in table 4.1.1.

There is some controversy on whether the definitions of losses and charging efficiency should be based on the particle number concentration itself [45] or on the particle fluxes (i.e., particle concentration times the carrying flowrate) [86, 103]. For chargers with a supplementary gas flow like shown in [16, 19, 89], the aerosol concentration is diluted within the appliance. Due to different aerosol flow rates entering and leaving the charger, the concentration ratio cannot be obtained by measuring the particle number upstream and downstream the charger and shall therefore be based,

Table 4.1.1: Table of flow rates utilized. All values are shown in lpm.

Q_i	Q_a	Q_T	Q_i/Q_a	ff
0.25	1.25	2	0.2	1.6
0.5	1.5	2	0.5	1.33
0.75	0.75	2	1	2.67

for each particle size, on the total number of particles, not on the number concentration. That is, the measured number of particles is multiplied by the corresponding flow rate to obtain the particle flux in each stream. This is a factor to take into account for comparison with numerical results from other devices, even though dilution has no effect on the possibility of single particles to be charged.

Calculated errors of the losses are greater when the flow factor is considered (eqs 4.1.4 and 4.1.5). Errors are calculated by $\Delta F(x_i) = \sum_i \left|\frac{\partial F}{\partial x_i}\Delta x_i\right|$.

$$\Delta L_{\text{diff}} = \frac{ff}{C_{\text{in}}}\left(\Delta C_{\text{out}}^{\text{off}} + \Delta C_{\text{in}}\frac{C_{out}^{\text{off}}}{C_{\text{in}}}\right) + \Delta ff\frac{C_{\text{out}}^{\text{off}}}{C_{\text{in}}}, \tag{4.1.4}$$

$$\Delta L_{\text{el}} = \frac{ff}{C_{\text{in}}}\left((\Delta C_{\text{out}}^{\text{off}} + \Delta C_{\text{out}}^{\text{on}}) + \frac{C_{\text{out}}^{\text{off}} + C_{\text{out}}^{\text{on}}}{C_{\text{in}}}\Delta C_{\text{in}}\right) + \Delta ff\frac{C_{\text{out}}^{\text{off}} - C_{\text{out}}^{\text{on}}}{C_{\text{in}}}. \tag{4.1.5}$$

The error given by the CPC is around 10% for concentrations below 5×10^4 #cm^{-3} [55], plus the $3 - 5$% of error added by the gas flow controller, leads to around 15% of uncertainty in accuracy. Moreover, when the in and out concentration values are too close each-other, they can be under- and over-estimated respectively.

The rate of particles lost due to diffusion is determined with the charger turned off because it is supposed that diffusion losses are independent of the charge state acquired afterwards by the particles. Diffusional losses are mainly attributed to the loss of neutral particles, accounting for particle diffusion and mixing flows inside the tubes with no electrical field applied. This means that the inner characteristics of the device, such us operating voltage or the distance between electrodes is not determinant. Since the diffusional effect is significant only for particles smaller than approx. 20 nm, the diffusional losses are reduced with increasing diameter, having very strong losses (close the 50%) for $D_p < 10$ nm (fig. 4.1.1).

However, when the charger is switched on there are additional electrostatic losses that will reduce the absolute particle concentration, hence diminishing the diffusional losses of both charged and uncharged particles [86]. Electrical losses for the needle position of 3 mm are much greater (above 20% for the smallest diameters) than for the gap of 10 mm, which barely reach 2%. This effect is related to the ion concentration, since with a lower needle position the electric field is more shielded from the charging region, so that the particles are more likely to be lost by electrostatic effects.

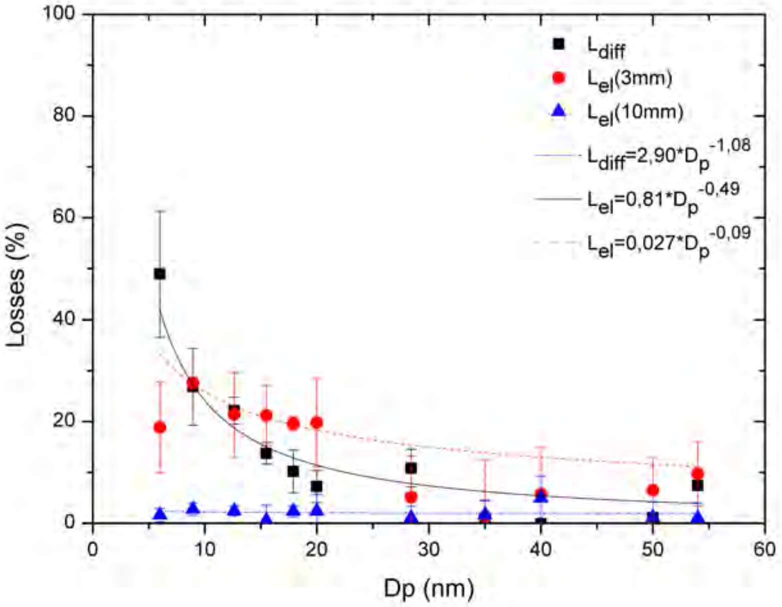

Figure 4.1.1: Losses of charged and neutral particles for several particle diameters considering the flow factor at different distances between electrodes.

Because the electric field has no influence on the neutral particles, their loss is independent on D_{gap}, therefore on the corona starting voltage, and can be attributed entirely to Brownian diffusion. However, the flow rate has an effect on the particle losses. With a fixed total flowrate, the residence time in the charging zone is the same for all sampled particles, regardless the proportion of each flow into the total. But the ionizer flow can be considered as a dilution gas for the aerosol flow, so the particle concentration decreases and particles are more likely to be lost by diffusion.

When the corona is switched on, the ion concentration is 'diluted' with the ratio of the ionizer flowrate to the total flowrate. Thus, the $N_i t$-product can be changed by varying this ratio, since a small Q_i in comparison to the Q_a leads to a strong decrease of the ion concentration and thereby of the $N_i t$-product. On the other hand, a high Q_i would lead to a high ion concentration but also a strong decrease in effective particle concentration. Also the residence time is varied, therefore, an optimal flow balance has to be found.

Three different ion flow rates were tested with particles of 15 nm diameter and fixed Q_a at 1.5 lpm, and losses of neutral and charged particles determined. In fig. 4.1.2a it is shown for neutral particles that the larger the ion flow Q_i, the higher the particle losses. This cannot be explained by diffusion, since the reduced time when increasing the ion flow rate should lead to smaller diffusion losses. However, the turbulence level might increase due to the inclined mixing arrangement, which explains the increasing losses. The same happens when particles are charged for the case of 10 mm gap in fig. 4.1.2b. On the contrary, for the 3 mm gap, losses of charged particles slightly decrease with increasing ion flow. This is probably due to the shorter residence time which reduces the loss of charged particles and the loss mechanism is probably due to the space charge effect of the ions entering the charging region.

Likewise, an increase in voltage will increase the ion concentration and therefore the electrical losses due to a stronger space charge effect, as is shown for 3 mm gap. But in the case of 10 mm gap, losses are almost constant with the increase of corona voltage, from which can be inferred that the space charge effect has a limited impact at this electrode distances.

4.1.1 *Particle deposition*

It is seen that a higher total flow increases the losses, but when it is fixed, the ratio of ion to aerosol flow also has an effect on the particle deposition in the charger. Losses can be resumed by the penetration of the particles through the setup.

It is possible to make a rough estimate of the diffusional deposition in a tube of radius R by assuming a residence time of $t = {}^{L}/_{u}$, where u is the velocity in a tube of length L and A and V its area and volume respectively (a complete deduction of eq. (4.1.6) can be seen in Reist [107]):

$$C_{\text{out}} = C_{\text{in}} - N\frac{A}{V} = C_{\text{in}} - 2C_{\text{in}}\sqrt{\frac{\mathcal{D}L}{\pi u}}\left(\frac{2\pi RL}{\pi R^2 L}\right), \tag{4.1.6}$$

where $\mathcal{D}$ is the diffusional coefficient, related with the particle mobility Z_p. Then, penetration can be expressed as:

$$P_{\text{diff}}(\phi) = \frac{C_{\text{out}}}{C_{\text{in}}} = 1 - 4\phi^{1/2},$$

naming $\phi = \frac{\mathcal{D}L}{Q}$. A general solution was summarized by Cheng et al. [22] for various geometries, expressed as a series of exponential functions:

$$P_{\text{diff}}(\phi) = \frac{C_{\text{out}}}{C_{\text{in}}} = \sum_{n=1}^{\infty} A_n \exp(-\beta_n \phi), \tag{4.1.7}$$

where A_n and β_n are constants. For penetration through a cylindrical tube, the eq. (4.1.7) depends on the parameter ϕ with an accuracy of 1% as following:

$$P_{\text{diff}}(\phi) = \begin{cases} 0.819\, e^{-11.5\,\phi} + 0.0975\, e^{-70.07\,\phi} + \\ \quad +0.0325\, e^{-178.95\,\phi} + 0.0154\, e^{-338.1\,\phi}, & \text{for } \phi > 0.007, \\ 1 - 5.50\,\phi^{2/3} + 3.77\,\phi + 0.813\,\phi^{4/3}, & \text{for } \phi \leq 0.007. \end{cases} \tag{4.1.8}$$

The theoretical penetration is close to 100%, closer for bigger particle diameters since diffusion affects strongly only to small particles. In the charging zone, where

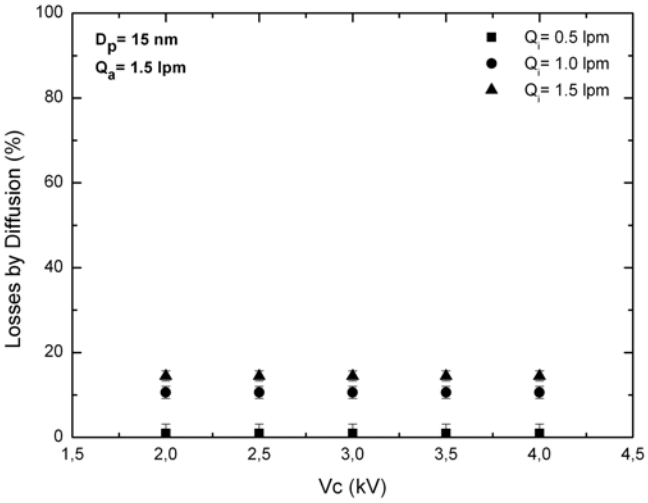

(a) Losses by diffusion

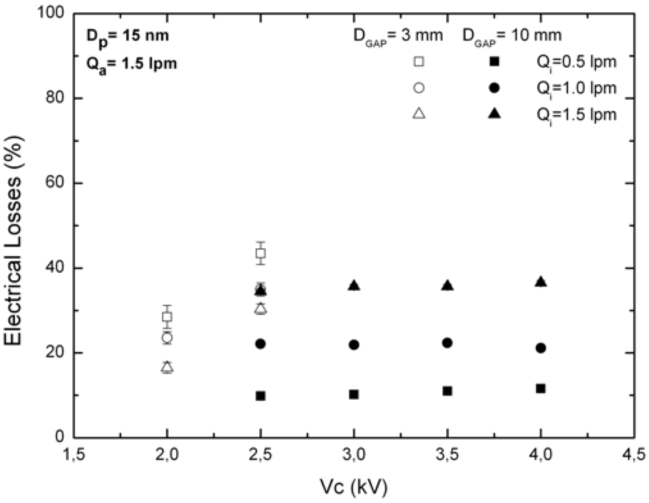

(b) Losses by electrical effects

Figure 4.1.2: Losses for neutral and charged particles of 15 nm at different corona operating voltages for an aerosol flow rate of 1.5 lpm and three different ion dilution flow rates. Two different distances from the electrode needle to the output were tested, 3 mm and 10 mm.

both flows reunite, the penetration decreases slightly compared with the incoming neutral particle flow.

For the different ratios between flows studied in fig. 4.1.3a, it can be seen how a fixed aerosol flow keeps a constant penetration percentage of the particles. However, for a fixed total flow rate, the penetration decreases for the smallest particle diameters as the dilution from the ion driving flow increases.

It has to be said that no space charge effects are considered for this calculation, thus the penetration in the charging zone might be overestimated. For this reason, in fig. 4.1.3b results were compared with data for 50 nm particles. It can be seen that a ratio greater that 1 leads to a very low penetration of charged particles through the charger, and shall be avoided. The increasing space charge effect of the incoming ions at higher Q_i/Q_a ratios drives the particles towards the outer walls, leading to lower penetration. From the graph, an acceptable ratio of the flows is 0.33, which corresponds to $Q_i = 0.5$ lpm and $Q_a = 1.5$ lpm and will be used in the following.

An accurate calculation of the penetration has to take into account the total loss of charged particles $L_T = L_{\text{el}} + L_{\text{diff}}$, which can be experimentally estimated as:

$$P_n = 1 - L_{\text{tot}} = ff \frac{C_{\text{out}}^{\text{on}}}{C_{\text{in}}}. \tag{4.1.9}$$

Total penetration and losses of charged and neutral particles in the 6 to 60 nm size range are shown in fig. 4.1.4. For the case where $D_{\text{gap}} = 10$ mm, the charger reaches above 50% penetration at 6 nm particle diameter, increasing gradually until 80% of the particles with diameters over 15 nm successfully go through the charger. This is not attained though when $D_{\text{gap}} = 3$ mm, since the charged particles are lost in a higher extent. The improved penetration for the charged particles at 10 mm of gap between electrodes are expected because the space charge effect is weaker.

In the fig. 4.1.4 are also compared our values with some available results from the literature [13, 96, 128] for devices in which a dilution flow was used. It is shown that while for particle diameters below 10 nm the penetration is still not high enough, for bigger sizes the values are acceptable, being the gap distance between electrodes of 10 mm the one giving better results.

As a resume, the losses can be considerably reduced by adjusting the flows or fixing a proper corona voltage. It can be seen that a low corona voltage can slightly increase the total losses, and that an ion flow equal or greater that the aerosol flow leads to too high losses, thus these ratios shall be avoided.

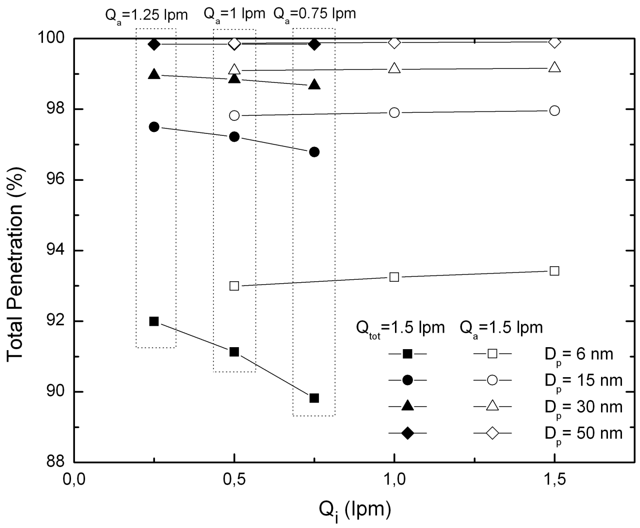

(a) Calculated penetration for particles through the charger at different flow rates.

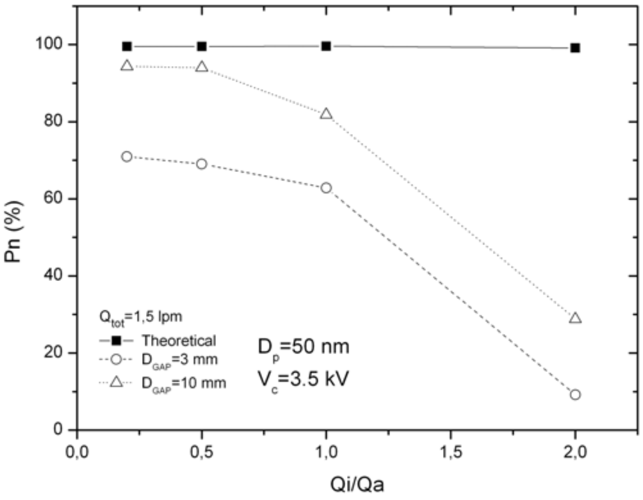

(b) Theoretical and experimental penetration for particles of 50 nm at different flow ratios for a fixed total flowrate of 2 lpm and an applied corona voltage of 3.5 kV.

Figure 4.1.3: Estimated penetration of particles through the charger device at different total and dilution flow ratios.

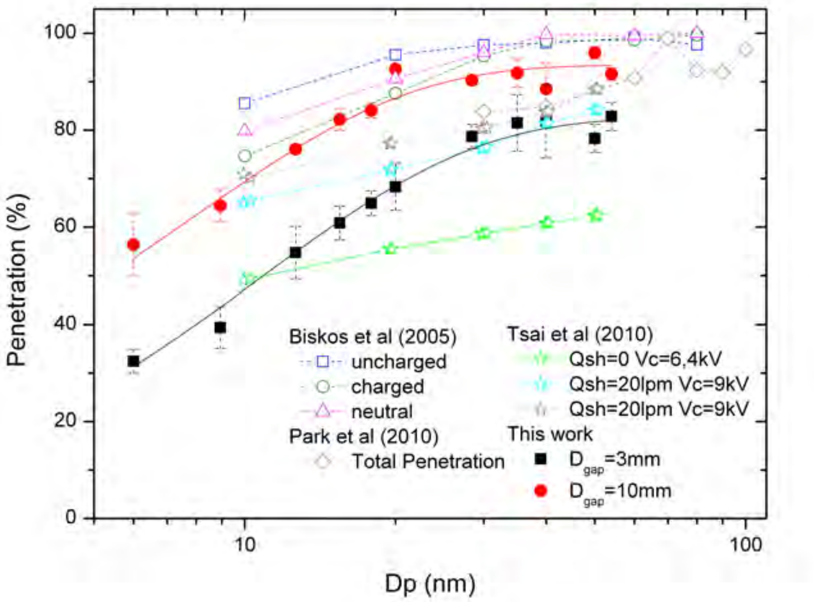

Figure 4.1.4: Total penetration of particles through the charger, compared with values present in literature.

4.2 CHARGING PROPERTIES OF THE CORONA CHARGER

For the complete characterization of a charger it is necessary to measure particle loss, charging efficiency and charge distribution. The charging efficiency is the most important performance parameter for aerosol chargers, since it describes the possibility of an individual particle to acquire charges during the process.

4.2.1 *Charging efficiencies*

Depending on the success of the particle to pass through the charger, this efficiency can be classified as intrinsic charging efficiency (ϵ_{int}) when only the rate of particles being charged is important, or extrinsic charging efficiency (ϵ_{ext}) when also the success to properly reach the outlet of the device is taken into account. Discrepancy between intrinsic and extrinsic charging efficiencies is attributed to the charged particle losses inside the charger [103].

The comparison of efficiencies is based exclusively on external measurements; knowledge of the internal physical charging conditions such as $N_i t$-product or electrical field is not required [86].

The intrinsic efficiency contains information about the 'true' charging probability of the particles, the total of the charged particles leaving the charger compared with the neutralized particles going in. Additional assumptions for its experimental determination are needed by considering the particles that were lost as part of the totals:

$$\epsilon_{\text{int}} = \frac{C_{\text{out}}^{q} + L_{\text{el}}}{C_{\text{in}} - L_{\text{diff}}}. \tag{4.2.1}$$

Substituting the expressions of the losses and normalizing each term by the total initial concentration C_{in}, the expression 4.2.2 for the intrinsic efficiency is obtained:

$$\epsilon_{\text{int}} = 1 - \frac{C_{\text{out}}^{0}}{C_{\text{out}}^{\text{off}}}. \tag{4.2.2}$$

The corresponding error:

$$\Delta\epsilon_{\text{int}} = \frac{\Delta C_{\text{out}}^{0}}{C_{\text{out}}^{\text{off}}} + \Delta C_{\text{out}}^{\text{off}} \frac{C_{\text{out}}^{0}}{\left(C_{\text{out}}^{\text{off}}\right)^{2}}. \tag{4.2.3}$$

On the other side, the extrinsic charging efficiency is the 'final' efficiency, the efficiency at which the corona charger will operate. It can be determined experimentally without additional assumptions, considering the quantity of charged particles exiting versus the total entering the charger:

$$\epsilon_{\text{ext}} = ff \frac{C_{\text{out}}^{\text{on}} - C_{\text{out}}^{0}}{C_{\text{in}}}, \tag{4.2.4}$$

$$\Delta\epsilon_{\text{ext}} = \frac{1}{C_{\text{in}}} \left(ff \left(\Delta C_{\text{out}}^{\text{on}} - \Delta C_{\text{out}}^{0}\right) + \Delta C_{\text{in}} \frac{\epsilon_{\text{ext}}}{C_{\text{in}}} \right) + \Delta ff \frac{\epsilon_{\text{ext}}}{ff}. \tag{4.2.5}$$

However, its definition also contains implicit information of losses and one cannot distinguish the contribution of these losses to the extrinsic efficiency unless all particles are considered to be charged [86].

Normally, corona discharge has poor charging efficiencies in the ultrafine particle size range ($D_p < 20\,\text{nm}$) due to high particle losses, produced because a high electric field is required to generate the high ion concentration needed for efficient diffusion charging, so a fraction of the particle losses is unavoidable [60].

Likewise, the flow factor is considered for the calculation of the efficiencies and it has to be taken into account for comparison with other chargers without dilution flow.

The charging efficiency is expected to rise with particle diameter and with ion concentration, whereas the intrinsic efficiency should be higher for the gap of 3 mm since more ions are generated., but also more are lost by electrical migration to the grounded electrode, reducing the efficiency. The operating voltage V_c will increase the efficiencies in a degree that depends on D_{gap} and on the particle diameter, similar to the losses.

The balance of flows has a manifest impact on efficiencies, as it had on losses. When the total flow increases, residence time is shortened and the ion concentration decreases due to dilution. With a constant total flowrate, a higher dilution flow increases both the intrinsic and extrinsic charging efficiencies (fig. 4.2.1) because of the higher number of ions that is supplied to the aerosol, apparently compensating the smaller residence time and the increase of electrical losses. This effect is more evident for the 10 mm gap, since the ion concentration is lower and more ion flow drags more ions, reducing losses. But when the ion flow is larger than the aerosol flow, extrinsic charging efficiency decreases drastically since most of ions are lost by the large space charge effect, which is supported by the fact that the intrinsic charging efficiency is unaffected by the flow ratios.

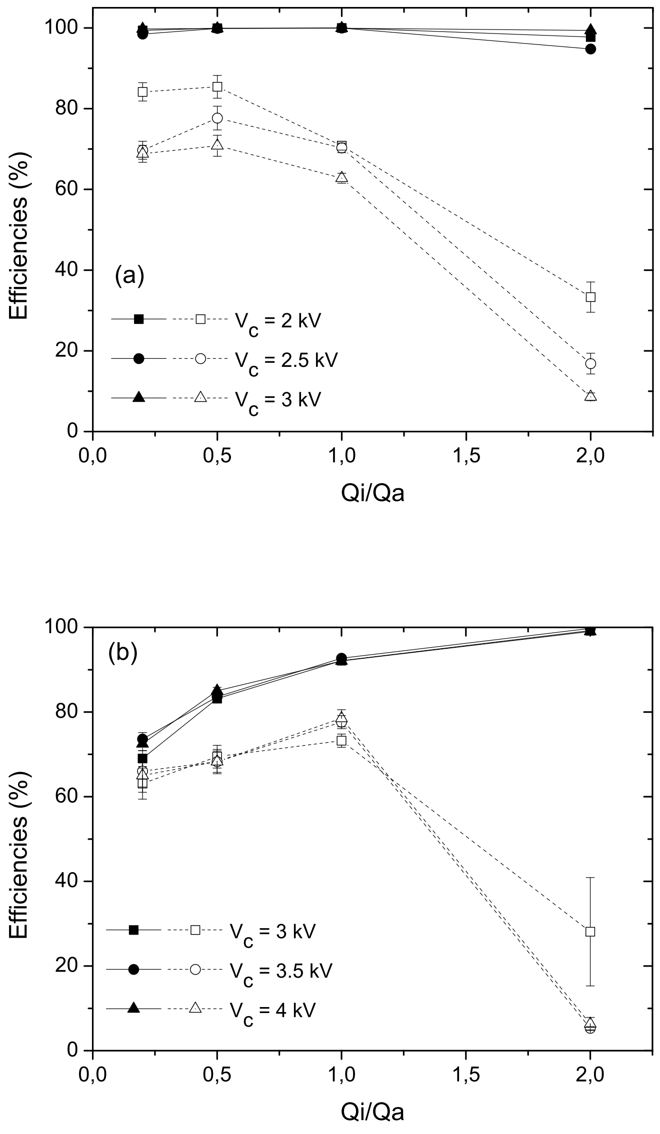

Figure 4.2.1: Intrinsic (solid symbols) and extrinsic (empty symbols) charging efficiencies of 50 nm particles for different flow ratios at a fixed total flow rate of 2.0 lpm. Fig. (a) refers to an electrode gap of 3 mm and (b) to 10 mm. Three different voltages are used for each measurement.

The operating voltage V_c does not influence the intrinsic charging efficiency. However, for a gap of 3 mm, the higher the voltage the lower the extrinsic efficiency, which is not the case for 10 mm. The reason can be found in fig. 3.1.10, which shows an increase in output current for 3 mm but not for 10 mm gap distance.

Fig. 4.2.2 shows that efficiencies increase with the particle diameter since larger particles tend to acquire easily more than one charge per particle. Also the effect of the inter-electrode distance on the charging by sizes is compared, determining that for the 3 mm gap, the intrinsic efficiency reaches practically 100% from 18 nm particles. Previously the effect of diffusional losses was found to be strong for small particles (see fig. 4.1.1) and the charging efficiency for diameters of 6 nm is around 65%. When the gap increases up to 10 mm, therefore diminishing the ion concentration, the intrinsic efficiency is much smaller, e.g. 50% for the particles with 40 nm in diameter.

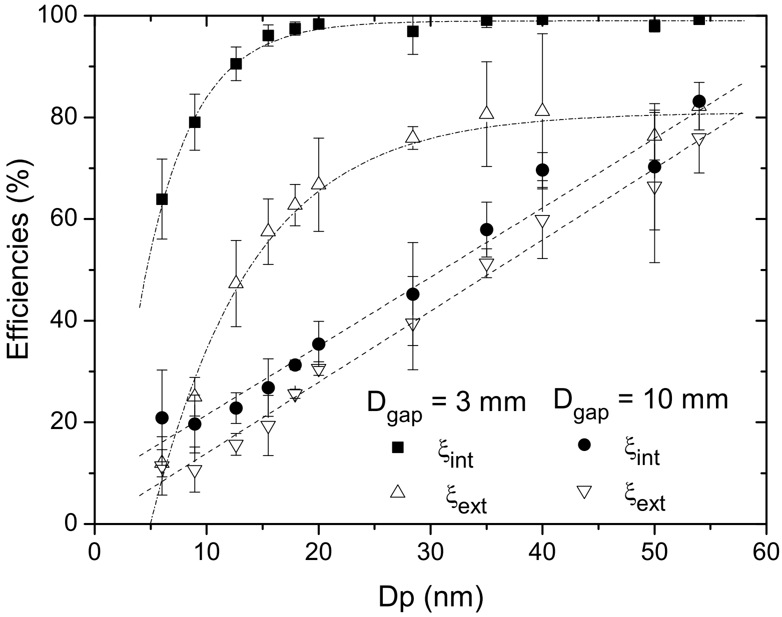

Figure 4.2.2: Variation of intrinsic (solid symbols) and extrinsic (empty symbols) charging efficiencies with particle diameters for gaps of 3 mm and 10 mm.

In the case of extrinsic efficiencies, at diameters below 15 nm the combination of electrical and diffusional losses is strong enough to decrease the real charging efficiency below 20% with the 3 mm gap. But following values are as high as 80% for 35 nm particles. However, for the 10 mm gap, the difference between intrinsic and extrinsic efficiencies is around 15%, even less as the particle size grows, which means that the 'true' and the 'final' efficiencies (i.e. intrinsic and extrinsic respectively) are quite close due to the smaller losses.

In fig. 4.2.3, the extrinsic charging efficiency of the charger is compared as function of particle diameter with collected data from other corona-based aerosol chargers. Results of the extrinsic efficiencies of [103] are included, along with data from [16],

[45] and [104], and also the charging efficiency in case of bipolar charging [53, 141] is plotted for reference.

The charging efficiency used in this study refers to the charged particles flux, which is different from the definition presented in other works (the fraction of charged particles among all the particles exiting from the charger). For this reason, the selected data for reference are from chargers that consider dilution, except that of Hernandez-Sierra et al. [45], in which there was no dilution of the aerosol stream.

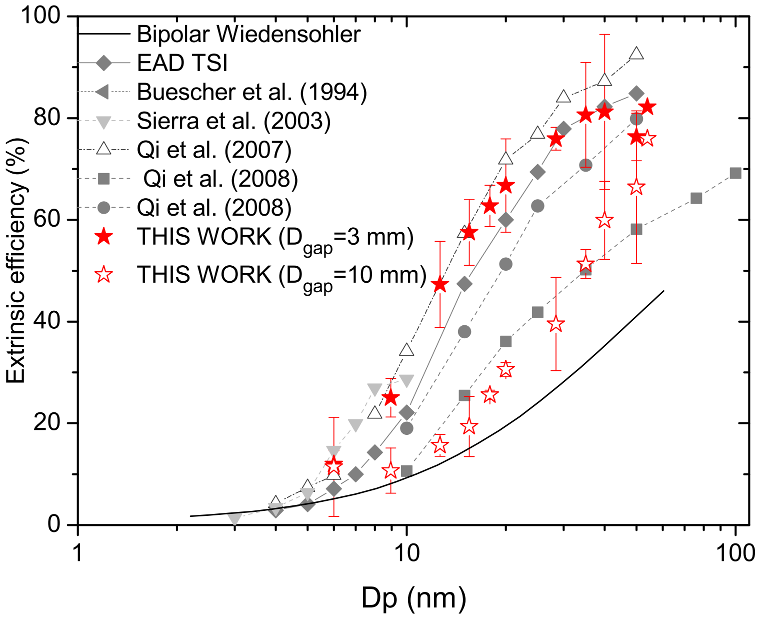

Figure 4.2.3: Extrinsic efficiencies for different particle sizes and gap distances compared with values from other devices presented in literature.

It can be seen that a wide spectrum of charging efficiencies is covered by the charger presented in this work when moving from a 3 to a 10 mm electrode gap. For particles as large as 35 nm and a gap of 3 mm, efficiencies of around 85% are reached, comparable with other highly efficient chargers, while with a 10 mm gap, lower efficiencies are attained, close to that of radioactive chargers for particles below 20 nm. Changing the position of needle electrode can adjust the $N_i t$-product and therefore the charging levels as the user desires.

The charging efficiency characterizes the charger performance and is dependent on the particle size, corona voltage, and aerosol flow rate. Table 4.2.1 summarizes the operation of different designs of unipolar aerosol chargers and some of the most representative bipolar chargers for comparison. Note that the sheath flow feature was

Table 4.2.1: Comparison of different unipolar chargers.

Author(s)	Ion source	Power type	Total flow (lpm)	Sheath flow (lpm)	Flow direction ion to aerosol	$N_i t$ ($\times 10^6\,s\,cm^{-3}$)	Extrinsic charging efficiency (%) $D_p = 10\,\text{nm}$	$D_p = 15\,\text{nm}$	$D_p = 50\,\text{nm}$
Wiedensohler [141]	^{85}Kr	+ DC	0 – 15	0 – 1.5	– –	– –	9.04	14.98	41.90
Liu and Pui [82]	Corona wire	+	5	1	⊥	1 – 30	1.30	– –	– –
Adachi et al. [1]	^{241}Am	+ DC	1	✓	– –	0.58 – 7.23	– –	58.00	– –
Wiedensohler et al. [142]	^{244}Cm	280 V AC	0.5	0.5	⊥	5	22.70	41.72	– –
Büscher et al. [16]	Corona wire	4.5 kV AC	2.5	0.5	⊥	7.5 – 15	19.46	39.99	– –
Chen and Pui [19]	^{210}Po	+ DC	6	4.5	‖	25.6	63.00	75.50	– –
		- DC					65.00	78.00	– –
Medved et al. [89]	Corona needle	+	1.5	0.3	→←	– –	40.00	– –	– –
Kruis and Fissan [73]	Corona wire	+ AC	– –	✗	⊥	10 – 80	30.00	– –	– –
Hernandez-Sierra et al. [45]	Corona needle	+/- 2.5 – 4 kV DC	0 – 10	✗	⊥	– –	28.69	– –	– –
Biskos et al. [14]	Corona wire	4 kV AC off	5	✓	⊥	19.7	24.95	41.24	71.45
		5 kV AC off				29.2	1.24	3.78	32.56
		6 kV AC off				30.0	0.12	1.81	16.48
Alonso et al. [6]	Corona needle	3 – 3.6 kV DC	0 – 10	✗	⊙	10.0 – 40.0	36.00	55.00	– –
			2	✗			31.00	44.15	– –
Qi et al. [102]	Corona needle	4 μA DC	5	1	⊗	9.0	34.19	57.36	92.44
		4 μA DC	10	1		5.4	27.68	50.61	89.92
Kwon et al. [76]	Surface discharge (SMAC)	+ DC	– –	✗	⊥	3.0	20.00	– –	– –
		- DC				3.5	25.00	– –	– –
Qi et al. [104]	Corona needle	1 μA DC	0.3	✗	⊙	– –	10.65	25.47	58.18
		2 μA DC	1.5	✗		– –	19.00	38.02	79.85
Vivas et al. [133]	Corona wire	+/- 4.5 kV AC	1.5	✗	⊥	0.08 – 6.0	– –	– –	37.29
			2.5	✗		0.08 – 6.0	– –	– –	26.86
THIS WORK	**Corona needle**	3.5 kV **DC**	1.5	0.5	⊙				
	$D_{\text{gap}} = 3\,\text{mm}$	7 μA				18.0	27.12 (19.11)	57.53 (44.43)	76.32 (59.71)
	$D_{\text{gap}} = 10\,\text{mm}$					2.04	11.44 (7.97)	19.08 (16.53)	66.43 (41.87)

– – no data available ‖ parallel ⊥ perpendicular →← frontal ⊙ surrounding aer./ion ⊗ surrounding ion/aer.

Table 4.2.2: Applied voltages to the first DMA and the correspondent midpoint mobility diameters.

V_{DMA} (kV)	0.1	0.2	0.4	0.6	0.8	1	2	3	4	6	7	8
D_p (nm)	6.32	8.84	12.64	15.49	17.90	20.02	28.42	34.94	40.51	50.01	54.23	58.20

not used in many one of these chargers. For this reason results from particle concentrations of our test charger (that is, calculated without dilution) are given within parenthesis nearby the particle flux efficiencies. The estimation of the $N_i t$-product is shown in the following section.

4.2.2 *Charge distribution*

Although the global characteristics of the device and its ability to charge particles have been studied in the previous sections, it remains to determine the charge distribution by particle size, which depends on the $N_i t$-product and will be crucial on calculating the sizes of particles once charged.

For this purpose, the mobility distribution of the charged particles is measured by a second DMA after the test charger, as explained in fig. 2.4.1. A typical example of this kind of measurement is shown in fig. 4.2.4 for several values of the voltage applied to the first DMA (fig. 4.2.4a), which selects the nominal diameter of the monodisperse particle distribution to be charged afterwards by the corona device (figs. 4.2.4b and 4.2.4c). Voltages selected and their correspondent mobility diameters are shown in table 4.2.2.

The different peaks in the figs. 4.2.5 (for a particle diameter of 35 nm as an example) correspond to the different number of charges on the particles. The relative area under each peak gives the fraction of charged particles carrying a certain number of elementary charges. To obtain absolute magnitudes, the number fraction is normalized so that the total area under the curves is one. For each particle diameter, this fraction of area is multiplied by the corresponding extrinsic charging efficiency, returning the fraction of charged particles.

The y-axis shows the number concentration normalized in such a way that the total area under the curve is 1. The whole scanning range of the Nano-DMA is covered, but due to the shape of the original distribution, the number of particles in the tails is much lower than close to the central diameter. This can cause a voltage shift, as it was explained by Alonso and Kousaka [5]. They showed that when particles classified by a DMA are passed through an identical second DMA operating with the same flow rates, the mean classification voltage for the second unit is usually different from the

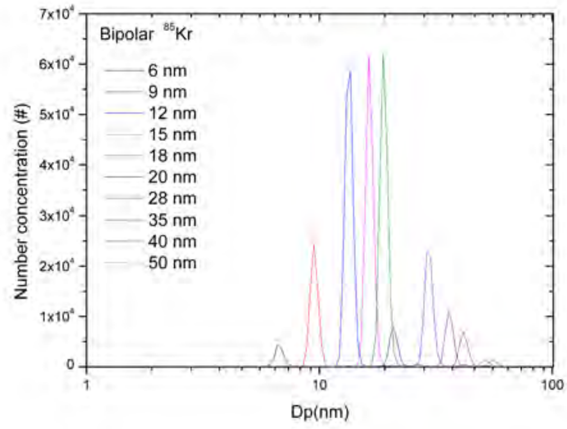

(a)

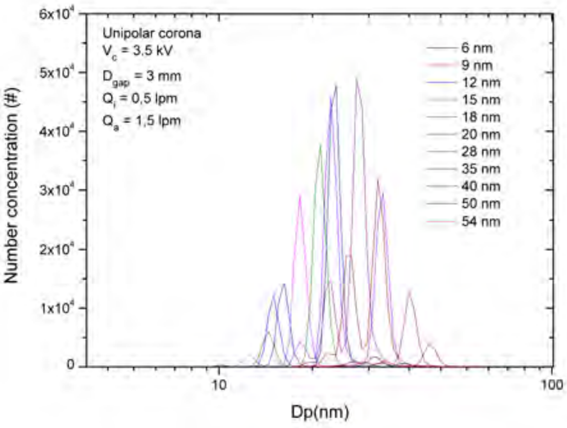

(b)

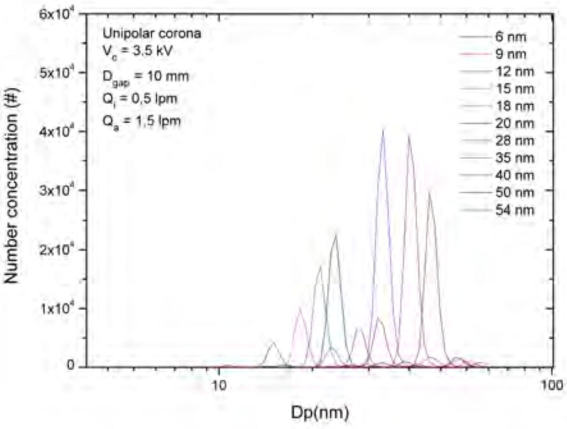

(c)

Figure 4.2.4: Number concentration of the whole rage of particle diameters measured before and after the test charger for two gap distances at $Q_a = 1.5\,\mathrm{lpm}$ and $Q_i = 0.5\,\mathrm{lpm}$.

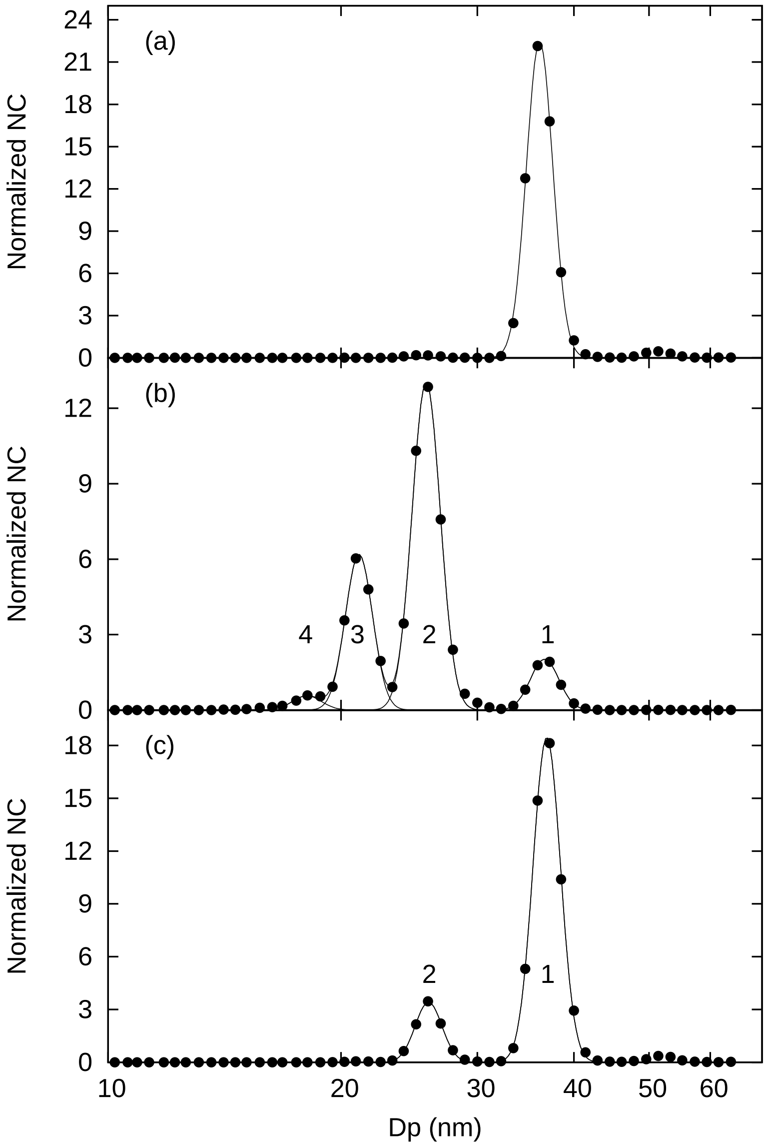

Figure 4.2.5: Normalized number concentration (NC) before and after the test charger for two gap distances at $Q_a = 1.5$ lpm and $Q_i = 0.5$ lpm. Fig. (a) is the distribution before corona, from the bipolar charging for reference, figs. (b) and (c) are for corona charging for an applied voltage of 3.5 kV and electrodes gap of 3 mm and 10 mm respectively.

fixed voltage applied to the first one, and the shifts are larger for particles in the tails, where concentration is lower than the mean.

In our case, the voltage shift is around 1 nm, as can be seen in the different plots of fig. 4.2.5, reaching 1.5 nm in the worst cases where concentration was relatively low. Considering the accuracy of the voltage supply from the device, which as provided by manufacturers is ±1 V for applied voltages under 500 V, ±6 V for voltages below 5 kV and ±2 V for voltages up to ±10 kV, and the uncertainty from the gas flow controllers, the error in the diameter is smaller than 1% as is shown in fig. 4.2.6, and is within the accuracy of the SMPS.

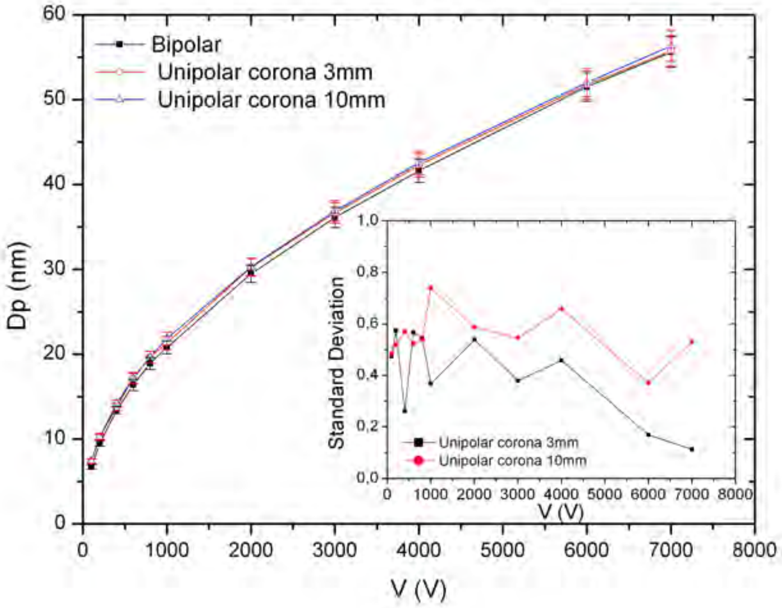

Figure 4.2.6: Voltage shift translated to diameter differences with error estimation (inner graph, over 100%).

A software was created to fit the curves and calculate the areas and mean diameters of each peak. The software is written in Python but combines C++ and Gnuplot functions for fitting, optimization and calculation of the curves, which are then plotted as can be seen in figs. 4.2.5.

The best fit calculation is based on Differential Evolution (DE) [119], a method that optimizes a problem by iteratively trying to improve a candidate solution with regard to a given measure of quality. DE is based on the following steps: a fixed number of vectors are randomly initialized, then evolved over time to locate the minimum of the objective function. At each iteration (generation), new vectors are generated by the combination of vectors randomly chosen from the current population (mutation). The out-coming vectors are then mixed with a predetermined target vector (recombination) and produces the trial vector. Finally, the trial vector is accepted for the next generation if and only if it yields a reduction in the value of the objective function (selection). DE can be used on optimization problems that are noisy, non differentiable, nonlinear or change over time, since it does not require the problem to be differentiable.

In our case, we fit the sum of Gaussians by DE taking as reference the quadratic error, and from the results calculates the area under each curve and the corresponding geometric mean diameter, as well as the standard deviation of each peak. To help the algorithm in the search for peaks, the number of lognormals and the mobility equivalent diameters were provided, since sometimes were too close each other and they could not be distinguished by the software itself. Peaks with an area of less than 1% were discarded.

Peaks appearing at the right of the nominal diameter are produced by particles which acquired a double charge in the ^{85}Kr charger at the DMA-1 and were classified because they have the same electrical mobility as the singly charged. They are usually unnoticed in the bipolar plot since are classified within the peak of the selected voltage. Anyway, the fraction of these particles is negligible in comparison with that of the main aerosol.

The experimentally found charge distributions are shown in fig. 4.2.7 for particles with diameters between 6 and 60 nm for two different electrode gaps and an optimum corona voltage of 3.5 kV, which maximizes the extrinsic efficiency. It can be seen that the number of charges per particle can be adjusted by moving the electrodes. When the needle is at the gap of 3 mm, particles acquire up to 6 charges, having a wide range of doubly and triply charged particles, while further away, the fraction of doubly charged particles is below 10% for diameters under 35 nm (fig. 4.2.7b). This means that for smaller electrode gaps, the effective $N_i t$-product is higher than for larger ones, which can easily be explained by a larger number of ions moving from the corona region into the charging zone. This effect can be very clearly seen in the charging level, however when looking at the measured output current (fig. 3.1.10), the differences between the output current for the 3 and 10 mm electrode gap are relatively small. Measuring the effective output current as a means to gain information on the effective $N_i t$-product is therefore not a good strategy.

The low amount of charges per particle facilitates the electrical mobility analysis for aerosol sizing, and a comparison with a bipolar charger in fig. 4.2.7b (data from SMPS-3080 from TSI, with a ^{85}Kr charger [53, 141]) shows that for particles below 20 nm could be possible a substitution of the radioactive chargers by this device. Notice that these results were obtained for certain characteristics, such as flow rates and voltages (therefore $N_i t$), and changing these can lead to results even closer to the bipolar distribution.

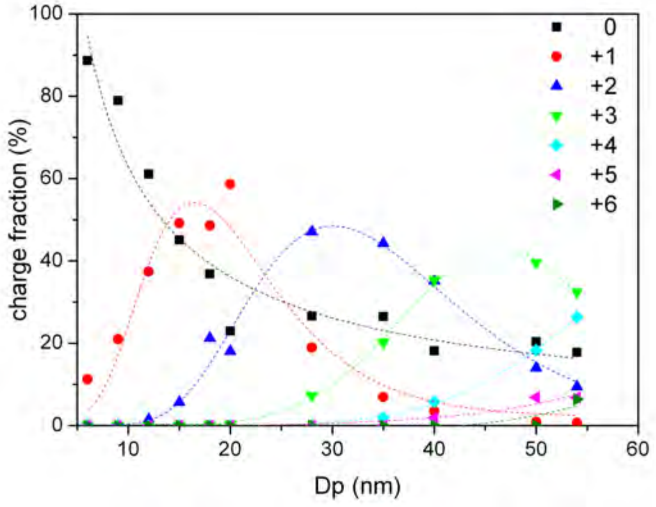

(a)

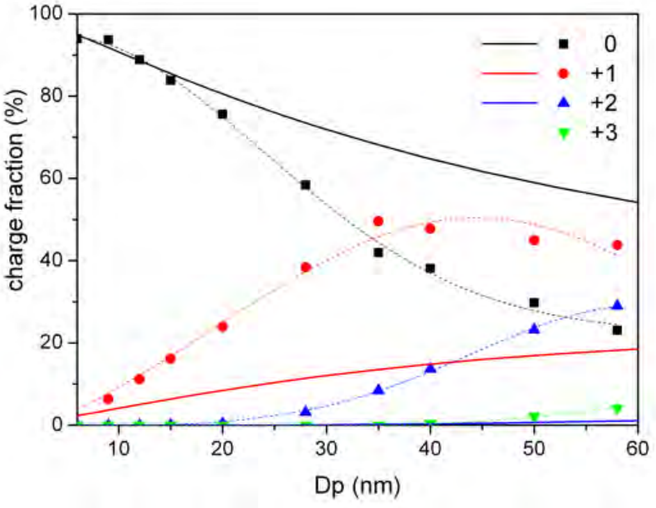

(b)

Figure 4.2.7: Charge distribution as a function of diameter for electrode gaps of (a) 3 mm and (b) 10 mm for flow rates of $Q_a = 1.5$ lpm and $Q_i = 0.5$ lpm and applied voltage of 3.5 kV. In (b) the bipolar distribution from Wiedensohler [141] is shown as thick lines for comparison.

4.2.3 *Particle mean charge*

The particle mean charge is another significant quantity associated with the diffusion charging, and depends fundamentally on the particle diameter and the $N_i t$-product in the charging zone.

$$\bar{q} = \sum_i q_i f(D_p, q_i). \tag{4.2.6}$$

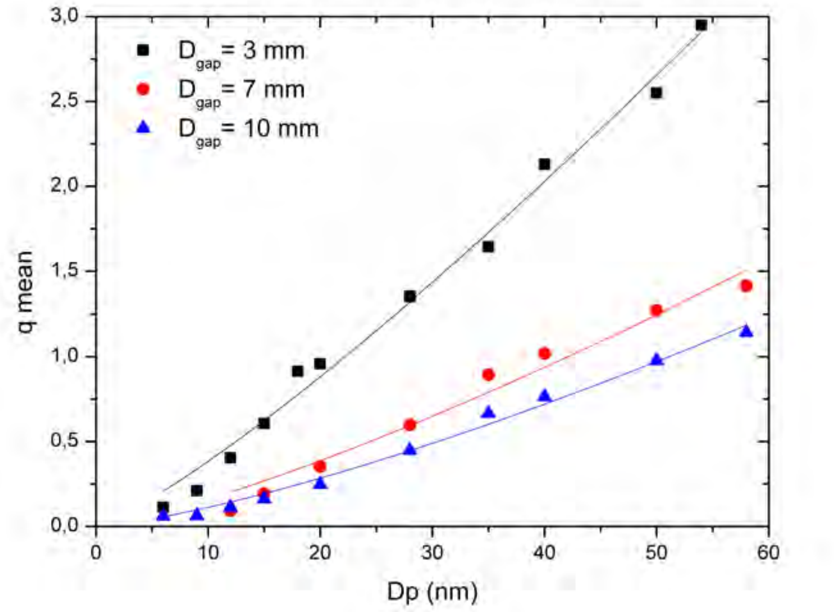

Figure 4.2.8: Mean charge per particle for different particle sizes and distances between electrodes at $V_c = 3.5\,\text{kV}$, $Q_i = 0.5\,\text{lpm}$ and $Q_a = 1.5\,\text{lpm}$.

Figure 4.2.8 shows that average charge increase with the particle sizes and ion concentration. Varying the position of the electrodes, particles with diameter below 50 nm obtain less than one charge on average for the furthest position of electrodes, while for $D_{\text{gap}} = 3\,\text{mm}$ these particles can acquire up to three charges. In addition, it is easy to describe the relationship between average charges and particle diameter by means of a power model as:

$$\begin{aligned} q_m(3\,\text{mm}) &= 0.024 D_p^{1.2}, \\ q_m(7\,\text{mm}) &= 0,00845 D_p^{1.27}, \\ q_m(10\,\text{mm}) &= 0,0051 D_p^{1.34}, \end{aligned} \tag{4.2.7}$$

determined with R^2 over $0,98967$ in all cases.

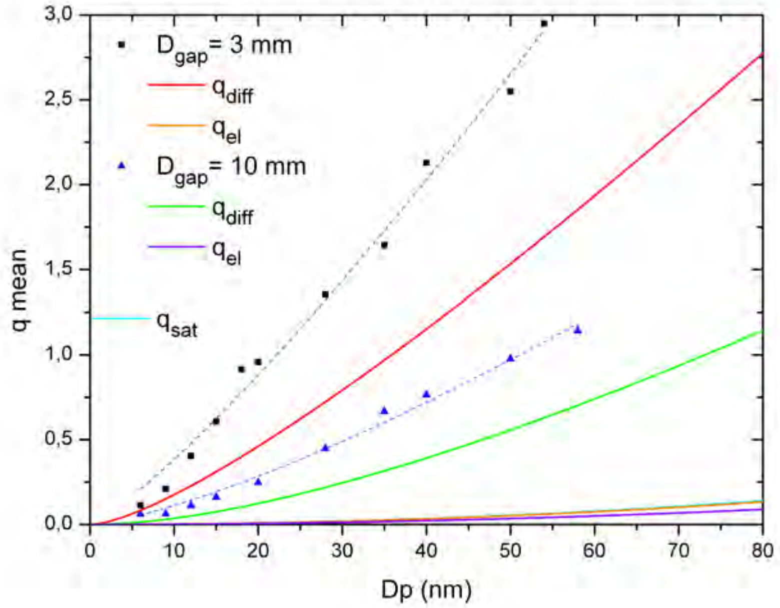

Figure 4.2.9: Mean charge per particle for different particle sizes and distances between electrodes at $V_c = 3.5\,\text{kV}$, $Q_i = 0.5\,\text{lpm}$ and $Q_a = 1.5\,\text{lpm}$.

Applying equations of diffusional and electrical mean charge ((1.4.1) and (1.4.2) respectively) it is shown in fig. 4.2.9 that the main reason for the charging of particles is the diffusion of ions, and that the field charge reaches almost the saturation level when the needle is close to the output.

The experimental results presented in this chapter show that having an electrode gap distance which can be easily varied is a very efficient method to modify the effective $N_i t$-product and control the charging efficiency and the related loss of particles. The charge of particles in mainly produced by diffusion, and it was shown that a variation on the corona applied voltage or current has only a limited effect on the measured output current. Therefore, it can be concluded that changing the electrode gap distance is a better strategy to vary the $N_i t$-product than changing electrical characteristics such as corona current.

5

MODELING OF THE RELEVANT PARAMETERS OF THE CHARGING PROCESS

An accurate characterization of the charger device can be obtained from combination of simpler measurements, such as the electrical current (giving the total electrical charge carried by the aerosol, see Sec. 3.2), volumetric flowrates and particle concentration at four different points of the setup. These points, shown in fig. 2.4.1, are the inlet concentration C_{in} of uncharged aerosol before entering the corona, the outlet concentration with the test charger turned off, $C_{\text{out}}^{\text{off}}$, the outlet concentration with the charger turned on, $C_{\text{out}}^{\text{on}}$, and the outlet concentration of uncharged particles with charger on, C_{out}^{0}, bearing in mind that the total concentration at the outlet is the sum of the charged C_{out}^{q} and uncharged particles: $C_{\text{out}}^{\text{on}} = C_{\text{out}}^{q} + C_{\text{out}}^{0}$. The concentration C_{out}^{0} is measured by removing the charged particles by means of an electrostatic precipitator (see Sec. 3.3).

The complete modelling of corona chargers is a very complex task, as it bases on a plasma discharge. Therefore, it is usually simplified as an electrodynamic phenomenon in which the electric field is caused by the applied field and the charge dynamics, and for the movement ions it is assumed that they obey the continuity equation. Even then, the solution of the partial differential equations that control the corona is difficult to obtain. It is primarily due to the fact that generation of ions occurs in a tiny area around the sharpest part of an electrode.

There are several methodologies to estimate the charge density of ions and particles. One can cite among others [2, 29, 66, 91], which show the difficulty of obtaining a numerical solution of the problem. This is related to the multiscale character of the problem: in a micron-sized region, ions are produced and then enter the charging region having sizes in the order of centimeters. When the fluid dynamics is also taken into account, the numerical solution of the charging model is very computational expensive (between 3 and 48 h for a single simulation) [23].

In this study, we apply an extension of the widely used limiting-sphere model of Fuchs [14, 16, 33] to predict the charge distribution of unipolar chargers with approximately cylindrical symmetry in the charging zone, although it will be shown that can be applied to other geometries and charger types such as the more complex radioactive charger used by Wiedensohler et al. [142]. The model allows the simultaneous determination of the $N_i t$-product and the ion and particle losses (due to both electrical and diffusional effects), through a fit of experimental results for charge distribution fractions. The $N_i t$-product represents the figure of merit of the particle chargers, which allows to calculate other variables. The electric losses are a consequence of the assumption of an electric field in the charging zone, both in the radial and axial directions. Additional measurements of current, electric field or losses are not necessary.

Charged particles experience electrostatic forces in the charging region, since there the ions generate a space charge. Therefore, some percentage of particles will migrate to the walls and get lost there. For ultrafine particle sizes below 20 nm, the probability of charging is lower than for larger diameters, and the fraction of multiply charged particles is very low. Moreover, their losses by diffusion to the walls will be large. Ion concentration varies from the ionization region through the tube, due to the diffusional and electrostatic losses and, when the ion and particle concentrations are comparable, the attachment to particles leads to ion scavenging.

Therefore, a precise estimation of the ion concentration is needed, taking into account the ion and particle losses. An extension of the Fuchs model is presented, and the mean value of the $N_i t$-product in the charging region is obtained. It leads to an improved fitting of the experimentally determined mean charge per particle of the test charger, estimating the amount of ion and particle losses independently.

5.1 THEORETICAL BACKGROUND

The basic theory for particle charging was developed by Fuchs [33] in his well known theory of the *limiting sphere*. Combined with the *birth-and-death* model, this theory gives a set of differential equations that determine the charge distribution given the initial conditions.

The evolution of a charge distribution by diffusion charging of monodisperse particles is usually approximated by the birth-and-death model given in Boisdron and Brock [15]. In this theory, the solution is given by a set of infinite Difference-Differential Equations (DDEs), a two-variable system consisting of a coupled ordinary differential and recurrence equations. This solution neglects both ion and particle losses and supposes that ions and particles are uniformly mixed in the charging region. Applied to unipolar particle charging, here ions of one kind (either positive or negative) are generated and there is no recombination:

$$\begin{aligned} \frac{\mathrm{d}N_0}{\mathrm{d}t} &= -\beta_0 N_i N_0, \\ \frac{\mathrm{d}N_1}{\mathrm{d}t} &= \beta_0 N_i N_0 - \beta_1 N_i N_1, \\ &\vdots \\ \frac{\mathrm{d}N_q}{\mathrm{d}t} &= \beta_{q-1} N_i N_{q-1} - \beta_q N_i N_q, \end{aligned} \tag{5.1.1}$$

where N_q is the particle concentration with q elementary charges and β_q is the attachment coefficients of an ion to an uncharged particle (β_0) or to a particle with q charges (β_q), which can be expressed as the ratio of the ionic flux to the particle over the ion concentration N_i.

The *limiting sphere theory* supposes an imaginary sphere concentric to the particle that separates two regions. Between this sphere and the particle's surface, the motion of the ions is determined by the thermal speed and interaction potential with the particle, while outside the sphere, ionic motion is described by the macroscopic diffusion-mobility theory. Fuchs, matching the two fluxes at the surface of the limiting-sphere, showed that the ionic flux to the particle is expressed:

$$J = \frac{\pi\gamma\bar{c}_i\delta^2 N_i \exp\left(\frac{-\phi(\delta)}{k_BT}\right)}{1+\frac{\gamma\bar{c}_i\delta^2}{4\mathcal{D}_i}\exp\left(\frac{-\phi(\delta)}{k_BT}\right)\int\limits_{\delta}^{\infty}\frac{1}{r^2}\exp\left(\frac{\phi(r)}{k_BT}\right)\mathrm{d}r}, \tag{5.1.2}$$

where $\mathcal{D}_i = k_BTZ_i/e$ is the diffusion coefficient of ions and $\bar{c}_i$ the mean thermal velocity of ions of molecular weight M_i:

$$\bar{c}_i = \sqrt{\frac{8k_BTN_A}{\pi M_i}}. \tag{5.1.3}$$

The limiting sphere radius δ can be calculated from the particle radius a and the mean free path of the ions λ as:

$$\delta = \frac{a^3}{\lambda^2}\left[\frac{1}{5}\left(1+\frac{\lambda}{a}\right)-\frac{1}{3}\left(1+\frac{\lambda^2}{a^2}\right)\left(1+\frac{\lambda^3}{a^3}\right)+\frac{2}{15}\left(1+\frac{\lambda^2}{a^2}\right)^{5/2}\right], \tag{5.1.4}$$

being the mean free path determined by the theory of Maxwell-Chapman-Enskog as:

$$\lambda = \frac{8Z_i}{3\sqrt{\pi}e}\sqrt{\frac{M_gM_ik_BT}{(M_g+M_i)N_A}}, \tag{5.1.5}$$

with M_g the molecular weight of the gas and N_A the Avogadro's constant.

At a distance r from the particle, the interaction potential ϕ depends on the ion-particle interaction force F, a combination of the Coulomb force (first term on eq. (5.1.6)) and the image force induced by the ion (second term):

$$\phi(r) = \int_r^\infty F\mathrm{d}r = \frac{1}{4\pi\epsilon_0}\left(\frac{qe^2}{r}-\kappa\frac{a^3}{2r^2(r^2-a^2)}\right), \tag{5.1.6}$$

where $\kappa = \frac{\epsilon-1}{\epsilon+1}e^2$ is the image force parameter for particles with dielectric constant ϵ.

The parameter γ express the probability of an ion to collide with a particle within the limiting-sphere limits and transfer its charge to the particle. In absence of further electrical forces, this parameter is reduced to the fraction $\gamma = a^2/\delta^2$, while in the case of charged particles is calculated according to the collision parameter b of the minimum apsoidal distance to the particle given by the Natanson´s equation:

$$b^2 = r^2\left(1+\frac{2}{3k_BT}\left(\phi(\delta)-\phi(r)\right)\right). \tag{5.1.7}$$

The minimum collision parameter b_m is calculated by setting the eq. (5.1.7) as $\mathrm{d}b^2/\mathrm{d}r = 0$, and therefore the associated collision probability as $\gamma = b_m^2/\delta^2$.
The previous system of DDEs (eqs. (5.1.1)) is solved by Biskos et al. [14] using Laplace transformation, assuming initial uncharged particles, that is $N_0 = 1$, $N_q = 0$, and no ion losses. For a given N_it value, the charged particle concentration has the form:

$$N_q = \begin{cases} \exp(-\beta_qN_it), & q = 0, \\ -\sum\limits_{j=0}^{q-1} k_{j,q-1}\frac{\beta_{q-1}}{\beta_j-\beta_q}\left[\exp(-\beta_jN_it)-\exp(-\beta_qN_it)\right], & q \neq 0, \end{cases} \tag{5.1.8}$$

where the coefficients $k_{j,q}$ are obtained recursively:

$$k_{j,q} = \begin{cases} 1, & j = q = 0, \\ -k_{j,q-1}\frac{\beta_{q-1}}{\beta_j - \beta_q}, & j < q, \\ \beta_{q-1}\sum\limits_{j=0}^{q-1}\frac{k_{j,q-1}}{\beta_j - \beta_q} = -\sum\limits_{j=0}^{q-1} k_{j,q}, & j = q \neq 0, \\ 0, & j > q. \end{cases} \tag{5.1.9}$$

This model (5.1.1) does not consider some phenomena, like diffusion to the walls or electrical migration. If these characteristics are taken into account, system (5.1.1) cannot be solved as shown in eqs. (5.1.8) and (5.1.9). A simple solution method is the *Semi-Implicit Method (SIM)* (also known as *Euler-Cromer method*). This method reaches a solution by iteration of discrete time steps Δt in the system (5.1.1):

$$\begin{aligned} \frac{\Delta N_0(t+\Delta t)}{\Delta t} &= -\beta_0 N_i N_0(t+\Delta t), \\ &\vdots \\ \frac{\Delta N_q(t+\Delta t)}{\Delta t} &= \beta_{q-1} N_i N_{q-1}(t+\Delta t) - \beta_q N_i N_q(t+\Delta t), \end{aligned} \tag{5.1.10}$$

considering $\Delta N_q(t+\Delta t) = N_q(t+\Delta t) - N_q(t)$. The semi-implicit method searches the solution in a later time $(t+\Delta t)$ to the last known system time, starting from $t = 0$.

The initial concentration is obtained by direct integration of the first term of expression 5.1.1 for neutral particles:

$$N_0(t) = N_0(0)\exp(-\beta_0 N_i t), \tag{5.1.11}$$

where the exponential term can be expressed in the form of the semi-implicit method:

$$N_0(t) = \frac{N_0(0)}{1 + \beta_0 N_i t}. \tag{5.1.12}$$

The following concentrations for multiple charged particles are calculated solving the set of eqs. (5.1.10) for $N_q(t+\Delta t)$:

$$N_q(t+\Delta t) = \frac{N_q(t) + \beta_{q-1} N_i \Delta t \cdot N_{q-1}(t+\Delta t)}{1 + \beta_{q-1} N_i \Delta t}. \tag{5.1.13}$$

From the previous equations we can calculate the fraction of charged particles by means of:

$$f_q = \frac{N_q}{\sum\limits_q N_q}. \tag{5.1.14}$$

The semi-implicit method has a global error of the order of Δt, but when choosing this interval small enough, the errors are comparable to the ones generated by the solution of Biskos et al., as fig. 5.1.1 shows. The results are equal for all the cases tested, therefore we consider the semi-implicit method as a valid tool for solving the problem.

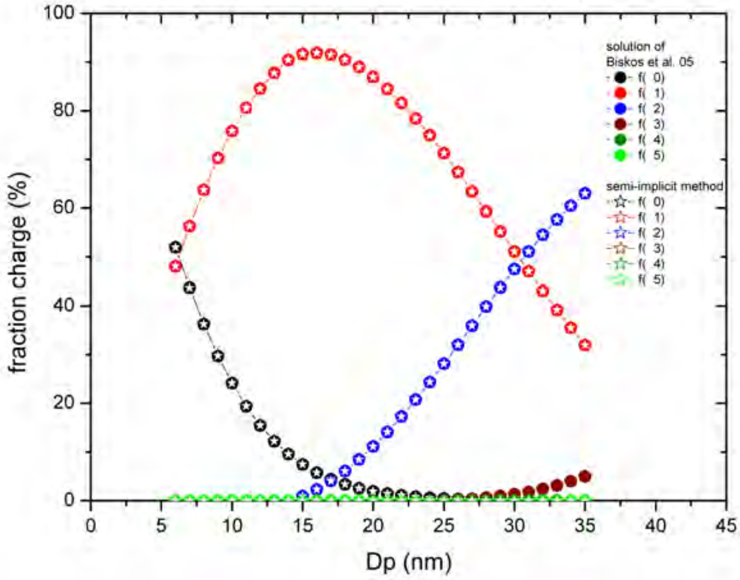

Figure 5.1.1: Comparison of simulated graphs for the same charging conditions by eqs. 5.1.8 and eqs. 5.1.13 from the semi-implicit method.

5.2 FIRST APPROACH TO THE $N_i t$- PRODUCT ESTIMATION

In corona chargers, the $N_i t$-product is a key parameter, as eq. ((5.1.8)) shows. A precise estimation of this product is needed to predict the charging levels of the particles. When N_i depends on time along the duct, the integral has to be used:

$$\overline{N_i t} = \int_0^t N_i(t)\mathrm{d}t, \tag{5.2.1}$$

which can be also written as the product of the mean ion number concentration and the mean aerosol residence time $\overline{N_i t}$. Therefore, it depends on some features of the device such as shape of the electrodes, dimensions and volume of the charging region, and the operating conditions of the charger (voltage applied to the electrode, flow rate, electric field).

The residence time in the charging region is defined as the quotient: $t = L/u_i$, where L is the length of the tube and the velocity of the ions $u_i = u_g$ can be assumed mainly due to the gas flow. For experiments with flow rates of 0.5 lpm for ion flow and 1.5 lpm for the particle flow, the maximum residence time is 0.30 s in the charging region ($R = 8\,\text{mm}$, $L = 50\,\text{mm}$).

To verify that the gas sheath is the main transport of the ions, other means of transport are calculated. For example, the diffusion time expressed as $t_\mathrm{d} = L^2/2\mathcal{D}_i$, and gives a total time of 353.13 s, meaning that diffusion is negligible against other forces. The electrical migration time, $t_\mathrm{el} = L/Z_i E$, will be shown in the following that is also negligible compared with the forces due to the gas sheath.

However, the mean ion concentration is unknown and for its estimation some assumptions must be done. In our case, the geometry of the electrode (needle) and the configuration of the device complicates the precise calculation of the electric field along the charging region. Around the electrode tip there is a plasma of ions creating a very intense field which decays as the flow moves the ions away. Therefore, in the discharge region, the velocity due to the electric field decreases with the distance from the source, while the velocity due to the gas flow is increased in the charging region, where aerosol and ion driving flows converge.

There are several ways to calculate the $N_i t$-product: directly with equations considering the electric field and current, or indirectly, extracting the value from measurements. These methods will be tested and compared for an experimental performance of the corona charger with monodisperse particles in the size range of 6 to 60 nm, number concentrations below $10^5\,\text{cm}^{-3}$, a corona starting voltage of 3.5 kV and flow rates of 0.5 lpm for ions and 1.5 lpm for aerosol particles.

A direct calculation of the mean number concentration of ions is given by:

$$N_i = \frac{I}{eA(u_g + Z_i E_x)}, \tag{5.2.2}$$

which multiplied with the residence time gives a value for the $N_i t$-product. This formula is widely used among authors [73, 3, 133, 61, 80], however the main variables are not precisely known or cannot be determined accurately. The electric field is difficult to estimate precisely (is not completely calculated until an integration constant is approximated from the experimentally measured pairs of voltage and current, subject to experimental error) and considers homogeneous charging along the whole charging region. Also the measured ion current can be underestimated due to space charge and diffusion losses through the tubes.

By this way, the estimated $N_i t$-product takes values between $1 - 7 \times 10^{11}\,\text{sm}^{-3}$, depending on the distance between electrodes and therefore on the ion current generated.

On the other hand, there is a particular case in which the transient eqs. (5.1.1) have an analytical solution [9]. Very small particles (diameters below 20 nm) acquire at most a single charge, since the attachment coefficients for doubly or multiply charged particles and ions are very small at this size range. Thus, the aerosol consists only of two species: neutral and singly charged particles. Besides, one can assume that the ion concentration remains constant throughout the process, since the probability of singly charging is quite low for nanoparticles and therefore, the fraction of ions lost due to charging of the particles is also small. Hence, the charging rate equation for N_0 is solved easily, resulting in:

$$f_0 = \exp\left(-\beta_0 N_i t\right). \tag{5.2.3}$$

Applying the particle conservation equation, $f_0 + f_1 = 1$ and under the assumption of initially neutral particles, the fraction of singly charged to the total of particles f_1 is obtained at the steady state condition, $\mathrm{d}N_1/\mathrm{d}t = 0$, results:

$$f_1 = 1 - \exp\left(-\beta_0 N_i t\right). \tag{5.2.4}$$

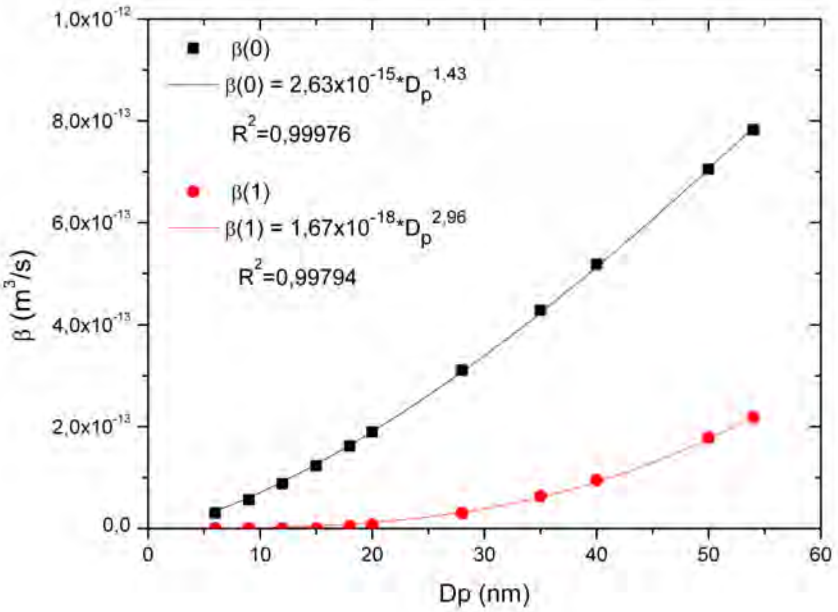

Figure 5.2.1: Fitting of the attachment coefficients.

These fractions can be roughly approximated to the charging efficiencies, supposing that the whole fraction of the initially neutral particles become singly charged at the steady-state.

The $N_i t$-product controls the charging process in eq. (5.2.4). In theory, a high charging efficiency can be achieved by increasing the ion concentration or the charging time. However, this is unattainable in practice, because during a large aerosol residence time in the charger particles and particularly ions would be entirely lost by diffusion and electric dispersion to the walls.

The calculated attachment coefficients from the set of eqs. (5.1.1) are accurately described by potential functions of the form $y = ax^b$, as shown in fig. 5.2.1. This allows to obtain a relation between the charge fraction and the particle diameter in eq. (5.2.4) and by solving the resulting equation, the $\overline{N_i t}$-product for the charger described previously is obtained. Fig. 5.2.2 shows the measured extrinsic charging efficiencies from this method, resulting an $\overline{N_i t} = 5.5 \times 10^{12}\,\text{sm}^{-3}$ for the 3 mm gap with a coefficient of determination of $R^2 = 0.9317$ and $1.85 \times 10^{12}\,\text{sm}^{-3}$ for 10 mm with $R^2 = 0.9739$. However, through this method of fitting, only singly charged particles with no losses are accounted, and the efficiencies for the gap of 3 mm, where there is a 20% of doubly charged particles at 20 nm, are underestimated.

For this reason the intrinsic charging efficiencies are fitted in fig. 5.2.3, since for the calculation of the intrinsic efficiencies only the rate of particles being charged is

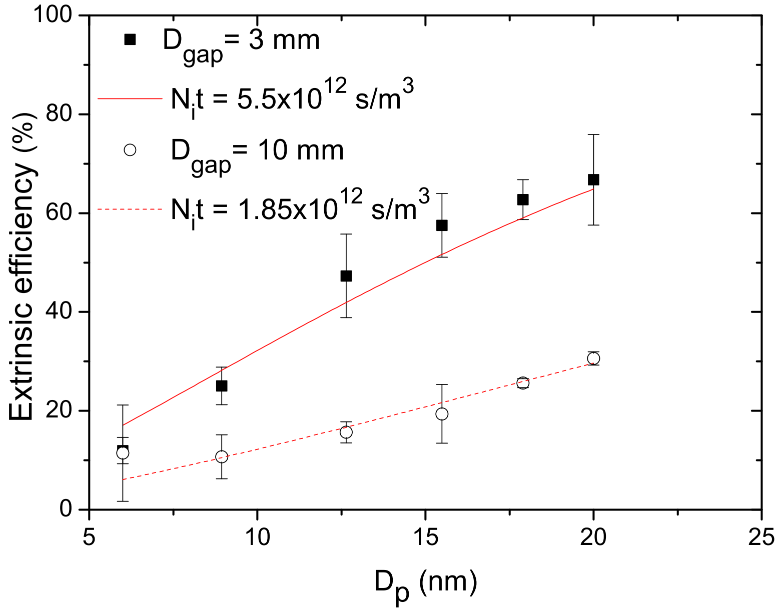

Figure 5.2.2: Comparison of experimental values of extrinsic charging efficiencies (points) and results from best fitting N_it values (lines) to eq. (5.2.4) for two different electrode gap distances.

important and this agrees better with the theory applied. The values obtained for the 10 mm gap ($\overline{N_it} = 2.33 \times 10^{12}\,\mathrm{sm}^{-3}$, $R^2 = 0.7919$) are very similar for both efficiencies. However, for the gap of 3 mm there is a difference of one order of magnitude with the previous calculation ($\overline{N_it} = 2.41 \times 10^{13}\,\mathrm{sm}^{-3}$, $R^2 = 0.9693$), and it is better approximated to the real value of $\overline{N_it}$ for these setup characteristics, as it will be shown in the following.

A most reliable method to accurately estimate the value of the $\overline{N_it}$ -product is by fitting the results of the charge distribution to the birth-and-death eqs. (5.1.1), being the $\overline{N_it}$ -product the adjustable parameter. This has the advantage that the multiple charged particles are now also described. We have performed the fitting by a self-developed software program based on the Levenberg-Marquardt method as described by Press et al. [101]. The $\overline{N_it}$ value of the generated distribution is varied until the difference between simulated (using the set of eqs. (5.1.1)) and experimental charge distributions is minimized. It must be noted that instead of the charge fraction, with multiple variables, the mean charge per particle is used in the calculation. The particle mean charge (eq. 4.2.6) is a significant quantity associated with the diffusion charging that depends on the particle diameter and the $\overline{N_it}$ -product in the charging zone.

By this method, the mean charge per particle is calculated and shown in figs. 5.2.4a and 5.2.4b for the gaps of 3 mm and 10 mm respectively. The Root Mean Square Error

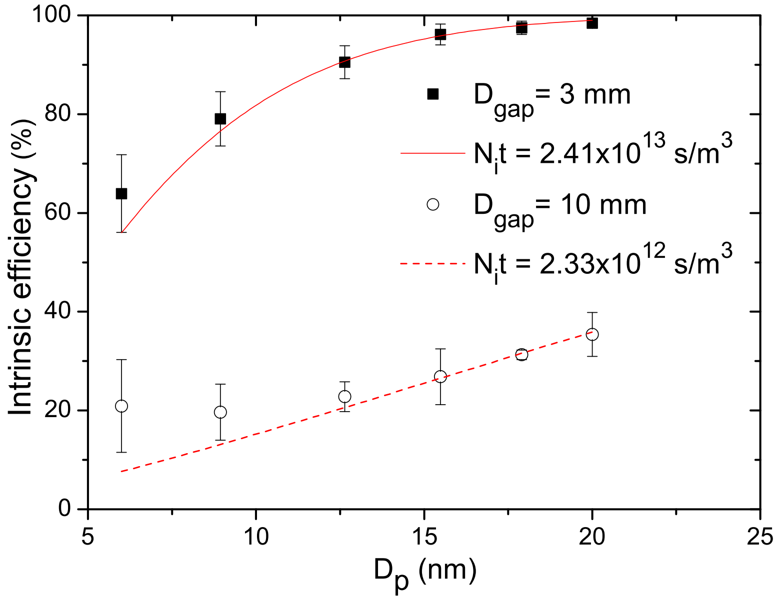

Figure 5.2.3: Fitting as in fig. 5.2.2, but now using the intrinsic charging efficiencies.

(RMSE) is estimated as the square root of the normalized sum of squared differences between the experimental and calculated data, that is:

$$\text{RMSE} = \sqrt{\frac{1}{n}\sum_{i=1}^{n}\left(\overline{q_i}_{\text{exp}} - \overline{q_i}_{\text{calc}}\right)^2}. \tag{5.2.5}$$

For fig. 5.2.4a, is obtained $\overline{N_i t} = 3.57 \times 10^{11}\,\text{sm}^{-3}$ with a RMSE of 0.28, while for fig. 5.2.4b, $\overline{N_i t} = 7.03 \times 10^{10}\,\text{sm}^{-3}$ with a RMSE of 0.055.

Despite the RMSE of the fit being below 0.2 in all cases, it can be seen that the fitting overestimates the charging for small particles and underestimates the multiple charging of particles from 35 nm onwards. This occurs because in the applied theory diffusion of ions or particles, as well as the electrostatics effects, are not considered. Therefore, the value of the $\overline{N_i t}$-product, although is similar to the calculated by the first method, is underestimated, and the fitting can be improved when some previous assumptions are taken into account.

5.3 EXTENDED MODEL FOR THE $N_i t$- PRODUCT CALCULATION

There are some characteristics of the device that are precisely known, such as geometry or flowrates. Some operational properties can be obtained by measurements, as the charge distribution or electrical current. However, there are other factors, as $N_i(0)$, the ion concentration at the beginning of the charging region, or the electric

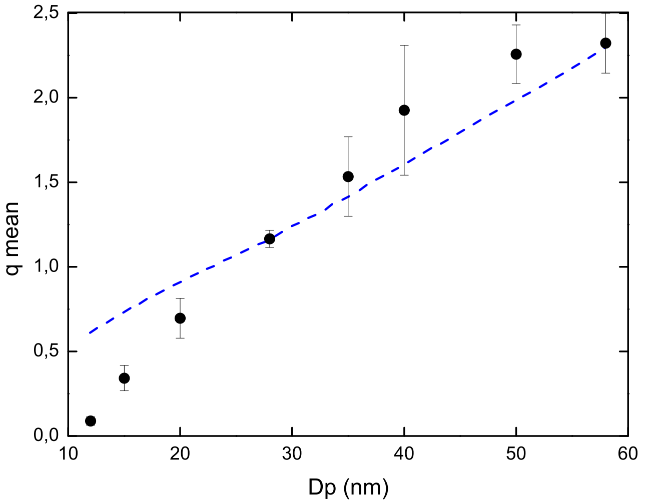

(a)

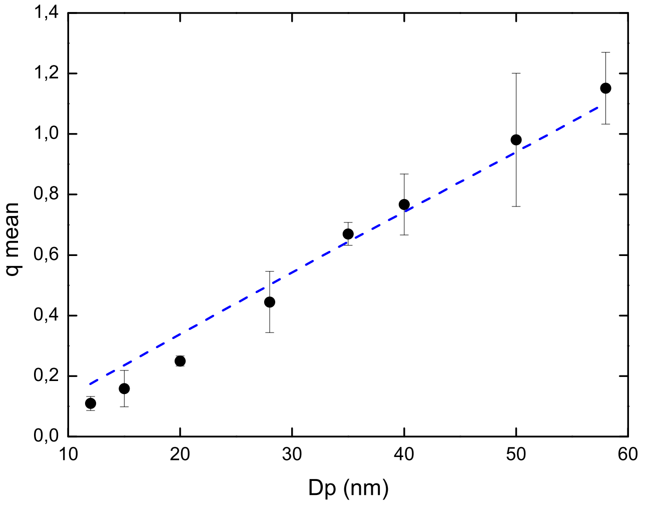

(b)

Figure 5.2.4: $\overline{N_i t}$ -product estimation by fitting the mean charge (dot symbols) for the gap of 3 mm. The dotted line is the result of the best fit using the birth-and-death eqs. (5.1.1).

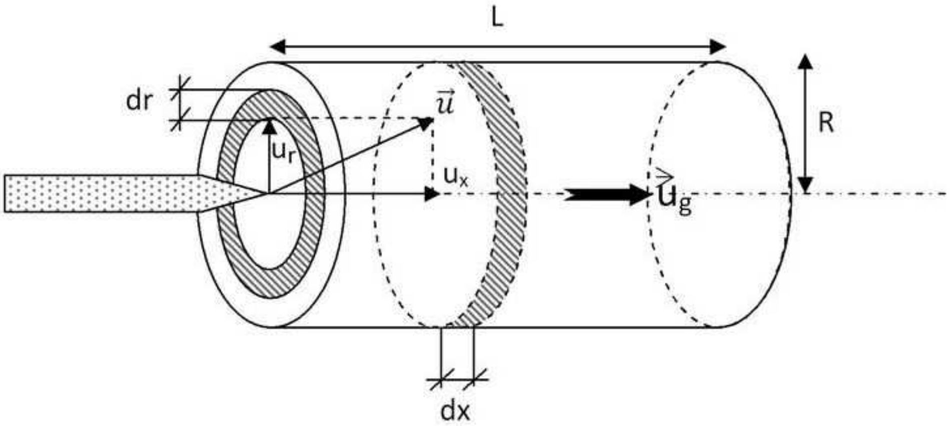

Figure 5.3.1: Velocities at which the ions are subjected along the charging tube.

field through the tube, which are unknown and very difficult to measure with precision.

In some previous works [3, 14], the fitting to the mean charge is performed using the initial ion concentration N_i^0, and no losses of ions or particles are considered. The results show serious deviations for ultrafine ($< 10\,\mathrm{nm}$) or larger diameters (above 50 nm, which implies multiple charges), and it is only acceptable for the intermediate values. In Alguacil and Alonso [3] it is claimed that the discrepancy is due to losses, but no further calculation is done.

We suppose that the difference between the estimated and the measured mean charge are caused by the initial assumptions on the Boisdron and Brock [15] theory, where ion and particle losses are neglected. Therefore a new model is proposed here, which includes these losses caused by means of an electrical field which leads to an additional velocity component of ions and charge particles and the diffusion losses. Plug flow with uniform mixing of ions and particles through the charging region is assumed.

With the sheath gas flow in axial direction u_g, the ion velocity can be decomposed in its axial and radial components:

$$\begin{aligned} u_x &= \frac{\mathrm{d}x}{\mathrm{d}t} = Z_i E_x + u_g, \\ u_r &= \frac{\mathrm{d}r}{\mathrm{d}t} = Z_i E_r. \end{aligned} \tag{5.3.1}$$

where r is an arbitrary radius within the total radius of the charging region R, and similarly x is an arbitrary axial distance within the length L. The electric field components E_x and E_r are considered constant throughout the charging region, as a first approximation.

Due to the radial component of the electric field, part of the ions are lost to the walls. The differential losses in a cylindrical channel can be expressed by a loss factor determined from the ratio between the total area occupied by the ions and the area where they probably are lost:

$$\mathrm{d}f_{Li} = -\frac{2\pi r \mathrm{d}r}{\pi R^2}, \tag{5.3.2}$$

where r is an arbitrary radius within the total R (fig. 5.3.1). Particles are widespread in any radial direction from the whole area $A = \pi R^2$ of the cross section of the cylindrical conduct. But only the particles closer to the walls are likely to be lost there, that is, particles within a differential area, $dA = 2\pi r dr$. Only when $|\mathrm{d}f_{L_i}| < 1$, the output of the charging region is reached. Close to the walls, $r \approx R$, then substituting $\mathrm{d}r$ from (5.3.1) for a given time interval $\mathrm{d}t$, this factor is expressed as:

$$\mathrm{d}f_{\mathrm{Li}} = -\frac{2}{R}\frac{Z_i E_r}{u_{\mathrm{g}} + Z_i E_x}\mathrm{d}x, \tag{5.3.3}$$

or alternatively:

$$\mathrm{d}f_{\mathrm{Li}} = -g_{\mathrm{Li}}\mathrm{d}t, \tag{5.3.4}$$

where $g_{\mathrm{Li}} = \frac{2}{R}Z_i E_r$ is an auxiliary coefficient to simplify notation, and from eqs. (5.3.1), the time interval $\mathrm{d}t = \mathrm{d}x/(u_{\mathrm{g}} + Z_i E_x)$.

Likewise, for particles the time interval $\mathrm{d}t$ will depend on the charge level, since for a given diameter the mobility of a particle with charge q is $Z_q = qZ_{q=1}$, and then:

$$\mathrm{d}f_{\mathrm{Lp}} = -\frac{2}{R}\frac{qZ_1 E_r}{u_{\mathrm{g}} + qZ_1 E_x}\mathrm{d}x, \tag{5.3.5}$$

which when defining $g_{\mathrm{Lp}} = \frac{2}{R}Z_1 E_r$, also an auxiliary coefficient, results in:

$$\mathrm{d}f_{\mathrm{Lp}} = -qg_{\mathrm{Lp}}\mathrm{d}t. \tag{5.3.6}$$

The term g_L is related to the effect of the electrostatic forces on the particles (g_{Lp}) or ions (g_{Li}), partly responsible of the diffusion losses.

The second loss mechanism is related to diffusion [47]. Another diffusional term will be added, related with the penetration of particles, whose equation was shown in 4.1.8. In this case, the auxiliary coefficient:

$$\phi(t) = \frac{x(t)\mathcal{D}}{Q_t}, \tag{5.3.7}$$

where $x(t)$ is the length covered by the ion or particle in the time t. Therefore, the term of diffusional elimination $P_n(t)$ will depend on the interval of time (or space) considered.

The ion concentration is expressed thereby as a function of time in the charging zone, since it is not uniform along the charging region due to the diffusion of ions and the combination of the governing forces: close to the ionizing output, the electrical force is stronger than at the output of the charging region, where the main transport is due to the gas flow.

The variation of the ion concentration is then dependent on the penetration of the ions through the tube $P_n(t)$, since the ions lost in a prior time cannot be charged or lost again, that is $N_i'(t) = P_n(t)N_i(t)$. A variation in concentration due to the losses can be expressed through the loss factor considering the differential change in each point:

$$\mathrm{d}f_{\mathrm{Li}} = \frac{\mathrm{d}N_i'(t)}{N_i'}. \tag{5.3.8}$$

Combining this equation with eq. (5.3.4) and approximating the term $\frac{\mathrm{d}N_i'(t)}{\mathrm{d}t}$ by discrete time steps, results:

$$\frac{\Delta\left[P_n(t+\Delta t)N_i(t+\Delta t)\right]}{\Delta t} = -g_{\mathrm{Li}}P_n(t+\Delta t)N_i(t+\Delta t). \tag{5.3.9}$$

Solving eq. (5.3.9) by the semi-implicit method we obtain:

$$N_i(t+\Delta t) = \frac{N_i(t)}{1+g_{\mathrm{Li}}\Delta t}d_L(t+\Delta t), \tag{5.3.10}$$

where the diffusion loss coefficient is:

$$d_L(t+\Delta t) = \frac{P_n(t)}{P_n(t+\Delta t)}. \tag{5.3.11}$$

It is assumed that the ion concentration is much higher than the particle concentration, so the charging of particles does not lead to a decrease in the ion concentration.

The equations describing the concentration of charged particles has to be reformulated too to include the losses. The fraction of particles lost due to electrostatic losses is depicted by the new term qg_{Lp}. Diffusional losses are taken care of by using $N_q'(t) = N_q(t)P_n(t)$, so that eqs. (5.1.10) are modified into:

$$\begin{aligned}\frac{N_q'(t+\Delta t) - N_q'(t)}{\Delta t} &= \beta_{\mathrm{q-1}}N_i(t+\Delta t)N_{\mathrm{q-1}}'(t+\Delta t) - \\ &- \left[\beta_q N_i(t+\Delta t) - qg_{\mathrm{Lp}}\right] N_{\mathrm{q}}'(t+\Delta t).\end{aligned} \tag{5.3.12}$$

To solve the complete problem we apply the *operator splitting method* (see [101] for details), also known as *time splitting* or *method of fractional steps*, which computes the solution in small steps through independent operators, one corresponding to the diffusion losses and the other to the rest of the evolution phenomena.

The solution is then obtained in two steps, first evolving the system by one operator in a Δt time step, and then is applied the other operator in Δt to the previously found solution.

In this way, the term for the concentration of charged particles is obtained:

$$N_{\mathrm{q}}(t+\Delta t) = \frac{N_{\mathrm{q}}(t) + \beta_{\mathrm{q-1}}N_i(t+\Delta t)\Delta t N_{\mathrm{q-1}}(t+\Delta t)}{1+\left(\beta_q N_i(t+\Delta t) + qg_{\mathrm{Lp}}\right)\Delta t}d_L(t+\Delta t), \tag{5.3.13}$$

where the ion concentration has the form of eq. (5.3.10) and the penetration coefficient as in eq. (5.3.11). A piece of code in Python for the estimation of eq. (5.3.13) can be found in Appendix C.

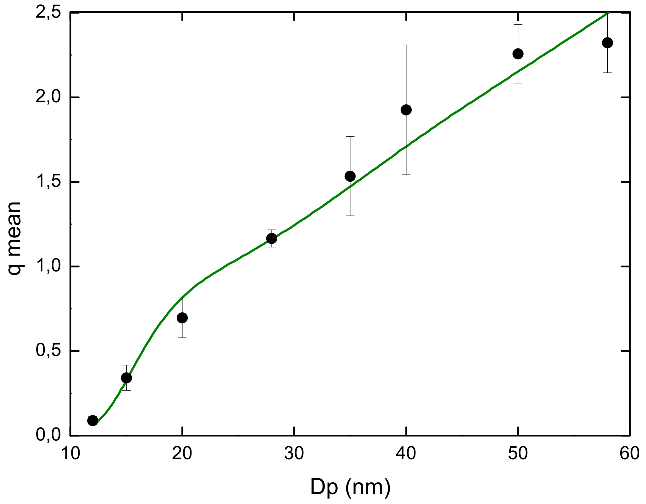

(a)

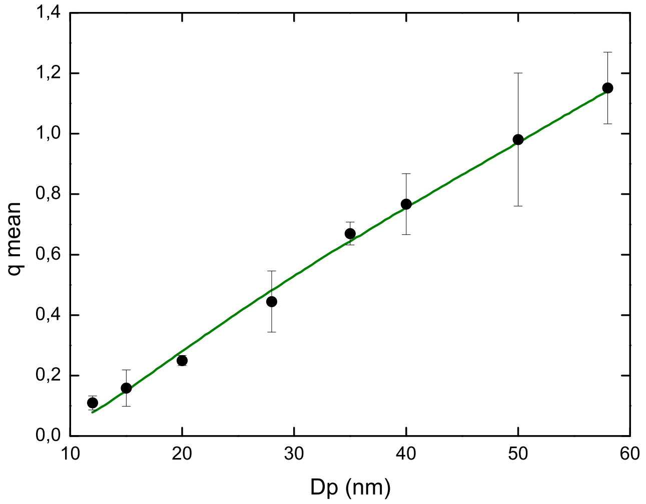

(b)

Figure 5.3.2: $N_i t$-product estimation by fitting the mean charge and considering diffusional losses and a constant electrical field in the charging zone.

With this corrected equation, the $\overline{N_i t}$ value is obtained by the same fitting of the mean charge procedure as described before. Results are shown in fig. 5.3.2 for gaps of 3 mm and 10 mm. We impose $E_x = 0$ as its effect is expected to be negligible compared to the axial flow velocity, and let N_i^0 and E_r be found by the minimization of the root mean square error. The radial field value obtained suggests that the ions leaving the needle are in principle distributed around the axis of the tube, creating the radial field as they expand to the walls.

The estimated $\overline{N_i t}$ value increases up to $1.81 \times 10^{13}\,\mathrm{sm}^{-3}$ for the gap of 3 mm and $2.38 \times 10^{12}\,\mathrm{sm}^{-3}$ for 10 mm, being very similar to the ones shown in fig. 5.2.3. The global error of the fitting decreases significantly (up to one order of magnitude) compared to the model without considering the losses, now being 0.11 and 0.023 for each gap, and the curve is better suited to the data as is provided by the error bars. However, it must be noticed that this experimental error is roughly estimated, since the properties represented here cannot be directly measured, but estimated from fittings and measurements from other characteristics, such as particle concentrations (as explained in 4.2.2).

It can be seen how the global error of the fitting decreases, the $N_i t$ value increases and the resultant plot fits much better the experimental points, describing a 'decay' for the smallest diameters due to the adjust for diffusional losses, while then increases linearly.

Note that the model determines the ion concentration that best fits the size-dependent mean charge without having to measure it, which can be subject to errors and noise. The obtained values are $N_i^0 = 2.05 \times 10^{16}\,\mathrm{m}^{-3}$ and $N_i^0 = 7.29 \times 10^{14}\,\mathrm{m}^{-3}$ for the 3 and 10 mm gaps respectively. It is important to remind that this is the ion concentration right at the output of the discharge region, and its value changes along the charging zone, hence a mean value such as the $\overline{N_i t}$ would be a better indicative of the charging process inside the device.

The model describes now the experimental data for the mean charge much better, especially for the smallest diameters. This is due to the fact that the smaller particles are much more likely to get lost because of electrostatic and diffusional losses. The radial electrical field, responsible for the losses of charged particles and ions, found by the fitting procedure takes values of $E_r = 3.5 \times 10^4\,\mathrm{V/m}$ for the 3 mm gap and $8.74 \times 10^3\,\mathrm{V/m}$ for 10 mm. The relatively high value of E_r supports our assumption that there is a considerable effect due to space charge.

5.3.1 *Correlation between the parameters of the model*

In an attempt to obtain a still better agreement to the experimental data, a constant axial field E_x was included as well. However, the results did not improve as the RMSE values were not reduced compared to the assumption of $E_x = 0$. A possible reason is that when $E_x > 0$, the total axial velocity is increased. Then, the residence time is reduced and the electrical losses decrease. This effect is in principle equivalent to an increase in N_i^0, as long as the attachment coefficients are small enough. Thus, N_i^0 and E_x are closely related parameters and the fitting procedure does not allow to differentiate between the two.

To investigate the effect of the three parameters N_i^0, E_r and E_x, we performed simulations varying one parameter in the model while the other two remain fixed. In fig. 5.3.3, the thick line corresponds to fitted data from experimental measurements from the gap of 10 mm, taken as reference. It has an initial ion concentration of $7.29 \times 10^{14}\,\mathrm{m}^{-3}$, a radial field of $8.74 \times 10^3\,\mathrm{V/m}$ and a null axial field, since the velocity due to the gas flow is much greater compared to the velocity given by electrostatics effects in the direction of the axis.

In Table 5.3.1, the parameters E_r, E_x and N_i are increased or decreased taking the values determined by the best fit described earlier as starting point. The resulting size-dependent mean charges are plotted in fig. 5.3.3. It can be seen that the effect of varying the axial field E_x is essentially equivalent to a change the initial ion concentration N_i^0 shown in the table 5.3.1. An increase of the axial field up to 600 V/m (top dotted line) with the other parameters fixed has the same effect as an increase in the initial ion concentration to $1.10 \times 10^{15}\,\mathrm{m}^{-3}$ for the reference components of the electric field, and vice versa. The bottom solid thin line shows the effect of placing an axial electric field opposed to the movement of the flow, $E_x = -610\,\mathrm{V/m}$, which is essentially equivalent to a decrease in ion concentration to $N_i^0 = 3.50 \times 10^{14}\,\mathrm{m}^{-3}$. However, although the resulting size-dependent mean charges are indistinguishable from each other, the mean $N_i t$ product is different in each case (values are summed up in table 5.3.1). Therefore, it is impossible to obtain the exact $\overline{N_i t}$-product when either the axial field or the initial ion concentration is unknown when using the fitting to charge fractions (or mean charge) as the solely method.

Table 5.3.1: Values used in simulations when one parameter in the model was changed while the other two remain fixed, and resultant $\overline{N_i t}$.

variable to change	N_i^0 ($\times 10^{14}\,\mathrm{m}^{-3}$)	E_x (V/m)	E_r ($\times 10^3\,\mathrm{V/m}$)	$\overline{N_i t}$ ($\times 10^{12}\,\mathrm{s\,m}^{-3}$)
N_i^0	11.0			3.62
E_x		600		2.38
E_r			5.80	3.59
reference	7.29	0.0	8.74	2.40
N_i^0	3.50			1.15
E_x		−610		2.45
E_r			17.5	1.22

However, the effect of varying the radial field is different. It has to be high enough to allow the ion and particle mixing, but low enough to avoid substantial losses. The main contribution to the radial field is the space charge of ions and charged particles, but a contribution of the discharge voltage cannot be ruled out. It is likely that it is not constant over the length of charging region, so that it has to be considered as a mean value.

When varying now E_r in an attempt to obtain the same results for the mean charges as by varying either N_i^0 or E_x, the curves in fig. 5.3.3 differ for particle

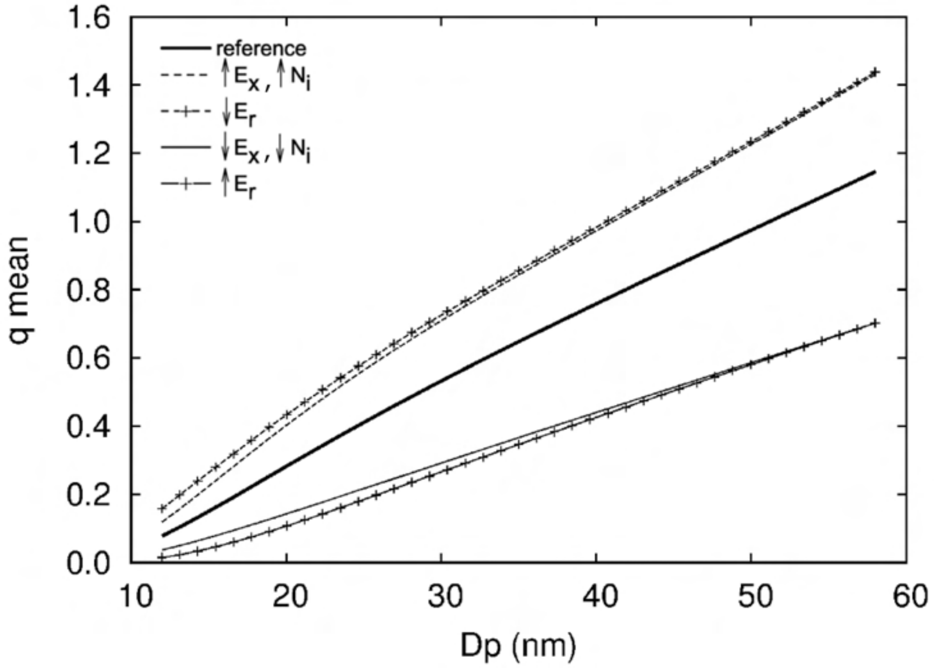

Figure 5.3.3: Simulation of the mean charge by fixing two of the fitting parameters and varying the third one indicated in the legend according to table 5.3.1. The thick line corresponds to the reference case which best fits the experimental data.

sizes below 40 nm. Top dotted-crossed line depicts a decrease of radial field value to 5.80×10^3 V/m, the bottom thin-crossed line an increase to 1.75×10^4 V/m. For particle sizes above 40 nm, the mean charge is equal to that obtained for the variation in N_i^0 or E_x, but for lower diameters the slope of the mean charge plot is different. This demonstrates that the radial field is indeed an independent variable in the model, and can be used to reach a better agreement between experimental data and calculated results.

Using the best-fitting value for N_i^0 of 7.29×10^{14} m^{-3} it is also possible to investigate what is the effect of assuming a negligible radial field, $E_r = 0$. This means that we neglect the space charge induced by the ions, which is not realistic, but it is interesting to see which is the effect on the mean charges. In fig. 5.3.4 it can be seen that the mean charges are increased by a factor of 2 to 4 when not taking into account the space charge-induced losses. The behavior below 20 nm is due to the effect of the Brownian diffusion, which has a strong effect on the smallest particles, and the attachment coefficients, which control the charging of the particles.

5.3.2 *Effect of N_i^0 and E_r on the extrinsic charging efficiency*

In fig. 5.2.2, extrinsic efficiency was used to calculate the mean $N_i t$-product. However, multiple charging of particles was not considered then, and since it depends on all

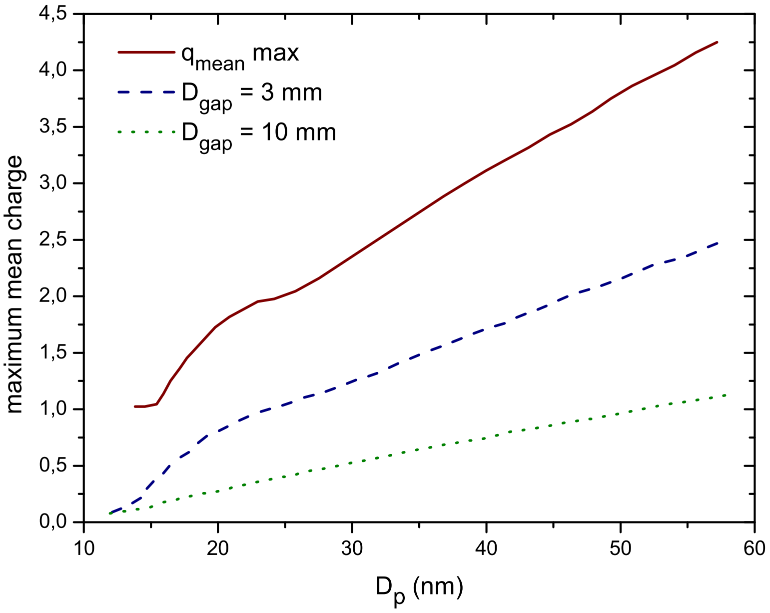

Figure 5.3.4: Simulation of the size-dependent mean charge using the earlier found value for N_i^0 but now assuming a negligible radial field, $E_r = 0$.

fractions of charge f_q, it contains more information than the mean charge and this is therefore preferred for fitting.

The knowledge of the charging efficiency of ultrafine particle sizes can be complicated, it is difficult to measure and poor efficiencies are commonly obtained. However, the efficiency depends to a certain extent on the losses, thus is not possible to increase the initial ion concentration N_i^0 without an increase in space charge, which leads to a rise in E_r. This effect is simulated by increasing both parameters the same constant factor, leading to a net decrease in extrinsic charging efficiency, as shown in fig. 5.3.5. This decay is much more pronounced for the smaller particle sizes because, due to the increase in E_r, the losses rise more rapidly than the gain in charging that a higher N_i^0 could cause.

Although losses are minimized, there is still a maximum of the charging efficiency for the ultrafine particles, due to the properties of the attachment of ions. This limit is presented in fig. 5.3.5 and shows that for particles below 6 nm, a 100% of charging efficiency is not possible with the present initial conditions.

Therefore, it is recommended to make sure that a unipolar charger is producing not too large quantities of ions, because in that case the smallest particles will not be efficiently charged. This can be reached, e.g., by using a smaller discharge voltage or a larger gap distance. This effect can also be seen in the experimental data for extrinsic efficiencies from other authors [3, 26, 57, 103], where losses increase when the discharge voltage increases. Another advantage of keeping a low discharge voltage is the increase of the electrode life.

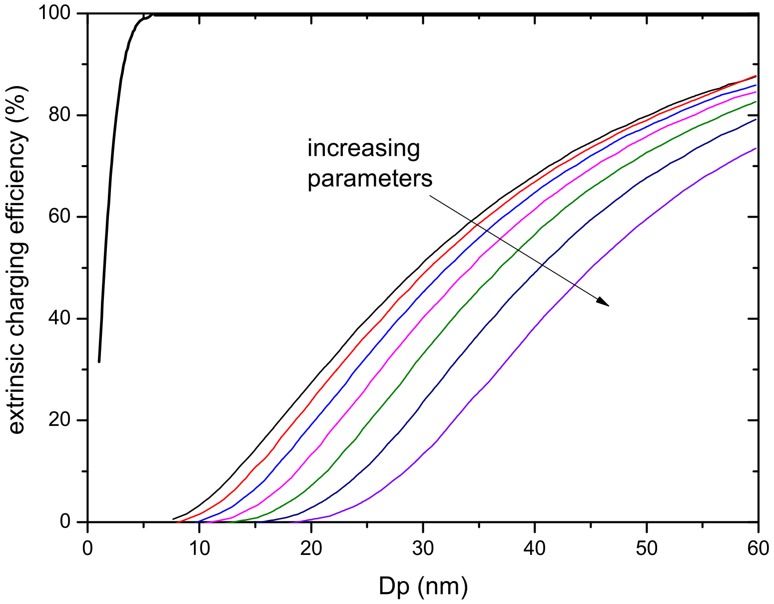

Figure 5.3.5: Simulation of the extrinsic charging efficiency when increasing simultaneously E_r and N_i^0 by a constant factor $k = 1.5$ (from left to right), starting at $N_i^0 = 7.29 \times 10^{14}\,\mathrm{m}^{-3}$ and $E_r = 8.74 \times 10^3\,\mathrm{V/m}$. The uppermost thick line is the limit charging efficiency with no losses.

5.3.3 *Application of the model to literature data*

For further validation of the model, it is applied to experimental data from other authors. A unipolar charger from Alguacil and Alonso [3] is considered, based also on corona discharge. Here, the corona discharge and charging of particles take place in the same region, with a needle as electrode. In the paper, large uncertainties in the calculation of the $\overline{N_i t}$-product due to losses are mentioned, which the authors tried to consider in a recalculation in an admittedly 'very rough manner'. This is due to their assumption that the particle losses are not dependent on charge distribution, but only on particle size and corona voltage. This led to a $\overline{N_i t}$-product between 1.0 and $4.0 \times 10^{13}\,\mathrm{sm}^{-3}$.

The measured charge levels are used to calculate the mean charge, using the approximation with the birth-and-death eqs. (5.1.1) without consideration of losses. This leads to an $\overline{N_i t} = 4.62 \times 10^{11}\,\mathrm{sm}^{-3}$ with a RMSE of 0.095 for the figure 5.3.6a, from particles charged at a corona operating voltage of 3 kV, and $\overline{N_i t} = 5.62 \times 10^{11}\,\mathrm{sm}^{-3}$ with a RMSE of 0.20 for the voltage of 3.6 kV in figure 5.3.6b.

When losses are considered, by means of fitting N_i^0 and E_r, the $\overline{N_i t}$-product reaches a value of $7.14 \times 10^{12}\,\mathrm{sm}^{-3}$ (RMSE $= 0.033$) for fig. 5.3.6a, where the radial field is as high as $3.48 \times 10^5\,\mathrm{V/m}$ and $N_i^0 = 3.09 \times 10^{17}\,\mathrm{m}^{-3}$. For fig. 5.3.6b, $\overline{N_i t} = 1.23 \times 10^{13}\,\mathrm{sm}^{-3}$ (RMSE $= 0.10$) with $E_r = 9.09 \times 10^5\,\mathrm{V/m}$ and $N_i^0 = 1.37 \times 10^{18}\,\mathrm{m}^{-3}$. The high losses can be understood as consequence of the joint regions of ion generation and particle charging that create very high electrical fields.

Analogously, an analysis of a completely different device by Wiedensohler et al. [142] was performed. Here, a unipolar charger based on two opposing radioactive α-sources was used to produce ions which are drawn into the charging zone by an AC electric field. An extra sheath air flow is used to decrease the losses. Minimal particle losses are claimed, and a very good agreement between experimental and calculated data is obtained when the ion concentration was varied to match the experimental points, obtaining $\overline{N_i t} = 5.01 \times 10^{12}\,\mathrm{sm^{-3}}$.

Using our first approach, the estimated $\overline{N_i t}$ for their data is $1.34 \times 10^{11}\,\mathrm{sm^{-3}}$, with a RMSE of 0.096, with quite a good agreement. When losses are considered, the value of $\overline{N_i t}$ is $5.19 \times 10^{12}\,\mathrm{sm^{-3}}$ (with a lower RMSE of 0.037 and a $N_i^0 = 1.19 \times 10^{14}\,\mathrm{m^{-3}}$), which is close to that obtained by the authors. Moreover, by this method an assessment of the electrostatic losses due to the radial field is obtained. The value found $E_r = 9.95 \times 10^2\,\mathrm{V/m}$, which is much lower than the values found for the devices based on a corona discharge. This supports the claim of the authors that this charger has a low amount of electrostatic losses.

Therefore, it has been proven that the model can be used to obtain data which are difficult to acquire experimentally, such as the extrinsic charging efficiency of ultrafine particles or the initial ion concentration. It also gives an estimation of the electrical losses in the device through the radial field for any device characteristics or geometries, showing good agreement with experimental results.

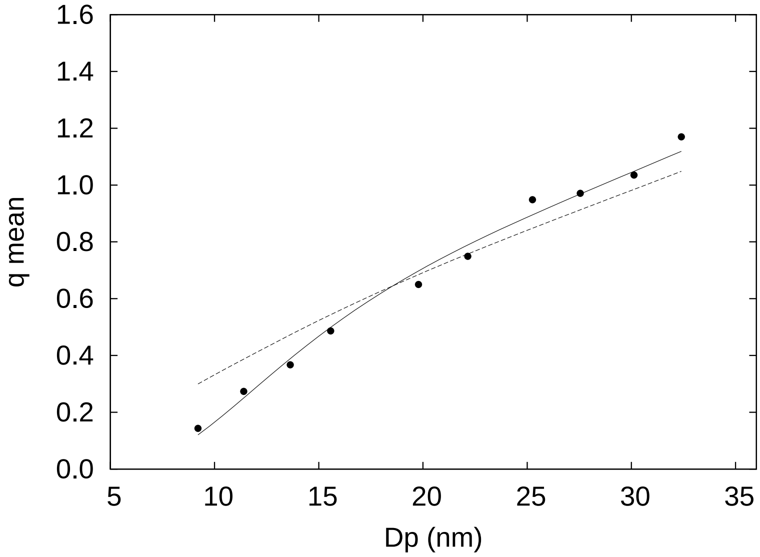

(a)

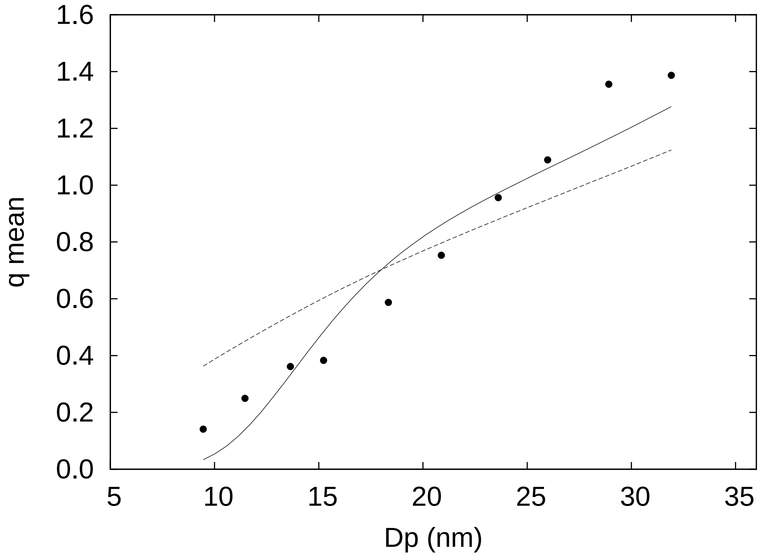

(b)

Figure 5.3.6: The mean charge as function of particle diameter for the corona unipolar charger of Alguacil and Alonso [3] at operating voltages of a) 3 kV and b) 3.6 kV. The dots are the experimental results, fitting from birth-and-death eqs. (5.1.1) leads to the dotted line, the solid line is obtained with the extended model (5.3.12).

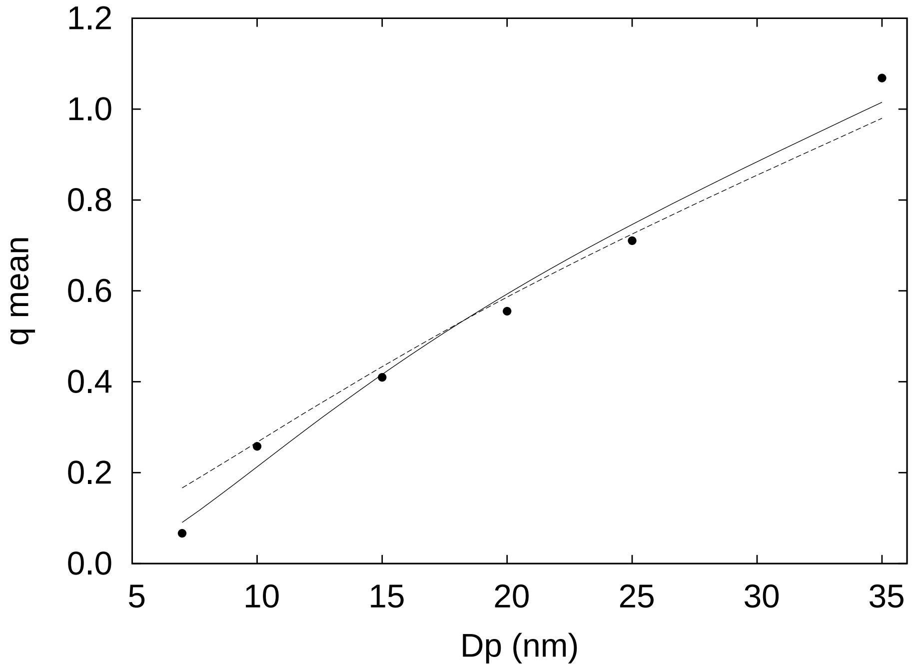

Figure 5.3.7: The size-dependent mean charge for the corona unipolar charger of Wiedensohler et al. [142] at an operating AC voltage of 190 V. The fitting from birth-and-death eqs. (5.1.1) is shown as dotted line, the solid line is obtained with the extended model (5.3.12).

Part II

SIZE RETRIEVAL FROM ELECTRICAL MOBILITY MEASUREMENTS

6

INVERSION TECHNIQUE FROM ELECTRICAL MOBILITY MEASUREMENTS

Knowledge of the PSD is a fundamental requisite to characterize an aerosol population. The interest in an accurate characterization has grown particularly in the submicrometer and nano size range. Differential mobility analysis is the most common principle to measure submicron aerosol size distributions. Some reasons for the increasing interest in electrical mobility-based sizing are:

- It is a discrete method: particles are counted and sized individually.
- It can be made in real time: the measurement and analysis of results takes between few seconds and minutes.
- It is capable of characterize a wide range of sample sizes, between 1 nm and 1 μm.
- Is a method independent of the composition or properties of the particles.
- Has a high resolution, around ±10% of particle size or better at higher flow ratios, and a low uncertainty in measurements (±3.5%).
- It does not change the particles by coagulation or by forces which can break agglomerates, the particles remain gas borne.
- In the sub-micrometer range, gravitation and inertia are negligible. Therefore the velocity of a particle is independent of its mass and depends only on the charge of the particle and its size.

Several studies have been done in order to achieve the maximum precision, but there are difficulties due to the ill-posed nature of the problem, since the PSD cannot be directly measured and must be inferred from related mobility measurements by means of inversion techniques.

A number of methods have been developed and tested to achieve the best approach to the solution, such as the iterative method [4, 49, 74], linear data inversion techniques [37], least squares solution [134] or regularization methods [39, 122].

In this work, two main methods to reconstruct the size distribution are implemented in a software developed in VisualC++, where the mobility measurements can be introduced from real measurements or simulated. It takes into account all the characteristics of a PSD, such as the multiple charging of particles, diffusion and penetration of particles through the tubes and the probability of particles to be adequately selected for measurement. It is studied in depth which factors may improve the quality of results.

A review of the inversion methods is outlined and the approach to the problem in discussed theoretically in the following sections.

6.1 THE MOBILITY MEASUREMENT THEORY

A model describing the relationship between the observations $M \in \mathbb{R}^m$ and the parameters of interest $N \in \mathbb{R}^n$ is represented as:

$$M = \mathcal{K}(N), \tag{6.1.1}$$

where $\mathcal{K}(N) : \mathbb{R}^n \to \mathbb{R}^m$ is a known mathematical model to relate both quantities. When the problem is to calculate M from eq. (6.1.1), it is well-posed, in the sense that the solution is unique and small errors from M are not propagated. But in some cases the problem is the opposite: based in data M from observations, an estimation of the parameters N is sought. The real measurements are to some extent corrupted with noise and error (like the shape effect in case of non-spherical particles, systematical errors and everything else we could not measure) $\epsilon \in \mathbb{R}^m$, and previous expression must be corrected:

$$M = \mathcal{K}(N) + \epsilon. \tag{6.1.2}$$

When $\mathcal{K}(N)$ is linear respect to N, can be expressed matritially as $\mathcal{K}N$, with $\mathcal{K} \in \mathbb{R}^{m\times n}$.

The theory of Knutson and Whitby [69, 70] is based on integration of the particle trajectory equation inside the DMA. Through mobility analysis, the particle size is represented by the size of a sphere with the same mobility as the particle (eq. (1.3.4)), naming this equivalent diameter as *mobility diameter*, D_{Zp}.

When measured by an electrical system device, the particle size and the mobility distributions are related by a Fredholm-type integral equation:

$$M(D_{Zp}) = \int_{D_{\text{p min}}}^{D_{\text{p max}}} \mathcal{K}_q(D_p, D_{Zp}) N(D_p) \mathrm{d}D_P + \epsilon(D_{Zp}), \tag{6.1.3}$$

where D_p indicates the inputted diameters from the PSD and D_{Zp} the measured mobility diameters.

One of the main drawbacks of this technique is that, due to the proportionality between number of charges and diameter, different particle sizes with multiple charges can have the same mobility as smaller singly charged particles.

The measured number concentration M, or instrument response, gives the number of particles within each of the mobility intervals m. It depends on the concentration of particles within the size interval N and on the non-negative kernel function $\mathcal{K}$ of the instrument that maps the measured data to the size distribution for each diameter and charge q.

In a matrix form analog to eq. (6.1.2), relationship (6.1.3) can be expressed as:

$$M_m \approx \mathcal{K}^q_{mn} \cdot N_n + \epsilon_m. \tag{6.1.4}$$

The equation is approximate due to the error not only in the data, but also in the approach of the integral (6.1.3) to a set of discrete linear equations. The indexes m

and n are the number of discrete measurements and output channels respectively, that is, the number of bins in which is divided each distribution.

The feasibility of an estimate for the parameters from the noise-corrupted data is called the *inverse problem*, and it is *ill-posed* in the sense that a stable solution may not exist.

In most systems, the number of intervals m and n are chosen equal, so that the control matrix is generally squared. However, owing to the presence of multiply charged particles, the relationship between electrical mobility and particle size is not reciprocal (small single charged particles have the same mobility as larger multiple charged ones). Also due to the experimental error, $\mathcal{K}_{mn}$ becomes a singular matrix. Mathematically, an inversion could lead to negative values, which has no physical meaning for the PSD.

In general, the rank of the control matrix determines the reliability of finding a solution. For determined systems ($m = n$), there may be a unique solution; if the system is under-determined ($m < n$), it has many possible solutions, whereas if $m > n$ is an overdetermined system and there is no exact solution [122, 134].

One of the goals of this work is to develop an inversion method with an independently chosen number of measurement and output channels. In the case of an ill-posed inverse problem, further information about the solution must be incorporated in order to stabilize the problem and obtain an adequate solution for any case.

6.2 DATA INVERSION TECHNIQUES

In the discretisation process from eq. (6.1.3) to eq. (6.1.4), information about each continuous function is unavoidably lost. Added to singularity of the control matrix $\mathcal{K}^q_{mn}$ and the uncertainties in measurement and noise ϵ, leads to the non uniqueness of the solution for the size distribution N_n from the set of data M_m. The ill-posedness of the problem can be rectified replacing it by an approximate well-posed problem whose solution can be assumed to be close to the actual size distribution function. However, there are as many solutions as possible replacements for the problem, some of them throwing inaccurate results.

Different approaches have been proposed and used in solving the inverse problem. Each approach has its advantages and disadvantages, and may yield accurate results in certain measurement conditions. The main methodology is based on deterministic methods, such as the Least Squares (LS), Tikhonov regularization or iterative methods [4, 11, 24, 25, 30, 37, 100, 108, 122, 130], but more recently, statistical techniques have been improved [28, 134]. In this work, only deterministic methods are applied.

The simplest and more direct way to solve eq. (6.1.4) is to reduce the number of possible solutions applying the LS method, which minimizes the norm of the residual:

$$N_{\mathrm{LS}} = \arg\min \|\mathcal{K}N_{\mathrm{inv}} - M\| \,. \tag{6.2.1}$$

The main difficulty in these problems is that when the control matrix is strongly ill-conditioned, small errors in the data can be extremely magnified in the solution, even allowing negative values for the particle size distribution sought. Therefore, ill-posed problems need to be somehow regularized.

6.2.1 *Non Negative Least Squares Method*

A way to avoid these negative values is by means of the Non-Negative Least Squares (NNLS) algorithm. It was first developed by Lawson and Hanson [78] and it is a reformulation of the least squares solution but adding conditions in such a way that forces the solution to have all terms positive, that is:

$$N_{\mathrm{NNLS}} = \arg\min \|\mathcal{K}N_{\mathrm{inv}} - M\| \;;\; N_{\mathrm{NNLS}} \geq 0. \tag{6.2.2}$$

These conditions would form the additional information for the problem. A dual vector of the solution is constructed:

$$w = \mathcal{K}^T \left(M - \mathcal{K}N\right), \tag{6.2.3}$$

that returns $w_n \leq 0$ when $N_{\mathrm{NNLS}} = 0$ and $w_n \cong 0$ when $N_{\mathrm{NNLS}} > 0$. The indexes of the matrix are saved into two vectors, initially $P = \{\varnothing\}$ and $Z = \{1, 2, \ldots, n\}$. Variables indexed in the set Z are held at value zero, while variables indexed in the set P are free to take values different from zero. When the previous elements of the matrices fulfill several constraints of positivity (mainly that the sought vector $N_{\mathrm{NNLS}} \geq 0$), the corresponding index from Z will be moved to P and the dual vector w recalculated. A solution will be reached when vector Z is empty or when all values from w are negative.

Since it executes a large number of iterations for each index of the matrix, this method can be very slow, especially when n is large. The total number of iterations cannot be known in advance, but Lawson and Hanson proved that it is finite. Moreover, is only valid for systems where $m \geq n$, excluding the under-determined problems.

Because the solution is slowly improved, a prompt termination would lead to an acceptable solution, but not the optimal. The biggest drawback of this method is the convergence; there is no single factorization, then the results can converge to a different local minimum. For this reason the initialization of the algorithm gains importance.

6.2.2 *Standard Tikhonov Regularization*

The Tikhonov regularization technique [125], also known as ridge regression, is widely used to solve ill-posed problems encountered in signal processing, such as noise reduction, image restoration or data inversion. The basic idea of the method is to replace eq. (6.2.1) by the minimization problem:

$$N_\lambda = \underset{N \in \mathbb{R}^n}{\arg\min} \left\{ \|\mathcal{K}N - M\|^2 + \lambda \|N\|^2 \right\}, \tag{6.2.4}$$

where λ is a positive constant called the *regularization parameter* which determines the balance between the fit and smoothness of the distribution. It has to be chosen such that N_λ becomes as close as possible to the noisy-free solution. There are two main strategies to calculate the regularization parameter, called *a priori* if the parameter is estimated before doing numerical computations, or *a posteriori*, when it comes from the initial response M and the results (e.g.. N_λ) [11]. This last strategy covers the Discrepancy Principle of Morozov [93], the L-Curve (LC) regularization of Hansen and O'Leary [39] or the Generalized Cross-Validation (GCV) of Golub et al. [34], among others (a complete description of Tikhonov parameter choice rules can be found in [38]). Only the two last will be used in the following, and since properties of parameter choice rules are well documented in a number of papers [17, 39, 63, 84, 108, 114, 123, 135], we will give only a brief explanation about their operation.

The main advantage of using the Tikhonov regularization is the diagnosis of the problem that can be made by the Singular Value Decomposition (SVD), which exposes the geometric structure of the original matrix. It achieves a pseudoinverse of the kernel matrix, $\mathcal{K}^+$, by disaggregating the kernel matrix into two orthogonal matrices:

$$U = (u_1, \ldots, u_m) \subset \mathbb{R}^{\mathrm{m}\times\mathrm{m}} \text{ and } W = (w_1, \ldots, w_n) \subset \mathbb{R}^{\mathrm{n}\times\mathrm{n}}, \tag{6.2.5}$$

multiplied by a diagonal matrix formed by non-negative elements, called the *singular values* of the control matrix:

$$\Sigma = \operatorname{diag}(\sigma_1, \ldots, \sigma_s) \subset \mathbb{R}^{\mathrm{m}\times\mathrm{n}}. \tag{6.2.6}$$

For convenience, they are usually ordered decreasingly, $\sigma_1 \geq \ldots \geq \sigma_r \geq \sigma_{r+1} = \ldots = \sigma_s = 0$, where $s = \min\{m, n\}$. Therefore, the control matrix with $\operatorname{rank}(\mathcal{K}) = r$ can be discomposed:

$$\mathcal{K} = U\Sigma W^T = \sum_{k=1}^{s} u_k \sigma_k w_k^T. \tag{6.2.7}$$

The pseudoinverse $\mathcal{K}^+$ of the control matrix is written in SVD form as:

$$\mathcal{K}^+ = W\Sigma^+U^T = \sum_{k=1}^{s} \frac{w_k u_k^T}{\sigma_k}, \tag{6.2.8}$$

which leads to the simple inversion $\mathcal{K}^{-1}$ when $\mathcal{K}$ is squared and full ranked. The singular vectors are the square roots of the eigenvalues of the matrices $\mathcal{K}^+\mathcal{K}$ and $\mathcal{K}\mathcal{K}^+$.

The criteria for a good inverse of the control matrix can rarely be met in an ill-conditioned problem. Errors propagate easily when inverting, leading to highly oscillatory and multiple solutions. The SVD guarantees that elements are mutually influenced in such a way that errors for given u_k would affect just the given w_k, increasing instability with larger index k [39, 145]. The degree of ill-conditioning of the control matrix is identified by the Condition Number (CN), the ratio of the largest singular value to the smallest, other than zero. It can be interpreted as a description of the sensitivity of solutions to inaccuracies in the data: the larger the condition number, the greater the ill-conditioning, being infinite for singular matrices. Its logarithm is an estimate of how many digits are lost in solving a linear system with that matrix.

For overdetermined problems, the condition number is reduced orders of magnitude and therefore provides a better approach to the solution. For the remaining cases, a way to dampen the oscillations is to set a lower limit for the singular values, using them as smoother [129]. This limit must be carefully chosen since a too large one could lead to a loss of information of the process. Thus the solution becomes less sensitive to observation errors, or even unique, by the regularization parameter λ. Expressing eq. (6.2.4) in vectorized form, the particle size distribution:

$$N_\lambda = \left(\mathcal{K}^+\mathcal{K} + \lambda\mathbb{I}\right)^{-1}\mathcal{K}^+ M = \sum_{k=1}^{r} \zeta_k \frac{u_k^T M}{\sigma_k} w_k, \tag{6.2.9}$$

where the filter factors ζ_k, known as Wiener weights, have the form:

$$\zeta_k = \frac{\sigma_k^2}{\sigma_k^2 + \lambda}. \tag{6.2.10}$$

The parameter λ weights the optimization process as it varies from 0, leading to unstable solution with drastic oscillations, to ∞, oversmoothing the solution and causing loss of information. There exists a relatively small interval of the regularization parameter that provides reasonable solutions. Normally it is estimated making a compromise between the model fit (the agreement between the input data and the forward solution), the uniqueness and the stability of the solution. This leads to a trade-off in eq. (6.2.4) between two functions for the calculation of the approximate inverse $\mathcal{K}^+$: the residual norm $\|\mathcal{K}N - M\|$, which optimizes the agreement between the data and solution, i.e. the model fit, and the regularized norm of the solution $\|N\|$, which optimizes the smoothness and stability of the solution. This last term has the additional benefit of generating unique solutions from problems with singular matrices or under-determined.

The L-Curve has emerged as a powerful tool for locating the optimal interval. Briefly, it consists on minimizing the previous definition of N_λ (eq (6.2.9)) for each value of λ. It is a parametric plot on a log-log scale between the residual norm $\|\mathcal{K}N - M\|$ and the regularized norm of the solution $\|N\|$, with two distinct parts: for large λ it is nearly vertical and represents over-smoothed solutions, and for small λ is almost horizontal, corresponding to under-smoothed solutions. The corner represents the point where the two errors are balanced, so this value is optimal [39]. Detailed properties of the L-Curve are given in Hagen and Alofs [37], Lloyd et al. [84]. To locate the corner of the L-Curve, the point of maximum curvature is sought as described in Johnston and Gulrajani [63].

Generally, the algorithm will find a value for λ which will recover at least 95% of the particles of the PSD, although in some cases this solution is not always as smooth as expected. Therefore, another regularization method is implemented to compare the results, based on the GCV.

The GCV method determines a reduced solution omitting one data point. A good choice for λ is the one for which the predicted value of the omitted data set is close to the true value. The optimal value is obtained by determining the minimizer of the function:

$$N_{\lambda_{\mathrm{GCV}}} = \frac{\left\| \mathcal{K} N_\lambda - M \right\|^2}{\left[\mathrm{trace} \left(\mathbb{I} - \mathcal{K} \left(\mathcal{K}^+ \mathcal{K} + \lambda \mathbb{I} \right)^{-1} \mathcal{K}^+ \right) \right]^2}, \tag{6.2.11}$$

where trace() is the sum of the diagonal elements [25].

Another way of improvement is customizing the value of the regularization parameter from the calculated one, since as shown in Talukdar and Swihart [122], the optimal value is in general an order of magnitude larger than the calculated by the L-Curve method, although this could have the effect of oversmooth the results.

The SVD main advantages are that the inversion can always be performed, even for singular matrices in under-determined problems, and that this decomposition is almost unique. Solution is indeed never unique because the starting data are obtained from physical measurements subject to an unknown random error, therefore we are trying to solve exactly a system which is originally erroneous. As it will be shown in the following, the selected number of size and mobility intervals plays an important role in the goodness-of-fit of the inversion, given that they affect the rank of the kernel matrix.

6.3 GEOMETRICAL APPROACH TO THE DMA TRANSFER FUNCTION

The DMA only selects charged particles with a given mobility Z_c fixed by the voltage of the device during each of the m intervals. The probability of the particles to leave via the sampling flow is determined by the DMA Transfer Function (Ω) Ω^q_{mn}.

Fig. 6.3.1a shows the ideal Ω, where only particles of selected mobility are allowed to pass through the DMA. However, the realistic model is shown in 6.3.1b. Two phenomena influence the shape of the Ω:

1. The diffusion of particles caused by Brownian motion. Diffusion, on one hand enhances particle losses, on the other reduces the DMA resolution, since particles are spread around the particle trajectories determined by the fluid flow and the electrical field lines.

2. The loss of particles inside the DMA. Particle losses occur especially at the DMA inlet and outlet because of distortions of the electrical and gas flow field. The presence of isolating parts inside the DMA can produce losses too, because they can acquire charges and distort the electrical field. Diffusion also contributes to the loss of particles. pushing them away from the ideal path.

For an ideal case, the transfer function can be fitted by a triangular shape centered at the mean mobility Z_c. Its relative width β_0 is dependent exclusively on the flow rates, the voltage applied to the DMA and its geometry, assumed here cylindrical with R_i and R_o as inner and outer radius of the DMA electrodes and L as the length between the entrance and exit slits:

$$Z_c = \frac{\ln(R_o/R_i)}{4\pi L} \frac{(Q_{\mathrm{sh}} + Q_{ex})}{V}, \tag{6.3.1}$$

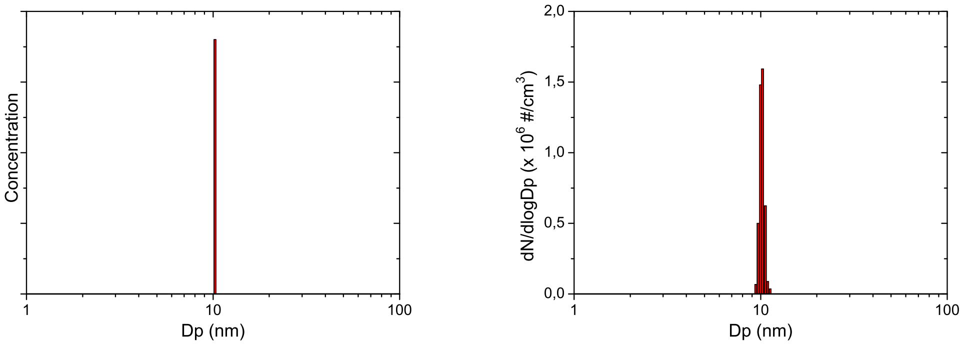

(a) (b)

Figure 6.3.1: Ideal *(a)* and real *(b)* transfer function for a particle diameter of 10 nm.

$$\frac{\Delta Z_c}{Z_c} = \beta_0 = \frac{Q_a + Q_m}{Q_{\mathrm{sh}} + Q_{ex}}. \tag{6.3.2}$$

The voltage applied to the inner electrode of the DMA is denoted as V, and the electric field is assumed uniform, neglecting field distortions at the aerosol entrance and the sampling exit slit. The flow field must be laminar. and for typical operating conditions symmetrical flows are used, implying that $Q_a = Q_m$ and $Q_{\mathrm{sh}} = Q_{ex}$.

The choice of the volume flows and the flow ratio is a compromise between a high resolution $\mathcal{R} = \beta_0^{-1}$ (therefore small β_0) and a high sample volume flow downstream the DMA, enough to avoid most of the losses. In practice. the volume flows depend mostly on instrumentation. For particle detector used in present experiments (TSI-CPC3775 [55]), the sample flow can be either 0.3 or 1.5 lpm, therefore sufficiently resolved number size distributions are reached when the aerosol to sheath flow ratio is kept constant at $\beta_0 = 0.1$.

The measurements of the concentrations in the different mobility bins are acquired by setting voltages that span the operating range of the DMA in use. This voltage can be varied in stepping or scanning mode. In the first case, the voltage is kept constant for each mobility bin and stepped up or down for the following bins. If the classifier operates in this way is called DMPS. Other case is when the voltage is continuously scanned and particles are continuously counted, as is done in the SMPS. In this case, the change of voltage during the particle transit time increases the measurement speed, but can alter the trajectory of the particle, resulting in a difference in the distribution when is measured increasing or decreasing the values of the voltage scan.

To avoid this, the voltage must be kept constant during the transit of the particles through the classifier (DMPS) or fixed at values that have a constant ratio among them, that is, exponentially ramping the voltage following the relationship;

$$V = V_0 e^{\pm t/\tau}, \tag{6.3.3}$$

where τ is the scan time (constant), t is the residence time from which particle is injected and V_0 the voltage applied to the central rod of the DMA.

Fast scan times are useful for measurements in which the aerosol changes during the sample period, but longer scan times provide higher particle size accuracy (and is preferred in low concentration measurements) because avoids the increase in granularity, smearing effects of the CPC response time and buffers the dependence on the flow ratio and the ratio of residence to scan time [27]. At slow scan rates, the scan transfer function can be approximated to the fixed one [41]. Since in principle our measurements are performed at stepping and slow-scanning operations ($\tau = 120\,\mathrm{s}$ and $t = 0.1567\,\mathrm{s}$), it can be approximated to stepping voltage, although it will be seen that the proceeding is equally valid for the scanning method too.

The shape of the TF depends mainly on the voltage applied to the DMA, and consequently, on the particle diameter to be selected, since small particles affected by Brownian diffusion broadens the TF and reduces the peak transmission efficiency, while for larger particles is good approximated by a triangle. But also the flow rates determine the final shape of the TF: for measurement of particles of a given mobility Z_c, the upper and lower bounds are given by $\tilde{Z}(1 \pm \beta_0)$ (being $\tilde{Z} = Z_p/Z_c$ for any given mobility Z_p), and the maximum transmission is located at $1/(1-\delta)$, where $\delta = (Q_s - Q_a)/(Q_s + Q_a)$ shows the unbalance between flows.

Stolzenburg [116] proposed a more realistic model with a bell shaped transfer function. through a semi analytical approach of the Gaussian shape of diffusional TF by means of stochastics (eq. (6.3.4)), but the model is not able to take losses into account.

$$\begin{aligned}\Omega(Z_p, Z_c) \quad = \quad & \frac{\sigma}{\sqrt{2}\beta_0(1-\delta)}\left[\mathcal{E}\left(\frac{\tilde{Z}-(1+\beta_0)}{\sqrt{2}\sigma}\right)+\mathcal{E}\left(\frac{\tilde{Z}-(1-\beta_0)}{\sqrt{2}\sigma}\right)-\right. \\ & \left. -\mathcal{E}\left(\frac{\tilde{Z}-(1+\beta_0\delta)}{\sqrt{2}\sigma}\right)-\mathcal{E}\left(\frac{\tilde{Z}-(1-\beta_0\delta)}{\sqrt{2}\sigma}\right)\right],\end{aligned} \tag{6.3.4}$$

where $\mathcal{E}(x) = \int_0^x erf(u)\mathrm{d}u = x erf(x) + \frac{e^{-x^2}}{\sqrt{\pi}}$, with $erf(x)$ the error function, and σ is the dimensionless broadening of the TF, that depends on a geometry factor of the DMA and on the Peclet number: $\sigma = G_{\mathrm{DMA}}\mathrm{Pe}$.

On the other hand, Stratmann et al. [120] evaluated individual DMA transfer functions experimentally, developing a model which describes the TF by the Full Width at Half Maximum (FWHM), namely ΔZ_c, and the height H of the fitting coextensive triangle. They proved that the triangular shape is a good approximation, since the error introduced is below the experimental uncertainty. In fig. 6.3.2 both representations are compared. It can be seen that, although the different shapes are more evident for small diameters (below 10 nm mainly), the triangular approximation matches the shape for particles large enough to ignore diffusion and loss effects.

For the application of a DMA as particle sizing device it is necessary to know its size resolution, which can be determined by the mentioned Peclet number, a dimensionless ratio of convective to diffusive particle transport inside the DMA [32]:

$$\mathrm{Pe} = \frac{qeV}{k_B T} f, \tag{6.3.5}$$

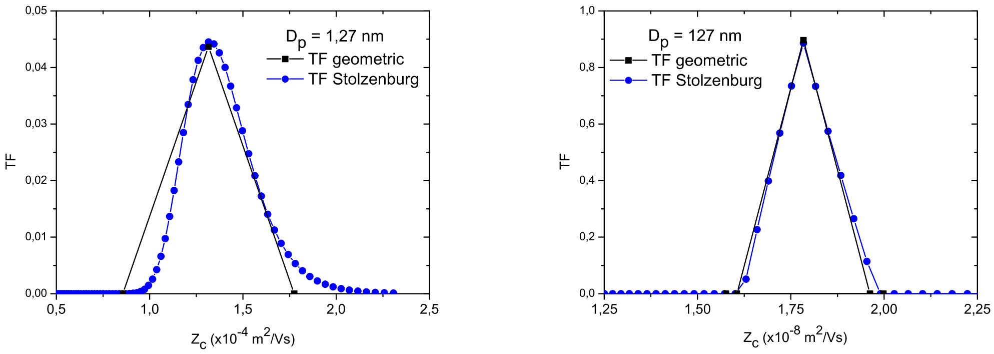

(a)

(b)

Figure 6.3.2: Comparison of the triangular and bell-shaped Stolzenburg transfer functions for small (6.3.2a) and large (6.3.2b) diameters.

where f is a geometry factor for the DMA that considers the non-uniformity of the DMA electric field. For cylindrical DMAs:

$$f = \frac{1 - {}^{R_i}/_{R_o}}{\ln\left({}^{R_o}/_{R_i}\right)}. \tag{6.3.6}$$

An advantage of using the Peclet number is that it allows comparison of various designs for different flow rates, voltages and particle size ranges. Therefore, β_0 depends on Pe no matter the DMA type and dimensions [31, 32]. An analytical expression for the relative FWHM of a triangular TF assuming diffusional broadening, μ, was obtained by Karlsson and Martinsson [65]:

$$\mu = \left(1 + \left(\frac{0.15}{\beta_0}\right)^2 \left(\frac{1}{\mu_0^2} - 1\right)\right)^{-1/2}, \tag{6.3.7}$$

where β_0 is the regular expression of the flow ratios obtained in eq. (6.3.2) and μ_0 is the experimental broadening expression obtained for a Vienna type DMA with a flow rate ratio of 0.15:

$$\mu_0 = 1.69\left(1 - \exp\left(-\left(\frac{\text{Pe}}{105}\right)^{0.33}\right)\right) - 0.69. \tag{6.3.8}$$

The FWHM and height calculated through this equations is well fitted to the experimental measurements, as is shown in fig. 6.3.3 for Nano-DMA (TSI 3085 [53]) data from Hummes et al. [50]. The geometrical TF can be calculated simply knowing the FWHM and the height of each TF, considering the penetration efficiency $P_n(D_p)$:

$$\Delta Z_c = \frac{\beta_0}{\mu} Z_c, \tag{6.3.9}$$

$$H = \mu P_n. \tag{6.3.10}$$

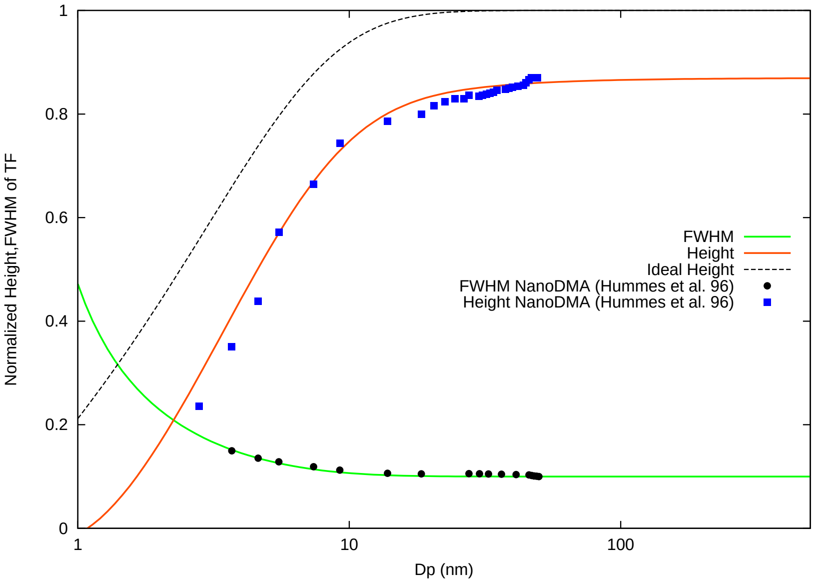

Figure 6.3.3: Fitted height and FWHM of the TF for Nano-DMA (TSI 3085) geometry compared with experimental data from [50].

It should also be noted that the maximum height of the transfer function is ideally 1, meaning that diffusional broadening and particle losses inside the DMA are neglected. But this leads to an under-prediction of particle number concentration in the ultrafine particle size range. For small particles, the transfer function can be strongly influenced by diffusion. The width broadens and the height decrease as particle size is reduced. Experimental data are available for the half-width to midpoint mobility ratio as well as for the height of the transfer function, e.g. for the Nano-DMA. and can be interpolated for any specific particle diameter.

In the work of Hoppel [49], the transfer function of each measurement is fixed by selecting suitable voltage steps so that they do not overlap each other. The method requires negligible contribution of particles beyond the size scope and only singly charged particles in the channels of smallest electrical mobility.

As a first approximation, all detected particles are considered singly charged, and the concentration $N_0(m)$ is divided by the fraction of charge $f_{q=1}(n)$ for each size channel n. This approximation overestimates the real number concentration due to the multiple charged particles appearing in every channel $Z_c(m)$, but in the next step the contribution of doubly charged particles is estimated. The general rule to calculate the contributions is:

$$N_q(m) = N_{q-1}(m) - \Delta N_q(m), \tag{6.3.11}$$

where ΔN_q is the number of particles with q charges in $N_{q-1}(m)$ and is calculated:

$$\Delta N_q(m) = \frac{f_q(n)}{f_{q-1}(n)} N_0 \left(\frac{Z_c(m)}{q} \right). \tag{6.3.12}$$

However, the selected mobilities in eq. (6.3.12) do not necessarily coincide with the preset channels $Z_c(m)$. The solution of Hoppel is to increase exponentially the electrical mobility with a flow ratio following $\beta = \frac{k-1}{k+2}$, where k is constant, obtaining adjoining and non-overlapping intervals.

In the present work, the number of input and output data channels (referring to mobility and size measurements, respectively) is independent each other and can be chosen arbitrarily. The number of intervals is estimated through the number of channels per decade that the instrument is able to measure. This variables are related by means of the expression for the constant distance between diameters for the log-distribution of the PSD, $d = \ln(D_p(i)/D_p(i-1))$:

$$d = \frac{\ln(D_{p\mathrm{Up}}/D_{p\mathrm{Low}})}{\text{num Decades}} = \frac{\ln(D_{p\mathrm{Max}}/D_{p\mathrm{Min}})}{\text{num Intervals}}, \tag{6.3.13}$$

where $D_{p\mathrm{Up}}$, $D_{p\mathrm{Low}}$ are the diameters for the range of the decade, usually a ratio of ten (e.g. $D_{p\mathrm{Up}} = 10\,\mathrm{nm}, D_{p\mathrm{Low}} = 1\,\mathrm{nm}$), and $D_{p\mathrm{Max}}$, $D_{p\mathrm{Min}}$ are the maximum and minimum diameters of the PSD range.

In many equipments, the number of channels per decade for both the input and output data are fixed to a multiple of 4 channels per decade (8, 16, 32, 64, ...), implying that $m = n$. We have chosen to set this number variable, being possible to choose a higher or lower precision for any ratio of diameters for the two, input and output data sets (it has to be remarked that when input data are imported from experiments, the number of channels per decade employed by the measuring device must be adopted). In this way it can be selected the number and resolution of the measurements, obtaining in turn an exact range of diameters or voltages. This implies that the applied voltages can take any desired value, starting and ending in the desired values and not in the closest similar to them. A consequence is that the transfer functions are overlapping, being able to cover more mobilities when the TF is broadened by diffusion. In fig. 6.3.4 a set of simulated geometrical TF is plotted along with the size intervals n for the output result (vertical lines). Although it is calculated for the same number of size and mobility intervals, $m = n$, it can be seen how each of the TF can cover more than one size interval. Modifying the number of intervals m or n, the covered area of the TF will change accordingly.

The estimation of the area of the TF within each size interval is calculated peak-by-peak, taking into account that each part can come from a different contribution of the mobility data intervals. That is, each complete mobility interval m is represented by the lower and upper boundaries of the width of the TF, $Z_l(q,m)$ and $Z_u(q,m)$ respectively. Each of these mobility sections is divided by the size intervals n, characterized by its lower and upper boundaries, $Z_l^*(q,n)$ and $Z_u^*(q,n)$. The area that falls into each size interval is then calculated geometrically, assuming the triangular shape of the TF and estimating the area of the portion of TF within the size interval.

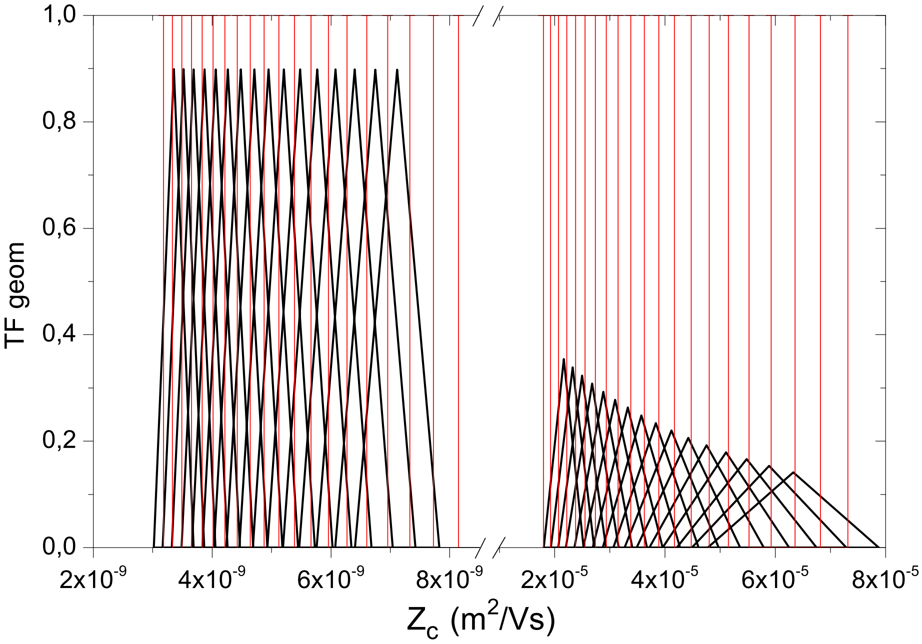

Figure 6.3.4: Transfer function for singly charged particles as calculated in this work. Mobility intervals m, represented by the central mobility of each triangular TF, and size intervals, n, by the vertical lines. Both intervals can be independently chosen, obtaining a different coverage of the TF area and therefore different precision in the inversion process.

Although in Appendix B all the final values are listed, a detailed example of the shadowed area estimation that lies within a section is represented in fig. 6.3.5 for $q = 1$. Mobilities are compared in each interval, in this case: $Z_u(m) > Z_u^*(n) > Z_c(m) > Z_l(m) \geq Z_l^*(n)$. The corresponding area of the TF is calculated assuming its triangular shape among the total area:

$$A_\Omega(m,n) = H(m)\Delta Z_c(m) - \frac{1}{2}ab, \tag{6.3.14}$$

where $a = Z_u(m) - Z_u^*(n)$. The unknown height b, by triangular similarities:

$$b = \frac{H(m)}{\Delta Z_c(m)}a. \tag{6.3.15}$$

Substituting in eq. (6.3.14), the TF is obtained depending only on known mobilities:

$$A_\Omega(m,n) = \frac{H(m)}{2 \cdot \Delta Z_c(m)} \left[2\Delta Z_c^2(m) - \left(Z_u(m) - Z_u^*(n)\right)^2\right]. \tag{6.3.16}$$

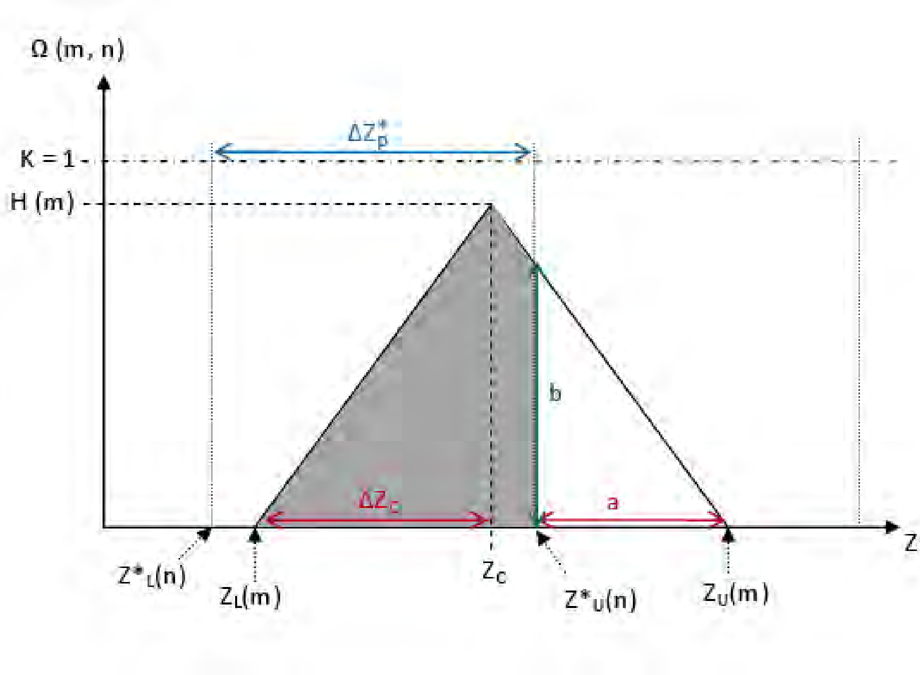

Figure 6.3.5: Example of the area estimation of the TF into a size interval.

In the case of the SMPS, it has to be taken into account the broadening of the range of mobilities classified in a counting interval, in contrast with the obtained with a fixed-voltage DMA. This has been done fitting the experimental mobility shift obtained for measurements performed with a Nano-DMA by Dubey and Dhaniyala [27] (fig. 6.3.6), where the shift depends on the ratio between residence and scanning times. In their work, they calculate the area of the triangular scanning TF on a time scale, obtaining:

$$A_\Omega(t) = \frac{1}{2}\Delta t H = \tau\beta_0 k(t), \tag{6.3.17}$$

where $k = 1 + k_1 {}^t/_\tau + k_2({}^t/_\tau)^2$ is a experimentally deduced function whose constants k_1, k_2 depend on the flow ratio. A change of variable is performed in order to express the area based on mobilities. Basically, the triangular area is $A_\Omega(Z_p) = \Delta Z_p H/2$, where the height is the same for the temporal and mobility based TF. Then, from eq. (6.3.17), $H = 2A_\Omega(t)/\Delta t$ which combined with eq. (6.3.3) results:

$$A_\Omega(Z_p) = \frac{A_\Omega(t)\Delta Z_p}{\tau \ln(Z_u/Z_l)}. \tag{6.3.18}$$

The importance of the TF estimation lies in the fact that is crucial for the control matrix calculation. The system for particle size characterization depends on the DMA through the TF, but also on the charge conditioner through the fraction of charge $f_c(q, D_p)$, on the particle counter through the penetration efficiency across the de-

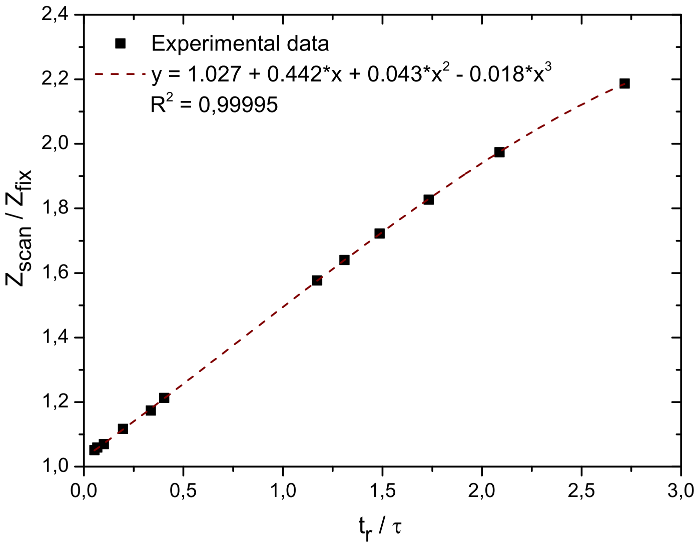

Figure 6.3.6: Quadratic fit of the experimental mobility shift from [27] for a Nano-DMA, in function of the ratio of times of the particles fly-through and the scanning process.

vice $P_n(D_p)$, and on the flow ratio between input and output of the system. Q_a/Q_m. Therefore, back to eq. (6.1.3), the log-distribution results:

$$\frac{\mathrm{d}M(D_{Zp})}{\mathrm{d}\ln D_{Zp}} = \int\limits_{D_{p\,\mathrm{min}}}^{D_{p\,\mathrm{max}}} \left[\frac{Q_a}{Q_m} f_c(q, D_p) P_n(D_p) \Omega(q, Z_p, Z_c)\right] \frac{\mathrm{d}N(D_p)}{\mathrm{d}\ln D_p} \mathrm{d}\ln D_P + \epsilon(D_{Zp}). \tag{6.3.19}$$

The calculation of the geometrical TF shows that $\Omega(q, Z_p, Z_c) = q\Omega(Z_p, Z_c)$, as occurs with mobilities, and since the variation of f_c, P_n and $N(D_p)$ is small across the width of the size intervals of integration, the above equation can be approximated by:

$$\begin{aligned}\frac{\mathrm{d}M(D_{Zp})}{\mathrm{d}\ln D_{Zp}} &= \frac{Q_a}{Q_m}\left(\sum_q q f_c(q, D_p)\right) P_n(D_p) \frac{\mathrm{d}N(D_p)}{\mathrm{d}\ln D_p} \cdot \\ &\quad \cdot \int\limits_{D_{p\,\mathrm{min}}}^{D_{p\,\mathrm{max}}} \Omega(Z_p, Z_c) \mathrm{d}\ln D_p + \epsilon(D_{Zp}).\end{aligned} \tag{6.3.20}$$

A change of integration variable simplifies the calculation of the TF area:

$$\int\limits_{Z_{p\,\mathrm{min}}}^{Z_{p\,\mathrm{max}}} \Omega(Z_p, Z_c) \left|\frac{\mathrm{d}\ln D_P}{\mathrm{d}Z_P}\right| \mathrm{d}Z_P = A_\Omega(m, n). \tag{6.3.21}$$

With the change of variable of integration, the integral refers to the area of the TF within the given size interval.

Hence, the required characteristic for the inversion process is the area of the TF corresponding to each mobility interval m that lies within each size interval n. In fig. (6.3.7) it can be seen that the geometric method presented here gives the same results for the total area than that calculating the bell-shaped TF with the Stolzenburg's equation (6.3.4), with a relative error below 1% for particles over 2 nm for both ideal (with no losses) and real types.

Also the area of TF resultant from scanning voltages were tested for the ideal and real cases. The difference with the fixed voltage area, which go below 2% from 15 nm in the case with losses, are probably due to the dependance on the scan time of the temporal area $A_\Omega(t)$ and the mobility shift in the conversion to $A_\Omega(Z_p)$.

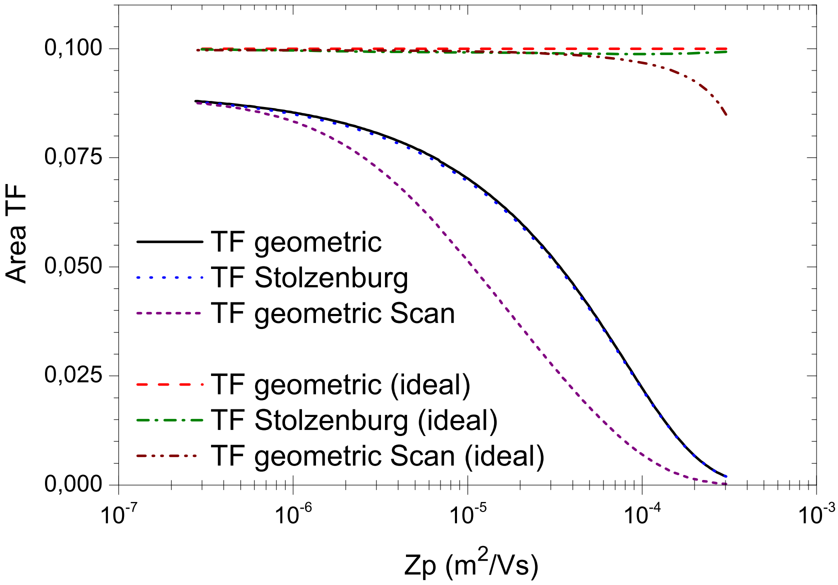

Figure 6.3.7: Comparison of the areas of the TF calculated with the eq. (6.3.4) and the triangular shape, for scanning or fixed voltage methods. Both methods cover practically the same area with a difference of about 1%.

It has to be stressed that the expression for the mobility used along the present work has been the semi-theoretical one derived by Alonso et al. [8], Z_d, that accounts for diffusion in classification of particles with very high mobility in a quite long DMA operated at relatively low flow rates:

$$Z_d = Z_{nd}\left[1-\left(2.49\ln^{-0.66}\left({}^{R_o}/{}_{R_i}\right)\right)\frac{\ln\left({}^{R_o}/{}_{R_i}\right)\mathcal{D}}{V_{nd}}\right], \tag{6.3.22}$$

where sub-index nd denotes the classical non-diffusive expression (eq. (1.3.4) for Z_{nd} and (6.3.1) for V_{nd}) and $\mathcal{D}$ is the diffusion coefficient. Although in most cases the difference between the non-diffusive and diffusive terms is negligible, we have decided to introduce it here for a more accurate inversion in situations where is not (ultrafine particle range mainly).

6.4 PARTICLE SIZE AND CHARGE DISTRIBUTION RETRIEVAL FROM ANY CHARGING METHOD

The calculation of the aerosol size distribution requires an accurate knowledge of the charge level and charge distribution of the incoming aerosol. Although bipolar radioactive chargers are widely used due to their well defined charge distribution, unipolar diffusion chargers are nowadays at the focus of interest, since they offer some advantages: due to the absence of ion recombination, unipolar ionization results in higher ion concentrations, and are exempt from expensive safety precautions and severe legal restrictions caused by the use the radioactive sources. Some recent unipolar devices are based on X-ray [67], UV photoionization [48], corona discharge [103, 133, 128, 80, 23, 57, 26] and others [75, 76] (see sec. 2.2).

However, inversion methods have been applied seldomly to unipolar chargers. Reasons might be that these are relatively recent devices, often still in an experimental phase and therefore without a homogeneous expression for the charge distribution, such as there is for the bipolar radioactive charging [143]. Furthermore, in unipolar chargers the ratio of multiply charged particles is higher than in bipolar chargers, complicating the multiple charge correction in the deconvolution.

Once the charge distribution is known, it can be fitted by a reproducible expression [64]. It is important to remember that each charger has its own fitting and coefficients vary from device to device, but once they are estimated, they can be implemented in the inversion algorithm for its usage.

Charge distribution from the previously developed unipolar corona charger was mathematically fitted to a lognormal distribution (eq. (6.4.1)), where the fitting parameters are the constant C, probability of acquiring n elementary charges, the geometric mean diameter $\bar{D}_{pg}$, the geometric standard deviation of the charge distribution σ_g and $f_0(D_p)$ denotes an offset in case there is some. Values of these coefficients are listed in table 6.4.1, along with the goodness of the fitting, indicated by the regression coefficient R^2.

$$f_c(D_p) = f_0(D_p) + \frac{C}{\sqrt{2\pi}\ln\sigma_g D_p}\exp\left(-\frac{\ln(D_p/\bar{D}_{pg})^2}{2\ln\sigma_g^2}\right). \tag{6.4.1}$$

The charge distribution was only tested up to 60 nm, hence bigger diameters will not be examined for the unipolar charger in the inversion process, since additional charging levels are unpredicted.

6.4.1 *Multiple charge correction*

One of the added difficulties for an accurate retrieval of the PSD is the multiple charging of particles. It causes a proportion of the particles measured under the same applied voltage to be corresponding to particles of different diameters, because they have identical mobility. This effect is more likely in bigger particle sizes, since they can acquire more charges. The most direct technique to separate the effect of singly charged particles from the rest is based in algorithms that remove recursively the contribution of particles with more than one charge.

Table 6.4.1: Coefficients for the lognormal fitting of the charge fractions of the corona charger shown in fig. 4.2.7.

$D_{\text{gap}}(mm)$	$f_c(q)$	$f_0(D_p)$	$\bar{D}_{pg}$	σ_g	C	R^2
3	1	-0.02065	20.47251	1.6373	13.4406	0.98987
	2	0.00192	33.63013	1.3967	12.86995	0.96662
	3	0.00131	47.07348	1.2406	10.62972	0.99802
	4	0.00125	69.94343	1.2823	16.75291	0.99868
	5	6.69×10^{-5}	102.50421	1.3247	25.18727	0.99867
10	1	-0.02375	66.93677	2.0618	48.98775	0.96978
	2	-2.44×10^{-4}	84.9966	1.5394	26.87955	0.9999
	3	-7.78×10^{-5}	134.0929	1.5506	23.01109	0.99934

Hoppel [49] developed a method whose basic idea is that eq. (6.1.4) for the response can be disaggregated depending on the charge contribution:

$$M_m^q \approx \sum_{n=1}^{n_{\text{tot}}} \left(\left(\mathcal{K}_{mn}^1 N_n^1 + \epsilon_m^1 \right) + \sum_{q>1}^{q_{\text{tot}}} \left(\mathcal{K}_{mn}^q N_n^q + \epsilon_m^q \right) \right) \approx M_m^1 + M_m^{q>1}, \tag{6.4.2}$$

and therefore retrieval of the singly charged PSD would be to invert $M_m^1 = M_m^q - M_m^{q>1}$ following some steps. First, estimation of M_m^1 assuming only singly charged particles present, leading to a first approximation of N_n^1 that will be used to calculate the contribution of the penultimate channel to the mobility measurements, $M_{m-1}^{q>1}$. The singly-charged distribution is re-calculated considering:

$$N_n^1 \approx \left[\mathcal{K}_{mn}^1 \right]^+ \left(M_m^q - M_{m-1}^{q>1} \right), \tag{6.4.3}$$

and this process is repeated for every mobility channel, m, to successively correct the presence of different particle sizes.

This algorithm was recently updated by He and Dhaniyala [41] by adding an intermediate step after the first approximation that increases the accuracy when no impactor is placed to cut out bigger particle sizes. They fit the bigger diameters of the zeroth order singly charged PSD by a Gumbel distribution function, and the resultant fit is the one used to correct the multiply charged contribution.

6.4.2 *Retrieval of the charge distribution by the TDMA setup*

The Tandem Differential Mobility Analysis (TDMA) [83, 105] is a popular technique to characterize particle changes (in shape, size, composition, amount, charge,...) or calibrate devices. The arrangement, already shown in fig. 2.4.1, consists on two identical DMAs in series. In between, a particle conditioner is placed. A fixed voltage is applied on the first DMA to classify particles of a certain size, while on the second DMA the voltage is varied and the output particle concentration measured with a particle counter. The response after the first DMA can be expressed as in eq. (6.3.20), while the second output has to take into account the previously selected distribution:

$$\begin{aligned}\frac{\mathrm{d}M_2(D_{Zp})}{\mathrm{d}\ln D_{Zp}} &= \frac{Q_{a1}}{Q_{m1}}\frac{Q_{a2}}{Q_{m2}}\left(\sum_q q f_{c2}(q,D_p)\right)P_{n2}(D_p)\frac{\mathrm{d}N_2(D_p)}{\mathrm{d}\ln D_p}\,\cdot \\ &\quad\cdot\int\limits_{D_{p\,\mathrm{min}}}^{D_{p\,\mathrm{max}}}\Omega_1(Z_p,Z_{c1})\Omega_2(Z_p,Z_{c2})\mathrm{d}\ln D_P+\epsilon(D_{Zp}). \qquad (6.4.4)\end{aligned}$$

Depending on the aerosol conditioner, the PSD can change its size due to agglomeration or coagulation (studies on particle growth are performed in [36, 105]). In our case, the aforementioned corona charger is used between the two DMAs. The TDMA is used in this experiment to estimate the charge distribution and efficiencies of the test charger as is shown in section 2.4: a fixed voltage is applied on the first DMA to classify particles of a certain size using a known charger, usually a radioactive one. The resulting distribution is neutralized with the same type of charger plus an electrostatic precipitator to remove remaining charged particles. The neutral distribution is then recharged with the test charger and measured with the second DMA, and from comparations of the concentrations obtained at different points of the setup, the charging properties of the charger can be estimated.

Thus, the mean charge can be calculated theoretically as shown in section 5.3 or experimentally through several steps as shown in section 4.2.3. However, this last is subjected to the uncertainties of the concentration measurements.

Another way to calculate the mean charge is proposed, that is through the inversion process. In eq. (6.3.19), inversion was employed to retrieve the size distribution input in the first DMA. Once is known, we can use it to calculate the charge distribution and the mean charge per particle of the second charger by inverting the response from the second DMA.

It is known there is a systematic error of up to a 2% between the mean mobility diameters measured by DMA-1 and DMA-2 [105], which can be partially corrected by adjusting the voltages of each DMA [5], however, there is always an unavoidable shift of about 1% (fig. 4.2.6) which is important to consider for a proper interpretation of the inversion results. Added to the uncertainties characteristic from the mobility measurement, the TDMA technique has to take into account variations of the concentration between DMAs. Some losses are present due to diffusion through the tubes and electrostatic effects produced by the charging-neutralization process (studies on coagulation were performed, throwing less than 0.5% in any case). Consequently, the concentration of particles that enters the DMA-2 will differ from the one entering the first DMA by:

$$\frac{\mathrm{d}N_2(D_p)}{\mathrm{d}\ln D_p}=P_{n0}(D_p)\frac{\mathrm{d}N_1(D_p)}{\mathrm{d}\ln D_p}, \qquad (6.4.5)$$

where P_{n0} represents the losses along the path, determined experimentally according to fittings of experimental data for 3 and 10 mm gap distances (fig. 6.4.1).

Since the tubing to the particle counter is the same for DMA-1 and DMA-2, $P_{n1} = P_{n2}$ (namely P_n), and considering that the mean charge can be expressed as $\bar{q}_2(D_p) = \sum_q q f_{c2}(q, D_p)$, eq. (6.4.4) results:

$$\begin{aligned} \frac{\mathrm{d}M_2(D_{Zp})}{\mathrm{d}\ln D_{Zp}} &= \frac{Q_{a1}}{Q_{m1}}\frac{Q_{a2}}{Q_{m2}}\bar{q}_2(D_p)P_n(D_p)P_{n0}(D_p)\frac{\mathrm{d}N_1(D_p)}{\mathrm{d}\ln D_p}\cdot \\ &\cdot \int_{D_{p\,\mathrm{min}}}^{D_{p\,\mathrm{max}}} \Omega_1(Z_p, Z_{c1})\Omega_2(Z_p, Z_{c2})\mathrm{d}D_P + \epsilon(D_{Zp}), \end{aligned} \qquad (6.4.6)$$

and analogous to the inversion performed to the PSD, the mean charge can be deconvoluted:

$$M_{m2} \approx \widetilde{\mathcal{K}}_{mn} \cdot \bar{q}_n + \epsilon_m, \qquad (6.4.7)$$

where $\widetilde{K}$ is the new definition of the kernel matrix according to eq. (6.4.6).

A similar proceeding has been used in [81, 118] to deconvolute the TF of the particle sizing devices, which could be also applied here. Since so far we have not found any reference about the charge distribution deconvolution, and we think it is an important issue for characterization of new particle chargers, this method is chosen among others.

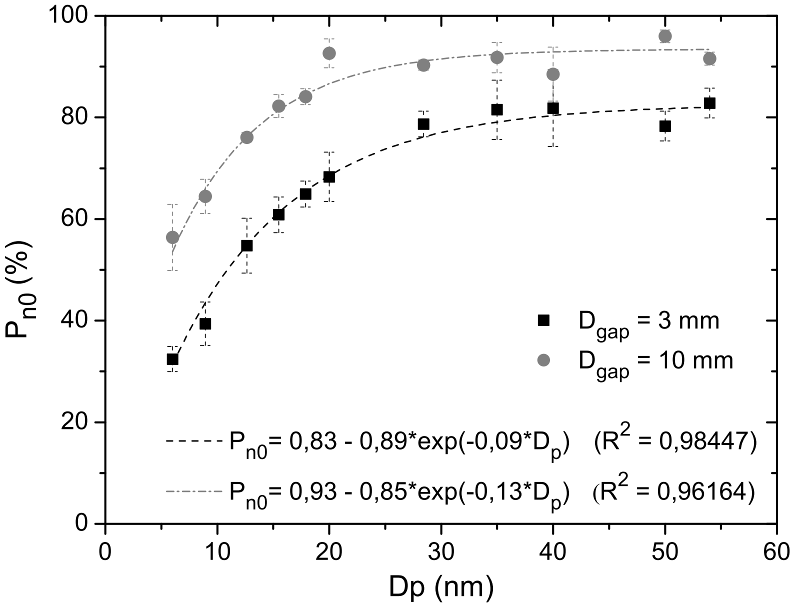

Figure 6.4.1: Fitting of the experimental penetration through the path between the two DMAs.

6.5 RESULTS AND DISCUSSION

The previous inversion theory was tested with two kinds of data, simulated and experimental. Simulated data are generated to test the validity of the techniques by comparison of the results with the original distributions. To imitate the process of measurement as precise as possibly, some uncertainty has been added to the measurements, which is around 5% for ambient aerosol and up to 10% for generated aerosol [35]. Both charging methods, radioactive and corona charger, are tested and inverted by NNLS and SVD methods, this last one comparing the regularization parameters from section 6.2.2. Inverted results of over-, under- and exact- determined systems are shown for these ratios of intervals.

Precision of the simulated inversion is estimated by means of the RMSE, which gives in a single value an estimation of the variance of the residuals from the inversion. It is calculated as the square root of the squared differences between the original (simulated, N) and calculated data, N^*, that is:

$$\mathrm{RMSE} = \frac{1}{N_{\max} - N_{\min}} \sqrt{\frac{1}{n}\sum_{i=1}^{n} (N_{\mathrm{i}} - N_{\mathrm{i}}^{*})^2}. \qquad (6.5.1)$$

On the other hand, in experimental measurements both the uncertainty and the original data are unknown. In these cases, precision of the inverted results is estimated by averaging the results of several tests of the same set of data, obtaining an estimation of the deviation from the original.

6.5.1 *Inversion of simulated data*

Two representative sets of lognormal PSD (eq. (6.4.1) without offset) are tested, one in the ultrafine particle size range, within the measurable range for a Nano-DMA ($\bar{D}_{pg} = 50\,\mathrm{nm}$, $\sigma_g = 1.3$, $C = 3.5 \times 10^{11}\,\#\mathrm{m}^{-3}$) and the other one for bigger diameters, within the measurable range of a Long-DMA ($\bar{D}_{pg} = 300\,\mathrm{nm}$, $\sigma_g = 1.5$, $C = 4.5 \times 10^{15}\,\#\mathrm{m}^{-3}$). It is assumed that particles out of the range selected are removed, which in practice is performed by means of an impactor.

In fig. 6.5.1 the inversion for the determined problem is represented for 64 channels/decade and a 5% of artificial added noise in both cases. For the smaller diameter range (fig. 6.5.1a), both SVD (shown here with the L-Curve regularization method) and NNLS methods work accurately, lead to indistinguishable results with the same deviation and an RMSE below 0.5%, while for the large diameter range (fig. 6.5.1b), the inversion performed by SVD is slightly better ($\mathrm{RMSE}_{SVD} = 0.8\%$, $\mathrm{RMSE}_{NNLS} = 1.2\%$). The L-Curve and GCV regularization methods also present very close results, although L-Curve has a lower NRMSE even for the noisiest data. Since the performances with the different methods are reasonably well done, in the following only the SVD-LC will be shown.

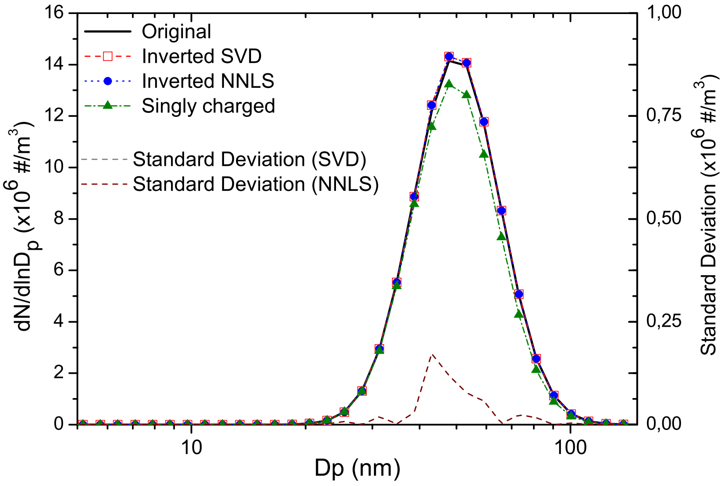

(a)

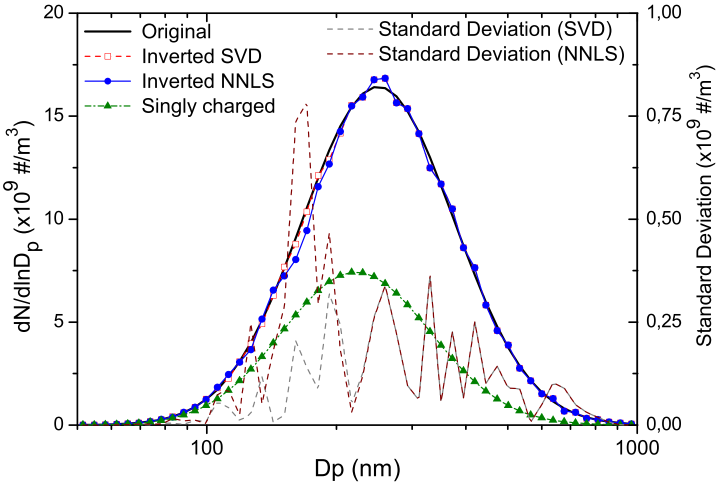

(b)

Figure 6.5.1: Simulated and inverted PSD for ranges measurable with Nano-DMA (a) or Long-DMA (b)

Along with the inverted PSDs, it is also shown the result of applying the Multiple Charge Correction algorithm from section 6.4.1. The singly and multiple charged distributions are very close in the smaller particle range, but they are clearly distinguishable as the particle size increases and acquires more charges. This is graphically shown in fig. 6.5.2, where the theoretical fraction of single charged particles among the total of the charged particles [141, 143] is compared with the results from previous plots. There is a good agreement between the estimated and obtained results, although for the rightmost diameters our prediction is clearly underestimated, probably due to the decrease in concentration in tails of the PSD.

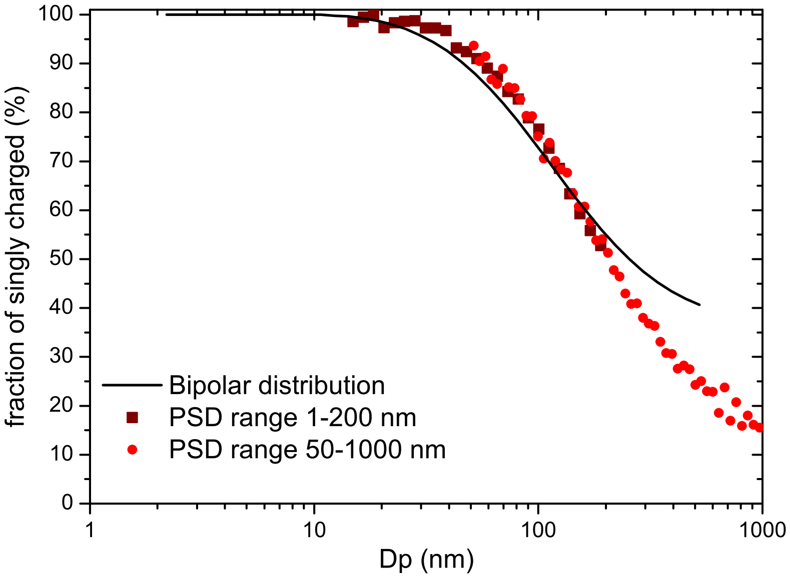

Figure 6.5.2: Fraction of singly charged particles among the total of particles charged for the bipolar radioactive distribution [141, 143] and recovered from the previous distributions with the Multiple Charge Correction algorithm.

Likewise, multimodal distributions are also tested. Since results of large and ultrafine diameters are analogous, only the smaller distribution will be shown, which allows performances with the mentioned corona charger. To test the ability of the algorithm to deconvolute more complicated distributions, a multimodal PSD with two close modes and a sharp peak in the ultrafine particle range is generated ($\bar{D}_{pg}$ =6, 10 and 23 nm; $\sigma = 1.18$, 1.3 and 1.05; $C = 3.0$, 5.0 and 1.2×10^{10} #m^{-3} respectively).

In fig. 6.5.3, inverted results are shown. Data was simulated with unipolar charging at two different $N_i t$ (given by the gap distance of the needle electrode). It can be seen that the inversion is better performed for the gap distance of 10 mm (RMSE = 1.6%) than for the 3 mm gap, which has 3% of RMSE, probably because the higher $N_i t$-product produces more uncertainty in the estimation of the kernel matrix.

On the other hand, the mean charge of the test charger in the TDMA arrangement is estimated from the recovered PSD with the bipolar charger, being under test the bipolar ^{85}Kr and the unipolar corona chargers with the gaps at 3 and 10 mm. Recovered results are shown also in fig. 6.5.3. The bipolar mean charge is deconvoluted with an NRMSE of 2%, while the unipolar charger with $D_{\text{gap}} = 10$ mm is slightly underestimated with an NRMSE of 8% and for $D_{\text{gap}} = 3$ mm is clearly underestimated, reaching up to 20% of NRMSE. It is important to notice from eq. (6.4.6) that there is a recovered function only for the inverted $N_1(D_p)$ values different from zero. Besides, the uncertainties on this one will propagate to the retrieval of the mean charge, hence the differences between the real and estimated mean charge for the shorter gap distance.

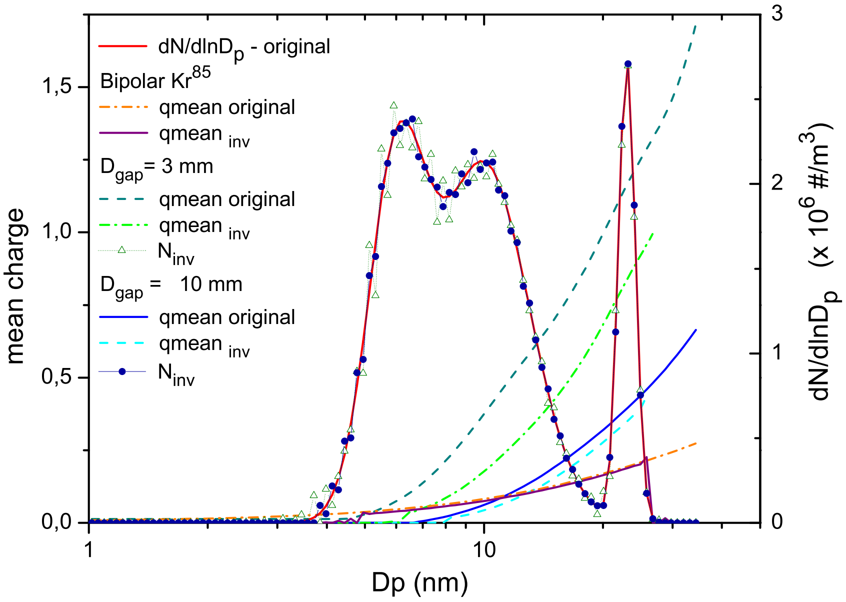

Figure 6.5.3: Inverted PSD for the unipolar corona charger (right axis) and inverted mean charge for the unipolar and bipolar test chargers in a TDMA configuration (left axis).

In fig. 6.5.4a is represented the variation of the error from the inversion process with the artificial noise. It is expected that the greater the uncertainty, the greater the error in the inversion, as happens in the PSD inversion. However, although the inverted mean charge has a higher error, it is almost insensitive to added noise, what indicates that the main contributors to the residuals in the second inversion are the errors from the first one.

While the CN seems to be in general rather insensitive to errors and noise during measurement of the data, as lower graph of fig. 6.5.4a shows, the number of intervals affects directly the size of the matrix and thus the precision of the results, following in fig. 6.5.4b the expected trend of being more precise for over- than for under-determined systems. When the problem is set out as an over-determined problem ($m > n$), the control matrix is not longer square, as well as the matrix of the singular values. This means that there will be a singular value for which all rows are zeroes, weakening the propagation of errors between the eigenvectors. The condition number of the system gets strongly reduced by several orders of magnitude, so the problem is “better-posed” than the determined one.

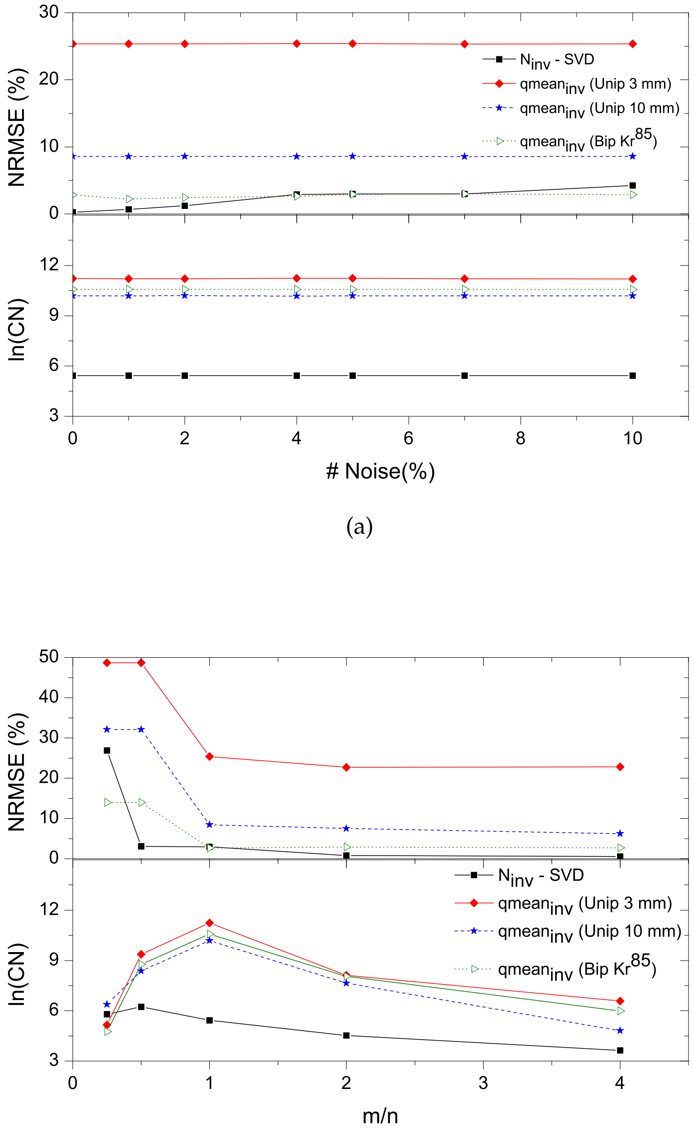

(a)

(b)

Figure 6.5.4: Reliability of the results for an increasing artificial uncertainty during the measurements (a) and for a variable ratio of mobility measurement (input, m) intervals or size (output, n) intervals (b). The over-determined problem is given when $m > n$, exactly determined when $m = n$ and under-determined when $m < n$. RMSE and the logarithm of the condition number give an idea of the accuracy of the inverted PSD or mean charge.

It can be seen how the error of the inversion of the PSD decreases to levels below 2% as soon as $m/n \geq 1$. The same happens for the inverted mean charge, but as in previous cases, there is an accumulated uncertainty from previous inversion that the second calculation cannot outpace, reaching a lower "limit" for the RMSE.

It must be highlighted however that, although on one hand the extra equations from the over-determined problem can be used as the additional information for example to cushion high levels of noise on measurements, on the other hand can result in an oversmooth of the retrieved data, loosing for instance information about very narrow peaks. Besides, it is common in real measurements to have a limited number of channels to measure, therefore the importance of being able to solve under-determined problems. However, in the lower plot of fig. 6.5.4b, the logarithm of the CN shows a lower precision loss for the under-determined problems than for determined, increasing and decreases with m/n. This can lead to confusion without comparing to the high error rate, but it is produced because the worst under-determined case has such a lack of information that the difference between the smallest and largest singular value is minimal.

6.5.2 *Inversion of experimental measurements*

The results from simulated measurements were useful to have the certainty of the applicability of the presented methods to experimental data, and to minimize the factors that could affect the inversion process. Real data from bipolar or unipolar charging, measured by stepping and slow-scanning voltages in the DMA are tested.

In fig. 6.5.5 the inversion of a set of data measured with the DMPS system can be seen. Three ratios of intervals were tested, and deviation of data represented. While the under- and determined problems give results with similar shape and area to the mobility distribution, the over-determined problem shows the nature of the shape near the tails, two small peaks probably due to multiple charged particles that entered with the selected mobility in the classifier.

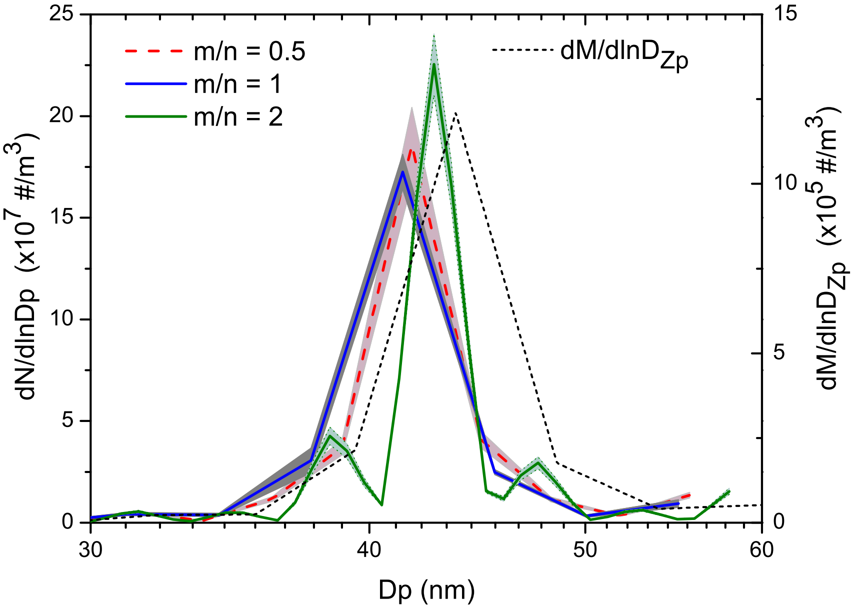

Figure 6.5.5: Deconvolution in left axis of the mobility distributed data from right axis for the over-, under- and determined problems. Data were acquired in the DMPS system for symmetric flows of $Q_a = 1.5\,\text{lpm}$ and $Q_{sh} = 15\,\text{lpm}$ with 64 channels per decade.

Measurements in the TDMA configuration are usually done for monodisperse distributions, with very narrow peaks and low concentration of particles, which complicates the inversion. In fig. 6.5.6a a set of monodisperse measurements added up to form a wider distribution is shown, along with the recovered result form inversion. The PSD was used to calibrate the corona charger ($D_{\text{gap}} = 10\,\text{mm}$) with a TDMA configuration as in fig. 2.4.1 at slow-scan rates to avoid smearing effects. Although the singly charged particles are calculated, its plot shows results almost indistinguishable from the total. Calculating the fraction of particles with charge unity, in fig. 6.5.6b can be seen that it is quite overestimated, in the same amount as the doubly charged particles are underestimated. A reason for this could be the fact that it was only possible to measure up to 3 charges in the charge distribution characterization (table 6.4.1), therefore higher particle charges are present in the measurements that are not being taken into account.

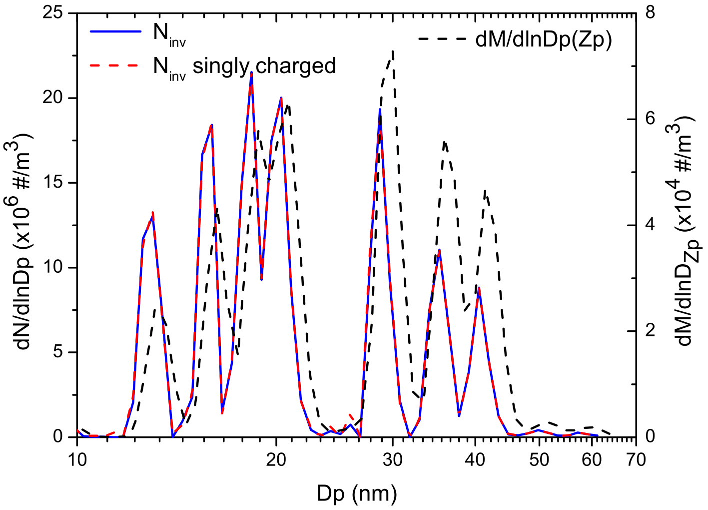

(a)

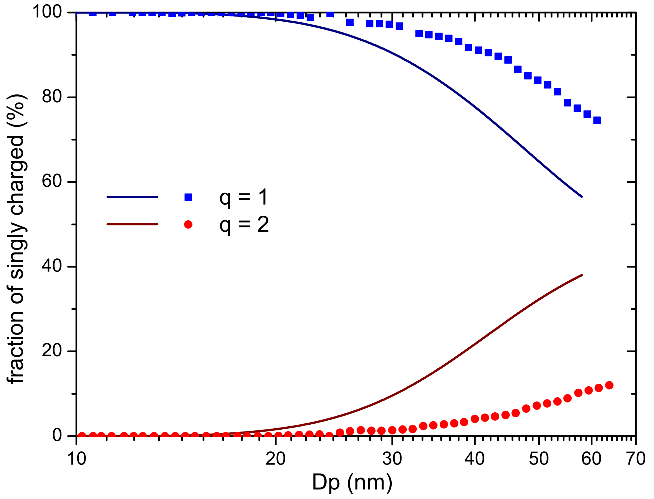

(b)

Figure 6.5.6: (a) Measured and inverted set of added monodisperse measurements for calibrating the corona charger in a TDMA arrangement. (b) Fraction of singly charged particles among the total of particles charged for the unipolar distribution of the corona charger with $D_{\text{gap}} = 10\,\text{mm}$ and recovered from the previous distribution with the Multiple Charge Correction algorithm.

The retrieval of the mean charge of the previous distribution is shown in fig. 6.5.7. Oscillations due to errors and uncertainties in the data appear below 20 nm, overestimating the results, although then the difference with the theoretical values is reduced, probably due to a greater concentration and level of charge of the particles. The ultrafine particle range is always the more delicate range, due to forces to which particles are subjected, like diffusion or electrostatic effects, and also because they are present at much lower concentrations and with a lower charging efficiency, therefore a precise estimation requires more effort.

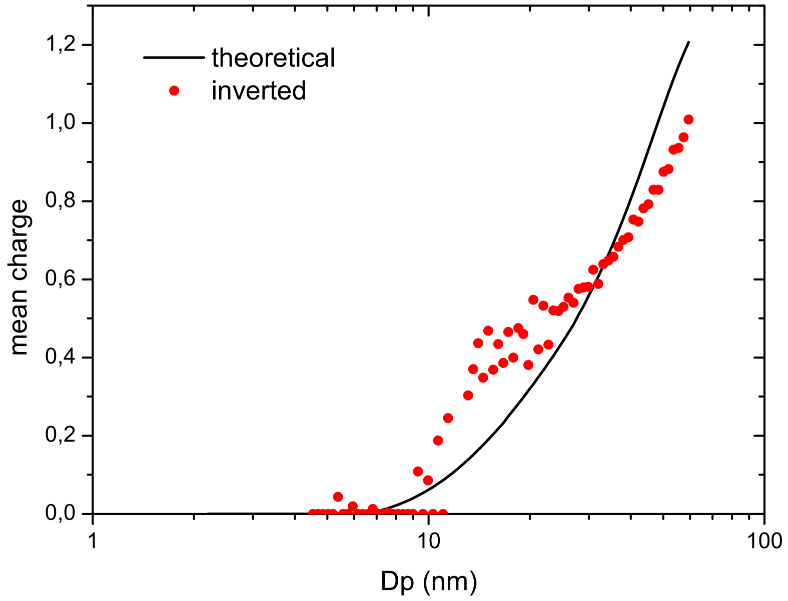

Figure 6.5.7: Inverted mean charge for the unipolar test charger with $D_{\mathrm{gap}} = 10\,\mathrm{mm}$ in a TDMA configuration.

Summarizing, it was conducted a complete study of the appropriate requirements for obtaining an accurate size distribution inversion from mobility data based unipolar or bipolar charging, obtaining best results for the SVD method combined with the L-Curve regularization parameter in all cases. The geometrical estimation of the area of the overlapping triangular-shaped TFs in an arbitrary enviroment of voltage steps or scans is applied instead of the bell-shaped definition. The possibility of choosing independent and arbitrary size or mobility intervals affects to the inversion results through the rank of the kernel matrix. The methodology was also applied to retrieve the contribution of singly charged particles among the total distribution and the mean charge per particle when is measured by a TDMA arrangement, depending these on the good characterization of the neccesary parameters for the inversion.

Part III

CONCLUSIONS

CONCLUSIONS

The complete characterization of a particle size distribution is performed, starting from the basic principles of unipolar electrical charging of the nanoparticles, to the mathematical methodology about the estimation of its real size from indirect techniques.

- Firstly, a new indirect corona device with cylindrical geometry was designed and tested. It is a flexible design in which many of the features can be modified for a better control of the charging process, as well as the reproducibility of the results. It has a sheath flow to drive the ions towards the charging zone, avoiding the direct contact of aerosol and corona needle.

- The developed corona charger is able to vary the $N_i t$-product over a wide range, for smaller values which lead to charging levels close to the bipolar charge equilibrium, as well as high values which lead to high charging levels which are relevant for electrostatic particle deposition or particle detection devices which become more sensitive when the charging level increases. Thus, it can perform in a similar way as radioactive neutralizers, as well as obtain high efficiencies as previous unipolar devices. This could be significant in substitution of such radioactive devices by a unipolar source which has similar characteristics but it is exempt of the restrictions due to the radioactivity. It has a wide range of charging efficiencies for the nanoparticle range, adjustable by controlling the amount of ion concentration by the position of the needle electrode. This method of adjusting the $N_i t$-product seems to result in a broader range of charging levels than by adjusting electrical characteristics such as corona current.

- Though the particle losses are relatively high, they are comparable to other devices shown in literature and can probably be reduced by optimizing further the flows or the corona voltage. It is remarkable also that an ion flow equal or greater than the aerosol flow leads to high losses, so a more detailed study of this effect might lead to further optimization of the charging conditions.

- It was also developed a model based on solving the birth-death equations for particles having different charge levels, allowing to estimate the $N_i t$-product in the charging region of unipolar chargers. However, it does not describe experimentally determined mean charge levels very well. A better agreement is obtained when ion and particle losses due to a radial electric field are included, by fitting two essential parameters which are however very difficult to measure: the ion concentration at the entrance of the charging zone and the radial field. This realistically describes the decrease in ion concentration along the length of the charging zone. The inclusion of an additional axial electric field is unnecessary for this configuration, as it shown to be equivalent to an increase in initial ion concentration and cannot be discriminated from that.

- It is shown that the model results can be used to obtain data which are difficult to acquire experimentally, such as the extrinsic charging efficiency of ultrafine particles or the initial ion concentration. It also gives an estimation of the electrical losses in the device through the radial field. The model was used to analyze data for unipolar chargers by other authors and different device characteristics, again showing good agreement with experimental results.

- It also was dealt with the inverse problem of the estimation of the aerosol size distribution function from the mobility measurements. A complete study of the appropriate requirements for obtaining an accurate inversion of mobility data has been conducted based mainly on the NNLS and the SVD algorithms, this last one comparing two methods of regularization, L-Curve and GCV. The methodology was prepared to be used with any type of charger, once its charge distribution is defined, and an approximation is done in order to use data from scanning or stepping voltage configurations in the DMA. Great flexibility is allowed in choosing the number of intervals and the number of data channels, allowing arbitrary voltage steps and overlapping DMA transfer functions.

- The transfer function was estimated by a simple geometrical calculation from the areas within each output interval, only needing the mobilities that define the Ω to calculate it, being an accurate approximation when compared with the bell-shaped approximation. The analysis of the kernel matrix is a key to understanding the origin of the instabilities, since its rank conditions the number of potential mathematical solutions to the problem.

- From the direct comparison of both SVD and NNLS methods, it was found that the errors are similar and usually depend on the characteristics of the distribution. However, the SVD method combined with the L-Curve regularization has the advantage of having greater flexibility in selecting the number of channels with higher efficiency, since it is capable of accurately solve even the underdetermined systems. The inversion performed in this way provides good fit with less than 1% of error for noise levels of 5%, which could be even less when the intervals are properly chosen.

- A method to calculate the contribution of the singly charged particles to the total distribution was successfully applied to unipolar and bipolar chargers, although in tails, where concentration is lower, the fraction of singly charged particles is somehow miss-estimated. Also the technique was applied for the TDMA arrangement with the possibility of retrieving the mean charge per particle of the distribution. The results show a good approximation when the original PSD is estimated accurately, even when errors can propagate and distort the inverted mean charge.

Some possible future works have arisen from the final and intermediate results obtained in the course of this thesis, as well as further improvements could be applied to current findings.

Further characterization of the unipolar corona charger has to be done, for example for a larger range of particles, since we have focused on the nanoparticle range. Also the charging properties for polydisperse distributions shall be tested, and an interesting question would be to test the ability of ionic unipolar charging to imprint charge to the particles at massive flow rates, which could have many industrial applications. However a different setup should be necessary, since the particle spectrometers used in experiments could only deal with volume flows below 20 lpm.

During the study of the electrical characteristics of the charging device, several attempts of simulate the corona discharge process were made. The Poisson and Laplace approximations for the electrical field generated inside the corona were calculated by finite elements methods, but due to the plasma generated around the electrode tip, further study was necessary and was not possible to include it in the content of this thesis. Also a theoretical expression of the Peek's equation (which was derived experimentally in the decade of the 1920s and is still in use nowadays, eq. (2.1.1)) valid for multiple geometries of corona discharge was draft, although extensive study of its validity and versatility to adapt to the multiple possible corona discharge geometries is needed.

The inversion methodology is almost infinite, there are plenty of inversion techniques that could be applied regarding on the quality of the data and the expected results. A comparison or combination of the presented deterministic methods with some statistical technique could have improved results, although statistical inversion methods require a lot of care to not include data with weight enough to perturb the results. Also, as a first approximation, the inversion of the mean charge was established, but further attempts with more kinds of data would be necessary to cushion the errors of the previous inversion and ensure a correct operation of the algorithm.

CONLUSIONES

En el transcurso de esta tesis se ha realizado una caracterización completa de la función distribución del tamaño de partículas, partiendo de los principios básicos de la carga eléctrica unipolar de nanopartículas, hasta la metodología matemática acerca de la estimación de su tamaño real mediante técnicas indirectas.

- En primer lugar, un nuevo dispositivo de descarga corona indirecta con geometría cilíndrica fue diseñado y probado. Es un diseño flexible en el que muchas de las características pueden ser modificadas para un mejor control del proceso de carga, así como de la reproducibilidad de los resultados. Tiene un flujo auxiliar para conducir los iones hacia la zona de carga, evitando el contacto directo del aerosol con el electrodo de descarga.

- El cargador de corona desarrollado es capaz de variar el producto $N_i t$ en un amplio intervalo, desde valores pequeños cercanos al de equilibrio del cargado bipolar, hasta valores que conducen a niveles altos de carga, relevantes para la deposición electrostática de partículas o en el caso de dispositivos de detección de partículas que se vuelven más sensibles cuando el aumenta el nivel de carga. Por tanto, se abarca un rango en el que puede desde trabajar de una manera similar a neutralizadores radiactivos, como obtener una alta eficiencia como la de otros dispositivos unipolares. Esto podría ser significativo en sustitución de tales dispositivos radiactivos por una fuente unipolar de características similares, pero exenta de las restricciones debidas a la radiactividad. Las eficiencias de cargase ajustan mediante el control de la concentración de iones a través de la posición del electrodo de aguja. Este método de ajuste del producto $N_i t$ parece dar lugar a un rango más amplio de los niveles de carga que modificando las características eléctricas como puede ser la corriente de corona.

- Aunque las pérdidas de partículas son relativamente altas, en realidad son comparables a otros dispositivos mostrados en la literatura y, probablemente, se pueden reducir aún más mediante la optimización de los flujos o la tensión de corona. Es notable también que un flujo de iones igual o mayor que el flujo de aerosol conduce a grandes pérdidas, por lo que un estudio más detallado de este efecto podría conducir a una mayor optimización de las condiciones de carga.

- También se ha desarrollado un modelo basado en la solución de las ecuaciones de *nacimiento-y-muerte* para partículas con diferentes niveles de carga, lo que permite estimar el producto $N_i t$ en la región de cargado de los cargadores unipolares. Sin embargo, no se ajusta del todo a los niveles de carga medios determinados experimentalmente. Se obtiene un mejor ajuste cuando se incluyen las pérdidas de iones y partículas expresadas por medio de un campo eléctrico radial, mediante la introducción de dos parámetros esenciales que sin embargo son muy difíciles de medir: la concentración de iones en la entrada de la zona de carga y el campo radial. Esto describe de manera más realista la disminución de la concentración iónica a lo largo de la zona de cargado. La inclusión de un campo eléctrico axial adicional no es necesaria, ya que demostró ser equivalente e indiscernible a un aumento de la concentración inicial de iones.

- Se ha demostrado que los resultados del modelo pueden ser utilizados para obtener datos que son difíciles de adquirir experimentalmente, tales como la eficiencia extrínseca de carga de las partículas ultrafinas o la concentración inicial de iones. También se obtiene una estimación de las pérdidas eléctricas en el dispositivo a través del campo radial. El modelo se utilizó también para analizar los datos para los cargadores unipolares de diferentes características de otros autores, mostrando de nuevo una buena concordancia con los resultados experimentales.

- Asimismo, fue tratado el problema inverso de la estimación de la función de distribución de tamaño de aerosol a partir de mediciones de la movilidad. Se ha realizado un estudio completo de los requisitos adecuados para la obtención de una inversión exacta dede los datos de movilidad basándose principalmente en los algoritmos NNLS y SVD, este último comparando dos métodos de regularización, la Curva-L y GCV. Se preparó el algoritmo para ser utilizado con cualquier tipo de cargador con una distribución de carga definida, así como para utilizar los datos de configuraciones de voltaje fijo o escaneado en el DMA. Se ha conseguido una gran flexibilidad en la elección del número de intervalos de medida y el número de canales de datos, lo que permite saltos de voltaje arbitrario y funciones de transferencia de DMA superpuestas.

- La función de transferencia se estimó mediante un cálculo geométrico simple a partir de las áreas dentro de cada intervalo de tamaño de datos, sólo necesitando las movilidades que definen laΩ para su cálculo, siendo una aproximación precisa en comparación con la estimación en forma de campana. El análisis de la matriz del núcleo (*kernel*) es clave para entender el origen de las inestabilidades en la inversión, ya que su rango condiciona el número de posibles soluciones matemáticas para el problema.

- De la comparación directa de ambos métodos, SVD y NNLS, se encontró que los errores generados son similares y por lo general dependen de las características de la distribución. Sin embargo, el método SVD combinado con la regularización de la Curva-L tiene la ventaja de tener una mayor flexibilidad en la selección del número de canales, y obtiene mejores resultados, ya que es capaz de resolver con precisión incluso los sistemas subdeterminados. La inversión así realizada proporciona buen ajuste con menos de 1% de error para los niveles de ruido de 5%, incluso menor cuando los intervalos están adecuadamente elegidos.

- Un método para el cálculo de la contribución de las partículas de una sola carga a la distribución total fue aplicado con éxito a los resultados de cargadores unipolares y bipolares, aunque en las colas, donde la concentración es menor, la fracción de partículas de una sola carga está ligeramente subestimada. También se aplicó la inversión a medidas realizadas mediante la disposición de TDMA, con la posibilidad de recuperar la carga media por partícula de la distribución. Los resultados muestran una buena aproximación cuando los originales PSD se calculan con exactitud, ya que los errores se pueden propagar y distorsionar la carga media obtenida mediante inversión.

Algunos posibles futuros trabajos han surgido a partir de resultados intermedios y finales obtenidos en el curso de esta tesis, así como otras mejoras que se podrían aplicar a los resultados presentados.

Ha de completarse una caracterización más a fondo del cargador de corona unipolar, por ejemplo, para un rango más amplio de partículas, ya que nos hemos centrado en el tamaño nanométrico. También las propiedades de cargado para distribuciones polidispersas deberán ser definidas, y una cuestión interesante sería la de comprobar la capacidad de imprimir carga unipolar iónica para partículas en velocidades de flujo masivo, lo que podría tener muchas aplicaciones industriales. Sin embargo, se necesitarían diferentes dispositivos de medida, ya que los espectrómetros de partículas utilizados en los experimentos sólo podían hacer frente a flujos de volumen por debajo de 20 lpm.

Durante el estudio de las características eléctricas del dispositivo, se hicieron varios intentos de simular el proceso de descarga del corona. Se calcularon aproximaciones de Poisson y Laplace por métodos de elementos finitos para el campo eléctrico generado en el interior de la zona de descarga corona, pero debido a las distorsiones creadas por el plasma generado alrededor de la punta del electrodo, es necesario un estudio más profundo del tema y no se pudo incluir en el contenido de esta tesis. También se derivó una expresión teórica de la ecuación de Peek (que fue derivada experimentalmente en la década de los años 20, y todavía se usa hoy en día, ec. (2.1.1)) válida para múltiples geometrías de corona, aunque es aún necesario un amplio estudio de su validez y versatilidad para adaptarse a las múltiples posibles geometrías de descarga corona.

La metodología de inversión es casi infinita, hay cientos de técnicas de inversión que se podrían aplicar dependiendo de la calidad de los datos y los resultados esperados. Una comparación o combinación de los métodos deterministas presentados con alguna técnica estadística podrían haber mejorado los resultados, sin embargo los métodos estadísticos de inversión requieren de mucho cuidado para no incluir datos con peso suficiente para perturbar los resultados. Asímismo, como una primera aproximación, se estableció la inversión de la carga media, aunque serían necesarios nuevos intentos con más tipos de datos para amortiguar los errores de la primera inversión y garantizar un correcto funcionamiento del algoritmo.

Part IV

APPENDICES

A

SCHEMATICS OF THE CORONA DESIGN

A draft of the assembled components of the corona design is shown in detail in fig. A.0.8. Names of the components are in german language, since the device was built in the workshop of the University of Duisburg-Essen.

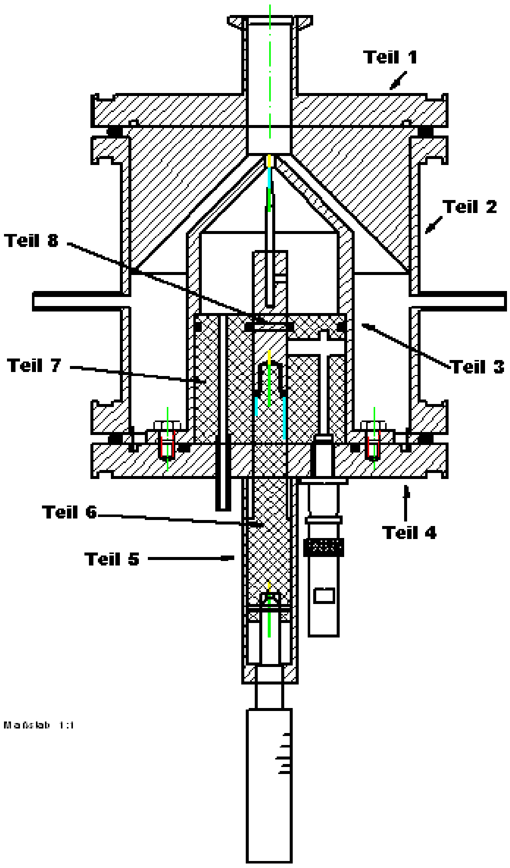

Figure A.0.8: Assembled components of the corona unipolar charger.

Individual design of each piece (*'Teil'*, in german) is shown in figs.A.0.9 to A.0.17. The pieces shown in drafts A.0.9 and A.0.10 are assembled as shown in picture A.0.11 for the entrance and exit of the aerosol flow. The conductor pieces are made of stainless steel (*'Edelstahl'*), polished in the inner parts to avoid losses of ions or particles in flaws. Most of the pieces are put together by screws, although some specified parts are welded (*'schweißen'*). All units are given in milimeters.

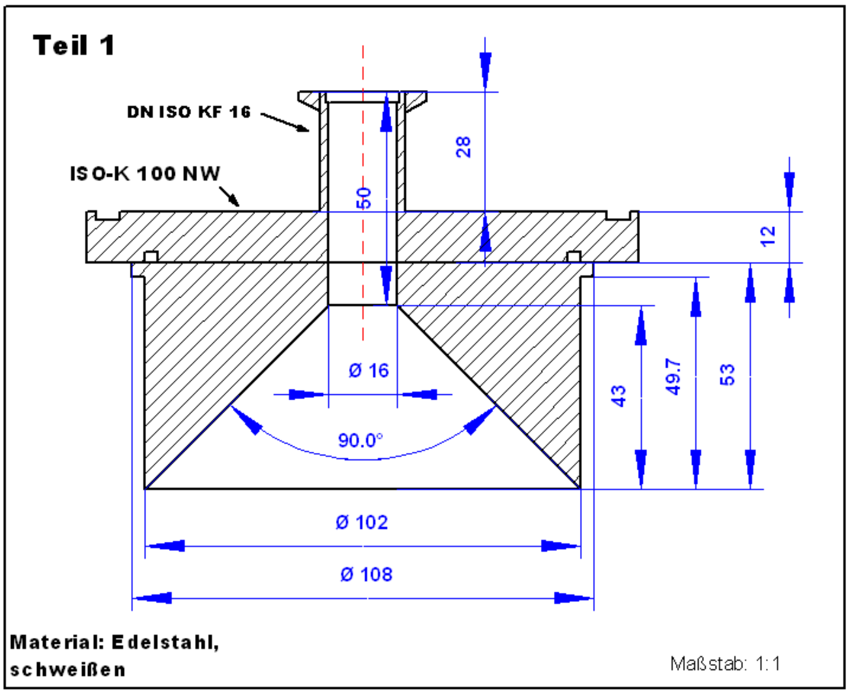

Figure A.0.9: Output and charging region.

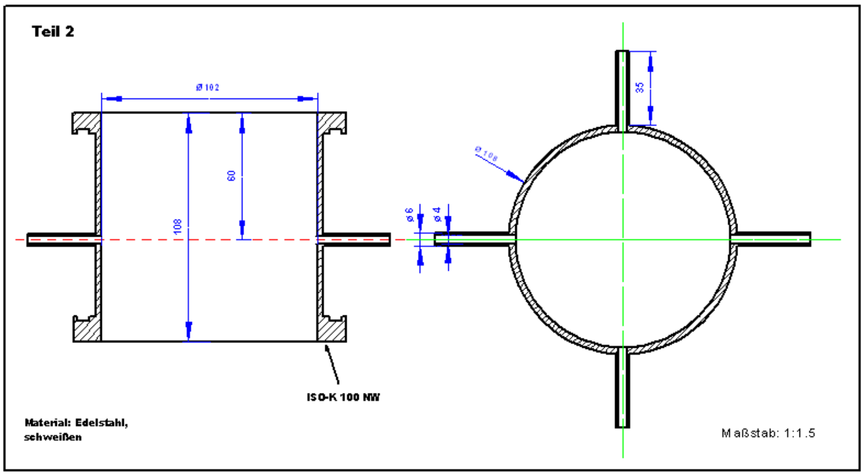

Figure A.0.10: Surrounding piece and input channels of the aerosol flow.

Figure A.0.11: Connections for the input of the aerosol flow.

The ionizing region and support of the needle electrode is made of the parts shown in the following figures. Isolator chosen for the electrode where the voltage is applied was Delrin, a thermoplastic known for its high stiffness and heat resistance properties (fig. A.0.15). The inner surface of the ionizing chamber (fig. A.0.12) was finely polished to avoid impurities contaminating the flux of ions.

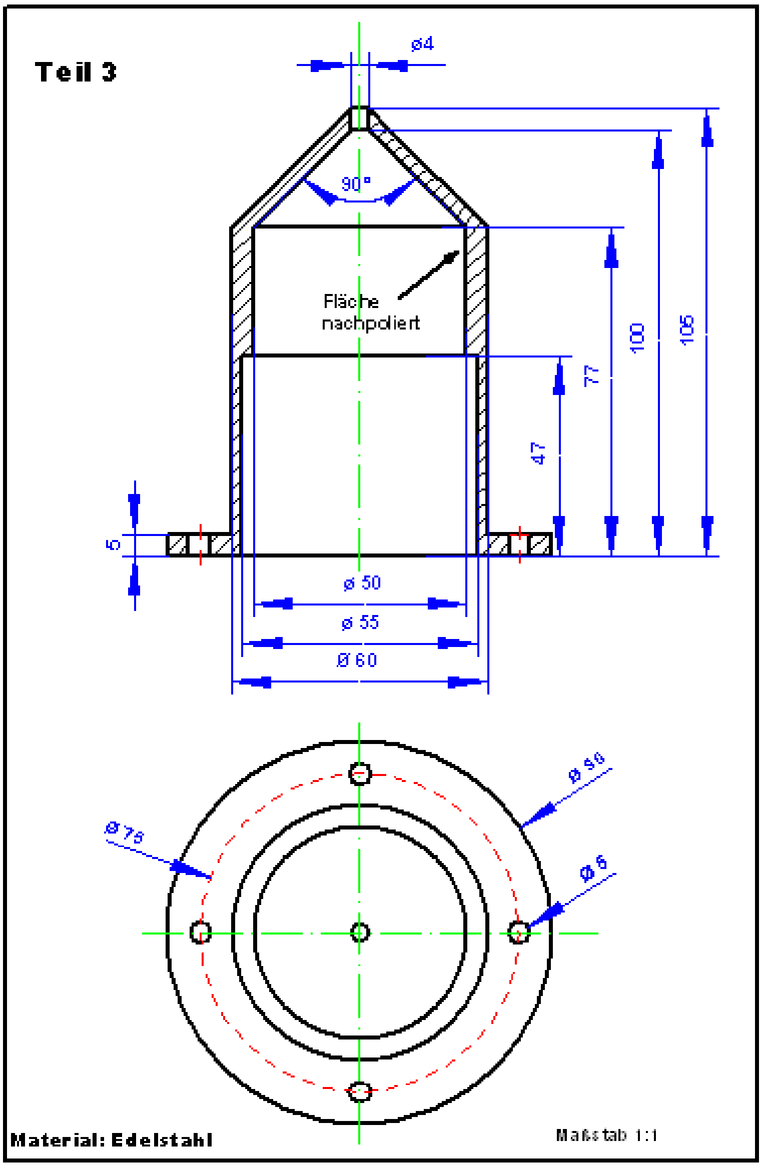

Figure A.0.12: Ground electrode working also as ceiling for the ionizer chamber.

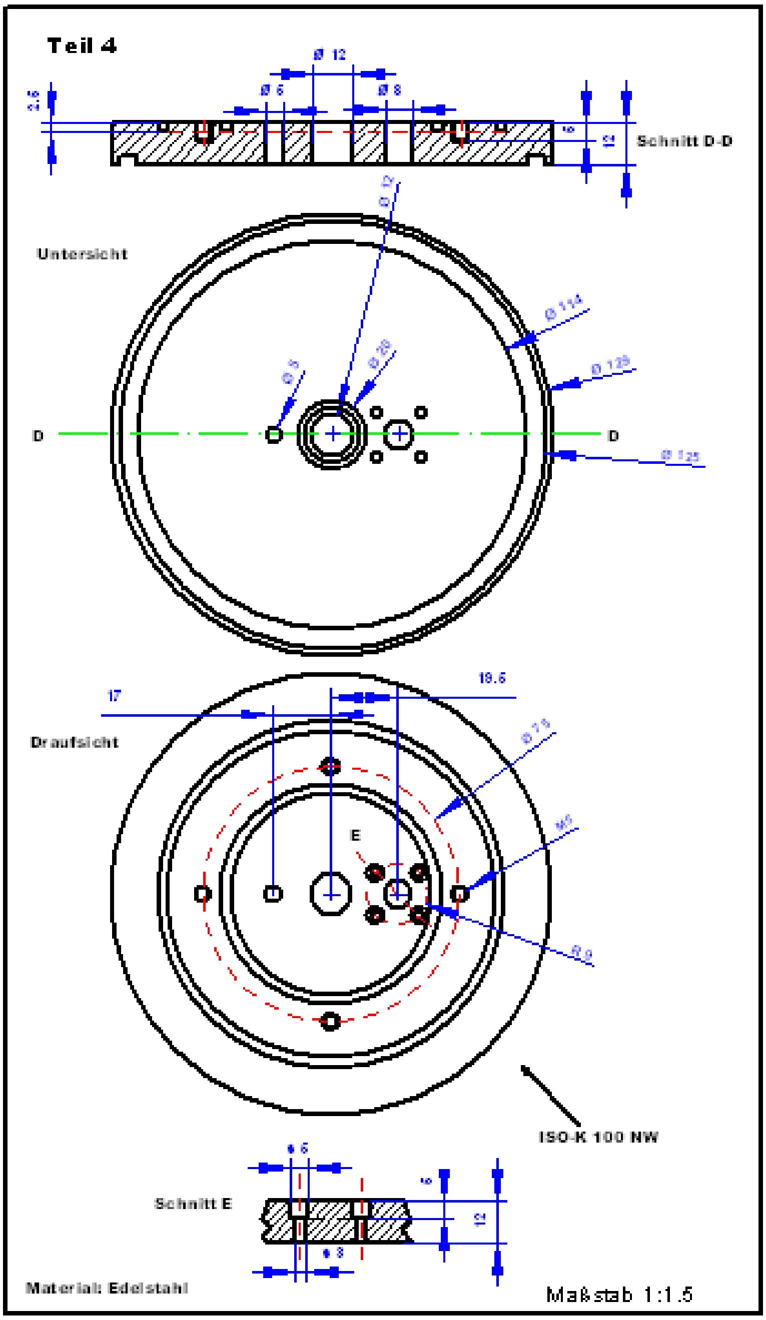

Figure A.0.13: Base and closing for both ion and particle chambers.

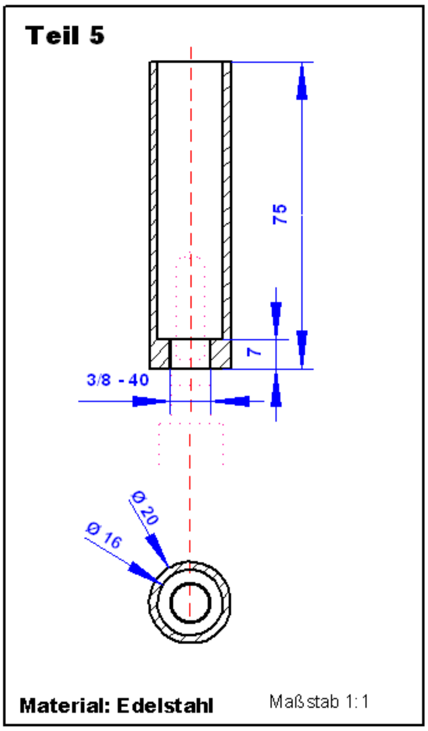

Figure A.0.14: Connection piece between micrometer and basement.

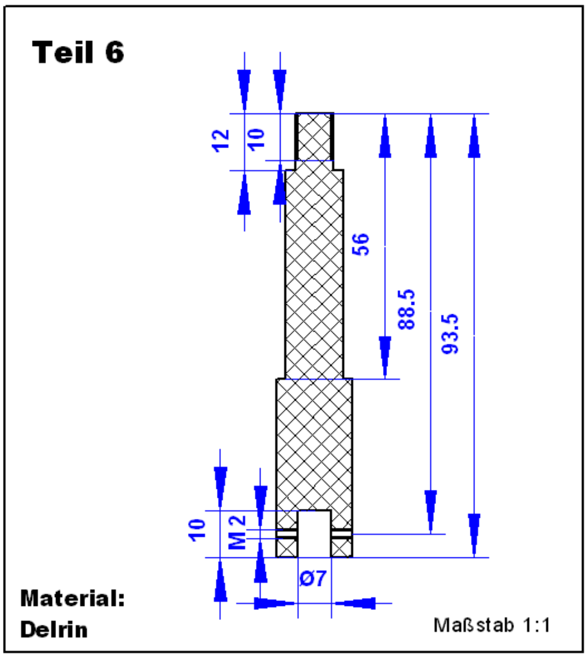

Figure A.0.15: Connection piece between needle stand and micrometer.

The isolator shown in fig. A.0.16 was also made of Delrin, and was used for supporting the gas conductor (left hole), the needle stand (center hole, fig. A.0.17) and the high-voltage connection (right hole). The needle connections can be seen in pictures shown in fig. A.0.18.

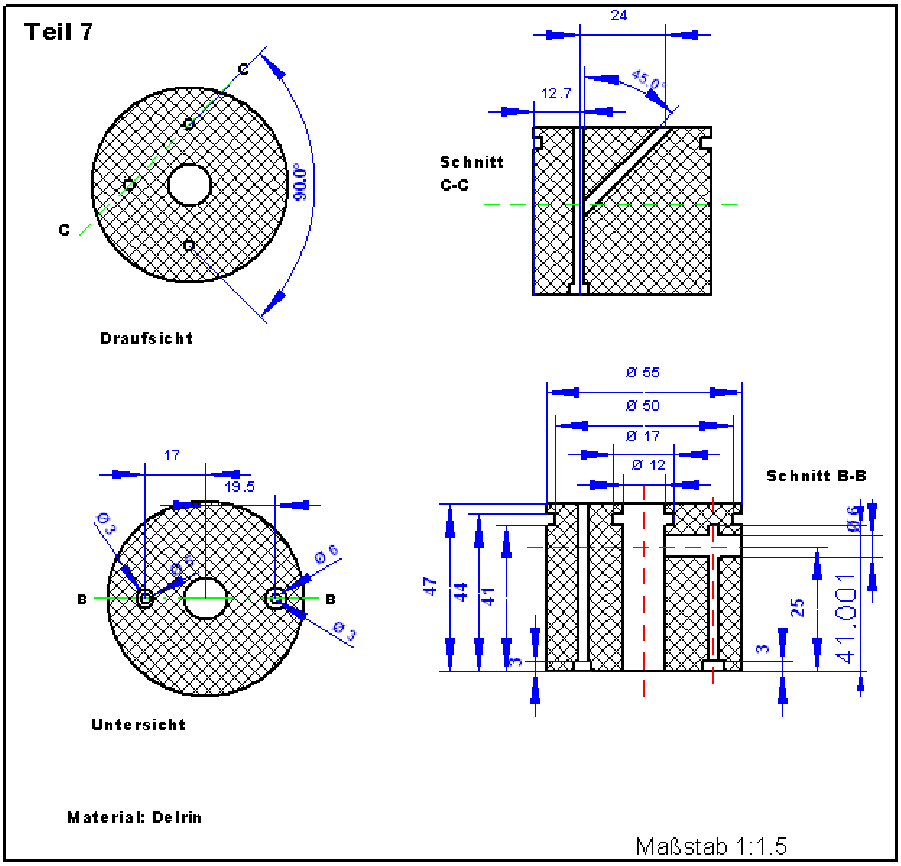

Figure A.0.16: Isolator made of Delrin.

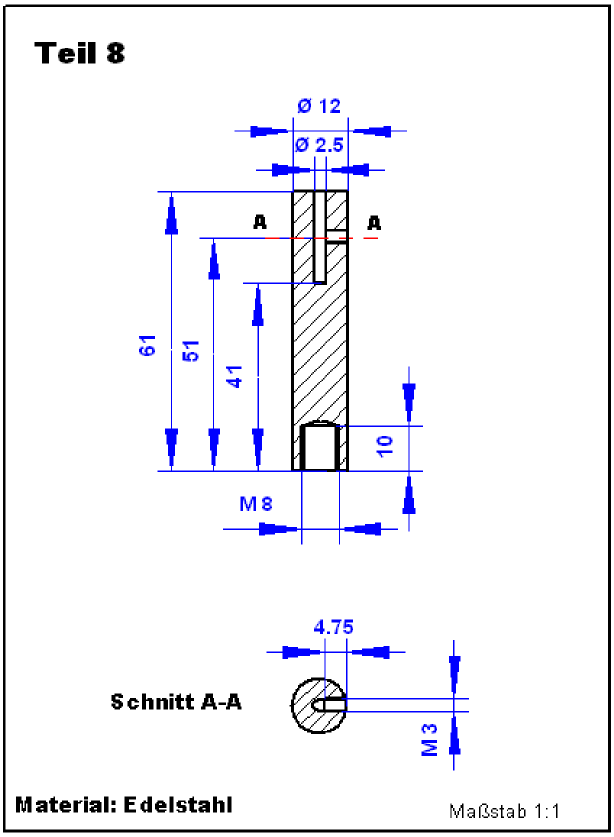

Figure A.0.17: Needle and micrometer support.

Figure A.0.18: Picture of the corona needle and chamber for ion generation.

B

ESTIMATION OF THE AREA OF THE TRANSFER FUNCTION

In order to show in detail the geometrical calculations for the area of the Ω, $A_\Omega(q,m,n)$, we will illustrate a standard case of a single triangular TF with generic height and width.

The mobility mean diameters of each data channel are obtained from the measurements, and the corresponding central mobility $Z_c(q,m)$ calculated from them. We can infer the width $\Delta Z_c(q,m)$, height $H(q,m)$, and variation due to diffusion of each peak of the TF from the experimental data of the corresponding DMA.

From $Z_c(q,m)$ and $\Delta Z_c(q,m)$, mobility values for both upper $Z_u(q,m)$ and lower $Z_l(q,m)$ bounds of the TF are calculated, similarly is done for the size intervals $Z_u^*(q,n)$ and $Z_l^*(q,n)$. These parameters characterize the transfer function and its limits within the selected size channels. In fig. B.0.19 all these mobility limits are represented. The width of the mobility intervals is the FWHM given by eq. (6.3.9) in chapter 6, while the width of the size intervals is $\Delta Z_p(q,n) = Z_u^*(q,n) - Z_l^*(q,n)$. For simplicity in notation, all references to the number of charges q will be omitted in the following.

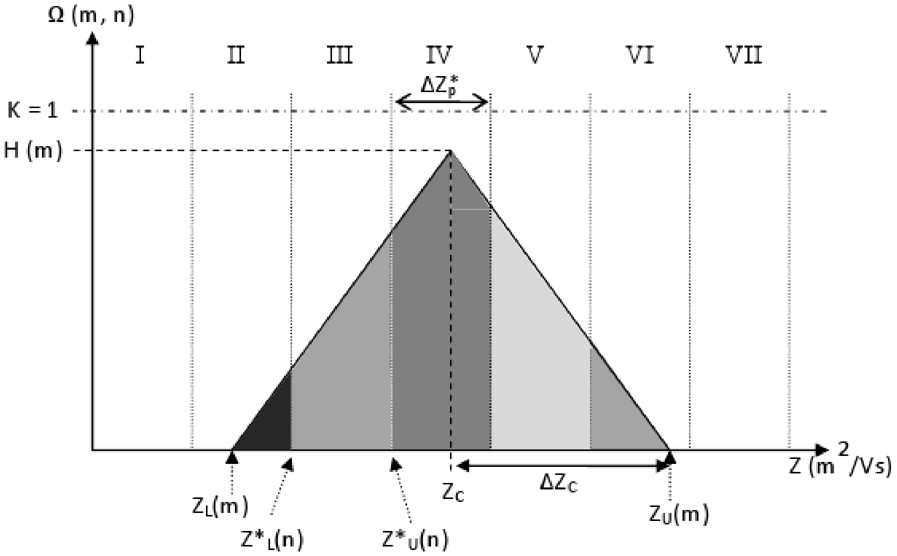

Figure B.0.19: Contribution from different parts of the transfer function into different size channels.

We calculate independent contributions of the TF in each size interval, even when they overlap. The value in every size region is the average probability of a particle whose electrical mobility is within the mobility range of that interval of being classified by the DMA. Depending on the fraction of the TF within the interval, there can be several cases, numbered from I to VII in fig. B.0.19, and some others resulting from combination of II+III+IV (case A, shown as example in section 6.3, fig. 6.3.5), IV+V+VI (case B), or II+III+IV+V+VI (case C), this last being the whole TF is within a size interval.

It has to be considered if the calculation is done increasing mobilities or voltages, since in this case the value of the mobilities will be decreasing and therefore the sections would have the same values as presented here but reflected: the leftmost value of the transfer function will be the upper value, and the rightmost the lower, that is, result for section II would be the one from VI, III from V and so on. Here it will be shown the case of increasing mobilities due to its simplicity.

The areas are calculated by triangulation, remarking that the TF is symmetrical around $Z_c(m)$. Although the extremes of each size region coincide, $Z_l^*(n) = Z_u^*(n+1)$, the size intervals do not have the same width since they are usually lognormally distributed. Given that the only known values are the mobilities and full height at half width, the area of the shaded region will be determined by setting all the parameters as a function of these ones through simply geometric relations. The total ideal height of the size intervals is supposed to be $K = 1$.

SECTION I: There is no portion of area of the TF selected if the compared mobilities are:

$$Z_u^*(n) \leq Z_l(m) \text{ (section I) or } Z_l^*(n) \geq Z_u(m) \text{ (section VII).} \tag{B.0.2}$$

Therefore, $A_\Omega(m,n) = 0$.

SECTION II: This section is defined when the mobilities are (fig. B.0.20):

$$Z_l^*(n) \leq Z_l(m) < Z_u^*(n) \leq Z_c(m). \tag{B.0.3}$$

The value of the transfer function which falls within this interval is given by:

$$A_\Omega(m,n) = \frac{1}{2} a_{\mathrm{II}} b_{\mathrm{II}}, \tag{B.0.4}$$

where b_{II} is an undetermined height that can be expressed by triangular similarities as:

$$\frac{b_{\mathrm{II}}}{H(m)} = \frac{a_{\mathrm{II}}}{\Delta Z_c(m)}. \tag{B.0.5}$$

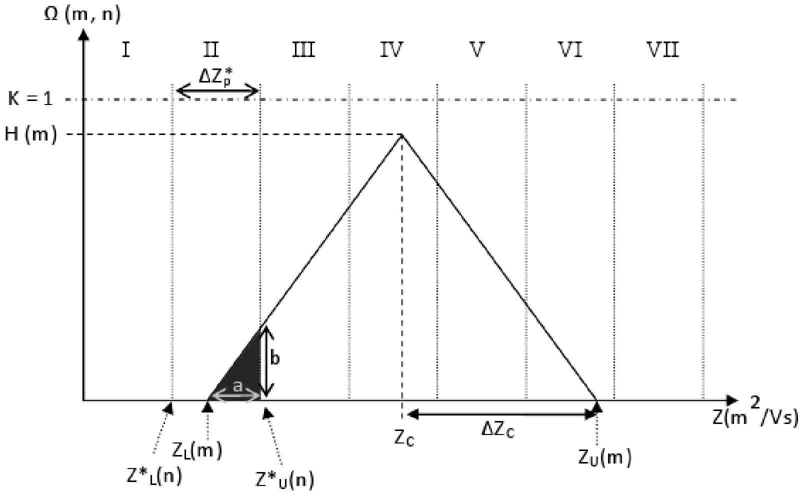

Figure B.0.20

Substituting in the previous eq. (B.0.4), we obtain the normalized probability in such a way all the parameters are known:

$$A_\Omega(m,n) = \frac{H(m)}{2\Delta Z_c(m)} \left[Z_u^*(n) - Z_l(m)\right]^2 . \tag{B.0.6}$$

SECTION III: This case is given when the mobilities are arranged as shown in fig. B.0.21:

$$Z_l(m) < Z_l^*(n) < Z_u^*(n) \leq Z_c(m). \tag{B.0.7}$$

Then, the transfer function is defined:

$$A_\Omega(m,n) = \frac{1}{2} a_{\text{III}} (b_{\text{III}} + c_{\text{III}}). \tag{B.0.8}$$

The unknown heights ae calculated in the same way as in section II, now with $a_{\text{III}} = \Delta Z_p^*(n)$.

$$b_{\text{III}} = \frac{H(m)}{\Delta Z_c(m)} \left(Z_l^*(n) - Z_l(m)\right) \text{ and } c_{\text{III}} = \frac{H(m)}{\Delta Z_c(m)} \left(Z_u^*(n) - Z_l(m)\right), \tag{B.0.9}$$

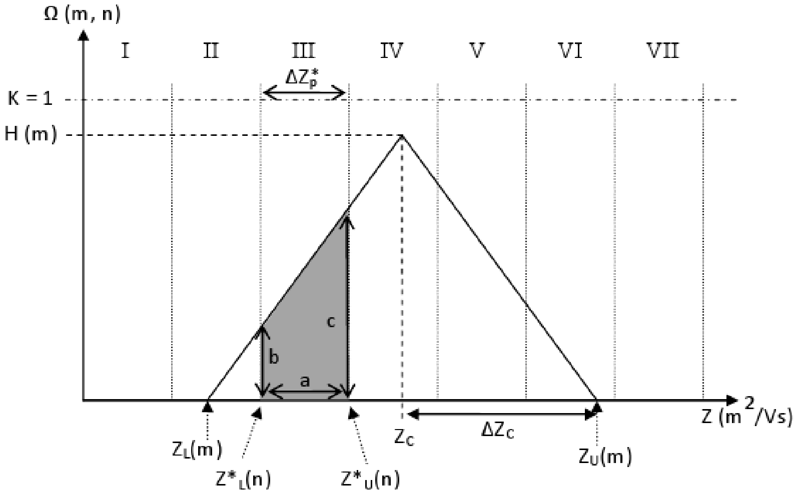

Figure B.0.21

$$A_{\Omega}(m,n) = \frac{H(m)\Delta Z_p^*(n)}{2\Delta Z_c(m)}\left(Z_u^*(n) + Z_l^*(n) - 2Z_l(m)\right). \tag{B.0.10}$$

SECTION IV: The mobilities of this section are arranged as follows (see fig. B.0.22):

$$Z_l(m) < Z_l^*(n) < Z_c(m) < Z_u^*(n) < Z_u(m). \tag{B.0.11}$$

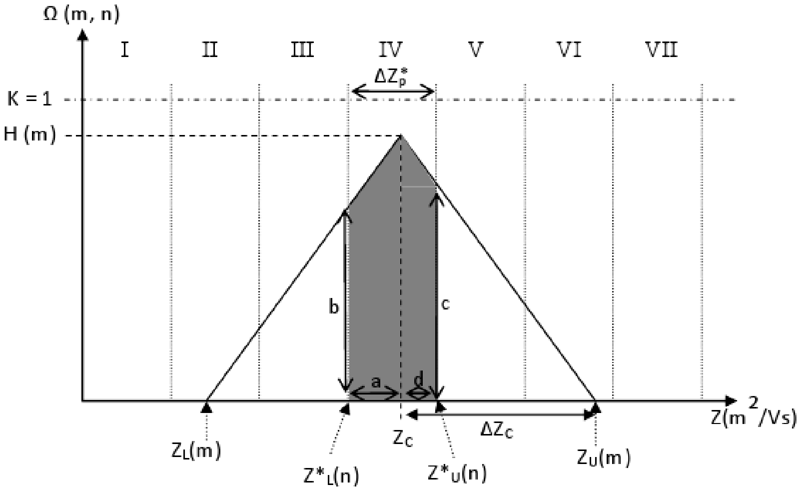

Figure B.0.22

The width of the size interval is divided in two regions by the central mobility: $\Delta Z_p^*(n) = a_{\rm IV} + d_{\rm IV}$.

$$A_\Omega(m,n) = \frac{1}{2} a_{\rm IV}\left(H(m) + b_{\rm IV}\right) + \frac{1}{2} d_{\rm IV}\left(H(m) + c_{\rm IV}\right). \tag{B.0.12}$$

The heights can be expressed as:

$$b_{\rm IV} = \frac{H(m)}{\Delta Z_c(m)}\left(Z_l^*(n) - Z_l(n)\right) \quad \text{and } b_{\rm IV} = \frac{H(m)}{\Delta Z_c(m)}\left(Z_u(n) - Z_u^*(n)\right), \tag{B.0.13}$$

Substituting by their corresponding values in mobilities:

$$\begin{aligned} A_\Omega(m,n) \quad &= \quad \frac{H(m)}{2\Delta Z_c(m)}\left[\left(Z_u(m) - Z_u^*(n)\right)\left(Z_u^*(n) - Z_c(m)\right) + \right. \\ &\left. + \left(Z_l^*(n) - Z_l(m)\right)\left(Z_c(n) - Z_l^*(n)\right) + \Delta Z_p^*(n)\Delta Z_c(m)\right]. \end{aligned} \tag{B.0.14}$$

SECTION V: In this section the mobilities are arranged as follows (fig. B.0.23):

$$Z_c(m) \leq Z_l^*(n) < Z_u^*(n) < Z_u(m). \tag{B.0.15}$$

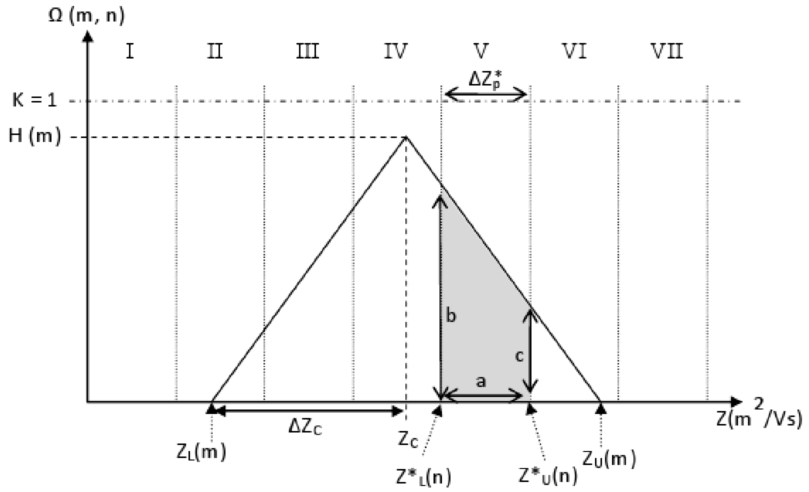

Figure B.0.23

The procedure is analogue to that of section III, therefore we will give directly the final result:

$$A_{\Omega}(m,n) = \frac{H(m)\Delta Z_p^*(n)}{2\Delta Z_c(m)} \left(2Z_u(m) - Z_u^*(n) - Z_l^*(n)\right). \tag{B.0.16}$$

SECTION VI: Similarly to calculations of section II, the mobilities of section VI are arranged as shown in fig. B.0.24:

$$Z_c(m) \leq Z_l^*(n) < Z_u(m) \leq Z_u^*(n). \tag{B.0.17}$$

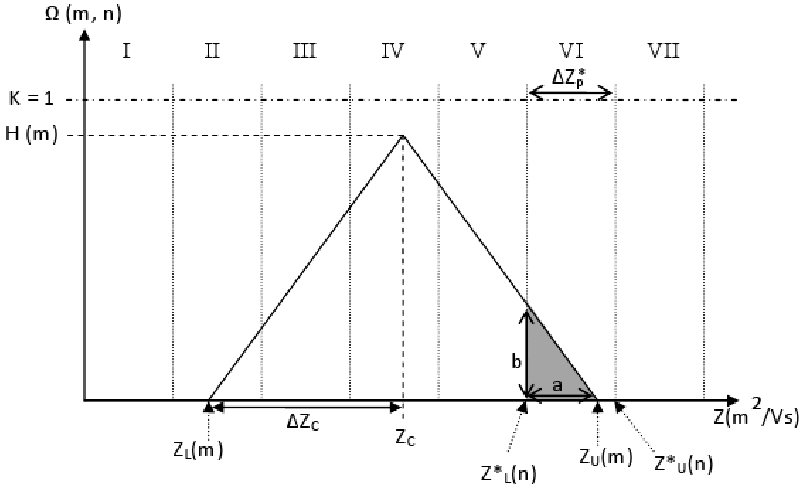

Figure B.0.24

$$A_{\Omega}(m,n) = \frac{H(m)}{2\Delta Z_c(m)} \left[Z_u(m) - Z_l^*(n)\right]^2. \tag{B.0.18}$$

SECTION A (COMBINATION OF SECTIONS II, III AND IV): As it was shown in fig. 6.3.5, this case is given when the mobilities are arranged as follows:

$$Z_l^*(n) \leq Z_l(m) < Z_c(m) < Z_u^*(n) < Z_u(m), \tag{B.0.19}$$

and the final result of the transfer function area is:

$$A_{\Omega}(m,n) = \frac{H(m)}{2\Delta Z_c(m)} \left[2\Delta Z_c^2(m) - \left(Z_u(m) - Z_u^*(n)\right)^2\right]. \tag{B.0.20}$$

SECTION B (COMBINATION OF SECTIONS IV, V AND VI): This case is analogous to the case A with mobilities set toward the right way round, as fig. B.0.25 shows:

$$Z_l(m) < Z_l^*(n) < Z_c(m) < Z_u(m) \leq Z_u^*(n). \tag{B.0.21}$$

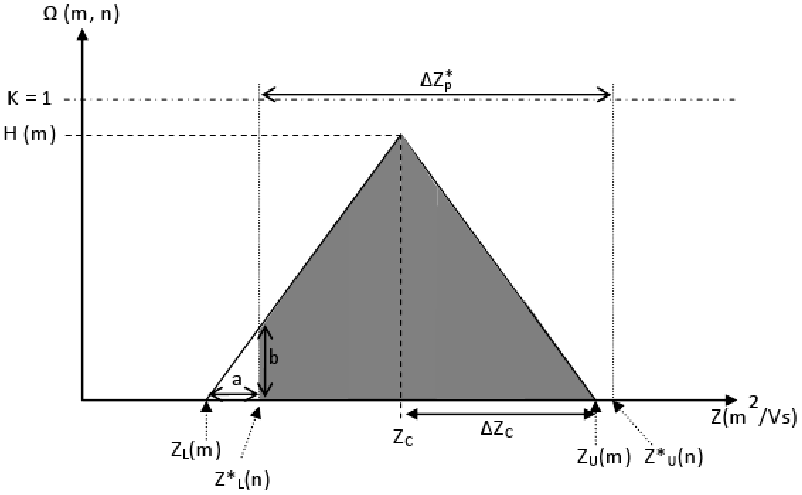

Figure B.0.25

The final result:

$$A_\Omega(m,n) = \frac{H(m)}{2\Delta Z_p(n)} \left[2\Delta Z_c^2(m) - (Z_l^*(n) - Z_l(m))^2 \right]. \tag{B.0.22}$$

SECTION C (COMBINATION OF SECTIONS II, III, IV, V AND VI): This is the simplest case, in which the whole transfer function lies within a size interval, that is:

$$Z_u^*(n) \geq Z_u(m) > Z_c(m) > Z_l(m) \geq Z_l^*(n), \tag{B.0.23}$$

and its value is the total area of the triangle:

$$A_\Omega(m,n) = H(m)\Delta Z_c(m). \tag{B.0.24}$$

C

CODE IN PYTHON FOR THE SIM CALCULATION

A short piece of the code to solve eqs. (5.3.10) and (5.3.13) is shown here. Only the fundamental fragment is displayed, and parts of preparation of the data to be read by the programm are ommitted, since they might depend on the user data. In our case, is passed a list with diameters in nanometers and the fraction of charged particles in succesive columns, obtaining a file with the final values of N_i^0, E_r and the $N_i t$-product with the estimation errors and the fitting data of the mean charge.

Listing 1: Partial code in Python for the calculation of the Nit-product by the Semi-Implicit Method.

```
# Attachment coefficients calculation
# for a corona unipolar device
# Simulation of 1-ff0 from Ni0, Ex and Er
# with constant electrical field in both axis
# all calculation in SI basic

import os
from numpy import *
from sys import *
from scipy import *
from scipy import special
from scipy.integrate import quad, odeint
from scipy.optimize import fminbound, fsolve, curve_fit
import matplotlib.pyplot as plt
from fileutils import *

#-------------------------------------------------------------------------

Difi = Zi*kB*T/ee  # positive ion diffusivity, Einstein's formula

gi = 4.0*Zi/diam1  # auxiliary constant

# diffusion removal coefficient for ions (1/s)
fDifix = 0.0
if IDW:   ## is True:
  fDifix = pi*Difi/(Qa+Qi)

ci = sqrt(8*kB*T*NA/(pi*Mi)) # mean thermal velocity of ions

# diffusion in tubes
# Reist (1993), p. 154
def diftube (p):
   if p <= 1.0e-10: return 1.0
   if p <= 0.02: return 1.0-2.5638*p**0.66667+1.2*p+0.1767*p**1.33333
   else: return 0.81905*exp(-3.6568*p)+0.09753*exp(-22.305*p)+ \
```

```
                0.0325*exp(-56.961*p)+0.01544*exp(-107.62*p)

# relative diffusion from x to x1
def diftubeDx (fdif, x, x1):
   return diftube(fdif*x1)/diftube(fdif*x)

# for ions and gas molecules of equal mass approx:
lami = 8.0/3.0*Difi/sqrt(pi*kB*T*(Mi+Mg)*NA/(Mi*Mg)) # mean free path of ions

kappa = (epsp-1)/(epsp+1)*ee**2 # image force parameter

epp1, epm1 = epsp+1, epsp-1  # auxiliary values

vflux = (Qa+Qi)/(pi/4*diam1**2) # flux velocity

tres = len1/vflux     # residence time

# other parameters
EPSv = 0.0
EPS0 = 1.0e-300

# color list
colors = ["b", "g", "r", "k", "m", "y", "c"]

#-------------------------------------------------------------------------

# particle radius
def part_rad (Dp):
  return Dp/2.0

# limiting sphere radius
def deltaf (a):
  x = lami/a
  return a/x**2*((1+x)**5/5-(1+x**2)*(1+x)**3/3+2/15.0*(1+x**2)**2.5)

# Cunninghan coefficient
def Cc (Kn):
  return 1+Kn*(1.267+0.4*exp(-1.1/Kn))

# diffusion coefficient for a particle of a particle
def Difpf (Dp):
  Kn = 2*lamg/Dp
  return kB*T*Cc(Kn)/(3*pi*mu*Dp)

# electrical mobility
def Zp1 (Dp):
  Kn = 2*lamg/Dp
  return ee*Cc(Kn)/(3*pi*mu*Dp)

EPSphi = 1.0e-17  # for potential series

# ion particle interaction potential
```

```
def phi (r, a, n):
  x = (a/r)**2
  v1 = PNC*n/r
  t1 = epm1/(epp1+1)*x**2
  v2 = t1
  for m in range(2, 1000):
    t = m*epm1/(m*epp1+1)*x**(m+1)
    if t/t1 < EPSphi: break
    v2 += t

  return ee**2/(4*pi*eps0)*(v1-v2/(2*a))

# function b^2
def b2 (r, delta, a, n):
  return r**2*(1+2/(3*kB*T)*(phi(delta, a, n)-phi(r, a, n)))

# probability of collision and transfer of charge
def gammaprob (n, a, delta):
  rm = fminbound(b2, a, delta, args = (delta, a, n), xtol = 1.0e-16) #[0]
  b2m = b2(rm, delta, a, n)
  v = b2m/delta**2
  return 1 if v > 1 else (0 if v < 0 else v)

# integrating function
def faux (x, a, n):
  return exp(phi(1/x, a, n)/(kB*T))

# ion particle combination coefficient
def betaf (a, n):
  delta = deltaf(a)
  eaux = exp(-phi(delta, a, n)/(kB*T))
  intaux = quad(faux, 0, 1/delta, args=(a, n), epsrel = 1.0e-12)[0]
  gg = eaux*ci*delta**2*gammaprob(n, a, delta)
  return pi*gg/(1+gg/(4*Difi)*intaux)

## evolution by semi-implicit method
def evolSIM (Ni0, Er, Ex, beta, g1, fdp, Z1p, nstep=3000):
  '''
  evolution by semi-implicit method
  '''
  m = len(beta)
  Npn = zeros_like(beta)
  Npn[0] = 1.0

  vfluxi = vflux+Zi*Ex    # apparent ion velocity
  gip = 4.0*Zi*Er/diam1/vfluxi

  xa = linspace(0.0, len1, nstep+1)
  Dx = len1/float(nstep)
  Ni = Ni0*ones((nstep+1))

  x = 0.0
```

```
  for it in range(nstep+1):
    if it == 0: continue

    Ni[it] = Ni[it-1]/(1.0+gip*Dx)*diftubeDx(fDifix, xa[it-1], xa[it])
    dd = diftubeDx(fdp, xa[it-1], xa[it])

    Npn[0] *= dd/(1.0+beta[0]*Ni[it]*Dx/vflux)
    for n in range(1, m):
      vfluxp = vflux + n*Z1p*Ex
      Npn[n] = (Npn[n]+Dx/vfluxp*Ni[it]*beta[n-1]*Npn[n-1])/   \
               (1.0+(beta[n]*Ni[it]+n*g1*Er)*Dx/vfluxp)*dd

  return Npn

# extrinsic charge fraction calculation
def extrinsic (fff, charge):
  return sum(fff[:, 1:], axis=1)

# mean charge calculation
def qmean (fff, charge):
  return sum(fff*charge, axis=1)

# First approximation by Semi-Implicit Method (SIM)
def SIM (Ni0, Er, Ex, nstep=3000):
  Nb = zeros_like(fff)
  for i, Dp in enumerate(Dpv):
    NSIM = evolSIM(Ni0, Er, Ex, beta[i,:], g1[i], fdifp[i], Zpp[i], nstep=nstep)
    s = max(EPS0, sum(NSIM))
    Nb[i,:] = NSIM/s

  return Nb

def error2SIM (Ni0, Er, Ex):
  fSIM = SIM(Ni0, Er, Ex)
  return sum((fff-fSIM)**2)

def errorqmed2SIM (Ni0, Er, Ex):
  fSIM = SIM(Ni0, Er, Ex)
  qmedSIM = qmean(fSIM, charge)
  return sum((qmed-qmedSIM)**2)

def func (Dpv, lNi0, lEr, lEx):
  Ni0, Er, Ex = exp(lNi0), exp(lEr), exp(lEx)
  print("Nio = %e, Er = %e, Ex = %e" % (Ni0, Er, Ex))
  fSIM = SIM(Ni0, Er, Ex)

## evolution by SIM
def calc_Nit (Ni0, Er, Ex, nstep=3000):
  '''
  calculation of global Ni*t
  '''
  vfluxi = vflux+Zi*Ex    # apparent ion velocity
```

```
xa = linspace(0.0, len1, nstep+1)
Ni = Ni0*ones((nstep+1))
Dx = len1/float(nstep)
Dt = Dx/vfluxi
Nit = 0.0
gip = 4.0*Zi*Er/diam1/vfluxi

for it, x in enumerate(xa):
   if it == 0:
      Ni[0] = Ni0
      Nit += 0.5*Ni[0]
      continue

   Ni[it] = Ni[it-1]/(1.0+gip*Dx)*diftubeDx(fDifix, xa[it-1], xa[it])
   if it == nstep:
      Nit += 0.5*Ni[it]
   else:
      Nit += Ni[it]

return Nit*Dt
```

BIBLIOGRAPHY

[1] M. Adachi, Y. Kousaka, and K. Okuyama. Unipolar and bipolar diffusion charging of ultrafine aerosol particles. *Journal of Aerosol Science*, 16(2):109–123, 1985. (Cited on pages 33 and 69.)

[2] K. Adamiak and P. Atten. Simulation of corona discharge in point-plane configuration. *J. Electrostat.*, 61:85–98, 2004. (Cited on page 79.)

[3] F. Alguacil and M. Alonso. Multiple charging of ultrafine particles in a corona charger. *Journal of Aerosol Science*, 37(7):875–884, 2006. (Cited on pages xviii, 18, 21, 84, 89, 96, 97, and 99.)

[4] D. J. Alofs and P. Balakumar. Inversion to obtain aerosol size distributions from measurements with a differential mobility analyzer. *Journal of Aerosol Science*, 13(6):513–527, 1982. (Cited on pages 103 and 105.)

[5] M. Alonso and Y. Kousaka. Mobility shift in the differential mobility analyzer due to brownian diffusion and space-charge effects. *Journal of Aerosol Science*, 27(8):1201 – 1225, 1996. (Cited on pages 70 and 121.)

[6] M. Alonso, M. I. Martin, and F. J. Alguacil. The measurement of charging efficiencies and losses of aerosol nanoparticles in a corona charger. *Journal of Electrostatics*, 64(3-4):203–214, 2006. (Cited on pages 20, 23, and 69.)

[7] M. Alonso, F.J. Alguacil, and J.P. Borra. A numerical study of the influence of ion–aerosol mixing on unipolar charging in a laminar flow tube. *Journal of Aerosol Science*, 40(8):693–706, 2009. (Cited on page 24.)

[8] M. Alonso, F.J. Alguacil, and V. Gomez. Approximate relationship between voltage and mobility for brownian particles in cylindrical dmas. *Journal of Aerosol Science*, 58(0):62 – 70, 2013. (Cited on page 118.)

[9] A. Alonso M., Hernandez-Sierra, and F.J. Alguacil. Electrical charging of aerosol nanoparticles and some practical applications. *Rev. Metal. Madrid*, (39): 41 – 57, 2003. (Cited on page 84.)

[10] A. G. Bailey. The science and technology of electrostatic powder spraying transport and coating. *J. Electrost.*, 45(2):85–120, 1998. (Cited on page 33.)

[11] F. S. V. Bazan and J. B. Francisco. An improved fixed-point algorithm for determining a tikhonov regularization parameter. *Inverse Problems*, 25(4):045007, 2009. (Cited on pages 105 and 107.)

[12] R. Benocci, M. Urbano, and L. Mauri. Study of a positive corona discharge in argon at different pressures. *The European Physical Journal D*, 37(1):115–122, 2005. (Cited on page 17.)

[13] G. Biskos, K. Reavell, and N. Collings. Electrostatic characterisation of corona-wire aerosol chargers. *Journal of Electrostatics*, 63(1):69–82, 2005. (Cited on pages 18, 19, and 62.)

[14] G. Biskos, K. Reavell, and N. Collings. Unipolar diffusion charging of aerosol particles in the transition regime. *Journal of Aerosol Science*, 36(2):247–265, 2005. (Cited on pages 19, 23, 69, 79, 81, 82, and 89.)

[15] K. Boisdron and J. R. Brock. On the stochastic nature of the acquisition of electrical charge and radioactivity by aerosol particles. *Atmospheric Environment*, (4):35 –50, 1970. (Cited on pages 80 and 89.)

[16] P. Büscher, A. Schmidt-Ott, and A. Wiedensohler. Performance of a unipolar "square wave" diffusion charger with variable nt-product. *Journal of Aerosol Science*, 25(4):651–663, 1994. (Cited on pages 18, 19, 23, 57, 67, 69, and 79.)

[17] D. Calvetti, B. Lewis, L. Reichel, and F. Sgallari. Tikhonov regularization with nonnegativity constraint. *Electronic Transactions on Numerical Analysis*, 18: 153–173, 2004. (Cited on page 107.)

[18] Cambustion. DMS500 Fast Particulate Spectrometer, 2007. (Cited on page 9.)

[19] D. R. Chen and D. Y. H. Pui. A high efficiency, high throughput unipolar aerosol charger for nanoparticles. *Journal of Nanoparticle Research*, 1(1):115–126, 1999. (Cited on pages 22, 23, 57, and 69.)

[20] J. Chen. *Direct current corona-enhanced chemical reactions*. PhD thesis, University of Minnesota, USA, 2002. (Cited on page 23.)

[21] S. Cheng, M. Ranade, and J. Gentry. Design of high volume corona charger. *Journal of Aerosol Science*, 26:S745–S746, 1995. (Cited on page 19.)

[22] Y. Cheng, Y. Yamada, H. Yeh, and D. Swift. Diffusional deposition of ultrafine aerosols in a human nasal cast. *Journal of Aerosol Science*, 19(6):741–751, 1988. (Cited on page 60.)

[23] C. L. Chien, C. J. Tsai, H. L. Chen, G. Y. Lin, and J. S. Wu. Modeling and validation of nanoparticle charging efficiency of a single-wire corona unipolar charger. *Aerosol Sci. Technol.*, 45:1468–1479, 2011. (Cited on pages 79 and 119.)

[24] D. R. Collins, R. C. Flagan, and J. H. Seinfeld. Improved inversion of scanning DMA data. *Aerosol Science and Technology*, 36(1):1–9, 2002. (Cited on page 105.)

[25] J. Crump and J. Seinfeld. A new algorithm for inversion of aerosol size distribution data. *Aerosol Science and Technology*, 1(1):15–34, 1981. (Cited on pages 105 and 109.)

[26] M. Domat, F.E. Kruis, and J.M. Fernandez-Diaz. Investigations of the effect of electrode gap on the performance of a corona charger having separated corona and charging zones. *Journal of Aerosol Science*, 68(0):1–13, 2014. (Cited on pages 96 and 119.)

[27] P. Dubey and S. Dhaniyala. Analysis of scanning dma transfer functions. *Aerosol Science and Technology*, 42(7):544–555, 2008. (Cited on pages xviii, 111, 116, and 117.)

[28] P. Dubey and S. Dhaniyala. Improved inversion of scanning electrical mobility spectrometer data using a new multiscale expectation maximization algorithm. *Aerosol Science and Technology*, 47(1):69–80, 2013. (Cited on page 105.)

[29] L.M. Dumitran, O. Blejan, P.V. Notingher, A. Samuila, and L. Dascalescu. Particle charging in combined corona-electrostatic fields. *IEEE Transactions on Industry Applications*, 44(5):1385–1390, 2008. (Cited on page 79.)

[30] M. Fiebig, C. Stein, F. Schröder, P. Feldpausch, and A. Petzold. Inversion of data containing information on the aerosol particle size distribution using multiple instruments. *Journal of Aerosol Science*, 36(11):1353–1372, 2005. (Cited on page 105.)

[31] H. Fissan, C. Helsper, and H.J. Thielen. Determination of particle size distributions by means of an electrostatic classifier. *J. Aerosol Sci.*, 14:354–357, 1983. (Cited on pages 9 and 112.)

[32] R. C. Flagan. On differential mobility analyzer resolution. *Aerosol Science and Technology*, 30(6):556–570, 1999. (Cited on pages 111 and 112.)

[33] N.A. Fuchs. *The Mechanics of Aerosols*. Pergamon Press, New York, 1964. (Cited on pages 79 and 80.)

[34] G. Golub, M. Heath, and G. Wahba. Generalized cross-validation as a method for choosing a good ridge parameter. *Technometrics*, 21:215–223, 1979. (Cited on page 107.)

[35] M. Gysel, G. B. McFiggans, and H. Coe. Inversion of tandem differential mobility analyser (TDMA) measurements. *Journal of Aerosol Science*, 40(2):134–151, 2009. (Cited on page 123.)

[36] M. Gysel, G.B. McFiggans, and H. Coe. Inversion of tandem differential mobility analyser (tdma) measurements. *Journal of Aerosol Science*, 40(2):134 – 151, 2009. (Cited on page 121.)

[37] D. E. Hagen and D. J. Alofs. Linear inversion method to obtain aerosol size distributions from measurements with a differential mobility analyzer. *Aerosol Science and Technology*, 2(4):465–475, 1983. (Cited on pages 103, 105, and 108.)

[38] P. C. Hansen. *Rank-deficient and discrete ill-posed problems*. Society for Industrial and Applied Mathematics (SIAM), 1998. ISBN 0-89871-403-6. (Cited on page 107.)

[39] P.C. Hansen and D.P. O'Leary. The use of the L-curve in the regularization of discrete ill-posed problems. *SIAM J. Sci. Comput.*, 14:1487–1503, 1993. (Cited on pages 103, 107, and 108.)

[40] D. J. Harney. *An Aerodynamic Study of the Electric Wind*. PhD thesis, California Institute of Technology, USA, 1957. (Cited on pages 34, 35, and 40.)

[41] M. He and S. Dhaniyala. A multiple charging correction algorithm for scanning electrical mobility spectrometer data. *Journal of Aerosol Science*, 61(0):13 – 26, 2013. (Cited on pages 111 and 120.)

[42] B. L. Henson. A space-charge region model for microscopic steady coronas from points. *Journal of Applied Physics*, 52(2):709–715, 1981. (Cited on page 41.)

[43] S. V. Hering and M. R. Stolzenburg. A method for particle size amplification by water condensation in a laminar, thermally diffusive flow. *Aerosol Science and Technology*, 39(5):428–436, 2005. (Cited on page 8.)

[44] M. Hermann, B. Wehner, O. Bischof, H. Han, T. Krinke, W. Liu, A. Zerrath, and A. Wiedensohler. Particle counting efficiencies of new TSI condensation particle counters. *Journal of Aerosol Science*, 38(6):674–682, 2007. (Cited on page 10.)

[45] A. Hernandez-Sierra, F. J. Alguacil, and M. Alonso. Unipolar charging of nanometer aerosol particles in a corona ionizer. *Journal of Aerosol Science*, 34 (6):733–745, 2003. (Cited on pages 20, 23, 57, 68, and 69.)

[46] G. W. Hewitt. The charging of small particles for electrostatic precipitation. *AIEE Transactions*, 76:300–306, 1957. (Cited on pages 18 and 19.)

[47] W. C. Hinds. *Aerosol technology: properties, behavior and measuremnt of airborne particles*. Wiley-Interscience, New York, 1998. (Cited on pages 4, 5, 6, 7, and 90.)

[48] E. Hontañon and F. E. Kruis. Single charging of nanoparticles by UV photoionization at high flow rates. *Aerosol Sci. Technol.*, 42:310 – 323, 2008. (Cited on pages 22 and 119.)

[49] W. A. Hoppel. Determination of the aerosol size distribution from the mobility distribution of the charged fraction of aerosols. *Journal of Aerosol Science*, 9(1): 41–54, 1978. (Cited on pages 10, 103, 113, and 120.)

[50] D. Hummes, S. Neumann, H. Fissan, and F. Stratmann. Experimental determination of the transfer function of a differential mobility analyzer (DMA) in the nanometer size range. *Particle & Particle Systems Characterization*, 13(5):327–332, 1996. (Cited on pages xviii, 10, 112, and 113.)

[51] E. Husain and R.S. Nema. Analysis of paschen curves for air, n2 and sf6 using the townsend breakdown equation. *Electrical Insulation, IEEE Transactions on*, EI-17(4):350 –353, 1982. (Cited on page 18.)

[52] TSI Inc. Operation and service manual for Electrical Aerosol Detector (EAD) spectrometer, model 3070, revision B, 2004. (Cited on page 20.)

[53] TSI Inc. Operation and service manual for electrostatic classifiers, series 3080, revision G, 2006. (Cited on pages 31, 68, 74, and 112.)

[54] TSI Inc. Operation and service manual for Scanning Mobility Particle Sizer (SMPS) spectrometer, model 3936, revision L, 2006. (Cited on page 31.)

[55] TSI Inc. Operation and service manual for Condensation Particle Counter (CPC), model 3775, revision E, 2007. (Cited on pages 31, 58, and 110.)

[56] TSI Inc. Fast Mobility Particle Sizer (FMPS) spectrometer, model 3091, 2007. (Cited on page 9.)

[57] P. Intra. Corona discharge in a cylindrical triode charger for unipolar diffusion aerosol charging. *Journal of Electrostatics*, 70(1):136 – 143, 2012. (Cited on pages 96 and 119.)

[58] P. Intra and N. Tippayawong. Aerosol size distribution measurement using multi-channel electrical mobility sensor. *Aerosol and Air Quality Research*, 21(4): 329–340, 2006. (Cited on page 24.)

[59] P. Intra and N. Tippayawong. Measurements of ion current from a corona-needle charger using a faraday cup electrometer. *Chiang Mai J. Sci.*, 36(1):110–119, 2009. (Cited on page 38.)

[60] P. Intra and N. Tippayawong. Progress in unipolar corona discharger designs for airborne particle charging: A literature review. *Journal of Electrostatics*, 67(4): 605–615, 2009. (Cited on pages 1, 5, 19, and 65.)

[61] P. Intra and N. Tippayawong. Effect of needle cone angle and air flow rate on electrostatic discharge characteristics of a corona-needle ionizer. *Journal of Electrostatics*, 68(3):254 – 260, 2010. (Cited on pages 18, 21, 38, 42, and 84.)

[62] P. Intra and N. Tippayawong. An overview of unipolar charger developments for nanoparticle charging. *J. Aerosol Res.*, 11:187–209, 2011. (Cited on pages 19 and 24.)

[63] P. R. Johnston and R. M. Gulrajani. Selecting the corner in the L-curve approach to Tikhonov regularization. *IEEE Transactions on Biomedical Engineering*, 47:1293–1296, 2000. (Cited on pages 107 and 108.)

[64] H. Kaminski, T. A. J. Kuhlbusch, H. Fissan, L. Ravi, H.-G. Horn, H.-S. Han, R. Caldow, and C. Asbach. Mathematical description of experimentally determined charge distributions of a unipolar diffusion charger. *Aerosol Science and Technology*, 46(6):708–716, 2012. (Cited on page 119.)

[65] M. N. A. Karlsson and B. G. Martinsson. Methods to measure and predict the transfer function size dependence of individual DMAs. *Journal of Aerosol Science*, 34(5):603–625, 2003. (Cited on page 112.)

[66] B. Khaddour, P. Atten, and J.-L. Coulomb. Numerical solution of the corona discharge problem based on mesh redefinition and test for a charge injection law. *Journal of Electrostatics*, 66:254–262, 2008. (Cited on page 79.)

[67] D. S. Kim, Y. M. Kim, Y. T. Kwon, and K. Park. Evaluation of a soft X-ray unipolar charger for charging nanoparticles. *Journal of Nanoparticle Research*, 13: 579 – 585, 2010. (Cited on pages 18 and 119.)

[68] W. A. Kleefsman and C. Van Gulijk. Robust method to compare aerosol chargers. *Journal of Aerosol Science*, 39(1):1–9, 2008. (Cited on pages 15 and 23.)

[69] E. O. Knutson and K. T. Whitby. Accurate measurement of aerosol electric mobility moments. *Journal of Aerosol Science*, 6(6):453–460, 1975. (Cited on page 104.)

[70] E. O. Knutson and K. T. Whitby. Aerosol classification by electric mobility: apparatus, theory, and applications. *Journal of Aerosol Science*, 6(6):443–451, 1975. (Cited on pages 9 and 104.)

[71] Y. Kousaka, T. Niida, K. Okuyama, and H. Tanaka. Development of a mixing type condensation nucleus counter. *Journal of Aerosol Science*, 13(3):231–240, 1982. (Cited on page 8.)

[72] Y. Kousaka, K. Okuyama, and M. Adachi. Determination of particle size distribution of Ultra-Fine aerosols using a differential mobility analyzer. *Aerosol Science and Technology*, 4(2):209–225, 1985. (Cited on page 8.)

[73] F. E. Kruis and H. Fissan. Nanoparticle charging in a twin hewitt charger. *Journal of Nanoparticle Research*, 3(1):39–50, 2001. (Cited on pages 18, 19, 20, 23, 34, 69, and 84.)

[74] F.E. Kruis and H. Fissan. A modified Hoppel algorithm for inversion of mobility distributions with diffusional-broadened transfer function, multiple charges and arbitary interval width. *Abstract for the Sixth International Aerosol Conference, Taipei, Taiwan*, page 1013, 2002. (Cited on page 103.)

[75] S. Kwon, T. Fujimoto, Y. Kuga, H. Sakurai, and T. Seto. Characteristics of aerosol charge distribution by Surface-Discharge microplasma aerosol charger (SMAC). *Aerosol Science & Technology*, 39(10):987–1001, 2005. (Cited on pages 21, 24, and 119.)

[76] S. Kwon, H. Sakurai, and T. Seto. Unipolar charging of nanoparticles by the surface-discharge microplasma aerosol charger (SMAC). *Journal of Nanoparticle Research*, 9(4):621–630, 2006. (Cited on pages 21, 26, 69, and 119.)

[77] S. Kwon, H. Sakurai, T. Seto, and Y. Kim. Charge neutralization of submicron aerosols using surface-discharge microplasma. *Journal of Aerosol Science*, 37(4): 483–499, 2006. (Cited on pages 18 and 21.)

[78] C. L. Lawson and R. J. Hanson. *Solving Least Squares Problems*. SIAM (revised republication of the first published in Prentice-Hall), 1974. (Cited on page 106.)

[79] H. M. Lee, C. S. Kim, M. Shimada, and K. Okuyama. Bipolar diffusion charging for aerosol nanoparticle measurement using soft x-ray charger. *Journal of Aerosol Science*, 36:813–829, 2005. (Cited on page 22.)

[80] L. Li and D. R. Chen. Performance study of a DC-corona-based particle charger for charge conditioning. *Journal of Aerosol Science*, 42(2):87–99, 2011. (Cited on pages 21, 23, 84, and 119.)

[81] W. Li, L. Li, and D.-R. Chen. Technical note: A new deconvolution scheme for the retrieval of true dma transfer function from tandem DMA data. *Aerosol Science and Technology*, 40(12):1052–1057, 2006. (Cited on page 122.)

[82] B. Y. H. Liu and D. Y. H. Pui. On the performance of the electrical aerosol analyzer. *Journal of Aerosol Science*, 6(3-4):249–264, 1975. (Cited on pages 18, 19, and 69.)

[83] B. Y. H. Liu, D. Y. H. Pui, K. T. Whitby, D. B. Kittelson, Y. Kousaka, and R. L. McKenzie. The aerosol mobility chromatograph: A new detector for sulfuric acid aerosols. *Atmospheric Environment (1967)*, 12(1–3):99 – 104, 1978. (Cited on page 120.)

[84] J. J. Lloyd, C. J. Taylor, R. S. Lawson, and R. A. Shields. The use of the L-curve method in the inversion of diffusion battery data. *J. Aerosol Sci.*, 28:1251–1264, 1997. (Cited on pages 107 and 108.)

[85] A. Marquard, J. Meyer, and G. Kasper. Characterization of unipolar electrical aerosol chargers—Part II:Application of comparison criteria to various types of nanoaerosol charging devices. *Journal of Aerosol Science*, 37(9):1069–1080, 2006. (Cited on pages 20 and 23.)

[86] A. Marquard, J. Meyer, and G. Kasper. Characterization of unipolar electrical aerosol chargers—Part IA review of charger performance criteria. *Journal of Aerosol Science*, 37(9):1052–1068, 2006. (Cited on pages 57, 58, 64, and 65.)

[87] B. G. Martinsson and M. N. A. Karlsso. Methodology to estimate the transfer function of individual differential mobility analyzers. *Aerosol Science & Technology*, 35(4):815–823, 2001. (Cited on page 10.)

[88] P. H. McMurry. The history of condensation nucleus counters. *Aerosol Science and Technology*, 33(4):297–322, 2000. (Cited on page 8.)

[89] A. Medved, F. Dorman, S. Kaufman, and A. Pocher. A new corona-based charger for aerosol particles. *Journal of Aerosol Science*, 31:616–617, 2000. (Cited on pages 18, 20, 57, and 69.)

[90] X. Meng, H.i Zhang, and J.(J.) Zhu. A general empirical formula of current–voltage characteristics for point-to-plane geometry corona discharges. *Journal of Physics D: Applied Physics*, 41(6):065209, 2008. (Cited on page 40.)

[91] A.M. Meroth, T. Gerber, C.D. Munz, P.L. Levin, and A.J. Schwab. Numerical solution of nonstationary charge coupled problems. *Journal of Electrostatics*, 45: 177–198, 1999. (Cited on page 79.)

[92] L. Metnieks and L. W. Pollak. *Introduction for Use of Photo-Electric Condensation Nucleus Counters*. School of Cosmic Physica, Dublin Institute of Advanced Studies, 1959. (Cited on page 8.)

[93] V.A. Morozov. On the solution of functional equations by the method of regularization. *Soviet Math. Dokl.*, 7:414–417, 1966. (Cited on page 107.)

[94] D. Park, M. An, and J. Hwang. Development and performance test of a unipolar diffusion charger for real-time measurements of submicron aerosol particles having a log-normal size distribution. *Journal of Aerosol Science*, 38(4):420–430, 2007. (Cited on page 21.)

[95] D. Park, S. Kim, M. An, and J. Hwang. Real-time measurement of submicron aerosol particles having a log-normal size distribution by simultaneously using unipolar diffusion charger and unipolar field charger. *Journal of Aerosol Science*, 38(12):1240–1245, 2007. (Cited on page 21.)

[96] D. Park, Y.-H. Kim, S.-G. Lee, C. Kim, J. Hwang, and Y.-J. Kim. Development and performance test of a micromachined unipolar charger for measurements of submicron aerosol particles having a log-normal size distribution. *Journal of Aerosol Science*, 41(5):490–500, 2010. (Cited on pages 21 and 62.)

[97] J. Park, C. Kim, J. Jeong, S.-G. Lee, and J. Hwang. Design and evaluation of a unipolar aerosol charger to generate highly charged micron-sized aerosol particles. *Journal of Electrostatics*, 69(2):126–132, 2011. (Cited on page 21.)

[98] F. Paschen. Über die zum funkenübergang in luft, wasserstoff und kohlensäure bei verschiedenen drucken erforderliche potentialdifferenz. *Annalen der Physik*, 273(5):69–96, 1889. (Cited on page 16.)

[99] F. W Peek. *Dielectric phenomena in high voltage engineering*. McGraw-Hill Book Company, inc., 1920. (Cited on pages 17 and 18.)

[100] S. Pfeifer, W. Birmili, A. Schladitz, T. Müller, A. Nowak, and A. Wiedensohler. A novel inversion algorithm for mobility particle size spectrometers considering non-sphericity and additional aerodynamic/optical number size distributions. *Atmospheric Measurement Techniques Discussions*, 6(3):4735–4767, 2013. (Cited on page 105.)

[101] W.H. Press, S.A. Teukolsky, W.T. Vetterling, and B.P. Flannery. *Numerical Recipes. The Art of Scientific Computation*. Cambridge University Press, Cambridge, 1986. (Cited on pages 86 and 91.)

[102] C. Qi, D. R. Chen, and D. Y. H. Pui. Experimental study of a new corona-based unipolar aerosol charger. *Journal of Aerosol Science*, 38(7):775–792, 2007. (Cited on page 69.)

[103] C. Qi, D. R. Chen, and D. Y. H. Pui. Experimental study of a new corona-based unipolar aerosol charger. *Journal of Aerosol Science*, 38(7):775–792, 2007. (Cited on pages 20, 24, 57, 64, 67, 96, and 119.)

[104] C. Qi, D. R. Chen, and P. Greenberg. Performance study of a unipolar aerosol mini-charger for a personal nanoparticle sizer. *Journal of Aerosol Science*, 39(5):450–459, 2008. (Cited on pages 20, 23, 68, and 69.)

[105] D. J. Rader and P. H. McMurry. Application of the tandem differential mobility analyzer to studies of droplet growth or evaporation. *Journal of Aerosol Science*, 17(5):771 – 787, 1986. (Cited on pages 120 and 121.)

[106] S. A. RAMEM. User manual for corona charger, model cc-8020, v2.1, 2010. (Cited on page 20.)

[107] P. C. Reist. *Aerosol Science and Technology*. McGraw-Hill, Inc., New York, 1993. (Cited on pages 5, 7, 16, and 60.)

[108] M. Rojas and T. Steihaug. An interior-point trust-region-based method for large-scale non-negative regularization. *Inverse Problems*, 18:1291, 2002. (Cited on pages 105 and 107.)

[109] H.G. Scheibel and J. Porstendörfer. Generation of monodisperse ag- and nacl-aerosols with particle diameters between 2 and 300 nm. *Journal of Aerosol Science*, 14:113–126, 1983. (Cited on page 31.)

[110] A. Schmidt-Ott and B. Federer. Photoelectron emission from small particles suspended in a gas. *Surface Science*, 106:538–543, 1981. (Cited on page 21.)

[111] J.H. Seinfeld. *Atmospheric Chemistry and Physics of Air Pollution*. John Wiley and Sons, New York, 1986. (Cited on page 1.)

[112] G. J. Sem. Design and performance characteristics of three continuous-flow condensation particle counters: a summary. *Atmospheric Research*, 62(3-4):267–294, 2002. (Cited on page 8.)

[113] M. Shimada, B. Han, K. Okuyama, and Y. Otani. Bipolar charging of aerosol nanoparticles by a soft X-ray photoionizer. *Journal of Chemical Engineering of Japan*, 35:786–793, 2002. (Cited on page 21.)

[114] D. M Sima, S. Van Huffel, and G. H Golub. Regularized total least squares based on quadratic eigenvalue problem solvers. *BIT Numerical Mathematics*, 44 (4):793–812, 2004. (Cited on page 107.)

[115] M. Stano, M. Sabo, M. Kučera, S. Matejčík, H. Y. Han, H. M. Wang, and Y. N. Chu. Ion mobility spectrometry study of negative corona discharge in nitrogen - oxigen mixtures in nitrogen drift gas. *Acta Physica Universitatis Comenianae*, L-LI(1 & 2):77 – 83, 2009 - 2010. (Cited on page 23.)

[116] M. R. Stolzenburg. *An ultrafine aerosol size distribution measuring system*. PhD thesis, University of Minnesota, USA, 1988. (Cited on page 111.)

[117] M. R. Stolzenburg and P. H. McMurry. An ultrafine aerosol condensation nucleus counter. *Aerosol Science and Technology*, 14(1):48–65, 1991. (Cited on page 8.)

[118] M. R. Stolzenburg and P. H. McMurry. Equations governing single and tandem dma configurations and a new lognormal approximation to the transfer function. *Aerosol Science and Technology*, 42(6):421–432, 2008. (Cited on page 122.)

[119] S. Storn and K. Price. Differential evolution – a simple and efficient heuristic for global optimization over continuous spaces. *Journal of Global Optimization*, 11:341–359, 1997. (Cited on page 73.)

[120] F. Stratmann, T. Kauffeldt, D. Hummes, and H. Fissan. Differential electrical mobility analysis: A theoretical study. *Aerosol Science and Technology*, 26(4):368–383, 1997. (Cited on page 111.)

[121] M. Tabrizchi, T. Khayamian, and N. Taj. Design and optimization of a corona discharge ionization source for ion mobility spectrometry. *Review of Scientific Instruments*, 71(6):2321, 2000. (Cited on page 33.)

[122] S. S. Talukdar and M. T. Swihart. An improved data inversion program for obtaining aerosol size distributions from scanning differential mobility analyzer data. *Aerosol Science and Technology*, 37(2):145–161, 2003. (Cited on pages 103, 105, and 109.)

[123] A. Tarantola. *Inverse problem theory and methods for model parameter estimation*. Society for Industrial and Applied Mathematics, Philadelphia PA, 2005. (Cited on page 107.)

[124] O. M. Thomson and G. P. Thomson. *Conduction of Electricity Through Gases, Vol. 3*. Cambridge University Press, UK, 1928. (Cited on page 35.)

[125] A. N. Tikhonov and V. Y. Arsenin. Solutions of ill-posed problems. Review author: Ralph A. Willoughby. *SIAM Review*, 21:266–267, 1979. (Cited on page 106.)

[126] J. Townsend. XI: The potentials required to maintain currents between coaxial cylinders. *Philosophical Magazine Series 6*, 28(163):83–90, 1914. (Cited on page 40.)

[127] C. J. Tsai, S. C. Chen, H. L. Chen, H. M. Chein, C. H. Wu, and T. M.Chen. Study of a nanoparticle charger containing multiple discharging wires in a tube. *Separation Science and Technology*, 43(13):3476–3493, 2008. (Cited on page 19.)

[128] C. J. Tsai, G. Y. Lin, H. L. Chen, C. H. Huang, and M. Alonso. Enhancement of extrinsic charging efficiency of a nanoparticle charger with multiple discharging wires. *Aerosol Science and Technology*, 44(10):807–816, 2010. (Cited on pages 19, 62, and 119.)

[129] S. Twomey. The application of numerical filtering to the solution of integral equations encountered in indirect sensing measurements. *Journal of the Franklin Institute*, 279(2):95–109, 1965. (Cited on page 108.)

[130] S. Twomey. Comparison of constrained linear inversion and an iterative nonlinear algorithm applied to the indirect estimation of particle size distributions. *Journal of Computational Physics*, 18(2):188–200, 1975. (Cited on page 105.)

[131] E. M. van Veldhuizen and W.R. Rutgers. *Proceedings of Frontiers in Low Temperature Plasma Diagnostics IV*. Eindhoven Univ. Technol, 2001. (Cited on pages 15 and 21.)

[132] F. Vega, N. Mora, F. Roman, N. Pena, F. Rachidi, and B. Daout. Design and construction of a corona charged high power impulse generator. In *2009 IEEE Pulsed Power Conference*, pages 1261–1265, Washington, DC, USA, 2009. (Cited on page 21.)

[133] M. Vivas, E. Hontañon, and A. Schmidt-Ott. Reducing multiple charging of submicron aerosols in a corona diffusion charger. *Aerosol Science and Technology*, 42(2):97–109, 2008. (Cited on pages 21, 23, 69, 84, and 119.)

[134] A. Voutilainen. *Statistical inversion methods for the reconstruction of aerosol size distributions*. PhD thesis, University of Kuopio, Finland, 2001. (Cited on pages 8, 103, and 105.)

[135] A. Voutilainen, F. Stratmann, and J. P. Kaipio. A non-homogeneous regularization method for the estimation of narrow aerosol size distributions. *Journal of Aerosol Science*, 31(12):1433–1445, 2000. (Cited on page 107.)

[136] J. Wang. A fast integrated mobility spectrometer with wide dynamic size range: Theoretical analysis and numerical simulation. *Journal of Aerosol Science*, 40(10): 890–906, 2009. (Cited on page 9.)

[137] J. Wang, V. F. McNeill, D. R. Collins, and R. C. Flagan. Fast mixing condensation nucleus counter: Application to rapid scanning differential mobility analyzer measurements. *Aerosol Science and Technology*, 36(6):678–689, 2002. (Cited on page 8.)

[138] R. J. Weber, M. R. Stolzenburg, S. N. Pandis, and P. H. McMurry. Inversion of ultrafine condensation nucleus counter pulse height distributions to obtain nanoparticle (3-10 nm) size distributions. *Journal of Aerosol Science*, 29(5-6): 601–615, 1998. (Cited on page 8.)

[139] K. T. Whitby. Generator for producing high concentration of small ions. *Rev. Sci. Instrum.*, 32:1351–1355, 1961. (Cited on page 20.)

[140] H. J. White. *Industrial Electrostatic precipitation*. Adddison-Wesley Co., Inc., Reading, Mass, 1963. (Cited on pages 5, 6, 16, and 19.)

[141] A. Wiedensohler. An approximation of the bipolar charge distribution for particles in the submicron size range. *Journal of Aerosol Science*, 19(3):387–389, 1988. (Cited on pages xvii, xviii, 10, 68, 69, 74, 75, 124, and 125.)

[142] A. Wiedensohler, P. Büscher, H. Hansson, B. Martinsson, F. Stratmann, G. Ferron, and B. Busch. A novel unipolar charger for ultrafine aerosol particles with minimal particle losses. *Journal of Aerosol Science*, 25(4):639–649, 1994. (Cited on pages xviii, 19, 22, 24, 69, 79, 98, and 100.)

[143] A. Wiedensohler, W. Birmili, A. Nowak, A. Sonntag, K. Weinhold, M. Merkel, B. Wehner, T. Tuch, S. Pfeifer, M. Fiebig, A. M. Fjäraa, E. Asmi, K. Sellegri, R. Depuy, H. Venzac, P. Villani, P. Laj, P. Aalto, J. A. Ogren, E. Swietlicki, P. Williams, P. Roldin, P. Quincey, C. Hüglin, R. Fierz-Schmidhauser, M. Gysel,

E. Weingartner, F. Riccobono, S. Santos, C. Grüning, K. Faloon, D. Beddows, R. Harrison, C. Monahan, S. G. Jennings, C. D. O'Dowd, A. Marinoni, H.-G. Horn, L. Keck, J. Jiang, J. Scheckman, P. H. McMurry, Z. Deng, C. S. Zhao, M. Moerman, B. Henzing, G. de Leeuw, G. Löschau, and S. Bastian. Mobility particle size spectrometers: harmonization of technical standards and data structure to facilitate high quality long-term observations of atmospheric particle number size distributions. *Atmospheric Measurement Techniques*, 5(3):657–685, 2012. (Cited on pages xviii, 119, 124, and 125.)

[144] K. Willeke and P.A. Baron. *Aerosol Measurement: Principles, Techniques and Applications*. Van Nostrand Reinhold, 1993. (Cited on pages 7 and 8.)

[145] J. K. Wolfenbarger and J. H. Seinfeld. Estimating the variance in solutions to the aerosol data inversion problem. *Aerosol Science and Technology*, 14(3):348–357, 1991. (Cited on page 107.)

[146] A. Yehia. Operating regimes of corona and silent discharges in coaxial cylindrical reactors. *Journal of Applied Physics*, 103(7):073301, 2008. (Cited on page 17.)

[147] J. Yli-Ojanperä, J. M. Mäkelä, M. Marjamäki, A. Rostedt, and J. Keskinen. Towards traceable particle number concentration standard: Single charged aerosol reference (SCAR). *Journal of Aerosol Science*, 41(8):719–728, 2010. (Cited on page 1.)

[148] L. Zhao and K. Adamiak. Ehd flow in air produced by electric corona discharge in pin–plate configuration. *Journal of Electrostatics*, 63(3–4):337 – 350, 2005. (Cited on page 34.)

PUBLICATIONS

Some ideas and figures have appeared previously in the following publications:

SCIENTIFIC ARTICLES

- M. Domat, F. E. Kruis, and J. M. Fernandez-Diaz. Investigations of the eect of electrode gap on the performance of a corona charger having separated corona and charging zones. *Journal of Aerosol Science*, 68: 1 - 13, 2014.
- M. Domat, F. E. Kruis, and J. M. Fernandez-Diaz. Determination of the relevant charging parameters for the modelling of unipolar chargers. *Journal of Aerosol Science,* 71: 16 - 28, 2014.

PARTICIPATION IN CONGRESSES

- M. Domat, M. A. Rodriguez-Braña, F. E. Kruis, and J. M. Fernandez-Diaz. Calculation of the electrical field and charge density in a corona unipolar charger with a complex geometry, *European Aerosol Conference*, Manchester (UK), September 4 - 9 (2011), Poster.
- M. Domat, F. E. Kruis, and J. M. Fernandez-Diaz. A unipolar charger as an alternative to a radioactive neutralizer, *International Aerosol Conference*, Helsinki (Finland), August 29 - September 03 (2010), Poster.
- J. M. Fernandez-Diaz, M. A. Rodriguez-Braña and M. Domat. Criticism of some equations for reducing electrical mobility to different thermodynamic conditions, *International Aerosol Conference*, Helsinki (Finland), August 29 - September 03 (2010), Poster.
- F. E. Kruis, M. Domat, N. L. Azong-Wara and J. M. Fernandez-Diaz. A new inversion technique for Differential Mobility Particle Sizers (DMPS), *European Aerosol Conference*, Thessaloniki (Greece), August 24 - 29 (2008), Poster.
- J. M. Fernandez-Diaz, M. Domat and M. A. Rodriguez-Braña. How many lognormal modes a particle size distribution has?, *European Aerosol Conference*, Thessaloniki (Greece), August 24 - 29 (2008), Poster.
- N. L. Azong-Wara, F. E. Kruis, M. Domat and J. M. Fernandez-Diaz.A new inversion technique for Differential Mobility Analizers, *ProcessNet Fachhausschuss Partikelmesstechnik*, TU München (Germany), March 10 - 14 (2008), Oral presentation.
- J. M. Fernandez-Diaz, M. Domat, M. A. Rodriguez-Braña and I. A. San Juan. Quality factors for the optimisation of electrical mobility based particle sizers, *European Aerosol Conference*, Salzburg (Austria), September 9 - 14 (2007), Poster.